THE UNIVERSITY *of* EDINBURGH

An investigation into pathogenic mechanisms leading to neuro-glial-vascular damage and cognitive decline in a mouse model of vascular cognitive impairment

THE UNIVERSITY *of* EDINBURGH

Joshua Beverley MSc BSc (Hons)

Doctor of Philosophy

2020

Table of Contents

Declaration

I declare that this thesis has been composed solely by myself and has not been submitted for any previous degree or qualification. The work described within this thesis comprises my own original work except where otherwise stated in the text. All external sources of data and information have been specifically referenced.

Joshua Beverley
18-12-2020

Acknowledgements

Firstly, I would like to thank Professor Karen Horsburgh for giving me the opportunity to carry out my thesis within her lab, and for always pushing me to work as hard and diligently as possible to produce the very best science I was capable of. I want to thank you for all the hours you spared to help guide me through my PhD as well as for your understanding and support when it came to my personal life.

Next, I want to thank everybody within the Horsburgh lab, as this truly would not have been the same experience without such a friendly, gifted, and supportive team. I especially want to thank Dr Juraj Koudelka who has consistently been there to offer help, support, and guidance throughout, not just by PhD, but also my masters. Your endless optimism and positive outlook were always helpful, even in the 12-hour multiphoton imaging days. Dr Emma Sigfridsson also deserves a special mention as we were together for almost my entire time within the lab. You were always a friendly face open to answering my silly questions during hours of animal work, which really helped to pass the time. I also want to thank Dr Jessica Duncombe who took so much time out to help me during the formative years of my training. Thanks also to Dr Mosi Li, Dr Jemma Pilcher, Dr Akihiro Kitamura, Dr Edel Hennessy, and Dr Jill Fowler for helping support my work and always being open to answering my questions and teaching me new things. I would also like to thank Dr Katie Askew and Dr Gaia Brezzo who brought new energy and expert opinions to the lab and provided great support for the final stages of my PhD. Thank you also to Dr Barry McColl for being my secondary supervisor and always being a friendly, approachable person to discuss my research. Thanks also to Dr Stefan Szymkowiak for always being so generous with your time. A huge thank you goes to the animal unit staff members Duncan, Keith, Will, and Jon who always made my life so much easier.

I also want to thank my family, mum, dad, and Oliver for always supporting me and believing in me. Your love and support mean everything to me, and I really would not be where I am today without it.

I of course must thank Helix. Being in lockdown writing my thesis with you 24/7 has been challenging but stopping to play and cuddle you has helped me through.

Lastly, I want thank Zoë. You have shown immeasurable levels of patience, understanding, and love throughout this process and I will be forever grateful. I can only imagine how tedious it was for you to hear me complain about writing my thesis for so long, but you never showed that and were always there to support me and keep me going. I would not have been able to do it without you.

Thank you all, I will look back with fondness on these memories forever.

Abstract

Vascular cognitive impairment (VCI) refers to the contribution of cerebrovascular disease to a spectrum of cognitive impairments, ranging from subjective cognitive decline to dementia. Compromised cerebral blood flow (CBF) has been heavily implicated in the pathogenesis of cerebrovascular disease, however, the key underlying mechanisms remain to be fully elucidated.

Bilateral common carotid artery stenosis (BCAS) is a surgical method in which micro-coils are applied permanently to both carotid arteries to reduce CBF. The BCAS mouse model recapitulates many of the pathological and functional hallmarks of VCI, making it a valuable experimental model. A prominent feature of the BCAS model is a robust increase in white matter microglial numbers, which are significantly associated with cognitive impairments.

The first aim of this thesis was to test the hypothesis that microglial proliferation directly leads to white matter damage and cognitive impairment following BCAS. BCAS surgery was found to elicit a significant and persistent reduction in CBF, alongside increased microglial proliferation. Pharmacological inhibition of microglial proliferation, through GW2580 treatment, prevented microglial proliferation, reduced microglial lysosomal expression, preserved white matter integrity, and restored spatial learning deficits.

The second aim was to investigate, using the $Cx_3Cr_1^{eGFP}$ microglial reporter line and intravital multiphoton imaging, structural and functional changes within microglial cells following BCAS. The additional pathogenic effects of amyloidosis as a co-morbidity using the transgenic App23 mouse model were also assessed. Microglial structure and process motility were found to be unaltered, at 1-week following BCAS, within both $Cx_3Cr_1^{eGFP/+}$ and $Cx_3Cr_1^{eGFP/+}$App23 mice. Following 3-months of BCAS, microglial density was found to be unaltered, alongside intact neurovascular coupling responses and spatial learning, although, spatial memory was impaired within $Cx_3Cr_1^{eGFP/+}$ mice. Microglial density was also found to be unchanged within $Cx_3Cr_1^{eGFP/+}$App23 mice following 3-months of BCAS. Neurovascular coupling, however, was significantly impaired within $Cx_3Cr_1^{eGFP/+}$App23 mice following BCAS surgery. Spatial learning and memory deficits were found within $Cx_3Cr_1^{eGFP/+}$App23 mice alone, with no additional BCAS mediated deficit. As a means of explaining the lack of microglial response within the $Cx_3Cr_1^{eGFP/+}$ mice, qPCR analysis was carried out and confirmed a ≈5-fold reduction in Cx_3Cr_1 receptor expression.

Considerable evidence has implicated cerebrovascular dysfunction as a pivotal mechanism in the pathophysiology of VCI and dementia. The studies in chapter 3 aimed to test the hypothesis that BCAS causes vascular dysfunction leading to the onset of neuro-glial-vascular damage. Multiphoton imaging of C57BL/6J wild-type mice found significantly reduced RBC

velocity alongside impaired arterial pulsation, and increased leukocyte trafficking, 1-month following BCAS surgery.

In conclusion, the work described within this thesis demonstrates that microglial proliferation plays a causative role in white matter damage and cognitive decline following BCAS, and that this can be successfully targeted to reverse pathological damage and functional deficits. Furthermore, Cx_3Cr_1 receptor signalling was found to play a significant role in the regulation of microglial responses following BCAS. Finally, BCAS was found to not simply be a model of reduced CBF, with impairments in arterial pulsation and increased endothelial activation providing a new framework to contextualise BCAS mediated effects in future studies.

Lay Summary

Dementia is a term used to describe a range of human conditions that predominantly occur at old age and are characterised by significant memory deterioration. Reductions in the amount of blood reaching the brain has been highlighted as an early feature of dementia progression. Reduced brain blood flow is thought to lead to memory impairments through damage to the brains wiring or white matter, which carries signals from one region of the brain to another. In the present thesis an animal model of reduced brain blood flow was used to help uncover the key mechanisms contributing to damage and memory impairments. Previous investigations using this model have highlighted inflammation and blood vessel dysfunction as key potential mechanisms.

Inflammation describes the body's natural defence against damage and infection. Within the brain, the microglial cell represents the primary mediator of inflammation. In response to acute injury or infection, microglial cells multiply to remove harmful molecules by engulfing them or releasing pro-inflammatory signals. Under chronic disease conditions, however, these microglial responses become uncontrolled, causing the excessive release of pro-inflammatory signals leading to damage. This thesis firstly explores the contribution of microglial multiplication to damage and memory impairments following chronic reductions in blood flow to the brain. Pharmacologically blocking microglial multiplication was shown to protect the brains wiring and prevent memory deterioration, within mice, when blood flow to the brain is reduced. The thesis then went on to use specialised microscopes to allow microglial cells to be studied within the brain of live mice following blood flow reductions. Microglial cells were found to be completely unaffected in response reduced brain blood flow. These findings were surprising considering the extensive evidence of microglial changes following blood flow reductions. To allow microglial cells to be visible using the specialised microscope, mice were genetically engineered so that microglial cells emit colour. Interestingly, in the process of attaching colour to these cells a component of the microglial cell was replaced. This component therefore appears to be crucial to the microglial response to reduced brain blood flow. In the final section of this thesis the techniques previously developed, to assess microglia within live mice, were reapplied to the study of the brains blood vessels following reduced brain blood flow. The brains blood vessels are not simply inactive tubes that hold blood and oxygen, they are dynamic vessels that perform key actions that help maintain healthy blood flow throughout the brain. Results demonstrate that reduced blood flow leads to increased blood vessel stress as well as impairments within a key blood vessel function.

Overall, the work presented within this thesis demonstrates that microglial multiplication is fundamental to damage and memory impairments following reduced brain blood flow in mice, and that targeting, or disruption of this response can have a beneficial impact. Furthermore, altered blood vessel function and stress were also observed following reduced brain blood flow, indicating additional mechanisms which could be driving disease progression and inflammatory signalling.

List of Figures

List of Tables

List of Abbreviations

Aβ	Amyloid beta
AD	Alzheimer's disease
APP	Amyloid precursor protein
BBB	Blood brain barrier
BCAS	Bilateral common carotid artery stenosis
BrdU	5-Bromo-2'-deoxyuridine
CAA	Cerebral amyloid angiopathy
CADASIL	Cerebral autosomal dominant arteriopathy with subcortical infarcts and leukoencephalopathy
CBF	Cerebral blood flow
CNS	Central nervous system
CSF	Cerebrospinal fluid
CSF-1	Colony stimulating factor 1
CSF1R	Colony stimulating factor 1 receptor
DAB	3,3' diaminobenzidine tetrahydrochloride
DMF	Dimethyl fumarate
FITC	Fluorescein isothiocyanate
FLAIR	Fluid-attenuated inversion recovery
eGFP	Enhance green florescent protein
ICAM-1	Intracellular adhesion molecule 1
ICP	Intracranial pressure
IL-34	Interleukin 34
IPC	Ischemic preconditioning
ISF	Interstitial fluid
IQR	Interquartile range
Lamp2	Lysosome-associated membrane protein 2
LSPIV	Line scanning particle image velocimetry
LPS	Lipopolysaccharide
MAG	Myelin associated glycoprotein
MRI	Magnetic resonance imaging
NO	Nitric oxide
PBS	Phosphate buffered saline
PET	Positron emission tomography

RBC	Red blood cell
ROIs	Regions of interest
SEM	Standard error of the mean
SVD	Small vessel disease
VaD	Vascular dementia
VCI	Vascular cognitive impairment
WMH	White matter hyperintensities

Chapter 1

Introduction

1.1 Overview

Dementia is characterised by the progressive and unfaltering deterioration of cognitive capacities, leading ultimately to a loss of independence and a need for constant care (Iadecola et al., 2019). In 2018, worldwide dementia cases were estimated to be 50 million, with projections indicating a rise to 152 million by 2050, driven predominantly by the advancing age of the population (Alzheimer's Disease International, 2018). Despite these alarming figures, no disease-altering treatment is currently available, and the cause of late onset dementias are not fully understood. Cerebrovascular disease represents the second most common cause, after Alzheimer's disease (AD), of age-related cognitive decline and dementia (R. N. Kalaria, 2016). Vascular cognitive impairment (VCI) results from all causes of cerebrovascular disease and is a term used to characterise a whole spectrum of cognitive impairments, ranging from mild to severe deficits, ultimately leading to dementia (Farooq & Gorelick, 2013). Vascular contributions to other dementia subtypes, most notably AD, are increasingly apparent, indicating potentially overlapping pathogenic mechanisms (R. N. Kalaria, 2016; Kapasi, DeCarli, & Schneider, 2017). Vascular risk factors such as ageing, hypertension and diabetes have been associated with an increased risk for VCI and dementia (P. B. Gorelick & Nyenhuis, 2013; M. Ihara & Yamamoto, 2016). It has been proposed that vascular risk factors alter vascular haemodynamic responses leading to detrimental effects on endothelial cell function. Endothelial dysfunction has been shown to impede cerebral haemodynamic changes and impair neurovascular coupling mechanisms, leading to both transient and chronic cerebral hypoperfusion, further exacerbating vascular pathology (Di Marco et al., 2015; Poggesi, Pasi, Pescini, Pantoni, & Inzitari, 2016; Joanna M. Wardlaw, Colin Smith, & Martin Dichgans, 2013). Such evidence has highlighted chronic cerebral hypoperfusion as a major contributor to cognitive decline and cerebrovascular pathology leading to VCI and dementia. Chronic cerebral hypoperfusion describes a sustained reduction in cerebral blood flow (CBF), that has been demonstrated to be present before the onset of cognitive decline (Ruitenberg et al., 2005). Disrupted CBF has been identified as a reliable predictor of dementia progression (Alsop, Dai, Grossman, & Detre, 2010; Chao et al., 2010), with the magnitude of CBF reductions correlating with the severity of cognitive impairment

(de Eulate et al., 2017). Reductions in CBF have also been closely related to white matter damage (Barker et al., 2014), with areas of impaired cerebrovascular reactivity found to proceed and therefore predict the appearance of white matter lesions (Sam et al., 2016).

The mechanisms by which chronic cerebral hypoperfusion leads to neuro-glial-vascular damage and cognitive impairments are not yet fully understood, however, animal models have provided a pathological system by which these mechanisms can be uncovered and targeted. Bilateral common carotid artery stenosis (BCAS) surgery is a well-established model of chronic cerebral hypoperfusion, that recapitulates many of the pathological features of VCI such as neuro-glial-vascular damage and cognitive impairments (Duncombe, Kitamura, et al., 2017). Microglial proliferation and activation, as well cerebrovascular dysfunction, have been highlighted as key potential mechanisms leading to neuro-glial-vascular damage and cognitive impairment following BCAS (Duncombe, Kitamura, et al., 2017). White matter microglial expansion is a commonly observed feature following BCAS, and has been correlated with increased white matter damage (Holland et al., 2011; McQueen et al., 2014; Reimer et al., 2011; Shibata, Ohtani R Fau - Ihara, Ihara M Fau - Tomimoto, & Tomimoto, 2004; Wakita, Tomimoto H Fau - Akiguchi, Akiguchi I Fau - Kimura, & Kimura, 1994) and cognitive impairments (Kitamura et al., 2017). Broad acting anti-inflammatory pharmacological approaches, found to improve white matter integrity and cognition following BCAS, were also associated with a reduction in microglial expansion (Fowler et al., 2017; Kitamura et al., 2017; Manso et al., 2017). To date however, direct proof of the causal contribution of microglial proliferation to BCAS mediated damage, has yet to be uncovered.

Microarray analysis, conducted 3 days following BCAS surgery, demonstrated significant alterations within endothelial related genes, alongside the increased expression of pro-inflammatory associated genes (Reimer et al., 2011). Markers of endothelial activation were also found to increase progressively following BCAS, alongside increasing white matter damage and the onset of cognitive impairment (Kitamura et al., 2017). Despite extensive clinical and pre-clinical evidence to implicate cerebrovascular dysfunction in the pathogenesis of VCI, further research is still required to evaluate additional cerebrovascular mechanisms, such as vascular pulsation and leukocyte trafficking, that may by relevant to the onset and progression of VCI.

The work described within this thesis was designed to test the hypothesis that microglial driven neuroinflammation, as well as cerebrovascular dysfunction, compromise the structure and function of white matter tracts, leading to impaired cognition following BCAS. The studies herein describe the investigation of microglial proliferation in the onset of white matter damage and cognitive impairments following BCAS. Furthermore, intravital multiphoton

imaging approaches were employed to allow for the *in vivo* evaluation of microglial, as well as cerebrovascular mechanisms, implicated in the onset and progression of disease within a BCAS mouse model of VCI.

1.2 The cerebral blood supply

The fundamental contribution of the cerebral vasculature to the broad spectrum of pathologies that underlie VCI, highlights the significance of healthy vascular structure and function to brain health. The brain is an extremely energy demanding organ, requiring approximately 15% of the bodies cardiac output despite only representing 2% of the bodies total mass (Williams & Leggett, 1989). This coupled to the fact that the brain has a very limited capacity for storing fuel reserves means that it is highly reliant on an efficient and effective supply of blood, delivering oxygen and energy substrates, in order to support neuronal activity (Hossmann, 1994; Ii et al., 2020).

The brain's vascular supply is delivered through the left and right internal carotid and vertebral arteries (Figure 1.1A), which merge to form a structure known as the circle of Willis which is situated at the base of the brain (Figure 1.1B/C) (Hossmann, 2006). Anterior middle and posterior cerebral arteries exit the circle of Willis and project along the brains surface, across the subarachnoid space, eventually branching to give rise to leptomeningeal arteries (Iadecola, 2013). The leptomeningeal arteries branch into smaller vessels that are able to penetrate deep into the brains parenchyma in the form of arteries and arterioles (Iadecola & Nedergaard, 2007). Arteries and arterioles contain an endothelial cell layer that forms the inner lining of the vessel which is surrounded by one or more layers of smooth muscle, suppling the contractile force to enable the diameter of the vessel to be altered (Jones, 1970). Penetrating vessels are separated from the brain by a basement membrane that delimits the perivascular (Virchow-Robin) space, which stores cerebrospinal fluid (Dyrna, Hanske S Fau - Krueger, Krueger M Fau - Bechmann, & Bechmann, 2013). On the adjacent side of the perivascular spaces, astrocytes join to generate the glia limitans membrane (Girouard & Iadecola, 2006).

As vessels penetrate deeper into the brain, perivascular spaces disappear allowing astrocytic end-feet to make direct contact with the basal lamina to form intracerebral arterioles. Intracerebral arterioles become progressively smaller, lose their smooth muscle layer, and eventually give rise to a vast capillary network, which is supported by the contractile effects of pericytes to direct blood flow throughout the parenchyma. The organisation of the cerebral vasculature means that region specific variations in blood supply exist, due to heterogeneity in capillary density directed by regional blood flow and metabolic demands (Ward & Lamanna, 2004). For example, white matter regions are predominantly supplied by capillaries

situated at the end of the vascular supply chain. Such vascular organisation results in white matter receiving approximately 1/3 of the blood flow supplying the grey matter, this alongside a lack of collateral blood supply renders white matter particularly susceptible to CBF alterations (Harris & Attwell, 2012).

The vascular organisation of the brain means that the vessels supplying the majority of the CBF are located outside the brain's parenchyma. As a consequence, elaborate vascular signalling mechanisms, such as cerebrovascular autoregulation and functional hyperaemia, are essential to coordinate diameter changes of arterioles within the intracerebral microvasculature (Bagher & Segal, 2011; Iadecola, 2004; E. A. Winkler et al., 2019). An added complication of this vascular arrangement is that penetrating arteries and venules, unlike the larger leptomeningeal vessels, do not have compensatory anastomotic branches, and therefore single occlusions can be sufficient to cause small ischemic lesions (microinfarcts) (Blinder et al., 2013; Nguyen, Nishimura, Fetcho, Iadecola, & Schaffer, 2011; Nishimura, Rosidi, Iadecola, & Schaffer, 2010; Shih et al., 2013). Deep white matter regions are particularly vulnerable to reductions in CBF as they are supplied by arterioles exiting the cortical network, a region on the border of the non-overlapping territories of the anterior and middle cerebral arteries (Brown & Thore, 2011; De Reuck, 1971). It is therefore essential that the health of the neuro-glial-vascular unit and cerebral vasculature is maintained to ensure that ischemic conditions are not able to develop.

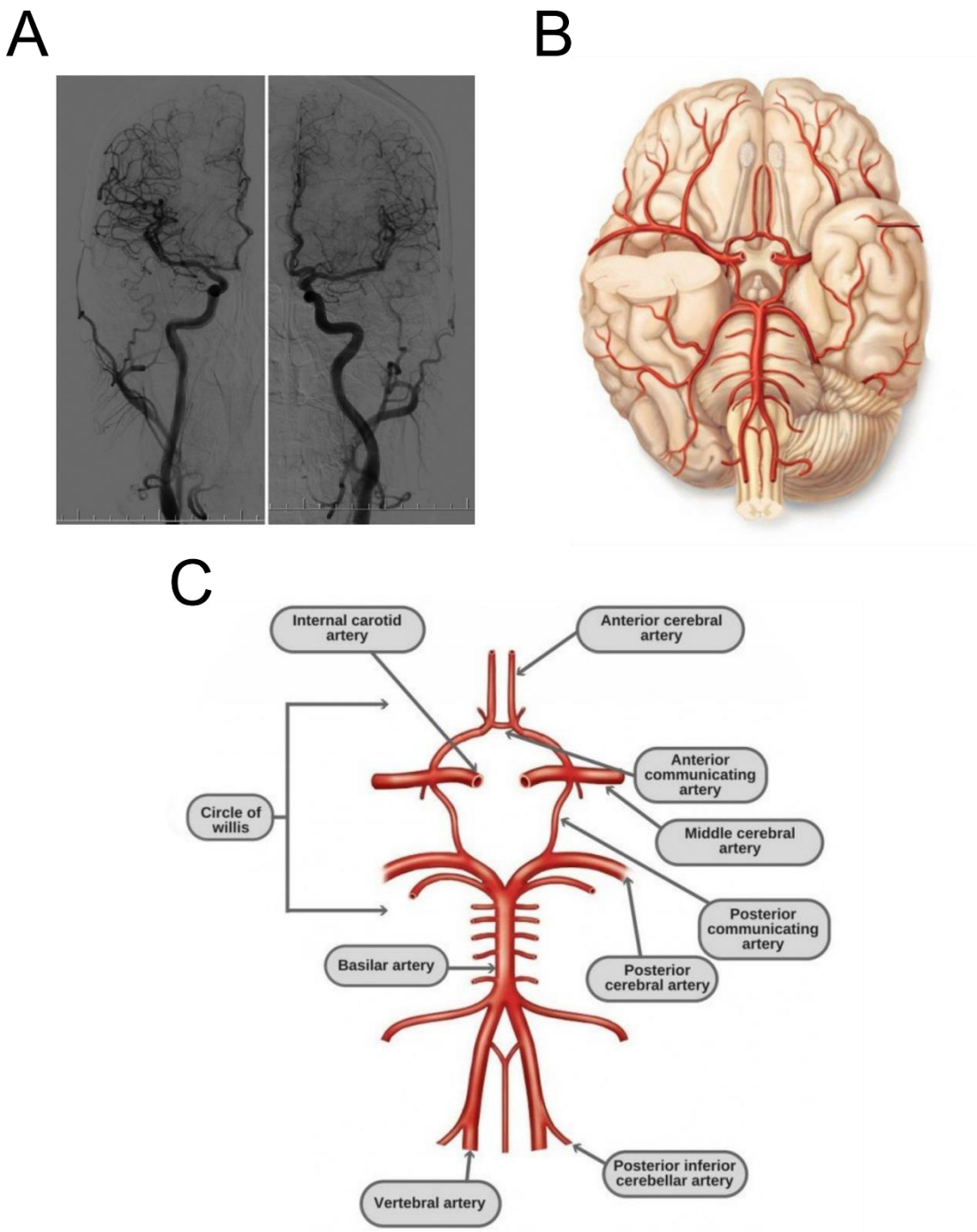

Figure 1.1 Cerebrovascular anatomy. **(A)** Left and right internal carotid artery supplying blood flow to the brain, as seen by angiography (Chandra, Li, Stone, Geng, & Ding, 2017). **(B)** CBF is delivered through the left and right internal carotid and vertebral arteries, which merge to form a structure known as the circle of Willis which is situated at the base of the brain and can be seen within the centre of the image. Vessels branch off from the circle of Willis to form small blood vessels that deliver blood throughout the brain. **(C)** Illustration of the vessels that

form the circle of Willis. Images B and C adapted from https://www.scienceabc.com/humans/circle-of-willis-anatomy-diagram-and-functions.html.

1.3 Cerebrovascular control mechanisms

The regulation of CBF to the brain is a challenging proposition, as not only does CBF need to be sufficient to meet the high metabolic demands of the brain, it also must be highly dynamic to match rapid changes in neuronal activity. Alongside these factors CBF can also be effected by intracranial pressure and peripheral changes in blood pressure making the moment to moment control of CBF crucial to avoid both hypoperfusion and hyperperfusion within the brain (Toth, Tarantini, Csiszar, & Ungvari, 2017). The supply of blood throughout the brain is tightly controlled through the coordinated action of a collection of different cell types, collectively known as the neuro-glial-vascular unit (Figure 1.2). The neuro-glial-vascular unit is comprised of neurons, astrocytes, oligodendrocytes, microglia, perivascular macrophages and microvascular endothelial cells which act in unison to match CBF to the energy demands of the tissue (Lok et al., 2007). Interruption in the supply of CBF to areas of the brain can lead to brain dysfunction and if present over a prolonged period of time even cell death (Kunz & Iadecola, 2009). To combat these varied conditions, cerebral blood vessels possess adaptive mechanisms to ensure that blood flow is always matched to neuronal activity and that this supply is maintained at a stable pressure.

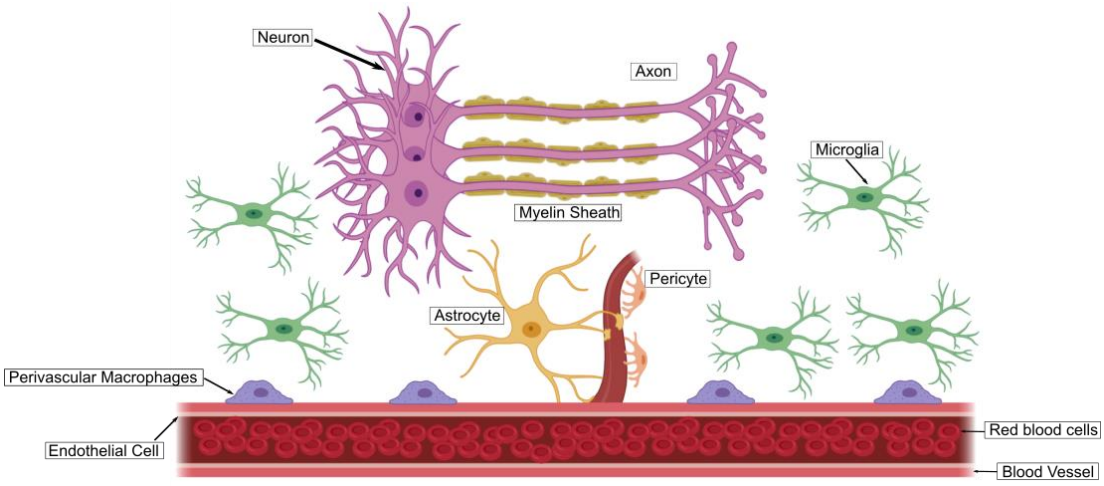

Figure 1.2 The neuro-glial-vascular unit. Cartoon illustration of the neuro-glial-vascular unit, which functions in unison to maintain homeostatic conditions within the brain. Image created with software from BioRender.com.

1.3.1 Cerebrovascular autoregulation

Cerebrovascular autoregulation describes a mechanism by which CBF pressure is maintained at a relatively stable state, despite changes in systemic blood pressure (Iadecola & Davisson, 2008; Paulson, Strandgaard S Fau - Edvinsson, & Edvinsson, 1990). Arterial pressure can vary drastically throughout the day, depending on the level of physical exertion, and therefore it is essential that the cerebrovasculature is not exposed to potentially harmful fluctuations in arterial pressure (Mancia, Parati G Fau - Albini, Albini F Fau - Villani, & Villani, 1988). Due to the ability of vascular smooth muscle cells to contract and relax (myogenic tone) in response to intravascular pressure, CBF can be maintained at a relatively consistent level despite varied levels of arterial pressure (Iadecola, 2013). Cerebral autoregulation can be subdivided into two processes that act on a continuum in response to changing systemic blood pressure. Firstly, dynamic cerebral autoregulation describes the vasculatures ability to respond to very fast changes in perfusion pressure, which is brought about through altered vascular resistance. Secondary, static cerebral autoregulation describes changes to vascular resistance to counteract longer term, more stable, changes in perfusion pressure. The overall result of these processes is that systemic blood pressure changes are counteracted within the vasculature of the brain to prevent excessive changes in vascular pressure (Toth et al., 2017).

1.3.2 Neurovascular coupling

Another essential adaptive response carried out by the cerebral vasculature is known as neurovascular coupling. Neurovascular coupling, or functional hyperemia, describes a process by which the supply of blood flow to a region of the brain is matched to its level of neuronal activity and therefore metabolic demand (Iadecola & Nedergaard, 2007). It has been extensively shown that neuronal activity can promote rapid, within seconds, increases in CBF that are region specific (Cox, Woolsey Ta Fau - Rovainen, & Rovainen, 1993; Ngai, Ko Kr Fau - Morii, Morii S Fau - Winn, & Winn, 1988; Silva, Lee Sp Fau - Iadecola, Iadecola C Fau - Kim, & Kim, 2000). It is thought that neuronal activity signals arterioles within the surrounding area, as well as more distal arteries, to relax causing an increase in blood supply specifically to that area (Kleinfeld, Mitra, Helmchen, & Denk, 1998; Takano et al., 2006). Various components of the neuro-glial-vascular unit have been shown to have a crucial role in these processes. For example astrocytes, whose end-feet processes are in direct contact with cerebral vessels, have been shown to link synaptic activity to cerebrovascular cells to enable an increase in CBF (Iadecola & Nedergaard, 2007). Accumulating evidence also suggests that vascular dilation can be mediated through vasoactive agents that are secreted by components

of the neuro-glial-vascular unit including neurons, astrocytes and endothelial cells (Iadecola & Davisson, 2008). These vasoactive agents include vasodilators such as nitric oxide (NO), prostacyclin and bradykinin (Iadecola & Nedergaard, 2007) as well as vasoconstrictors such as endothelin and endothelium-derived constriction factor (Andresen, Shafi Ni Fau - Bryan, & Bryan, 2006). The coordinated action of the neuro-glial-vascular unit is essential to match CBF to neuronal activity (neurovascular coupling) and therefore the health of each component is essential to prevent the harmful effects of hypoperfusion within the brain.

1.3.3 Cerebrovascular pulsation

Homeostatic processes within the brain, such as the maintenance of CBF and interstitial fluid equilibrium, rely on the tight regulation of intracranial pressure (ICP) and fluid flow (Wagshul, Eide, & Madsen, 2011). The mean ICP and flow are the most important factors in sustaining these processes, however, systemic variations in pressure and flow also play a fundamental role in maintaining tissue homeostasis. The predominant pulsatile force comes from variations in blood pressure over the cardiac cycle, although, other pulsatory forces, such as respiratory and vasomotor induced oscillations, can also have a significant effect on both ICP and flow (Wagshul et al., 2011). Vasomotor induced vascular oscillations, also known as cerebrovascular pulsatility, refers to spontaneous arteriole smooth muscle cell contractions which have recently become of interest to cerebrovascular disease due to their proposed role in the brains waste clearance mechanisms (Jeffrey J. Iliff et al., 2013b). Perivascular spaces are compartments that surround surface and penetrating blood vessels within the brain, which contain either interstitial fluid (ISF) or cerebrospinal fluid (CSF). A key function of these compartments is to facilitate the exchange of ISF and CSF, in a process known as paravascular drainage (Abbott, 2004). Paravascular drainage pathways facilitate the clearance of interstitial solutes and waste products from the brain's parenchyma (Abbott, 2004; Cserr Hf Fau - Ostrach & Ostrach, 1974; Ichimura, Fraser Pa Fau - Cserr, & Cserr, 1991; S. Yamada, DePasquale M Fau - Patlak, Patlak Cs Fau - Cserr, & Cserr, 1991). Multiphoton imaging approaches have demonstrated that a large proportion of subarachnoid CSF re-enters the brain along the paravascular pathways surrounding penetrating arteries, flowing into the terminal capillary beds where exchange with ISF can occur throughout the brain (Iliff et al., 2012; Xie et al., 2013). Cerebral arterial pulsatility has been identified as a key driver of paravascular CSF influx and therefore plays a crucial role in facilitating waste clearance from the brain parenchyma, thus has the potential to contribute significantly to the onset and progression of cerebrovascular disease (Jeffrey J. Iliff et al., 2013b).

1.4 Vascular cognitive impairment

Vascular cognitive impairment (VCI) refers to the contribution of vascular pathology to a spectrum of cognitive impairments, ranging from subjective cognitive decline and mild cognitive impairment to dementia (Farooq & Gorelick, 2013; van der Flier et al., 2018). VCI has been shown to be a causative mechanism within both Vascular dementia (VaD) and AD, and is associated with increased morbidity, disability and a poorer quality of life (Fitzpatrick, Kuller Lh Fau - Lopez, Lopez Ol Fau - Kawas, Kawas Ch Fau - Jagust, & Jagust, 2005; Hill, Fillit H Fau - Shah, Shah Sn Fau - del Valle, del Valle Mc Fau - Futterman, & Futterman, 2005; Knopman, Rocca Wa Fau - Cha, Cha Rh Fau - Edland, Edland Sd Fau - Kokmen, & Kokmen, 2003). Patients with VCI typically display mental slowness and have problems with executive functions, such as planning, initiation, decision making, hypothesis generation, organising, monitoring behaviour and cognitive flexibility (Iadecola et al., 2019; van der Flier et al., 2018). Major VCI is clinically defined as a deficit within at least 1 of these cognitive domains that is significant enough to impair daily living, alongside neuroimaging evidence of cerebrovascular disease (Iadecola et al., 2019; Skrobot et al., 2018).

1.5 Cerebrovascular disease

Cerebrovascular disease describes the underlying neuropathology of VCI, and encompasses a very heterogenous collection of pathologies that can accumulate within a single human brain (Figure 1.3) (Levit, Hachinski, & Whitehead, 2020). Clinical-pathological studies demonstrate a role for cerebrovascular disease, not only as a primary cause of cognitive decline, but also as an agonist for the expression of dementia resulting from other causes, including AD and neurodegeneration (Philip B. Gorelick et al., 2011; Schneider, Arvanitakis Z Fau - Bang, Bang W Fau - Bennett, & Bennett, 2007; Toledo et al., 2013). Cerebrovascular disease encompasses large and small vessel disease, however, the breadth of cerebrovascular disease, alongside the resulting clinical manifestations, remain topics of ongoing research (Jellinger, 2013; Raj N. Kalaria, 2016; Kalaria et al., 2004). Within hereditary cerebrovascular conditions known to result in VCI, such as cerebral autosomal dominant arteriopathy with subcortical infarcts and leukoencephalopathy (CADASIL) (Jellinger, 2013) and Moya Moya disease (Yamashita M Fau - Oka, Oka K Fau - Tanaka, & Tanaka, 1983), both large and small vessel disease can be found throughout the brain in a diffuse and multifocal distribution (Figure 1.3A). Alterations within the large and small cerebral vasculature have also been shown to be key contributors to cognitive impairment resulting from other pathologies, including AD (Iadecola et al., 2019). Such observations have led to the more commonly held view that sporadic, old age, dementias occur due to a combination of cerebrovascular disease

and AD (de la Torre, 2002). Indeed, evaluations of dementia patients at autopsy identified that vascular pathology was present within up to 75% of cases, highlighting the significant occurrence of mixed dementia at old age (*Pathological correlates of late-onset dementia in a multicentre, community-based population in England and Wales. Neuropathology Group of the Medical Research Council Cognitive Function and Ageing Study (MRC CFAS)*, 2001). Additional evaluations of AD patients, the most common form of late onset dementia, demonstrated cerebral vascular pathology in up to 80% of cases (Toledo et al., 2013). It is, therefore, becoming increasingly apparent that cerebrovascular dysfunction has an important role to play in the progression of cognitive impairment observed in ageing, VCI and AD (Iadecola, 2010).

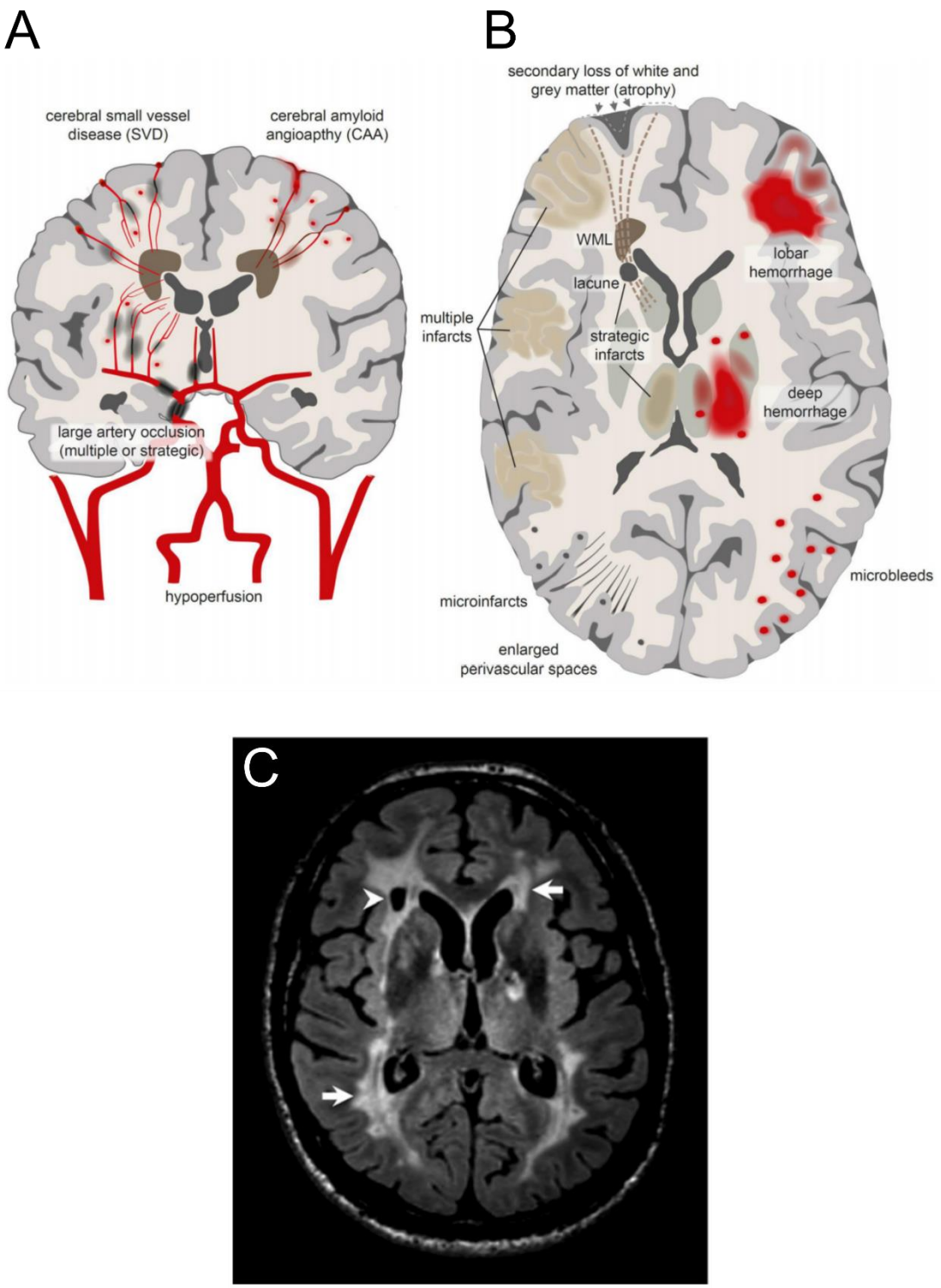

Figure 1.3 Major mechanisms leading to vascular cognitive impairment. **(A)** Vascular associated causes of VCI. **(B)** Brain parenchymal lesions resulting from VCI. **(C)** Fluid-attenuated inversion recovery (FLAIR) image showing extensive white matter hyperintensities (white arrows) and a lacune (white arrowhead). All images adapted from (Dichgans & Leys, 2017).

1.5.1 Large vessel disease

Alterations within the large and small cerebral vasculature have been highlighted as key mechanisms underpinning cerebrovascular disease and contributing to cognitive impairment (Iadecola et al., 2019). Large and small vessel forms of cerebrovascular disease are commonly found to co-exist within the aged brain. Large vessel disease describes pathologies effecting the larger extracranial vessels such as carotid artery stenosis (atherosclerosis), hyalinosis, vessel wall thickening, and fibroid necrosis (Li et al., 2018). Changes in the larger arteries supplying the brain likely compromises the vessels ability to dilate and constrict in response to peripheral blood pressure changes. The loss of cerebrovascular autoregulation leads to uncontrolled fluctuations in blood flow reaching the brain, resulting in abnormal tissue perfusion. Such blood flow changes leave deep cerebral structures and white matter regions particular vulnerable due to a lack of anastomoses and collateral blood flow (R. N. Kalaria, 2016).

1.5.2 Small vessel disease

Cerebral small vessel disease (SVD) describes a pathological disorder which is found within intracranial vessels including small arteries, arterioles, venules, and capillaries (Raj N. Kalaria, 2016). The term SVD, refers not only to intracranial vascular disease, resulting from varied pathological and neurological mechanisms, but also the resulting clinical manifestations and neuroimaging features (Li et al., 2018). Analysis of SVD pathology, highlights abnormalities within arterioles such as arteriolosclerosis, lipohyalinosis, and fibrinoid necrosis (Arvanitakis et al., 2017; Vinters et al., 2018). Capillaries and venules can also be found to be abnormal in the context of SVD, demonstrating that the pathogenesis of SVD is very complex. Cerebral amyloid angiopathy (CAA), is another common feature of cerebrovascular disease and describes the deposition of Aβ into the vascular wall of leptomeningeal and cerebral blood vessels (Attems, Jellinger K Fau - Thal, Thal Dr Fau - Van Nostrand, & Van Nostrand, 2011). Aβ deposits form within the basement membrane or smooth muscle cell layers and can lead to vessel wall rupture and haemorrhage, microbleeds, capillary occlusion, blood flow disturbances, and microinfarcts (Okamoto et al., 2012; Thal et al., 2009). CAA is most commonly observed within AD (Charidimou, Gang Q Fau - Werring, & Werring, 2012), but is also often identified within old aged patients in the absence of AD pathology (Cohen, Hedera P Fau - Premkumar, Premkumar Dr Fau - Friedland, Friedland Rp Fau - Kalaria, & Kalaria, 1997). Severe CAA is associated with cerebrovascular lesions that co-exist with AD, such as lacunar infarcts, microinfarcts, and haemorrhages (Ellis et al., 1996; Okamoto et al., 2012; Olichney et al., 1995).

1.5.3 Neuroimaging features of cerebrovascular disease

To satisfy a clinical diagnosis of VCI, patients need to demonstrate impairment within at least 1 cognitive domain, alongside neuroimaging evidence of cerebrovascular disease (Figure 1.3B) (Iadecola et al., 2019; Skrobot et al., 2018). Magnetic resonance imaging (MRI) has, for a number of years, been employed to identify structural alterations associated with neurological disorders and is considered the gold standard for the neuroimaging of VCI. The characteristic neuroimaging features of cerebrovascular disease include white matter hyperintensities, brain atrophy, subcortical infarcts, lacunes, enlarged perivascular spaces, and microbleeds (J. M. Wardlaw, C. Smith, & M. Dichgans, 2013). White matter hyperintensities, also known as leukoaraisosis, can be observed on T2-weighted MRI scans (Figure 1.3C), and are attributed to white matter lesions. White matter hyperintensities are commonly observed alongside lacunes and small (<1.5cm) white matter infarcts (Iadecola, 2013; Joanna M. Wardlaw, Colin Smith, et al., 2013), and are considered the most important neuroimaging feature of VCI, and are vital for the establishment of a clinical diagnosis (E. E. Smith, 2017).

1.5.4 Cerebrovascular disease pathology

Typical cerebrovascular pathology consist of white matter lesions, lacunes, micro-bleeds, superficial siderosis, enlarged perivascular spaces, and microinfarcts (van Veluw et al., 2017; Joanna M. Wardlaw, Eric E. Smith, et al., 2013). Less commonly observed ultrastructural abnormalities to the microvasculature, include capillary wall deterioration and erythrocyte accumulation, basement membrane thickening, pericyte degeneration, and pallor of perivascular myelin (Farkas, De Jong Gi Fau - de Vos, de Vos Ra Fau - Jansen Steur, Jansen Steur En Fau - Luiten, & Luiten, 2000; R. N. Kalaria, 2016; Lammie, Brannan F Fau - Slattery, Slattery J Fau - Warlow, & Warlow, 1997; Schreiber, Bueche, Garz, & Braun, 2013; Y. Yang & Rosenberg, 2011). Found individually, such cerebrovascular lesions can be asymptomatic, however, increasing numbers of individual lesions, and combinations of different lesion types, are associated with cognitive decline and dementia (Debette, Schilling, Duperron, Larsson, & Markus, 2019).

White matter lesions are consider the neuropathological hallmark of VCI and incorporate a range of white matter changes including rarefaction, vacuolation, incomplete infarction, lacunar infarcts, perivascular spacing, demyelination and axonal degeneration (Iadecola, 2013). Areas of white matter lesions show reduced vascular density and are associated with unstable carotid plaques (Altaf et al., 2006; R. N. Kalaria, 2016). The significance of white matter lesions to disease progression has been highted within a range of neuroimaging studies which have shown a clear association between white matter alterations and cognitive decline

(Joanna M. Wardlaw, Valdés Hernández, & Muñoz-Maniega, 2015). For example, white matter lesions detected by MRI were found to be significantly associated with impairments in the processing speeds of a large human cohort (de Groot et al., 2000). White matter alterations have also been shown to serve as accurate predictors of cognitive decline, with the severity of early white matter changes found to correlate with an increased rate of cognitive decline (Inzitari et al., 2009).

Cerebrovascular disease related brain damage, however, is not limited to lesions visible through standard neuroimaging techniques, with evidence from more sensitive MRI methods revealing alterations within the normally appearing white and grey matter that worsen as cerebrovascular disease burden increases (Baykara et al., 2016; Muñoz Maniega et al., 2017). The various pathologies of cerebrovascular disease lead to oedema and blood brain barrier (BBB) damage, resulting in the uncontrolled movement of fluid and macromolecules into the white matter (Giwa et al., 2012; Joanna M. Wardlaw, Colin Smith, et al., 2013). Disease of the microvasculature may also be associated with inflammatory processes through endothelial cell activation triggering leukocyte and macrophage recruitment (Raj N. Kalaria, 2016). Tissue injury because of cerebrovascular disease is commonly observed in both cortical and subcortical grey and white matter. The mechanisms by which such vessel abnormalities occur and lead to brain damage is still the source of debate. However, increasing evidence would suggest an important role for the components of the neuro-glial-vascular unit, such as microglia, oligodendrocytes, and astrocytes (J. M. Wardlaw, Smith, & Dichgans, 2019).

1.6 Vascular risk factors and underlying cerebrovascular causes of VCI

Due to the considerable variety of cerebrovascular disease pathologies alongside the co-existence of AD and other neurodegenerative diseases, ascertaining the genetic and modifiable risk factors contributing to VCI is challenging (Philip B. Gorelick et al., 2011). The primary risk factor for VCI and dementia is age, with several epidemiological studies also highlighting vascular risk factors such as hypertension and diabetes as key causative factors (Raz, Knoefel, & Bhaskar, 2016; Ruitenberg et al., 2005). Overlapping vascular risk factors associated with VCI and AD further strengthen the evidence for shared vascular pathologies, with estimates indicating that ≈50% of AD risk can be explained by cardiovascular risk factors (D. E. Barnes & Yaffe, 2011). The mechanisms by which vascular risk factors contribute to VCI are ill-defined, however, there is considerable evidence to suggest that endothelial dysfunction plays a pivotal role (Di Marco et al., 2015; Poggesi A Fau - Pasi, Pasi M Fau - Pescini, Pescini F Fau - Pantoni, Pantoni L Fau - Inzitari, & Inzitari, 2016; Joanna M. Wardlaw, Colin Smith, et

al., 2013). Evidence from animal and human studies indicates that these vascular risk factors may alter vascular haemodynamics, detrimentally impacting cerebrovascular regulation, leading to the disruption of crucial regulatory pathways such as endothelium-dependent vasodilation, neurovascular coupling and autoregulation (Di Marco et al., 2015; Iadecola & Davisson, 2008; Poggesi et al., 2016; J. M. Wardlaw et al., 2013; Joanna M. Wardlaw, Eric E. Smith, et al., 2013). Such impairments in cerebral haemodynamics can lead to transient or chronic cerebral hypoperfusion which has been shown to exacerbate cerebrovascular disease pathologies, such as white matter damage. In addition, it has been proposed that the BBB can become compromised early in VCI leading to a chronic hypoxic state and cerebral hypoperfusion (Di Marco et al., 2015; Poggesi A Fau - Pasi et al., 2016; Joanna M. Wardlaw, Colin Smith, et al., 2013). Such findings have highlighted chronic cerebral hypoperfusion as a major contributor to neurodegenerative processes leading to VCI and dementia.

1.7 Chronic cerebral hypoperfusion as a key mechanism leading to white matter damage and cognitive impairment

Chronic cerebral hypoperfusion has been shown to lead to diffuse white matter changes, which are strongly related with cognitive impairment (Longstreth et al., 1996; Poggesi A Fau - Pantoni et al., 2011). Neuroimaging studies have demonstrated that areas containing white matter hyperintensities exhibit reduced CBF (Brickman et al., 2009; Schuff et al., 2009). Perfusion deficits have also been identified within normally appearing white matter, which have been successfully used to predict the occurrence of future white matter alterations (Bernbaum et al., 2015; Promjunyakul et al., 2015). Such findings implicate reduced CBF in the onset and progression of white matter hyperintensities, which are known to correlate strongly with cognitive impairment (Barker et al., 2014). Furthermore, chronic reductions in CBF, has been identified within the prodromal stages of dementia (Ruitenberg et al., 2005) before the onset of clinical symptoms, and therefore could represent one of the earliest changes in disease progression (Austin et al., 2011). Disrupted CBF has been shown to be a reliable predictor of which patients will progress from mild to severe cognitive impairment and ultimately dementia (Alsop et al., 2010; Chao et al., 2010) and can identify which patients have an increased genetic risk of developing dementia (Thambisetty, Beason-Held L Fau - An, An Y Fau - Kraut, Kraut Ma Fau - Resnick, & Resnick, 2010). The magnitude of CBF reductions has been shown to correlate to the severity of cognitive impairment (de Eulate et al., 2017) with chronically hypoperfused patients displaying increased cognitive deficits in comparison to aged matched controls (Ruitenberg et al., 2005). A reduced resting CBF as well as reduced CBF responses to brain activation have also been described in multiple

neurodegenerative conditions including AD (Iadecola, 2004). Moreover, hemodynamic impairment of mean blood flow velocity, pulsatility index, and cerebrovascular reactivity were observed within the middle cerebral artery of AD patients. Thus highlighting haemodynamic impairment as an early and critical marker of vascular damage within AD (Raz et al., 2016; Stefani et al., 2009).

1.7.1 Carotid artery stenosis: A leading cause of chronic cerebral hypoperfusion

Carotid artery stenosis is one of the primary causes of chronic cerebral hypoperfusion, and describes the narrowing of the carotid arteries as a result of atherosclerosis, which is associated with reduced CBF and declining cognition (Balucani, Viticchi G Fau - Falsetti, Falsetti L Fau - Silvestrini, & Silvestrini, 2012). Carotid artery stenosis is also considered an important risk factor for white matter disease (Baradaran et al., 2016; Kandiah, Goh, Mak, Marmin, & Ng, 2012), and is associated with white matter damage and cognitive dysfunction (Jokinen et al., 2007; Ryberg et al., 2011; Tomimoto et al., 2004). Longitudinal clinical studies demonstrate that patients with moderate or severe intracranial stenosis have an accelerated rate of cognitive and functional decline relative to those without (Zhu, Wang Y Fau - Li, Li J Fau - Deng, Deng J Fau - Zhou, & Zhou, 2014). Carotid-artery occlusion or high-grade stenosis have been shown to cause cognitive impairments alone, even in the absence of macroscopic brain lesions (Balestrini et al., 2013; Cheng et al., 2012; Johnston et al., 2004). Additional clinical studies have also demonstrated that haemodynamic failure following carotid artery occlusion is independently associated with cognitive impairment (Marshall et al., 2012).

Despite substantial mounting evidence of the significance of reduced CBF to the onset and progression of VCI (de la Torre, 2000), the mechanisms underlying such damage and dysfunction remain largely unknown. Animal models, therefore, represent an important avenue by which key pathogenic mechanisms can be identified and the benefit of targeting such pathways can be evaluated.

1.8 Experimental models to study VCI

To enable the study of early pathological mechanisms contributing to VCI, rodent models of chronic cerebral hypoperfusion were developed. The first of these were established in rats through the occlusion or ligation of both common carotid arteries to elicit a severe, >70%, reduction in CBF (Farkas, Luiten Pg Fau - Bari, & Bari, 2007; Farooq & Gorelick, 2013). Such models were established in the Wistar and Sprague-Dawley rat strains, which are able to tolerate complete blockade of both common carotid arteries due to intact circle of Willis'

allowing for sufficient collateral blood flow (Farkas et al., 2007). Such models were then established within mice, however, due to the poor collateral flow through the circle of Willis, within C57BL/6J mice, models had to be adapted so that carotid arteries were temporarily, and not permanently, occluded to permit survival (G. Yang et al., 1997). Such approaches were found to lead to severe, 80-90%, reductions in CBF resulting in transient global ischemia (Kitagawa et al., 1998). Concerns over the occlusion models ability to accurately recapitulate the milder 20-30% blood flow reductions observed within human VCI, led to the development of the bilateral common carotid artery stenosis (BCAS) model in rats (Wakita et al., 1994). The BCAS model was then established within mice due to the increased accessibility of molecular technologies such as knockout and transgenic lines (Figure 1.4) (Shibata et al., 2004). BCAS mouse models have gone on to be used extensively within our laboratory and others as a tractable and reproducible model of VCI.

1.8.1 Bilateral common carotid artery stenosis

The BCAS model achieves cerebral hypoperfusion through the application of micro-coils, around both the common carotid arteries, resulting in a ≈50% reduction in luminal diameter (Shibata et al., 2004). This method takes advantage of a lack of collateral blood flow within C57BL/6J mice to elicit a significant and sustained reduction in CBF following surgery (Shibata et al., 2004). The most commonly used BCAS model, utilises 2x0.18mm micro-coils which achieve a 30-40% reduction in CBF immediately following surgery, with recovery overtime within young 3-4 month old mice, leading to an overall 15-20% CBF reduction (Holland et al., 2015; McQueen et al., 2014; Shibata et al., 2004). Other micro-coil sizes and combinations, such as the 0.16mmx0.18mm mixed coil model, are also used to elicit varying severities of CBF reductions (Fowler et al., 2017; Miki et al., 2009). Alongside the varying diameter of micro-coils and combinations used, periods of recovery between left and right micro-coil attachment can also differ between groups. Due to such a high degree of variability between BCAS methods, comparisons between research groups can be difficult. It is therefore crucial that blood flow reductions are accurately measured following surgery, as the level of cerebral hypoperfusion and not the diameter of the micro-coils is of crucial importance. Laser speckle and Doppler flowmetry are two of the most commonly used methods to monitor CBF reductions following BCAS surgery. Both imaging methods project visible-to-infrared laser beams onto the surface of the skull to detect scatter interference patterns generated by blood flow. Such approaches provide, relatively non-invasive, methods by which blood flow reductions can be assessed longitudinally flowing BCAS surgery (Postnov, Cheng, Erdener, & Boas, 2019). A key limitation of these techniques, however, is that they are constrained by

the limited depth of laser penetration that can be achieved, thus restricting blood flow assessments to the cortical surface. Arterial spin labelling MRI methods, however, demonstrated a ≈50% reduction in cortical and subcortical blood flow 24-hours following BCAS surgery, recovering to ≈70-75% of baseline by 1-month (Boehm-Sturm et al., 2017; Hattori et al., 2016). Thus, indicating that BCAS surgery elicits widespread blood flow reductions, that are not limited to the cortical vasculature.

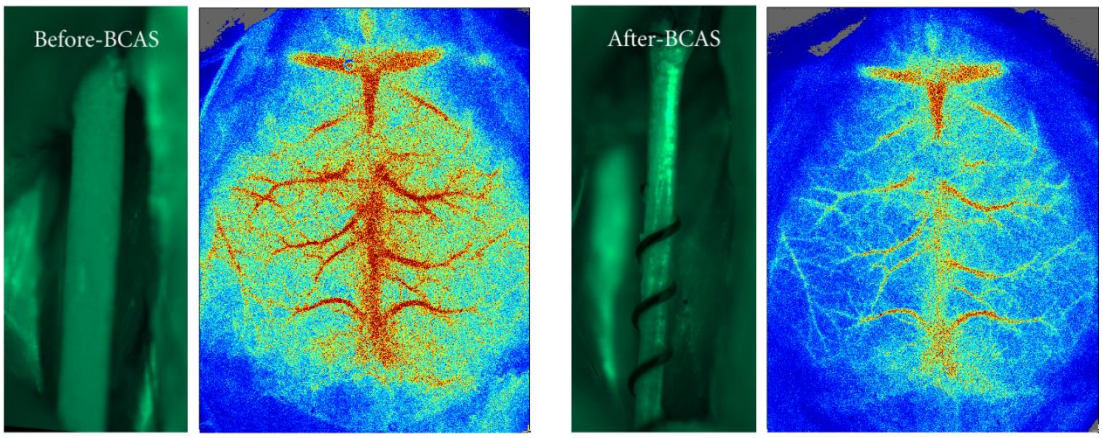

Figure 1.4 Bilateral common carotid artery stenosis surgery (BCAS). Representative images in green of FITC-perfused common carotid arteries before and after micro-coil application (Masafumi Ihara & Tomimoto, 2011). Images appear alongside laser speckle representative images of CBF measures before and after mixed coil BCAS surgery.

1.8.2 BCAS mediated neuropathological changes

As referred to previously, alterations within the brains white matter has been identified as a prominent feature of VCI and contributes to the onset and progression of cognitive impairments (Prins & Scheltens, 2015). A key feature of the BCAS model is the development of white matter damage in the absence of overt ischaemic neuronal perikaryal damage. Early investigations, 2-weeks following BCAS surgery, identified white matter rarefaction and vacuolation, associated with a prominent glial response (Shibata et al., 2004). Additional immunohistochemical evaluations, 1-month following BCAS, highlighted widespread white matter damage, as detected by increased levels of myelin associated glycoprotein (MAG) and degraded myelin protein (Holland et al., 2015; Reimer et al., 2011; Shibata et al., 2004; Wakita et al., 1994). BCAS has also been shown to lead to the selective disruption of key proteins within the paranodal axon-glial junctions, causing a loss of stability and function within myelinated axons resulting in impaired white matter function (Reimer et al., 2011). It is

important to note, however, that white matter damage and functional impairments are observed within the BCAS model in the absence of overt demyelination (McQueen et al., 2014).

Alterations within the cerebral vasculature, indicative of cerebrovascular disease begin to occur at more chronic timepoints following BCAS surgery. Sustained BCAS, >6-months, induces morphological changes to small vessels, such as increased thickening, fibrin deposition, and fibrosis of capillary walls (Holland et al., 2015). Overt BBB disruption is also apparent, 6-months following BCAS surgery, as determined through parenchymal fibrinogen deposits and a reduction in tight junction protein claudin-5 (Holland et al., 2015). Other studies, in which BCAS induced more significant blood flow reductions and white matter damage, report evidence of BBB dysfunction at the much earlier timepoints of 3- and 7-days following surgery (Seo et al., 2013). These differences likely reflect the variability in the severity of CBF reductions following BCAS surgery that exists between research groups.

1.8.3 BCAS mediated cognitive impairments

A fundamental aspect of both severe VCI and dementia is the development of cognitive deficits. It has previously been proposed that chronic cerebral hypoperfusion directly contributes to cognitive decline (de la Torre, 2000). Behavioural investigations, using the 8-arm radial maze and Y-maze tests, within the BCAS model have mainly reported deficits in spatial working memory (Maki et al., 2011; Shibata et al., 2007; Wakita et al., 1994; Washida et al., 2010). Following 1-month of BCAS spatial working memory, but not reference memory, was impaired indicating a potential selective frontal-subcortical circuitry deficit (Wakita et al., 1994). Spatial working memory was, however, found to be impaired 4-months following BCAS, as assessed through the 9-arm radial maze (Hase et al., 2018). Following chronic BCAS, >6-months, both spatial working memory and spatial reference memory were found to be impaired, as assessed by the 8-arm radial arm and Morris water mazes (Holland et al., 2015). Impairments in spatial learning are apparent 6-months following BCAS, as assessed via the Barnes maze (Nishio et al., 2010). The Barnes maze is land based version of the Morris water maze, which assesses the time taken for each mouse to locate an escape chamber that is present within 1 of the 20 available holes (C. A. Barnes, 1979). The advantage of the Barnes maze is that the motivation to explore is produced via aversive stimuli, such as bright lights and white noise audio. Such methods remove the need for the use of, potentially response altering, motivation methods such as dietary restriction as well as eliminating the physical stress induced by swimming reliant tasks. The onset of both working and reference memory impairments following chronic BCAS, likely reflects the presence of both white and grey

matter pathology, including whole brain and hippocampal specific atrophy (Holland et al., 2015; Nishio et al., 2010).

1.8.4 The interplay between BCAS and comorbidities

VCI and dementias are very heterogenous conditions, which is reflected at *post-mortem* by the variety of pathological lesions and mixed pathologies that are commonly observed within the elderly, such as white matter damage, microinfarcts, microbleeds, and amyloid pathology (Kalaria, 2012). Such findings indicate the importance of studying these various pathologies in conjunction, to more accurately model human disease conditions.

1.8.5 BCAS coupled to amyloidosis

It has been demonstrated that neurovascular pathology is present in up to 80% of sporadic late-onset AD patients (Toledo et al., 2013). Indicating, that cerebrovascular disease and amyloidosis are commonly found in conjunction. Aβ deposition is one of the key pathological hallmarks of AD and is proposed to be one of the fundamental drivers of pathophysiology. As rodents do not naturally form Aβ deposits, human amyloid precursor protein (APP) mutations are most commonly introduced to model amyloidosis *in vivo.* An example of such a model system is the App23 mice model, which was genetically engineered to overexpress human APP containing the Swedish KM670/671NL mutation. App23 mice develop both meningeal and parenchymal amyloid deposits by 6-months of age and display pathological, cognitive, and behavioural changes typical for AD patients (Shang J Fau - Yamashita et al., 2016; Sturchler-Pierrat et al., 1997). Previous studies within App23 mice in combination with BCAS have demonstrated exacerbated neuronal loss, BBB leakage, as well as worsened AD pathology including neurovascular unit disruption, loss of axon-glial integrity and cerebrovascular remodelling (Shang J Fau - Yamashita et al., 2016; Zhai Y Fau - Yamashita, Yamashita T Fau - Nakano, Nakano Y Fau - Sun, Sun Z Fau - Morihara, et al., 2016).

BCAS has also been applied to a number of different transgenic APP models, with reports of varied effects on amyloid deposits, cerebrovascular pathology and cognition. The C57BL/6-Tg(Thy1-APPSwDutIowa)BWevn/J mouse model (J. Davis et al., 2004) demonstrated increased leptomeningeal Aβ, associated with microinfarcts and impaired microvascular function, following BCAS surgery (Okamoto et al., 2012). Transgenic mice with Swedish, Dutch and Iowa mutations (Tg-SwDI) demonstrated increased parenchymal levels of soluble Aβ peptides (Aβ40/42), APP as well as APP proteolytic products following BCAS surgery (Salvadores, Searcy, Holland, & Horsburgh, 2017). Alterations in the pools of APP and amyloid peptides following BCAS have also been associated with increased CAA,

microinfarct load and haemorrhages (Salvadores et al., 2017). Furthermore, BCAS surgery within App Swedish and Indiana mutated mice (AppSw/Ind) exacerbated neuronal loss, altered Aβ metabolism and led to impairments in spatial learning, not observed within AppSw/Ind mice alone (M. Yamada et al., 2011).

Despite clear evidence of a harmful synergistic effect of BCAS and amyloidosis, the mechanisms by which pathology and function are exacerbated remain unclear. A common feature of human AD, transgenic APP models and BCAS models is a pronounced pro-inflammatory environment, including the activation of microglia and the release of pro-inflammatory cytokines (Duncombe, Kitamura, et al., 2017; Heneka et al., 2015; Heppner, Ransohoff, & Becher, 2015). Such mechanisms, however, require additional study in order confirm a causal role in the detrimental synergistic effect of BCAS and amyloidosis.

1.9 Potential pathophysiological mechanisms underlying white matter damage and cognitive impairment

1.9.1 Neuroinflammation

Neuroinflammation describes an endogenous protective response within the brain, primarily mediated by microglial cells, which functions to combat infection and limit tissue damage caused by invading pathogens, dying cells, and cellular debris (Salter & Stevens, 2017). Once consider the rudimentary macrophages of the brain, microglial have emerged as fundamental players within a variety of central nervous system (CNS) disorders, ranging from neurodevelopmental conditions such as autism to neurodegenerative disorders such as VCI and dementia. Alongside significant roles within disease conditions, crucial microglial functions within the healthy brain have also been reported, with key roles in neurodevelopment and homeostatic maintenance (Salter & Stevens, 2017). The emergence of intravital imaging, microglial reporter lines, as well as more sophisticated molecular tools, provides new opportunities to help uncover the role of microglia in the onset and progression of VCI and dementia.

1.9.2 Genetic models and intravital imaging aid microglial research

The study of microglial physical dynamics and biological functions, in both healthy and diseased brains, have been the focus of intense scientific activity over recent years. The emergence of genetic models alongside more sophisticated neuroimaging methods has

uncovered novel microglial functions as well as the redefinition of classical ones (Diego Gomez-Nicola & V. Hugh Perry, 2015). A major breakthrough within microglial research came following the generation of a transgenic knock-in mouse expressing green fluorescent protein (GFP) driven by the myeloid specific chemokine receptor Cx_3Cr_1. $Cx_3Cr_1^{eGFP}$ mice express green florescent protein within microglia, perivascular macrophages, peripheral macrophages, and monocytes (Jung, Aliberti, et al., 2000). The ability to readily visualise microglial cells, without the need for immunohistochemistry or specialised staining, alongside the development of multiphoton microscopy, provided unprecedented methodologies to assess microglial functions *in vivo* (R. M. Ransohoff & J. El Khoury, 2015). Multiphoton microscopy is a minimally invasive imaging method offering high spatial resolution, in the range of micrometres, as well as very fast imaging acquisition (Hierro-Bujalance, Bacskai, & Garcia-Alloza, 2018). Multiphoton microscopy possesses several distinct advantages over other commonly used neuroimaging approaches. For example, through the use of low energy near infrared light, with excitation limited to a single plane of focus, phototoxicity and tissue damage is dramatically reduced, allowing for chronic *in vivo* imaging over extended periods (Hierro-Bujalance et al., 2018). As multiphoton microscopy florescence is limited to a single point of focus, absorption and scattering of light is limited, allowing for much deeper imaging, with common set ups reaching depths of ≈500µm (Levene, Dombeck Da Fau - Kasischke, Kasischke Ka Fau - Molloy, Molloy Rp Fau - Webb, & Webb, 2003). Transgenic microglial reporter lines alongside multiphoton imaging have allowed for structural and functioning imaging of microglia within the living brain, providing a greater understanding of microglial behaviour both under homeostatic and disease conditions.

1.9.3 Microglia under normal homeostatic conditions

Microglia are the resident myeloid cell population of the CNS parenchyma, acting as active sensors of disturbances within their own microenvironment, with the capacity to initiate a diverse spectrum of responses to help restore tissue homeostasis (U. K. Hanisch & H. Kettenmann, 2007; Kreutzberg, 1996). Microglia have an abundant array of functions under normal homeostatic conditions including synaptic organisation, trophic neuronal support during development, phagocytosis of apoptotic cells in the developing brain, myelin turnover, control of neuronal excitability, phagocytic debris removal as well as brain protection and repair (Figure 1.5) (Bachiller et al., 2018). The development of single cell isolation techniques, alongside RNA sequencing advancements, have helped to delineate microglial cells from other mononuclear phagocytes within the CNS. Analysis of these datasets revealed microglial

specific transcripts such as P2ry12, P2ry13, Tmem119, Gpr34, siglech, Trem2, and Cx_3Cr_1 (Beutner et al., 2013; Hickman et al., 2013).

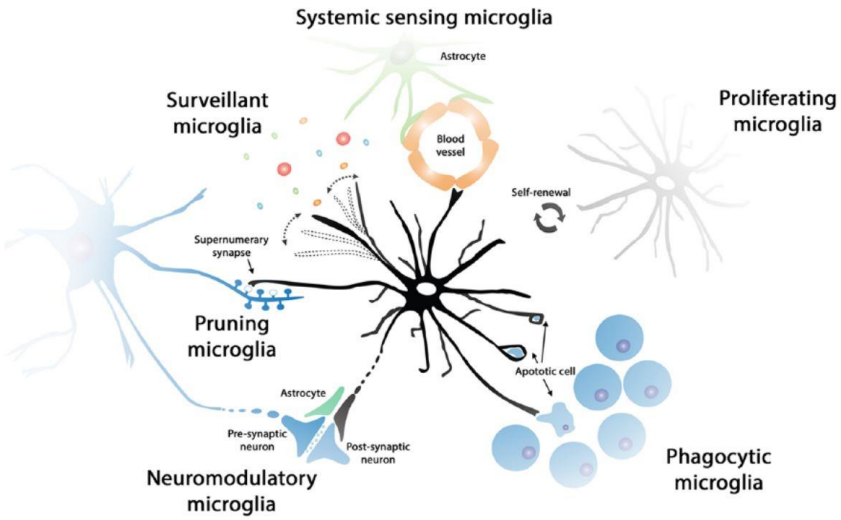

Figure 1.5 Functional processes carried out by microglia within the healthy brain. Under normal homeostatic conditions, microglia carryout a range of significant functions to help support and maintain the components of the neuro-glial-vascular unit. Image taken from (D. Gomez-Nicola & V. H. Perry, 2015).

Fate mapping studies have demonstrated that microglia mainly originate within the yolk sac, colonising within the neuroepithelium in early embryogenesis, having been derived from primitive macrophages (Ginhoux et al., 2010). The microglial population is maintained by the self-renewal of proliferating resident cells, and function largely independently of bone-marrow-derived cells in the healthy brain (D. Gomez-Nicola & V. H. Perry, 2015). Microglial proliferation therefore relies on *in situ* mechanisms to regulate turnover, with little or no contribution from circulating progenitor cells (Lawson, Perry Vh Fau - Gordon, & Gordon, 1992; Prinz & Mildner, 2011). The colony stimulating factor 1 receptor (CSF1R) is a myeloid specific class III receptor tyrosine kinase responsible for signalling cascades required for the development, survival, recruitment, and proliferation of mononuclear phagocytes such as microglia, perivascular macrophages, and peripheral macrophages (Dai et al., 2002; Raivich & Kreutzberg, 1994; Rojo et al., 2019). CSF1R has two known ligands, colony stimulating factor 1 (CSF-1) and interleukin 34 (IL-34), which are both produced locally within the CNS (Easley-Neal, Foreman, Sharma, Zarrin, & Weimer, 2019). IL-34 is predominantly expressed by neurons (Greter et al., 2012; Y. Wang et al., 2012), whereas CSF1 is produced by astrocytes, oligodendrocytes, and microglia (Cahoy et al., 2008). The importance for CSF1R signalling

in microglial survival and proliferation was demonstrated clearly in CSF1R knockout mice which show almost a complete lack of microglia at 3-weeks of age, while adult CSF-1 and IL-34 null mice show regional specific microglia depletion (Ginhoux et al., 2010; Greter et al., 2012; Kondo & Duncan, 2009; Y. Wang et al., 2012).

Under healthy conditions microglia position themselves in tightly controlled mosaic organisations throughout the brain, independent of cell layers and blood vessels (Lawson, Perry Vh Fau - Dri, Dri P Fau - Gordon, & Gordon, 1990). Despite continuity in microglial mosaic formations across the brain, microglial cell density and morphology show a high degree of regional diversity (D. Gomez-Nicola & V. H. Perry, 2015). For example, microglia represent 12% of the total cells within the substantia nigra but only 5% within the corpus callosum of rodent brains (Lawson et al., 1990). Such density diversity is also evident in human brains with microglial representing 0.3% of cells within the cerebellar grey matter and 16.9% within the medulla oblongata (Mittelbronn, Dietz K Fau - Schluesener, Schluesener Hj Fau - Meyermann, & Meyermann, 2001). Microglial morphological diversity is also region dependent, with elongated and orientated cells visible within the white matter which contrasts the more abundantly found, radially orientated, morphology observed within the cerebral cortex (Lawson et al., 1990). Along with regional specific morphology, microglia also display variation in lysosomal content (Majumdar et al., 2007), membrane composition (Button et al., 2014), electrophysiological properties (De Biase et al., 2017) and gene transcriptome profiles (Hammond et al., 2019). Along with regional differences in transcriptomic prolife, microglial transcriptome diversity, particularly related to surface proteins and inflammatory markers, has been shown to differ between microglia even in close proximity (Jiang-Shieh, Wu Ch Fau - Chang, Chang Ml Fau - Shieh, Shieh Jy Fau - Wen, & Wen, 2003; Wu, Chien Hf Fau - Chang, Chang Cy Fau - Ling, & Ling, 1997). Generally speaking, however, microglia under normal homeostatic conditions show a transcription profile that is dominated by encoding for proteins associated with the sensing of endogenous ligands and microbes, referred to as the microglial sensome (Hickman et al., 2013).

Ramified morphology and the limited expression of molecules related to macrophage function, are attributed to a 'resting' microglial phenotype (U. K. Hanisch & H. Kettenmann, 2007). The emergence of *in vivo* multiphoton imaging techniques and transgenic $Cx_3Cr_1^{eGFP}$ reporter lines has demonstrated, however, that resting microglia are not dormant. Neuroimaging studies within both mice and zebrafish demonstrated that microglial processes are continually extending and retracting within their local environment, whilst maintaining a fixed soma position (Davalos et al., 2005; Nimmerjahn, Kirchhoff F Fau - Helmchen, & Helmchen, 2005; Wake, Moorhouse Aj Fau - Jinno, Jinno S Fau - Kohsaka, Kohsaka S Fau -

Nabekura, & Nabekura, 2009). Time-lapse recordings acquired through multiphoton imaging, within $Cx_3Cr_1^{eGFP}$ mice, demonstrated that microglial processes are continually rebuilt through *de novo* formation and withdrawal of processes, alongside motile filopodium-like protrusions (Davalos et al., 2005; Nimmerjahn et al., 2005). Microglial cells take turns scanning shared areas, thus ensuring that processes rarely come into contact with one another allowing for the mosaic distribution of microglia to effectively cover, and therefore monitor, the local environment (Nimmerjahn et al., 2005). It is estimated that through careful organisation, and dynamic process movement, that microglia can monitor the entire brain parenchyma every few hours (U. K. Hanisch & H. Kettenmann, 2007). The maintenance of this highly dynamic process movement is achieved through a diverse array of soluble or membrane-bound factors, with neuronal and non-neuronal origin (U.-K. Hanisch & H. Kettenmann, 2007; Kettenmann, Hanisch Uk Fau - Noda, Noda M Fau - Verkhratsky, & Verkhratsky, 2011). Examples of such factors altering microglial dynamics include ATP and CX_3CL_1 (Davalos et al., 2005; Liang et al., 2009), however the full scope of modulatory systems potentially effecting these processes are not fully understood (Diego Gomez-Nicola & V. Hugh Perry, 2015). Microglial surveillance functions challenge the view of a 'resting' phenotype, as such activities require constant morphological alterations alongside biochemical sensing and interpretation of environmental cues. The microglial resting state may therefore more accurately reflect a defined mode of activation (U. K. Hanisch & H. Kettenmann, 2007).

1.9.4 Microglial structural and functional alterations under pathological conditions

Microglia are often considered the immune cells of the CNS, with the remarkable capacity to respond to almost any form of CNS disturbance raging from local changes in homeostasis and infection to acute and chronic injury (Richard M. Ransohoff & Joseph El Khoury, 2015). Microglia have the ability to sense changes within their local microenvironment through the surface expression of varied receptors such as purino- and fractalkine receptors, receptors for complement fragments, immunoglobulins, adhesion molecules, and inflammatory stimuli (Raivich et al., 1999; van Rossum & Hanisch, 2004). The microglial response to such changes is termed "microglial activation" and describes alterations not only in function but also cell morphology (Diego Gomez-Nicola & V. Hugh Perry, 2015). Microglia, following activation, have the ability to shift into a range of functional states leading to changes in proliferation (Gomez-Nicola, Fransen Nl Fau - Suzzi, Suzzi S Fau - Perry, & Perry, 2013), morphology (Cuadros & Navascués, 1998), motility and migration (Mosher & Wyss-Coray, 2014), phagocytic activity (Sierra, Abiega, Shahraz, & Neumann, 2013), antigen presentation

(McGeer, Itagaki S Fau - Tago, Tago H Fau - McGeer, & McGeer, 1988), and the release of inflammatory mediators such as cytokines and chemokines (Kettenmann et al., 2011). Microglial activation results in chemotactic reorientations and other non-transcriptional events within seconds to minutes following stimulation. Within a few hours a massive induction of complex gene sets can be achieved, drastically altering microglial function (U. K. Hanisch & H. Kettenmann, 2007). Microglial activation is often accompanied by increased lysosomal and phagocytic activity, detected by the immunohistochemical markers lysosome-associated membrane protein 2 (Lamp2) and CD68, respectively. Such alterations highlight an increased capacity to remove cellular debris which forms a fundamental aspect of microglia's ability to combat infection and disease (Mosher & Wyss-Coray, 2014). Microglial phagocytosis has also been shown to be important for the removal of apoptotic debris in the developing and adult brain, which has a beneficial effect through the prevention of pro-inflammatory cytokine and chemoattractant release (Magnus, Chan A Fau - Grauer, Grauer O Fau - Toyka, Toyka Kv Fau - Gold, & Gold, 2001). However, there is evidence to suggest that microglia can actively phagocytose endangered, but potentially viable, neurons and therefore can contribute to neurodegenerative disease (Fricker et al., 2012; Jonas J. Neher et al., 2013; J. J. Neher et al., 2011). In addition to the removal of apoptotic or damaged cells, microglia can engulf and prune synapses (Schafer et al., 2012), clear axonal and myelin debris (Hosmane et al., 2012; Nielsen et al., 2009), and remove potentially toxic proteins such as Aβ (Sierra et al., 2013). Such results highlight the potentially detrimental effect of uncontrolled or misdirected microglial phagocytosis.

Traditionally, the study of microglial activation was carried out within animal models of disease or through tissue culture approaches, with the bacterial endotoxin lipopolysaccharide (LPS) most commonly used to elicit microglial activation. LPS mimics infection by Gram-negative bacteria, leading to a substantial antimicrobial defence and the activation of microglia (U. K. Hanisch & H. Kettenmann, 2007). Such a paradigm led to the view that microglial activation is an all or nothing reaction, causing the release of proinflammatory cytokines which are detrimental and neurotoxic (Diego Gomez-Nicola & V. Hugh Perry, 2015). More recent findings, however, have demonstrated that microglial activation is a plastic multifaceted response, which is not only context dependent, but also region and time dependent, being finely tuned to the nature of the stimulus, the local environment as well as the prior state of the cell (D. Gomez-Nicola & V. H. Perry, 2015). Therefore, the view that microglial activation is a monophasic, all or nothing, response is outdated and inaccurate (Bachiller et al., 2018)

Multiphoton imaging studies, using the $Cx_3Cr_1^{eGFP}$ microglial reporter mouse, have demonstrated that microglial activation following injury is associated with alterations in

microglial motility as well as structure. Focal laser induced injuries were shown to lead to local microglial activation, causing a switch of behaviour from patrolling to shielding of the injured site (Nimmerjahn et al., 2005). Additional, complementary studies, demonstrated that the rapid process-extension response towards sites of laser injury were mediated by ATP binding to the purinergic receptor P2ry12 (Davalos et al., 2005; Haynes et al., 2006). The directionality of process movement to areas of damage is thought to be guided through purinoreceptor stimulation and may involve astrocytic assistance (Davalos et al., 2005; Haynes et al., 2006). Intravital imaging approaches have also demonstrated that alterations in microglial morphological parameters, such as soma size and sphericity, can be assessed and used to highlight a change in activation state (B. M. Davis, Salinas-Navarro, Cordeiro, Moons, & De Groef, 2017; Kozlowski & Weimer, 2012). Advancements in such imaging approaches, as well as microglial transgenic reporter lines allow for changes in microglial activation state to be identified in real-time, *in vivo*, under disease conditions.

1.9.5 Evidence for microglial involvement in human VCI and other chronic degenerative diseases

There is mounting evidence to implicate neuroinflammatory mechanisms in the onset and progression of cerebrovascular disease. Recent GWAS studies, identified 5 risk loci associated with neuroimaging markers of white matter dysfunction, with these genes also shown to be highly expressed by microglial and macrophages populations (Armstrong et al., 2020; Persyn et al., 2020). *Post mortem* neuropathological evaluation of white matter lesions reveals myelin loss and axonal degeneration, associated with a prominent microvascular inflammatory response (Simpson, Fernando Ms Fau - Clark, et al., 2007; Simpson et al., 2009; J. M. Wardlaw et al., 2019). A key component of this response is the expansion and activation of microglial cells (Simpson, Ince Pg Fau - Higham, et al., 2007), with increased microglial number being detected frequently in human VCI cases (Akiguchi, Tomimoto H Fau - Suenaga, Suenaga T Fau - Wakita, Wakita H Fau - Budka, & Budka, 1997; Simpson, Fernando Ms Fau - Clark, et al., 2007; Simpson, Ince Pg Fau - Higham, et al., 2007). Furthermore, positron emission tomography (PET) imaging revealed indices of neuroinflammation as well as amyloid deposits within 50% of patients with mild cognitive impairment, potentially implicating microglial activation in early disease progression (Okello et al., 2009). Ageing, the greatest risk factor for VCI and dementia, alone has been shown to drive changes in microglial function (Wong, 2013). Increased microglial activation was also observed *post mortem* within cognitively normal old age patients when compared to young and 'SuperAger' groups (Gefen et al., 2019).

Alongside evidence implicating microglia in the onset of white matter disease and the progression of VCI, GWAS studies have also identified 25 genetic loci associated with increased risk for late-onset AD, with the majority of them related to neuroinflammation and predominantly expressed on microglial cells, such as ApoE, Soi1, and Trem2 (Corder et al., 1993; Guerreiro et al., 2013; Olichney et al., 1995). PET imaging, within symptomatic AD patients, also showed markers of microglial activation and tau pathology to be accurate predictors of further cognitive decline (Malpetti et al., 2020). Increased microglial numbers as well as increased levels of microglial proliferation were identified within both the grey and white matter of AD patients at *post mortem*. With such changes linked to elevated gene expression of the main components of the CSF1R signalling pathway such as CSF1R, CSF1, SpI1, CEBPA, and RUNX1 (Adrian Olmos-Alonso et al., 2016a).

Despite compelling clinical evidence implicating microglia in the onset and progression of VCI and dementia, direct evidence proving a causative role is yet to be reported. This has led to a reliance on animal models which allow for genetic and pharmacological approaches, not possible within clinical studies, to help provide definitive evidence of a direct causative microglial role in disease onset and progression.

1.9.6 BCAS models: The contribution of microglia to white matter disease and cognitive impairment

One of the most prominent features of the BCAS model is a robust increase in microglial number. In response to increasing durations of cerebral hypoperfusion, microglial numbers were observed to increase gradually in parallel with both white matter damage (Holland et al., 2011; McQueen et al., 2014; Reimer et al., 2011; Shibata et al., 2004; Wakita et al., 1994) and cognitive impairment (Kitamura et al., 2017). Increased microglial number has also been demonstrated within grey matter regions, such as the hippocampus, following BCAS surgery (J. M. Roberts, Maniskas, & Bix, 2018).

1.9.7 Pharmacological targeting microglial within BCAS and chronic degenerative disease models

Pharmacological anti-inflammatory treatments, shown to have a beneficial impact within the BCAS model, are associated with reduced microglial proliferation. The broad-acting anti-inflammatory drugs minocycline and dimethyl fumarate (DMF), were found to restore white matter function following BCAS, which was related to a reduction in the number of white matter microglia (Fowler et al., 2017; Manso et al., 2017). Similarly, the phosphodiesterase 3 inhibitor cilostazol was found to reduced working memory impairments and improve white

matter function following BCAS, which was once again associated with reduced microglial numbers (Kitamura et al., 2017).

The predominant system for the control of microglial/macrophage differentiation, maintenance, and proliferation in both health and disease is the CSF1R pathway (Martin-Estebane & Gomez-Nicola, 2020). CSF1R signalling therefore represents a viable target for the manipulation of microglial populations, with pharmacological inhibitors available that are capable of blocking microglial proliferation alone or ablating microglia entirely. The pharmacological ablation of microglia, through treatment with CSF1R inhibitor PLX2297 prior to BCAS surgery, was found to attenuate white matter damage and limit cognitive impairment (Kakae et al., 2019b). However, such treatments almost completely ablate microglial populations from the brain which has the potential to significantly impact the function of all components of the neuro-glial-vascular unit, making it very difficult to unpick the direct causative role of microglial proliferation.

GW2580 is a pharmacological compound which acts to specifically inhibit the tyrosine kinase activity of the CSF1R. GW2580 treatment leads to a blockade of microglial proliferation, without the elimination of the endogenous microglial population (Conway et al., 2005). Treatment with GW2580 was found to prevent the degeneration of synapses and impede disease progression within a APP/PS1 AD model (A. Olmos-Alonso et al., 2016), and has also been shown to be beneficial within other neurodegenerative diseases, including prion disease (Gomez-Nicola et al., 2013) and amyotrophic lateral sclerosis (Martínez-Muriana et al., 2016).

There is therefore compelling evidence linking increased microglial numbers to white matter damage and cognitive impairments following BCAS, however a specific targeted approach has yet to be applied to demonstrate a clear causative role for microglial proliferation in these processes.

1.10 Potential pathophysiological mechanisms underlying white matter damage and cognitive impairment

1.10.1 Cerebrovascular dysfunction and microvascular inflammation

As mentioned at the outset, the cerebrovascular blood supply is crucial to the maintenance of brain health and is required to be extremely dynamic to meet the rapidly changing metabolic needs of the brain. To successfully maintain homeostatic conditions within the brain, the cerebrovasculature carries out a number of dynamic functions such as autoregulation,

neurovascular coupling, as well as cerebrovascular pulsation. Alongside these crucial roles in the maintenance of homeostatic conditions, the cerebrovasculature also plays a fundamental role in inflammatory process through endothelial activation and the associated microvascular inflammatory response.

1.10.2 Microvascular inflammation

Endothelial cells form the inner lining of the BBB and have roles in many physiological processes, such as the transport of nutrients across the BBB, the export of critical toxins from the brain, angiogenesis, and the regulation of vascular tone (Sturtzel, 2017). Alongside its crucial role in homeostasis the endothelium also plays a fundamental role in inflammation. The endothelium dynamically regulates the inflammatory response within the brain through regulation of vascular permeability to macromolecules and leukocytes (Videm & Albrigtsen, 2008). The endothelium can become activated in response to an array of different compounds ranging from pro-inflammatory cytokines and complement activation products, to reactive oxygen species and endotoxins (Videm & Albrigtsen, 2008). Endothelial activation is characterised by 5 core changes which are: the increased expression of leukocyte adhesion molecules, the loss of vascular integrity, a change of phenotype from antithrombotic to prothrombotic, cytokine production, and the upregulation of HLA molecules (Hunt & Jurd, 1998). Adhesion molecules, such as integrin intercellular adhesion molecule-1 (ICAM-1), act to mediate leukocyte extravasation from the blood stream into the brain, in a process known as leukocyte extravasation, leading to pro-inflammatory environments within the brain (Figure 1.6) (Schnoor, Alcaide, Voisin, & van Buul, 2015). Initially, leukocytes must adhere to the endothelial membrane to facilitate their migration from the blood stream into the brain's parenchyma. Leukocytes flow through the blood stream, making brief contact with the endothelial wall where adhesion molecule expression is upregulated. This brief contact triggers the leukocyte to slow its movement, causing it to roll along the endothelium. Some leukocytes will then disengage from the endothelial wall and be carried away by the circulating blood flow. Others will form strong bonds to the endothelial wall causing them to come to a firm stop and adhere in place. Following adherence, leukocytes will either transmigrate into the brain, over the course of minutes, allowing them to enter the brain and facilitate inflammatory responses (Adams & Shaw, 1994), or they will detach and re-enter the circulation. Leukocyte rolling and adhesion alone, without transmigration, has been shown to lead to downstream signalling facilitating the recruitment and activation of microglial cells (H. Wang et al., 2015). The ability, therefore, for endothelial cells to facilitate neuroinflammatory

responses, highlights endothelial activation as a potentially relevant mechanism in the pathogenesis of VCI and dementia.

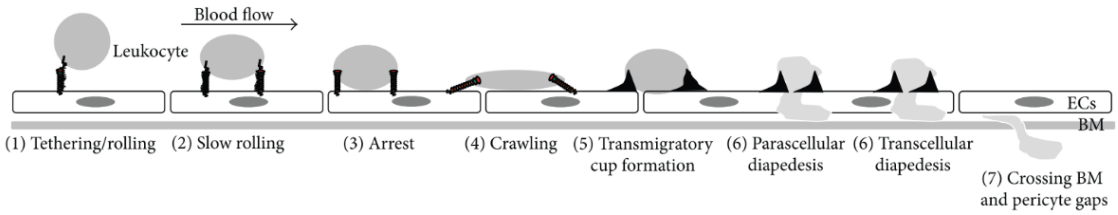

Figure 1.6 Schematic of leukocyte trafficking and transmigration. Illustration depicting the different steps of leukocyte interactions with endothelial cells during adhesion and transmigration. Leukocyte-endothelial reactions are mediated through leukocyte adhesion molecules, such as ICAM-1, expression on the endothelial cell wall. Figure adapted from (Schnoor et al., 2015)

1.10.3 Evidence for cerebrovascular dysfunction and microvascular inflammation in human VCI and other chronic degenerative diseases

Considerable evidence, gathered from both neuroimaging and pathological studies, indicates that cerebrovascular dysfunction has a crucial role to play in the pathophysiology of VCI and dementia (Di Marco et al., 2015; Poggesi et al., 2016; Joanna M. Wardlaw, Colin Smith, et al., 2013). Endothelial dysfunction has been highlighted as a pivotal mechanism underpinning cerebrovascular dysfunction, and leads to structural and functional changes within the cerebrovascular network (Poggesi A Fau - Pasi et al., 2016; J. M. Wardlaw et al., 2013).Vascular risk factors associated with chronic cerebral hypoperfusion, SVD and VCI have also been associated with endothelial dysfunction such as ageing (Vendemiale, Romano Ad Fau - Dagostino, Dagostino M Fau - de Matthaeis, de Matthaeis A Fau - Serviddio, & Serviddio, 2013), hypertension (Iadecola & Davisson, 2008; Virdis et al., 2013) and diabetes (Hamilton & Watts, 2013; A. C. Roberts & Porter, 2013). It is proposed that these risk factors may alter cerebrovascular haemodynamics, leading to alterations in endothelial cell function.

ICAM-1, a marker of endothelial activation has been implicated within a number of neurodegenerative disorders (Frohman, Frohman Tc Fau - Gupta, Gupta S Fau - de Fougerolles, de Fougerolles A Fau - van den Noort, & van den Noort, 1991; Grammas, 2011; Rentzos et al., 2005), with evidence from human MRI studies highlighting an association

between plasma ICAM-1 levels and the progression of white matter lesions (Markus et al., 2005). Endothelial dysfunction has also been associated with impairments in cerebrovascular reactivity, which are thought to impede cerebral haemodynamic responses that are crucial to normal homeostatic functions. Such impairments to the cerebrovasculature could in turn lead to neurovascular coupling deficiencies, which are associated with transient and chronic cerebral hypoperfusion and the further exacerbation of VCI related pathology (M. Bordeleau, A. ElAli, & S. Rivest, 2016; Di Marco et al., 2015; Poggesi et al., 2016; Joanna M. Wardlaw, Colin Smith, et al., 2013; J. M. Wardlaw et al., 2013). Impaired cerebrovascular reactivity has been identified within regions of normally appearing white matter of elderly individuals, and is thought to proceed and therefore predict the appearance of white matter lesions (Sam et al., 2016).

Alongside evidence for a significant role in VCI, impaired cerebrovascular reactivity and impaired haemodynamic responses are being increasingly recognised in the early stages of AD (Sweeney, Kisler, Montagne, Toga, & Zlokovic, 2018). Impaired cerebrovascular reactivity, determined through diminished vasodilation responses to CO_2 inhalation, was identified within early AD patients but not cognitively normal controls, as measured via transcranial Doppler (den Abeelen As Fau - Lagro, Lagro J Fau - van Beek, van Beek Ah Fau - Claassen, & Claassen, 2014) or functional MRI (fMRI) imaging (Yezhuvath et al., 2012). BOLD-fMRI imaging has also been used to demonstrate impaired neurovascular coupling, following visual stimulation and memory encoding, within a number of different brain regions of patients with mild cognitive impairment as well as AD (Rombouts et al., 2000).

Given the substantial evidence for a range of impaired cerebrovascular mechanisms within VCI and dementia, further study into such mechanisms within the context of VCI is necessary to uncover common pathogenic mechanisms underpinning shared pathology.

1.10.4 BCAS model: Evidence for cerebrovascular dysfunction and microvascular inflammation

Microarray analysis of white matter samples have demonstrated alterations within endothelial related genes as early as 3-days following BCAS, alongside increases in pro-inflammatory associated genes (Reimer et al., 2011). Endothelial activation, in a rat model of chronic cerebral hypoperfusion, was highlighted as one of the earliest changes leading to the progression of white matter pathology (Huang et al., 2010). In addition, treatment with the neuroprotective metabolic antioxidant lipoic acid, was found to reduce ICAM-1 expression, which was associated with significantly less severe white matter lesions and a reduction in activated microglia and reactive astrocytes (Huang et al., 2010). The role for endothelial

activation was further supported by the progressive upregulation of ICAM-1 observed up to 3-months following BCAS surgery (Kitamura et al., 2017). Multiphoton imaging approaches have provided support to such findings, through the identification of leukocyte rolling and adhesion as early as 24-hours following BCAS surgery (Yata et al., 2014). Alongside evidence of endothelial activation following BCAS, there are also reports to suggest impairments in cerebrovascular control mechanisms, with neurovascular coupling responses found to be significantly impaired 1-month following BCAS surgery (Duncombe, Kitamura, et al., 2017).

Despite these findings, investigations into the effects of BCAS on cerebrovascular mechanisms such as vascular pulsation and leukocyte trafficking have yet to be explored in detail.

1.11 Summary

Vascular cognitive impairment represents a monumental challenge to world health as the population ages. Currently, the mechanistic changes driving pathology and cognitive impairment remain largely unknown, and a more detailed and comprehensive understanding is crucial to the development of disease altering treatments. BCAS represents a key experimental model of VCI, recapitulating many aspects of cerebrovascular disease pathology, allowing pathological mechanisms to be interrogated and targeted. Microglial proliferation and activation as well as cerebrovascular dysfunction and microvascular inflammation have been highlighted, both clinically and pre-clinically, as potential mechanisms driving disease progression and cognitive impairment. This thesis aims to make use of targeted pharmacological treatments, transgenic mouse reporter lines, and intravital imaging approaches to interrogate the role of these processes more accurately in disease progression. Microglial proliferation and activation are commonly observed in both human and animal models of VCI, being linked to white matter damage and cognitive impairment. The primary aim of this thesis will be to determine the role of microglial proliferation in ensuing white matter damage and cognitive impairments, through a targeted pharmacological approach. Secondary to this, $Cx_3Cr_1^{eGFP/+}$ mice alongside intravital multiphoton imaging will be used to further interrogate microglial structural and functional alterations in response to BCAS. Additionally, these mechanisms will be further investigated in a co-morbid situation through combination of BCAS with the App23 mouse model of amyloidosis. The final aim will be to apply intravital multiphoton imaging approaches to the study of cerebrovascular dysfunction and microvascular inflammation following BCAS surgery.

1.12 Hypothesis

The overarching hypothesis of the present thesis is that microglial proliferation causes white matter damage underpinning vascular cognitive impairment.

1.13 Aims

The following general aims were investigated within chapters 3, 4, and 5 to address the above hypothesis and in parallel to provide further detail on microglial and cerebrovascular functions within a mouse model of VCI:

1. To assess, using an animal model of BCAS, CBF alterations and the extent of microglial proliferation within both white and grey matter regions. Following this the effect of blocking microglial proliferation, with the use of the CSF1R inhibitor GW2580, was assessed to determine if this would prevent white matter damage and cognitive impairments following BCAS surgery in mice.
2. To assess, using transgenic microglial reporter lines and intravital imaging, microglial structural and functional changes *in vivo* following BCAS. Following this the effect of co-morbid conditions on microglial structure and function were assessed, through the application of BCAS surgery to the APP overexpressing App23 mouse model.
3. To assess, through intravital imaging, changes in CBF within cortical vessels in real time alongside *in vivo* measurements of cerebrovascular function and endothelial activation following BCAS in mice.

Chapter 2

Materials and Methods

2.1 Animals

Mice were group housed on a 12-hour light and dark cycle with ab libitum access to food and water for all experiments. Detailed group numbers for each experiment can be found within study chapters under the relevant methods section. All experimental procedures were completed in compliance with the UK Home Office Animals (Scientific Procedures) Act 1986 under Home Office granted personal and project licences and in agreement with veterinary and local ethical approval (Biomedical Research Resources, University of Edinburgh) and ARRIVE guidelines (Kilkenny, Browne, Cuthill, Emerson, & Altman, 2010). Throughout experiments and analysis assessors were blind to surgery, genotype, and treatment status of all mice. Mice were randomly assigned to experimental groups, details of which can be found within the methods section of the relevant chapters.

2.1.1 C57BL/6J mice

Wild-type C57BL/6J mice were purchased from Charles River Laboratories (JAX™-C57BL/6J) and used for experiments detailed within chapters 3 and 5.

2.1.2 $Cx_3Cr_1^{eGFP/eGFP}$ mice

$Cx_3Cr_1^{eGFP/eGFP}$ mice were acquired as a generous gift from Professor Jeffrey Pollard, University of Edinburgh, and developed as previously described (Jung, Aliberti, et al., 2000). Briefly, the murine Cx_3Cr_1 gene locus was isolated from a 129/Sv phage library, through the hybridization with a human Cx_3Cr_1 cDNA probe, to generate a Cx_3Cr_1 targeting vector. A GFP neomycin resistant cassette, replacing the first 390bp of the Cx_3Cr_1 gene, was constructed using a fragment spanning the eGFP gene. Embryonic stem cells were then transfected with the targeting vector, with successful targeting assessed through Southern blot analysis. Embryonic stem cell clones, lacking the neomycin gene, were then injected into blastocysts to generate chimeric mice (Jung, Aliberti, et al., 2000).

2.1.3 App23 mice

App23 heterozygous mice were purchased from The Jackson Laboratory (B6. Cg-Tg(Thy1-APP)3Somm/J) and cross bred with $Cx_3Cr_1^{eGFP/eGFP}$ mice to generate mice for experiments detailed within chapter 4. App23 transgenic mice possess a 6.7 kbp murine Thy1 cassette driving the expression of the human APP isoform 751, which contains the Swedish double mutation App_{751}*K670N/M671L) (Sturchler-Pierrat et al., 1997).

2.1.4 $Cx_3Cr_1^{eGFP/+}$ and $Cx_3Cr_1^{eGFP/+}$ $App23^{+/-}$ mice

$Cx_3Cr_1^{eGFP/eGFP}$ mice were crossed with $App23^{+/-}$ mice to generate $Cx_3Cr_1^{eGFP/+}App23^{+/-}$ and $Cx_3Cr_1^{eGFP/+}App23^{-/-}$ mice that were used for the experiments detailed in chapter 4. To confirm genotypes for studies DNA was extracted and all mice were genotyped according to the methods detailed below.

2.1.5 DNA extraction for genotyping

DNA was extracted from ear or tail samples using 300µl of 50mM sodium hydroxide. Each sample, following the addition of sodium hydroxide, was centrifuged at 9000 rpm for 1-minute and then incubated at 95^0C for 30-minutes. Samples were cooled at room temperature for 10-minutes before being vortexed. 50µl of 1M Tris HCL pH 8.0 was then added and each sample was vortexed. Samples were then allowed to incubate at room temperature for 30-minutes before being used for genotyping or frozen at -20^0C for future use.

2.1.6 $Cx_3Cr_1^{eGFP/+}$ genotyping

PCR was performed using Taq Master Mix (hot start taq, Qiagen); 10µl were added to 2µl of DNA extracted from each sample along with 1µl of each of the 3 primers (Table 2.1) and 5µl of nuclease free H_2O. The PCR program used is detailed within Table 2.1. Upon completion the samples were maintained at 72^0C for 2-minutes before being held at 10^0C.

Samples were then run on a 3% agarose gel (Agarose, Promega; in Tri/Borate/EDTA buffer, Sigma-Aldrich) with 15µl Introgen™ SYBR™ Safe stain (ThermoFisher Scientific) at 120V for 1-hour. Cx_3Cr_1 heterozygous bands are visible at 410bp and ≈500bp with wild-type mice showing a single band at 410bp.

2.1.7 App23 genotyping

PCR was performed using Taq Master Mix (hot start taq, Qiagen); 10µl were added to 2µl of DNA extracted from each sample along with 2µl of each of the 4 primers (Table 2.1). The

PCR program used is detailed within Table 2.1. Upon completion the samples were maintained at 72^0C for 2-minutes before being held at 4^0C.

Samples were then run on a 3% agarose gel (Agarose, Promega; in Tri/Borate/EDTA buffer, Sigma-Aldrich) with 15µl Introgen™ SYBR™ Safe stain (ThermoFisher Scientific) at 120V for 1-hour. APP band is visible at 167bp and the GAPDH control band at 342bp.

Table 2.1 Primers and PCR cycling conditions used for genotyping

$Cx_3Cr_1^{eGFP/+}$ genotyping			App23 genotyping		
Primers					
Wild type- 5'-GTC-TTC-ACG-TTC-GGT-CTG-GT-3'			APP forward- 5'-AGG-ACT-GAC-CAC-TCG-ACC-AG-3'		
Common- 5'-CCC-AGA-CAC-TCG-TTG-TCC-TT-3'			APP reverse-5'-CGG-GGG-TCT-AGT-TCT-GCA-T-3'		
Mutant- 5'-CTC-CCC-CTG-AAC-CTG-AAA-C-3'			GAPDH forward-5'-CAA-ATG-TTG-CTT-GTC-TGG-TG-3'		
			GAPDH reverse-5'-GTC-AGT-CGA-GTG-CAC-AGT-TT-3'		
PCR cycling conditions					
94°C	15 minutes		95°C	15 minutes	
94°C	20 seconds	2 cycles	94°C	30 seconds	
65°C	15 seconds		52°C	45 seconds	35 cycles
68°C	10 seconds		72°C	45 seconds	
94°C	20 seconds	2 cycles	72°C	2 minutes	
64°C	15 seconds		4°C	hold	
68°C	10 seconds				
94°C	20 seconds	2 cycles			
63°C	15 seconds				
68°C	10 seconds				
94°C	20 seconds	2 cycles			
62°C	15 seconds				
68°C	10 seconds				
94°C	20 seconds	2 cycles			
61°C	15 seconds				
68°C	10 seconds				
94°C	20 seconds	2 cycles			
60°C	15 seconds				
68°C	10seconds				
94°C	20 seconds	28 cycles			
60°C	15 seconds				
72°C	10 seconds				
72°C	2 minutes				
10°C	hold				

2.2 Bilateral common carotid artery stenosis surgery

Bilateral common carotid artery stenosis surgery was performed according to the method previously described (Figure 2.1) (Shibata et al., 2004). In brief, mice are anaesthetised by inhalation of 5% isoflurane in oxygen which is then reduced 1.5% and maintained during surgery. A small cervical neck incision is made to allow the common carotid arteries to be exposed by careful dissection and displacement of the superficial muscles, surrounding connective tissues, and vagus nerve. A 0.16 (chapter 3) or 0.18mm (chapters 4 and 5) internal diameter micro-coil (Sawane Spring Co. Japan) is then placed around the left common carotid artery (Figure 2.1). To prevent a drastic reduction in CBF, the animal is allowed a 30-minute recovery period before being re-anesthetised for the application of the second micro-coil (0.18mm) around the right common carotid artery. The incision is then sutured, and the animal is placed within a heated incubator, maintained at 38^0C, to recover from anaesthesia. As a control for all experiments, sham mice undergo an identical procedure with the only exception being the application of micro-coils. All surgical procedures were conducted under aseptic techniques, and animals were monitored closely for the 72-hours following surgery for any signs of poor health. Following the 72-hour observation period, mice were checked twice weekly, and weight was monitored to ensure that mice remained sufficiently healthy throughout all experiments. Excessive weight loss and poor recovery following surgery resulted in mice being humanely culled and removed from studies. Details of animal exclusions following BCAS surgery can be found within the methods section of the relevant chapter.

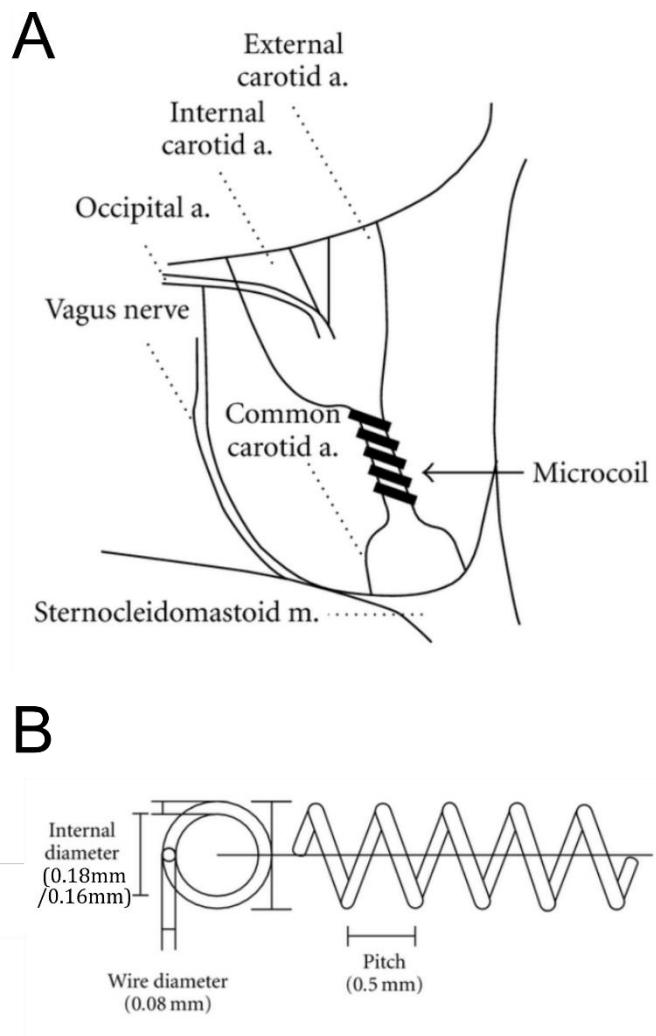

Figure 2.1 Bilateral common carotid artery stenosis (BCAS) surgery. **(A)** Schematic diagram showing a micro-coil positioned bellow the carotid bifurcation of the common carotid artery. Image adapted from (Shibata et al., 2004). **(B)** Specifications of the micro-coils used to restrict CBF during BCAS surgery. Image adapted from (Masafumi Ihara & Tomimoto, 2011).

2.3 Laser speckle imaging of resting cerebral blood flow

Superficial cortical perfusion was measured throughout all studies through the use of laser speckle imaging. Mice were initially anaesthetised at 5% isoflurane in 100% oxygen, before being transferred to a stereotaxic frame where isoflurane was maintained at 3%. Ear and tooth bars were used to stabilise the head below the laser and anaesthesia was delivered, with ventilation, via a nose cone at a rate of 150 breaths per minute. Body temperature was monitored throughout imaging with the use of a rectal probe and maintained at $37^0C \pm 0.5^0C$ using an electric heat blanket. A sterile scalpel is then used to create an incision through the

midline of the scalp, which is retracted using surgical clips to expose the skull. Once the incision has be completed, isoflurane was dropped to 2.5% and maintained for the reminder of imaging. The skull is cleaned, and residual fur is removed with the application of ultrasound gel, which also acts to prevent the skull surface drying during recording. For studies in which cranial windows have been implanted to facilitate multiphoton microscopy (chapters 4 and 5), laser speckle imaging is conducted directly through the window and therefore additional incisions are not required. Once stable, baseline blood flow within the barrel cortex is recorded using a laser speckle contrast imager (Moor FLPI2 Speckle Contrast Imager, Moor Instruments, UK), which generates speckle contrast images. Upon completion of at least 1-minute of stable blood flow the incision is sutured, and the mouse is placed within an incubator maintained at 38^0C and allowed to recover. The topical anaesthetic lidocaine is then applied to the scalp to limit post-operative pain. Laser speckle imaging was repeated longitudinally at different timepoints following surgery depending on the study. Details of laser speckle imaging timepoints can be found within the method section of the relevant chapters. For statistical analysis values are presented as a percentage change from baseline values.

C57/B6J mice were selected for all studies as they have an incomplete circle of Willis, due to a lack of posterior cerebral arteries (G. Yang et al., 1997). Thus meaning that compensatory blood flow mechanisms are not sufficient to rescue blood flow reductions following BCAS surgery, thus allowing CBF reductions to be maintained overtime (Qian, Rudy, Cai, & Du, 2018). Despite this, a subset of mice showed resistance to BCAS surgery with little evidence of reductions in CBF. Through the injection of a fluorescently conjugated dextran, non-responding mice were found to have intact circle of Willis' (Figure 2.2B) with posterior cerebral arteries clearly visible leading to a conferred resistance to BCAS surgery. As a result, strict exclusion criteria were applied to each study to ensure that BCAS surgery was indeed leading to sufficient CBF reductions. The CBF reduction criteria differed between studies due to variations in the size of micro-coil used. Details of exclusion criteria used, as well as the numbers of BCAS resistant mice, can be found within the methods section of the relevant experimental chapter.

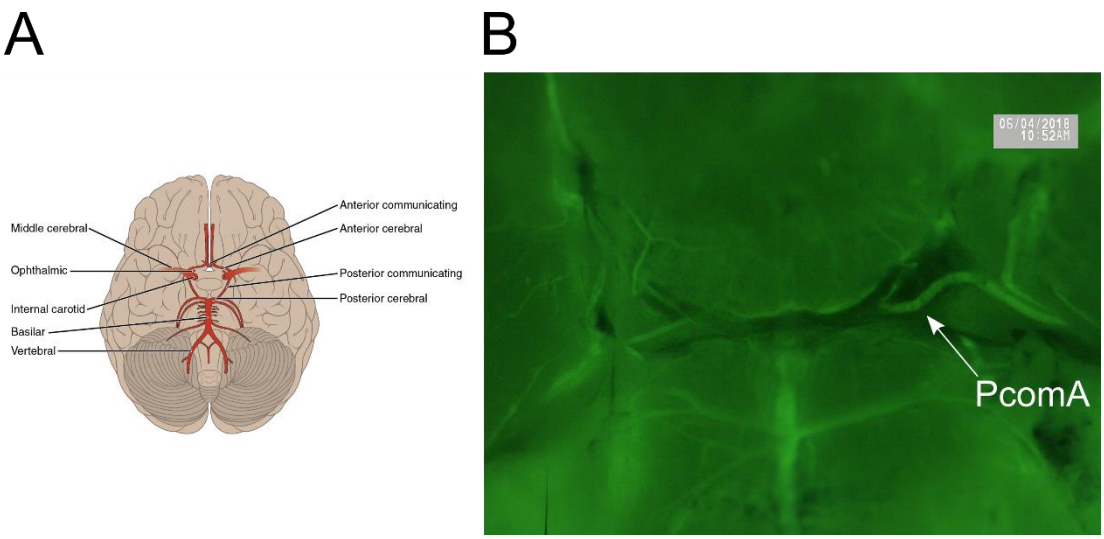

Figure 2.2 Intact circle of Willis within a subset of C57BL/6J mice confers BCAS resistance. **(A)** Schematic image of a completely intact circle of Willis. Image courtesy of OpenStax College, Radiopaedia.org, rID: 42608. **(B)** Florescent image generated within a BCAS resistant mouse, through injection of 70kDA FITC dextran immediately prior to tissue extraction. The posterior communicating artery (PcomA) is clearly visible and therefore provides compensatory blood flow to help counteract BCAS mediated CBF reductions.

2.3.1 Laser speckle imaging analysis

Laser speckle contrast images are analysed using the MoorFLPI-2 Review software (version 4.0). Regions of interest (ROI) are placed over the left and right hemispheres, between bregma and lambda. Care is taken to ensure that ROIs are away from large midline vessels, and that they do not overlap areas of skin, which can block the blood flow (Figure 2.3A). A mean flux value is generated from ROIs in the left and right hemisphere, which represents the average flux over 1-minute of stable blood flow recording (Figure 2.3B). Average flux values from the left and right hemispheres are then averaged to generate an overall value of flux to represent that imaging timepoint. Due to biological variation, the cortical CBF measurement for each animal was normalised to its own baseline value, which was obtained prior to surgery. Blood flow data is therefore expressed as percentage CBF of baseline.

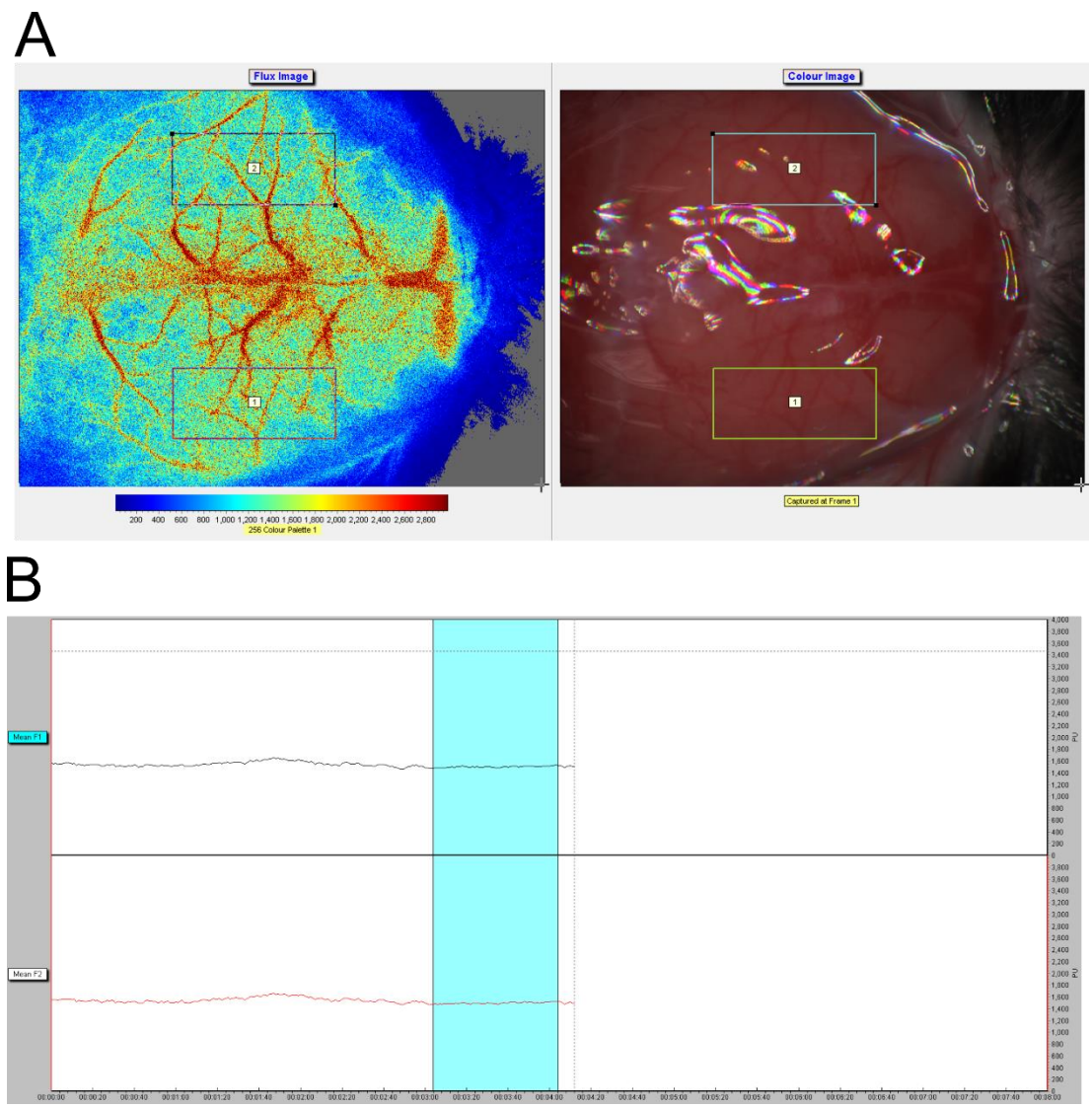

Figure 2.3 Laser speckle image analysis. **(A)** Representative images demonstrating the ROI positioning for CBF measurements via laser speckle imaging. **(B)** Representative trace for cortical blood flow flux values of a typical sham recording. Light blue region demonstrates the ROI used to generate an average flux value for the recording, across both the left (mean F1) and right (mean F2) hemispheres.

2.3.2 Laser speckle imaging of neurovascular coupling responses

Mice are anesthetised by a combination of α-chloralose (50mg/kg) and urethane (750mg/kg) delivered via intraperitoneal injection. The standard anaesthetic isoflurane is not used due to its vasodilatory properties. The mouse is placed in the stereotaxic frame where ear

and tooth bars are used to stabilise the head below the laser. Body temperature was monitored throughout imaging with the use of a rectal probe and maintained at $37^0C \pm 0.5^0C$ using an electric heat blanket. Laser speckle imaging was conducted directly through the cranial window. Before whisker stimulation, the left (unstimulated) whiskers are cut, and the right (stimulated) whiskers are trimmed to an approximate length of 1cm. A stable baseline blood flow recording within the barrel cortex is achieved and then recorded using a laser speckle contrast imager (Moor FLPI2 Speckle Contrast Imager, Moor Instruments, UK). The right whiskers are then deflected, with the use of an electric toothbrush, back and forth to generate a neurovascular coupling response within the contralateral barrel cortex. This process is repeated until at least 4 satisfactory neurovascular coupling responses are recorded. Following imaging the mouse is placed within an incubator maintained at 38^0C and allowed to recover before being returned to their home cage.

2.3.3 Laser speckle neurovascular coupling image analysis

Laser speckle contrast images were analysed with the use of the MoorFLPI-2 Review software (version 4.0). ROIs were positioned within the barrel cortex of the left hemisphere and mean response amplitude, across 30-seconds of stimulation, was recorded. Representative values were generated from an average of 4 stimulations per mouse. Data is presented as percentage increase from baseline. Stimulation recordings were excluded if baseline blood flow fluctuated during the assessment window or if operator error led to non-physiological responses. Details of recording exclusions based on these criteria can be found within the methods section of the relevant chapter.

2.4 Cranial window surgery in preparation for multiphoton microscopy

Prior to multiphoton microscopy it is necessary for a cranial window to be installed to facilitate laser penetration into the brain which would otherwise be attenuated by the skull. The cranial window procedure employed within the present studies was adapted from a method previously described within the literature (Drew et al., 2010). The surgery is conducted under sterile conditions using autoclaved instruments. Initially each mouse is weighed to ensure that the correct dose of the anti-inflammatories carprofen (5mg/kg) and dexamethasone (0.2mg/kg) is given to help reduce brain swelling and limit post-operative discomfort. The mouse is then anesthetised via inhalation of 5% isoflurane in oxygen. Once unconscious (unresponsive to foot pinch) the mouse is placed on a stereotaxic frame and maintained at 1.5-3% isoflurane delivered via a face mask. The mouse's temperature is checked via a rectal

thermometer and maintained at 37^0C $\pm 1^0$C throughout the surgery with the use of an electric blanket. Carporfen and dexamemethasone are then delivered by subcutaneous injection. The mouse's head is shaved, and ointment is applied to the eyes to prevent them drying out during the procedure. The scalp is then sterilised with ethanol and the skin directly between the ears extending to between the eyes is removed to expose the skull. A scalpel is used to gently scrape away any residual membrane to ensure the skull is dry. Vetbond glue is then applied to seal the edges of the scalp to the exposed bone. Once dry, superglue is applied covering all the vetabond as well as some areas of skull to ensure a firm seal. A dental drill (16,000 rpm) is used to drill a rectangle, approximately 6x4mm in width positioned across both hemispheres' inferior to bregma, until a very thin layer of bone remains. A drop of saline is then applied and allowed to soak into the skull before the craniotomy is removed via right-angled forceps. Gelfoam is applied to prevent any small bleeds that may occur. The gelfoam is removed and the skull around the craniotomy is dried before a 7mm glass coverslip is placed on top of the dura. Once exposed the dura is continuously bathed in saline to ensure that it is never allowed to dry. Cyanoarcylate-based glue is used to secure the glass coverslip in place. Once dry, superglue is applied to an aluminium head-plate which is gently secured to the skull ensuring that the whole window is clearly visible. Paladur dental cement is applied around the head-plate to ensure that it is firmly attached, and all visible gaps are filled. Once the head-plate has fully dried the mouse is placed within an incubator and allowed to recover from anaesthesia.

2.5 Multiphoton microscopy

Multiphoton microscopy experiments, detailed within chapter 4, were carried out using a Leica SP8 DIVE microscope, which has an upright configuration with a single position nosepiece containing the motorised IRAPO L x25/0.95 lens, over a custom made Scientifica platform for mouse imaging. The system contains a tandem scanner: containing a linear tuneable scanner with speeds up to 3.6kHz and an 8kHz resonant scanner. All images were captured using the integrated Leica LAS X control software. For multiphoton microscopy studies, detailed within chapter 5, a LaVision Biotech TriMScope microscope was used, with an upright stand fitted with a Nikon CFI-Apo 25x NA1.1 lens. All images were acquired and recorded on the LaVision Imspector software. For both multiphoton microscope set-ups a custom-made platform was used, to secure the anaesthetised mouse under the lens. Animal anaesthesia is achieved using a VetTech anaesthetic rig set up for isoflurane. The mouse is monitored with Kent Scientific PhysioSuite with MouseStat Pulse Oximeter and Heart Rate monitor together with a heat pad. This can be used to measure the animal's temperature, SpO2, respiratory rate and heart rate.

Prior to imaging mice are anesthetised at 5% isoflurane in 0.5 litres of O_2 per minute. To enable the cerebral vasculature to be visualised, a range of fluorescently conjugated tracers are injected intravenously via the tail vein (Table 2.2). To perform the tail vein injection the isoflurane level is reduced to 2% and the mouse is placed on a heat pad, set at 37^0C, with a warm paper towel wrapped around the tail to encourage vasodilation of the tail vein. The fluorescently conjugated tracers are then injected. The mouse is secured via their head-plate to the custom-made imaging platform that has previously been warmed within the imaging chamber. Eye ointment is gently applied to the eyes to avoid dehydration during imaging. A cotton bud soaked in distilled H_2O is then used to clean the cranial window. A rectal thermometer, attached to a heat pad, is inserted to ensure that the temperature is maintained between 36.5-37.5^{0}C throughout imaging. The holder is placed within the imaging chamber and a foot pad is attached to allow vitals to be monitored throughout. During imaging, isoflurane levels are kept between 1.25 and 2% and adjustments are made to ensure that heart and respiratory rates are maintained within acceptable ranges (Heart rate 400-600 beats per minute and respiratory rate 55-100 per minute). The holder is then secured, within the imaging chamber, using masking tape and the microscope lowered. Distilled H_2O is placed on top of the cranial window to aid laser penetration. Following imaging an injection of saline is delivered subcutaneously to aid rehydration. All imaging procedures are completed within 2-hours.

Table 2.2 Tracers used for multiphoton microscopy

Tracer/Antibody	Label	Size	Excitation/Emission (nm)	Concentration	Volume	Delivery	Supplier
Rhodamine B	Vasculature	70kDa	880nm/550-600nm	15mg/ml	100µl	Tail vein	Sigma
FITC-dextran	Vasculature	70kDa	492nm/518nm	15mg/ml	100µl	Tail vein	Sigma

2.5.1 *In vivo* assessment of microglial structure

To enable the soma structure of individual microglia to be analysed, 3 separate z-stacks (203.46µm x 203.46µm x 50µm) were acquired from each animal at various depths throughout the cerebral cortex. The maximum depth of imaging did not exceed 300µm. Microglial cells were readily visible using the $Cx_3Cr_1^{eGFP}$ microglial reporter line, with the Rhodamine B tracer injected within the tail vein to allow the cerebral vasculature to be visualised. Z-stack areas had to encompass at least 5 complete microglial cells and were positioned away from large vessels to prevent the attenuation of the microglial signal. Following the acquisition of the 3

microglial z-stacks the images were imported into the IMARIS software (Oxford Instruments) for further processing and structural evaluation.

The IMARIS surface function is used to isolate the microglial cell soma to allow structural measurements to be gathered (Figure 2.4). Smoothing was carried out at a surface area detail level of 2µm, followed by a local contrast background subtraction limited by the diameter of the largest sphere which fits into the object, which was set to 30µm. The z-stack then underwent thresholding through background subtraction, which was manually adjusted to ensure that microglial processes are stripped and just the cell soma remains. The resulting surfaces are then classified according to 2 parameters: Firstly, by the number of voxels, which is manually adjusted to ensure that only microglial cell somas are selected. Secondary, by distance to image border XYZ which is set to 0.5µm to ensure that only microglial somas that are fully visible and complete within the imaging view are analysed. This processing allows 3D reconstructions of each microglial soma to be generated within the IMARIS software, which then has the ability to generate structural measurements of each cell soma relating to volume, area, and sphericity (Figure 2.4C). Following processing, the surface 'masks' generated are compared to the original z-stack to ensure that each microglial cell is accurately represented (Figure 2.4D). The assessor was blind to surgical status and genotype throughout image acquisition and processing. This process is completed for each of the 3 z-stacks gathered per mouse.

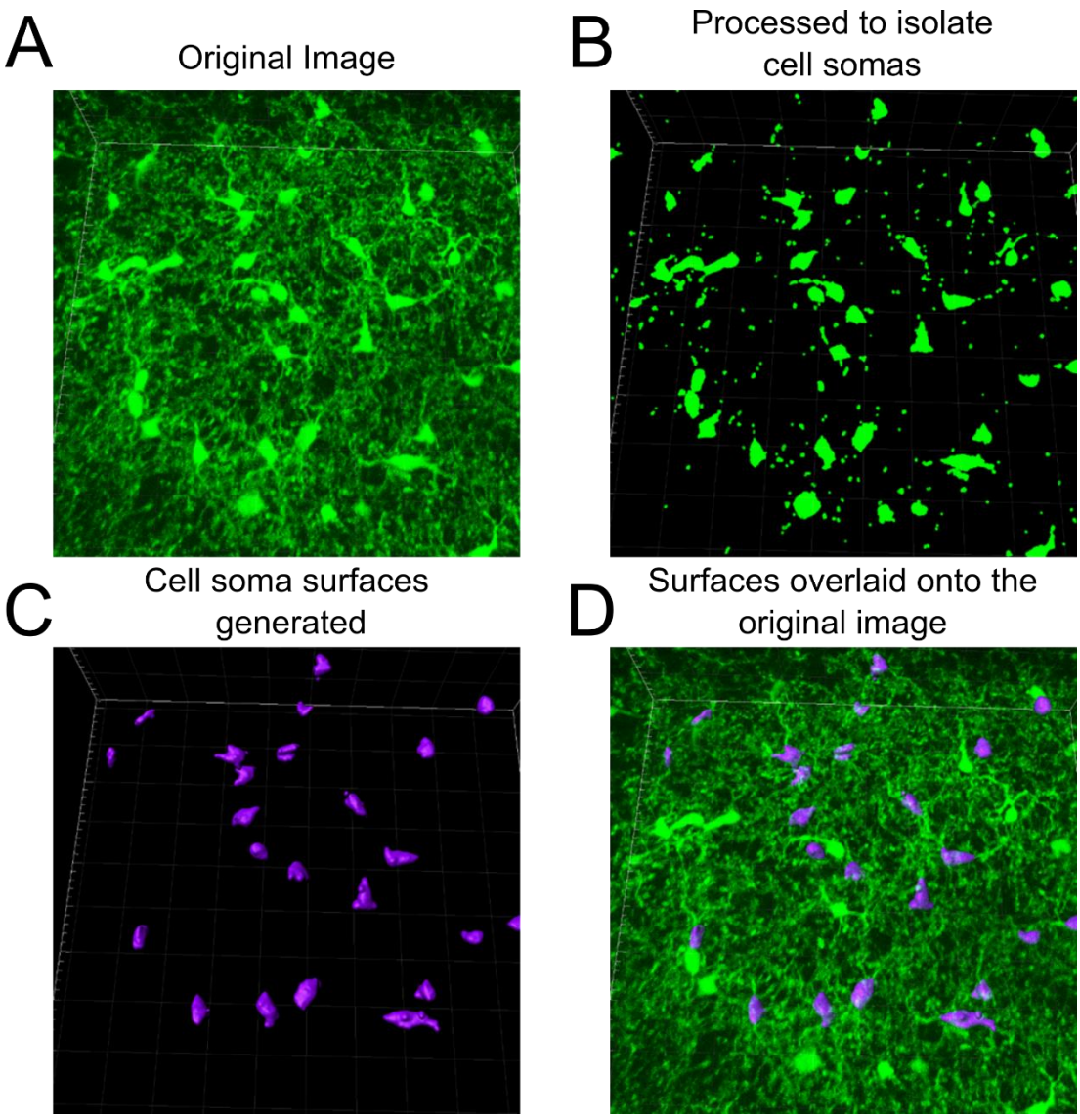

Figure 2.4 Microglial structural analysis. **(A)** 2D image of a 3D reconstruction of a 50µm z-stack gathered within the cerebral cortex via multiphoton microscopy. **(B)** Processing of the original z-stack, within the IMARIS software, to isolate microglial somas. **(C)** Surface casts of each microglial soma within the field of view that is visible in its entirety. **(D)** Image demonstrating the generated surfaces overlaid onto the original Z-stack, highlighting the microglial somas in purple that are analysed for area, volume, and sphericity.

2.5.2 *In vivo* assessment of microglial process dynamics

To capture dynamic microglial process movements in real time, *in* vivo, repeated z-stacks were gathered consecutively over a 15-minute period via multiphoton microscopy. Consecutive z-stacks were gathered within 3 regions for each mouse, giving a quantification

of process motility over 45-minutes. Each z-stack took ≈48-seconds to acquire with a step size of 2 μm, depth of 50 μm and a 203.46x203.46 μm field of view.

To calculate process motility z-stacks were processed and analysed using the ImageJ software (v1.46, NIH, Bethesda, MD, USA). Each z-stack was compressed to form a single maximum intensity image. 19 maximum intensity images were generated for each 15-minute imaging window and combined into a single stack. The StackReg plugin was then used to centre each image and then the imageCalculator plugin was used to calculate the pixel difference between 1 maximum intensity image to the next ($M=I_{\text{difference t=1 and 2}}/I_{\text{t=1}}$) (M=motility, I=intensity, t=stack number). Pixels present in t=1 but absent, 48-seconds later, in t=2 were defined as process retractions, whereas pixels that emerge in t=2 having been absent in t=1 are defined as process extensions. Process retractions and extensions are divided by the pixels present within t=1 to generate a process motility value as a percentage change, which represents process motility between stacks. Pixel differences across the entire 15-minute period were then averaged, with values from each of the 3 regions again averaged to generate an overall process motility value per mouse. Methodology was adapted from previously published workflows (M. A.-O. Kluge et al., 2017).

Microglial process coverage (surveillance measurement) was also calculated using the ImageJ software (v1.46, NIH, Bethesda, MD, USA). Each z-stack gathered over the 15-minute imaging was collapsed to form individual maximum intensity images using the ImageJ z-projection function. All maximum intensity images were then combined into a single stack before being binarized, using the 'Moments dark' autothreshold, to generate a mask of each stack slice. All binarised images within the stack are then summated to generate a single image displaying microglial coverage, of the entire field of view, over 15-minutes. The percentage area of microglial pixels is then calculated, representing the number of microglial pixels covering the entire field of view. A coverage value is then generated which represents the surveillance ratio, defined as the ratio of microglia-occupied pixels as a proportion of the total pixels within the field of view. This process was completed for all 3 regions and averaged to give an overall value of microglial coverage. Methodology was adapted from protocols previously published (Stowell et al., 2019).

2.5.3 *In vivo* cerebral RBC velocity measurement via line scan analysis

To calculate red blood cell (RBC) velocity within different components of the vascular network, line scanning was performed (Figure 2.5). Line scanning involves repeatedly imaging a single line, positioned within the central axis of a vessel, at a high scan speed of 1.5 kHz.

Line scans were positioned at a point along the vessel that was clearly visible with a strong signal, care was also taken to position scans away from vessel branch points to avoid turbulent flow (Figure 2.5A). Fluorescently conjugated dextran tracers upon introduction into the vasculature are too large to enter RBCs or escape the vascular lumen. As a result, RBCs appear on line scans as black loss of signal linear shadows, with the slope of each line being proportional to its velocity. Each line scan contains hundreds of RBCs and therefore by calculating the slope of each one, and averaging the values, a mean RBC velocity for the vessel can be generated, in a process known as line scanning particle image velocimetry (LSPIV). Line scan images are analysed using software and methodology that has been previously described (T. N. Kim et al., 2012) (Figure 2.5B) and the resulting values are converted to RBC velocity in mm per second using the formula outlined in Figure 2.5C.

RBC velocity was measured within both leptomeningeal veins and arteries. These vessels are identified based on their direction of blood flow, size, and structure. Leptomeningeal veins show convergent flow and tend to have larger diameters with a less rigid cell wall, whereas leptomeningeal arteries show divergent flow and tend to have smaller diameters with rigid cell walls. Strict exclusion criteria were applied to all RBC velocity images, such that any linescan recording whose quality was not sufficient to give accurate readings of RBC velocity were excluded. The quality of linescan images were evaluated based on the shape and location of points throughout the fitted pixel displacement graphs (Figure 2.5B). Poor quality linescans generate a large number of outliers and show a disjointed fitted pixel displacement graph and therefore cannot be used as an accurate measure of RBC velocity.

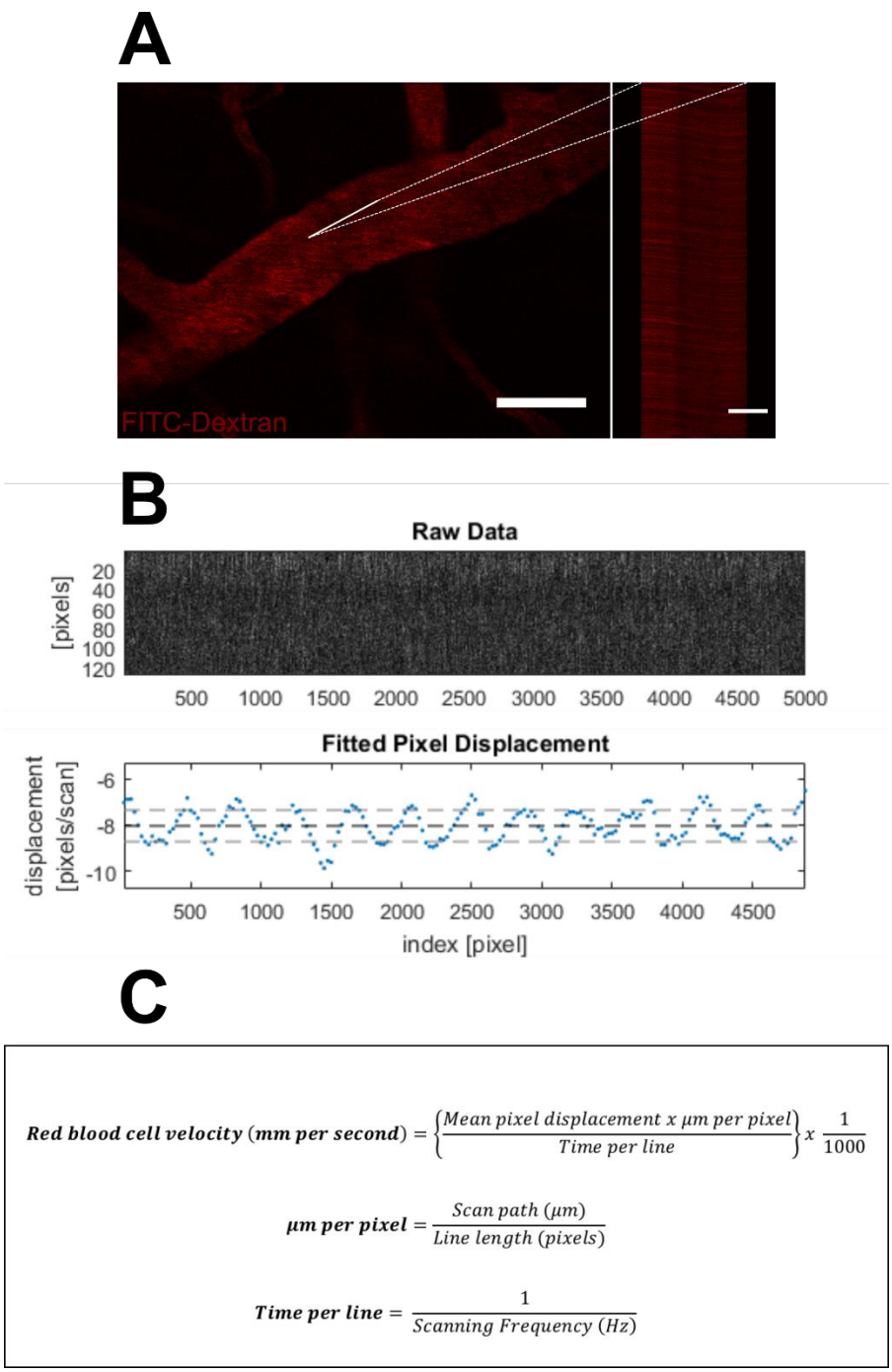

Figure 2.5 RBC velocity analysis via line scanning particle image velocimetry (LSPIV). **(A)** Representative images of line scanning location within a vessel and the resulting line scan image (white line denotes linescan location). Scale bar 50µm left image 25µm right. **(B)** Representative images taken from the LSPIV assessment, displaying the raw line scan image as well as the pixel displacement across the image width, with the dotted line

representing the mean pixel displacement. **(C)** Mean pixel displacement values are converted to RBC velocity values in mm/second by the formula detailed.

2.5.4 *In vivo* assessment of vascular pulsation

Cerebral vascular pulsatility was evaluated with the use of multiphoton microscopy using a method based on those described previously within the literature (Jeffrey J. Iliff et al., 2013b; Kress et al., 2014). Vascular pulsation represents an important physiological function of the vasculature which has been proposed to be the driving force behind waste clearance from the brain (Jeffrey J. Iliff et al., 2013b; Schley, Carare-Nnadi R Fau - Please, Please Cp Fau - Perry, Perry Vh Fau - Weller, & Weller, 2006). Small dynamic changes in vessel diameter were measured within leptomeningeal veins, leptomeningeal arteries, ascending veins, and penetrating arteries with the use of line scanning methods.

As described previously (section 2.5) the cortical vascular network can be readily visualised via multiphoton microscopy through the injection of fluorescently conjugated dextrans into the blood stream. Once visible, the pulsatility of individual vessels can be determined by positioning linescans orthogonal to the vessel's axis. Linescans were performed at a frequency of 1086.96 Hz and repeated for 4000 loops equalling a duration of 3600ms. Care was taken to position line scans at points along the vessel that are clearly visible, with a strong signal and away from branch points. The resulting images are processed and analysed using the ImageJ software (v1.46, NIH, Bethesda, MD, USA). Linescan images are converted to an 8-bit format, smoothed using a Gaussian filter and manually thresholded to generate a sharp, noise free, vessel wall boundary. Any residual individual pixels found to be outside the boundary of the vessel, were considered noise and manually removed using the 'fill' feature. The assessor was blind to surgical group throughout imaging acquisition and analysis.

Once a threshold has been applied to the image, the outside of the vessel will appear black indicating an absence of signal (low pixel intensity: value=0). Whereas the edge of the vessel will appear white (high pixel intensity: value >0) as the fluorescently conjugated dextran is unable to penetrate the vessel lumen generating a very intense signal within the vasculature. Any linescan image that post-processing was found to be excessively noisy, in which the vessel wall could not be readily identified, was excluded from the analysis.

A collection of ROIs are then applied to each image (individual ROI dimensions: width: 650 pixels, height: 10 pixels). Each ROI has a width of 650 pixels which exceeds the vessel wall on either side and allows the vessel width to be calculated. Regions of interest are placed

consecutively every 10 pixels resulting in a total of 400 regions with each region representing a recording of the vessel width every 9ms for a total of 3600ms.

The ImageJ ‘multi-plot’ function generates a distribution of pixel intensities across the entire breadth of the ROI. Therefore, in order to determine the width of the vessel measured by any given line, the point at which the values transition from low pixel density (ie 0) to high pixel density (ie >0) on each side of the scan is calculated. This point will reflect the position of the endothelial wall on either side and therefore by measuring the difference between these two points we can calculate the vessel width in pixels. The laser scan path for each line scan is then used to generate a pixel to micron ratio, allowing the conversion of vessel width to microns.

To calculate dynamic vessel width changes over time, vessel width (μm) within each region was plotted against time (ms). Vessel wall pulsatility (μm*ms) was calculated from the resulting graphs as the absolute value of area under the diameter-time plot, integrated to the running average calculated across the entire 3600ms sampling time, as performed previously (Jeffrey J. Iliff et al., 2013b). All peaks that were defined by fewer than 2 adjacent points were considered noise and excluded from the analysis, no criteria for the minimum peak height was applied. To calculate the total number of dynamic vessel pulses across the sampling time the total number of peaks were also calculated from the same diameter-time plots.

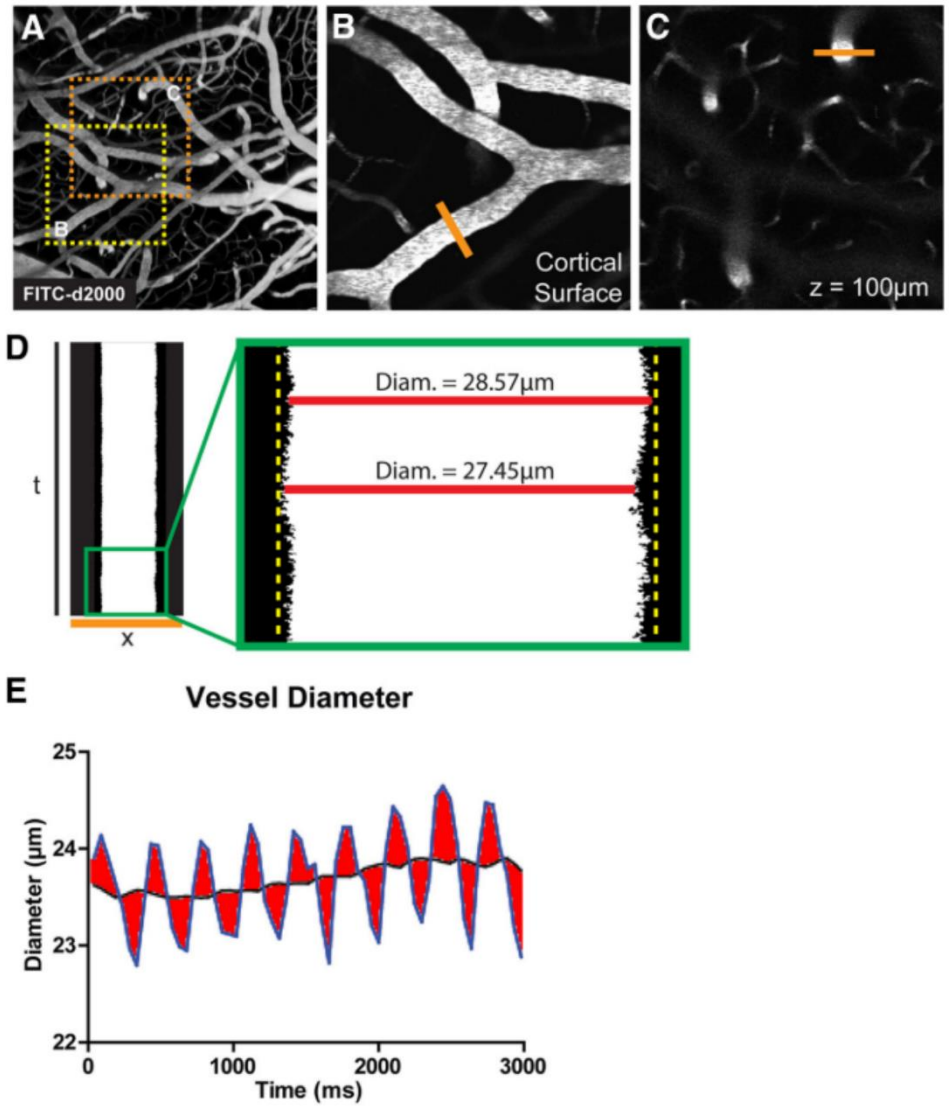

Figure 2.6 Method to assess vascular pulsation in vivo via multiphoton microscopy. **(A)** The cerebral vasculature is visualised through the intravenous injection of fluorescently conjugated dextran's (summarised in ***Table 2.2***). Cortical surface veins and arteries **(B)** as well as ascending veins and penetrating arteries **(C)** were identified and assessed for pulsation through line scans carried out orthogonal to the vessel axis (orange line). **(D)** The resulting line scan of each vessel is analysed to generate vessel width calculations every 9ms. **(E)** Vessel diameters are then plotted as a function of time. Vascular pulsatility is defined as the absolute value of the integral of the vascular diameter measured against a running average over 3600ms. Frequency of pulsation is measured as number of vessel wall changes, identified as peaks, on the diameter-time graphs over 3600ms. Images adapted from (Jeffrey J. Iliff et al., 2013b).

2.5.5 *In vivo* assessment of leukocyte trafficking behaviours

Upon the injection of a fluorescently conjugated tracer into the vasculature, leukocytes can be visualised as black (loss of signal) spheres. Time-lapse recordings of approximately 60-seconds are then taken and leukocyte trafficking is assessed within leptomeningeal veins and arteries. In order to be defined as rolling, a leukocyte must be travelling at least one order of magnitude slower than the velocity of RBCs, have a clearly defined edge, be visible in two consecutive frames and be travelling in the same direction as the blood flow (Sperandio, Pickard J Fau - Unnikrishnan, Unnikrishnan S Fau - Acton, Acton St Fau - Ley, & Ley, 2006). To be defined as adhered, a leukocyte must remain stationary against the endothelial wall for at least 30-seconds and have a clearly defined edge (Yata et al., 2014)

Both leukocyte rolling and adhesion were assessed within 5 veins and 5 arteries per mouse. The values for leukocyte rolling and adhesion are then combined, and the 5 vessel values averaged to generate an overall leukocyte trafficking value expressed per 100μm per minute.

2.6 Behavioural testing

Prior to behavioural testing, animals were handled daily for 2-weeks to help habituate the mice to each experimenter. Such practices help to limit anxious behaviour, which has the potential to significantly impact performance.

2.6.1 Barnes maze

Spatial learning and cognitive flexibility, within chapters 3 and 4, were assessed using the Barnes maze (C. A. Barnes, 1979). The Barnes maze is a land-based version of the Morris water maze and consists of a simple circular white platform (115 cm high x 91.5 cm wide) with 20 “escape holes” evenly spaced around the edge (San Diego Instruments) (Figure 2.7A). Under either hole 3, 8, 13, or 18 a black escape chamber is placed. The escape chamber remains in the same position for each mouse throughout their training period, however, its position its shifted clockwise, 5 holes, between mice to avoid olfactory cues influencing behaviour. To further limit the influence of olfactory cues ethanol is used between trails to clean the table (70%) and escape chamber (30%). Prior to the commencement of the task a holding cylinder (10.5 cm in diameter) was used to place the animals within the maze. The maze is brightly lit, and an aversive noise is played to motivate animals to escape. The mice use large spatial cues that are positioned on the walls around the maze to aid navigation and data is recorded using the Any-Maze tracking software (v4.99, Stoelting Europe, Ireland).

The aim of the Barnes maze is to assess the animals’ ability to learn and remember the location of the escape chamber. Spatial learning was assessed during an initial learning phase

and spatial memory in a 72-hour probe test. Cognitive flexibility is then tested in a reversal learning phase, with memory of the reversal chamber location once again assessed via a 72-hour probe test (Figure 2.7).

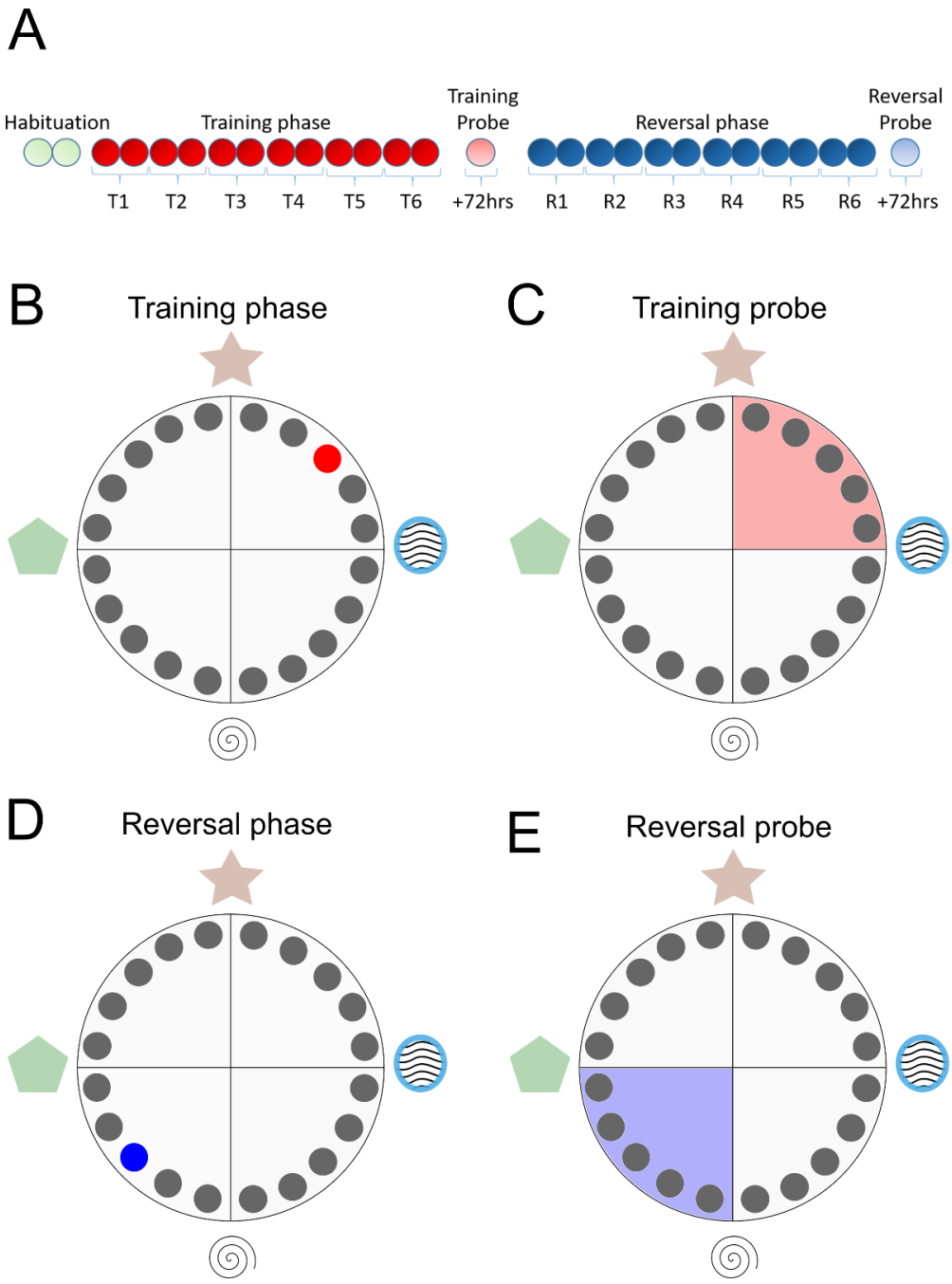

Figure 2.7 Schematic illustrations of the Barnes maze. **(A)** Timeline representing the Barnes maze task with each sub-section. Each circle represents a single trial, with T1 and R1 representing a training and reversal day respectively. **(B)** Illustration of the Barnes maze set up during the training phase. Shapes positioned around the maze represent visuals cues that

remain in a consistent position for all phases. The hole marked in red highlights the escape chamber location. **(C)** Illustration of the Barnes maze set up during the training probe. The red shaded quadrant indicates the location of the target zone, in which duration spent is recorded as a measure of memory. **(D)** Illustration of the Barnes maze set up during the reversal phase. The escape chamber, marked in blue, has be moved 180^0 to the opposite side of the maze in relation to its position during the training phase. **(E)** Illustration of the Barnes maze set up during the reversal probe. Blue shaded area represents the target zone representing the new reversal escape chamber location.

2.6.2 Acclimatisation phase

To limit stress and anxiety responses associated with a novel environment, animals were acclimatised to the Barnes maze and the behavioural room for 3 consecutive days prior to the start of the task. During acclimatisation, to allow the mice to become accustomed to their new surroundings, no bright lights or aversive noise were used. For the first 2-days of acclimation, animals were placed in the holding cylinder for 10-seconds, and then returned to their home cage. On day 3, animals were placed within the holding cylinder for 10-seconds and then allowed to freely explore the maze for 3-minutes. Following the 3-minutes, animals were gently guided into the escape chamber where they were held for 1-minute before being returned to their home cage.

2.6.3 Training phase

Spatial learning trails commenced the day following the completion of the acclimatisation phase (Figure 2.7B). Animals completed 2 trails per day, with a 1-hour trial interval, over 6 consecutive training days. Trails consisted of each animal being held within the holding cylinder for 10-seconds before the cylinder was removed and an aversive noise started playing (85db). Each mouse then had 3-minutes to locate and enter the escape chamber. Upon entering the escape chamber, the aversive noise is immediately stopped, and the hole covered for 1-minute to prevent the animal from leaving. Upon the completion of the 1-minute hold, the mouse is returned to their home cage. If animals were unable to locate the escape chamber during the 3-minute time period, they would be guided to the escape chamber and kept within for 1-minute before being returned to their home cage. As soon as the mouse entered the escape chamber the aversive noise ceased. The time taken for each mouse to enter the escape chamber is referred to as escape latency and used as a measure of spatial learning. All maze equipment was cleaned with 70% ethanol between each animal, and the escape chamber was carefully cleaned with 30% ethanol and rinsed with water to avoid aversive alcohol vapours building up.

2.6.4 Training 72-hour probe

Long-term spatial memory was assessed using a probe test carried out 72-hours after the final trial of the spatial learning phase (Figure 2.7C). Conditions remained constant for this phase apart from the removal of the escape chamber, and a shorter trial duration of 60-seconds. Trail length was reduced to help limit the effect of mice re-commencing search strategies once they have realised the escape chamber is missing. For analysis, the maze was segmented into 4 quadrants and the time each animal spent within each quadrant was calculated. Memory was assessed as the proportion of time spent within the quadrant previously home to that animals' respective escape chamber, which is referred to as the target quadrant. The percentage of trail time spent within the target quadrant is then compared to results from other experimental groups to discern differences in spatial memory. The time spent within the target quadrant is also compared to the 3 other quadrants to determine if a clear preference is apparent.

2.6.5 Reminder phase

Following the 72-hour probe, animals were subjected to 2 additional trials, in which the escape chamber is returned to help re-establish the chamber location memory following the probe trial. Conditions and trial duration were kept constant with the training phase.

2.6.6 Reversal phase

As a test of executive functioning and cognitive flexibility, the chamber location was shifted 180° to the opposite side of the maze for the reversal training phase (Figure 2.7D). Conditions and trial duration were the same as that described for the spatial learning phase. Reversal training trails were performed twice a day, with a 1-hour trail interval, for 3 consecutive days. Escape latency was once again recorded and analysed as a measure of relearning (cognitive flexibility).

2.6.7 Reversal 72-hour probe

The reversal 72-hour probe is performed as described previously within section 2.6.4 and assess the time spent within the target quadrant previously home to the reversal phase escape chamber location (Figure 2.7E).

2.6.8 Barnes maze exclusion criteria

In order to accurately test spatial learning and memory as well as cognitive flexibility, animals need to be motivated to actively explore the maze and they also need to sufficiently understand that the aim of the task is to enter the escape chamber. To ensure this the following strict exclusion criteria were applied; animals must enter a minimum of 3 quadrants in 2 of the first 5 training phase trials and animals must voluntarily enter the escape chamber at least 3 out of the final 6 trials to demonstrate that they have learned the task objective. Details of exclusions can be found within the method sections of the relevant chapters.

2.7 Substance administration

2.7.1 GW2580 administration

GW2580 (LC Laboratories, PKC Pharmaceutical Inc., USA, and Test Diet Europe) was administered at 0.1% concentration within diet ad libitum starting 24-hours following BCAS surgery.

2.7.2 5-Bromo-2'-deoxyuridine (BrdU) administration

5-Bromo-2'-deoxyuridine (BrdU, B5002, Sigma-Aldrich) was administered via oral gavage, once daily, for the final 3-days of the short term and chronic studies detailed within chapter 3. BrdU was prepared at a concentration of 50mg/kg in 0.5% Hypromellose (H3785, Sigma-Aldrich) and 0.1% Tween®80 (P1754, Sigma-Aldrich).

2.8 Tissue collection and processing

2.8.1 Rapid brain extraction

Animals from the study described within chapter 3 were sacrificed via cervical dislocation. Brains were then rapidly removed and transferred to ice-cold artificial CSF. A 1.6mm slice of brain section was then collected at -1.65mm posterior of bregma, in a Cellsafe^{+} Biopsy Capsule (Cell Path). The tissue samples were then fixed in 4% paraformaldehyde for 24-hours before being manually processed for paraffin embedding (Section 2.8.3). Tissue extracted for the experiments detailed within chapter 3, was gathered in this way to facilitate additional electrophysiological studies that do not fall within the scope of the present thesis.

2.8.2 Transcardial perfusion and brain extraction

Animals from studies described within chapters 4 and 5 were sacrificed under deep anaesthesia (5% induction, maintained at 3%) by transcardial perfusion with 40ml of 0.9% heparinised (0.002%) phosphate buffered saline (PBS). The heart is exposed through a midline incision followed by the dissection of the mediastinum. A butterfly needle in then placed within the left ventricle and clamped to secure its position. The right atrium is then cut with scissors and the perfusion is carried out at 2ml/minute until blood and tissues are successfully cleared. The brain is then carefully removed and placed within 4% paraformaldehyde for 24-hours in preparation for paraffin embedding (section 2.8.3) or freezing with isopentane (section 2.8.5),

2.8.3 Paraffin processing

For the studies described within chapter 3, fixed brain tissue slices were transferred to PBS and maintained within the cell sure tissue cassettes throughout paraffin processing. Brains extracted for studies detailed within chapter 5, were transferred from paraformaldehyde to PBS and sectioned into two 3mm coronal blocks, either side of bregma, using a mouse matrix. Both tissue blocks were then placed within a single tissue cassette for paraffin processing. The protocol undertaken for manual paraffin processing of tissue is described within Table 2.3.

Table 2.3 Manual processing for paraffin embedding

Solution	Duration (minute)	Temperature (^{0}C)
H_2O	*30*	*Room temperature*
70% Ethanol	*30*	*Room temperature*
70% Ethanol	*30*	*Room temperature*
90% Ethanol	*30*	*Room temperature*
90% Ethanol	*30*	*Room temperature*
100% Ethanol	*60*	*Room temperature*
100% Ethanol	*90*	*Room temperature*
Xylene	*60*	*Room temperature*
Xylene	*60*	*Room temperature*
Paraffin wax	*60*	*60*
Paraffin wax	*60*	*60*
Paraffin wax	*60*	*60*
Paraffin wax	*60*	*60*

2.8.4 Microtome sectioning

Paraffin embedded tissues generated for studies detailed within chapters 3 and 5 were cut to 6µm coronal tissue sections at -1.70mm posterior to bregma (Paxinos, 2001) using a rotary microtome (Leica RM2135, Leica Microsystems, Germany) and mounted on superfrost plus slides (VWR International). Mounted sections were dried on a heated pad for ≈30-minutes and then allowed to rest at room temperature for at least 24-hours prior to staining.

2.8.5 Processing for freezing and cyrosectioning

For the study detailed within chapter 4, brains were transferred from 4% paraformaldehyde to 30% sucrose for 72-hours, then frozen in -42^{0}C isopentane (chilled using dry ice). 10µm coronal sections were then collected at -1.70mm posterior of bregma (Paxinos, 2001) using a cryostat (Leica CM1950). Tissue sections were then mounted onto superfrost plus slides (VWR International) and allowed to dry at room temperature for at least 12-hours. Mounted sections were then stained directly after the drying duration or stored at -20^{0}C for future use.

2.9 Flow cytometry

For the flow cytometry cohorts detailed within chapters 3 and 4, mice were transcardially perfused and brains extracted according to the method detailed within section 2.8.2. With the exception of perfusion flow rate, which was increased from 2 to 4ml/minute to ensure that tissues could be processed as swiftly as possible. For flow cytometry experiments detailed within chapter 3, following extraction the brain was quickly cut into 2 mm sagittal slices using a matrix, then transferred to ice cold 1X HBSS with 25 mM HEPES. The corpus callosum was then dissected out using a dissecting microscope and transferred to fresh tubes containing ice cold 1X HBSS with 25 mM HEPES and kept on ice prior to processing. For flow cytometry experiments detailed within chapter 4, following extraction the brain was quickly cut into 2 hemispheres using a matrix, then transferred to ice cold 1X HBSS with 25 mM HEPES.

For processing of tissue into a single cell suspension, all tools and reagents were kept ice cold throughout, and centrifugation steps were performed at 4˚C. Tissue samples were quickly minced in 1X HBSS (without Ca^{2+} or Mg^{2+}; Gibco) with 25 mM HEPES (Fisher Scientific) (HBSS with HEPES) using a scalpel prior to transfer to a or 2 ml dounce homogeniser with loose pestles. Tissue samples were homogenised with 30 passes of the dounce then filtered through a pre-wet 70 µm cell strainer (BD2 Falcon) which was washed with 2 ml HBSS with HEPES. Samples were centrifuged at 600 *x g* for 5-minutes prior to resuspension in a 30% PercollPLUS solution with 5 ml HBSS with HEPES overlaid on top. The cell suspension was

then centrifuged at 600 *x g* for 20-minutes with no break. Cells were resuspended in FACS buffer (1X PBS (Gibco) with 25mM HEPES and 0.1% BSA (Sigma Aldrich)) and incubated with Mouse BD Fc Block™ (BD Biosciences) for 30-minutes on ice. Cells were then immunostained with primary antibodies directed against CD11b (clone: M1/70), CD45 (clone: 30-F11), Ly6C (clone: HK1.4), Ly6G (clone: 1A8) at 1:200 (Ly6C) or 1:500 dilution for 30-minutes on ice. Cells were washed then analysed and sorted using a FACS Aria II (BD Biosciences). Cell sorting was performed by staff in the QMRI Flow Cytometry and Cell Sorting Facility (University of Edinburgh). Sorted cells were centrifuged at 6000 RPM for 5-minutes at 4˚C then either resuspended in 350 µl RLT Buffer (Qiagen) and stored at -80˚C or processed immediately for RNA extraction.

2.10 RNA extraction and cDNA synthesis

For RNA extraction and cDNA synthesis within studies described in chapter 3, sorted cells from isolated corpus callosum samples were processed immediately post-sort and RNA was extracted using the High Pure RNA Isolation Kit (Roche) according to the manufacturer's instructions. RNA quantities were determined by Agilent 4200 Tapestation (Agilent Technologies). cDNA was synthesised from 1.5 ng RNA using the Superscript IV Reverse Transcriptase (Life Technologies), according to the manufacturer's instructions and used undiluted for qPCR reactions. cDNA samples were stored at -20ºC until use.

For RNA extraction and cDNA synthesis within studies described in chapter 5, sorted cells in RLT Buffer were defrosted and vortexed for 1-minute to homogenise cells and RNA was extracted using the AllPrep DNA/RNA/miRNA Universal Kit (Qiagen) according to the manufacturer's instructions. Sorted cells were processed immediately post-sort and RNA was extracted using the High Pure RNA Isolation Kit (Roche) according to the manufacturer's instructions. RNA quantities were determined by Agilent 4200 Tapestation (Agilent Technologies). cDNA was synthesised from 15 ng RNA using the Superscript IV Reverse Transcriptase (Life Technologies), according to the manufacturer's instructions and used undiluted for qPCR reactions. cDNA samples were stored at -20ºC until use.

2.11 Quantitative (q)-PCR

cDNA libraries were analysed by qPCR using the DyNAmo ColorFlash SYBR Green kit (Thermo Scientific) according to the manufacturer's instructions. Briefly, the cDNA template was mixed with DyNAmo ColourFlash SYBR Green master mix (Fisher Scientific), nuclease-free H_2O and the following custom designed gene-specific primers (200 nM final concentration; Sigma Aldrich): CSF1R (forward: 5'-gaaggaaggccgaggctatg-3', reverse: 5'-

gagaagccactgtccctgc-3'), Aif1 (forward: 5'-tggaggggatcaacaagcaa-3', reverse: 5'-tccatttccattcagatcaaatcc-3'), 18s (forward: 5'-cccagtaagtgcgggtcat-'3, reverse: 5'-ccgagggcctcactaaacc-3') and Cx_3Cr_1 (forward: 5'-gccaactccatgaacaaccg-3', reverse: 5'-ttgacttccgagttgcggag-3'). Primers were validated to confirm efficiency prior to use. qPCR cycles were performed on a Bio-Rad CFX96 thermocycler (Bio-Rad Laboratories) as follows: hot-start denaturation cycle 95°C for 10-minutes, 40 cycles of amplification at 95°C for 15-seconds, 62.5°C for 20-seconds, and 72°C for 30-seconds, followed by one cycle of 95°C for 1-minute, 55°C for 30-seconds, with a ramp up to 30-seconds at 95 °C with continuous detection of fluorescence. Cycle threshold (Ct) values of target genes were normalized Aif1 for CSF1R quantification and to 18S for Cx_3Cr_1 quantification. The data are expressed as fold change relative to control group (wild-type or shams) using the 2^ (−ΔΔCt) method.

2.12 Immunohistochemical staining

2.12.1 Immunohistochemical DAB staining

Paraffin sections were deparaffinised for 30-minutes within a tabletop oven set to 60^0C, followed by 2 x 15-minute xylene washes. Sections were then washed with ethanol at 100% for 2 x 5-minutes, 90% for 5-minutes, and 70% for 5-minutes. Endogenous peroxidases were then quenched using 3% hydrogen peroxide in methanol for 30-minutes. Slides were washed in running water for 15-minutes before antigen retrieval, if required (Iba-1, but not for MAG staining). For citric acid retrieval, sections were incubated in 10 mM citric acid (pH6) and then heated to 95^0C for 10-minutes within a Decloaking chamber (Biocare Medical). Following removal, sections were washed in PBS and blocked at room temperature for 1-hour with 10% normal serum and 0.5% bovine serum albumin, before incubation at 4^0C overnight (minimum 16-hours) with primary antibody diluted in block. Sections were then removed from the cold room and allowed to rest at room temperature for 10-minutes followed by 2 x 5-minute PBS washes. Biotinylated secondary antibodies were then applied for 1-hour at room temperature. To further amplify the signal, the Vector ABC Elite Kit (Vector Labs, UK) is then applied and allowed to incubate for 1-hour at room temperature. To allow visualisation of peroxidase activity, 3,3' diaminobenzidine tetrahydrochloride (DAB, Vector Labs, UK) is applied for 3-minutes before being washed off with distilled H_20. Sections were then washed in running water before dehydration through a series of ethanol washes (70% for 2-minutes, 90% for 2-minutes. 100% for 2 x 5-minutes). The sections are then place within xylene for 15-minutes before mounting with DPX (Sigma, UK). Primary and secondary antibody details and concentrations can be found within Table 2.4.

Table 2.4 Antibodies used for immunohistochemical staining

Primary Antibody	Target	Dilution	Retrieval method	Supplier	Secondary Antibody	Dilution	Supplier
Anti-Iba1	*Microglia/ Macrophages*	*1:1000 (DAB)*	*Citrate 95^{0}C*	*Menarini, MP290-CR05*	*Biotinylated anti-rabbit*	*1:100*	*Vector BA1100*
		1:250 (IF)	*Citrate 95^{0}C*	*Menarini, MP290-CR05*	*Anti-rabbit Alexa Fluorophore 555*	*1:200*	*Invitrogen A31572*
		1:8000 (Tyramide)	*Tris-EDTA 97.5^{0}C*	*Wako 019-19741*	*Biotinylated goat anti-rabbit* *Alexa Fluorophore-488 Superboost Kit, Streptavidin*	*1:500* *1:200*	*Vector BA1000* *Thermofisher B40932*
Anti-CD107b (Lamp2)	*Lysosomal protein*	*1:100 (IF)*	*Tris-EDTA 97.5^{0}C*	*Biolegend 108501*	*Anti-rat Alexa Fluorophore-555*	*1:500*	*ThermoFisher A-21434*
Anti-BrdU	*Bromodeoxy-uridine*	*1:50 (IF)*	*Citrate 95^{0}C*	*Abcam ab6326*	*Biotinylated anti-rat* *Streptavidin Alexa Flurophore-488*	*1:100* *1:100*	*Vector BA4900* *Invitrogen S11223*
Anti-MAG	*Myelin associated glycoprotein*	*1:15,000 (DAB)*	*N/A*	*Abcam ab89780*	*Biotinylated anti-mouse*	*1:100*	*Vector BA2001*

2.12.2 Immunofluorescent labelling

Following the deparaffinisation steps detailed within section 2.12.1, slides are rinsed for 15-minutes in running water. For Iba-1/BrdU staining citric acid retrieval was carried out as described above in section 2.12.1, details of Lamp2 immunofluorescent staining can be found within section 2.12.3. Following citric acid retrieval sections were washed in PBS and blocked at room temperature for 1-hour (10% normal serum, 0.5% bovine serum albumin in PBS), before incubation at 4^{0}C overnight (minimum 16-hours) with primary antibody diluted in block. Primary antibodies were diluted in blocking solution made up in 0.3% Triton-X PBS. The following day sections were then washed in PBS before incubation with biotinylate secondary antibodies for 1-hour at room temperature and protected from light. The sections were then washed with PBS, followed by Tris-buffer before being allowed to air dry for 15-20-minutes before mounting with Vectashield Hardset containing DAPI (Vector, UK). Primary and secondary antibody details and concentrations can be found within Table 2.4.

2.12.3 Tyramide Immunofluorescent labelling

For Iba-1/Lamp2 immunofluorescent staining an alternative staining protocol using tyramide was employed. Following the deparaffinisation steps detailed within section 2.12.1, slides were rinsed in running water for 10-minutes. Tris-EDTA (pH9) antigen retrieval was then carried out within a water bath set to 97.5^{0}C for 30-minutes. Following a 20-minute cooling period at room temperature, the slides were washed with PBS before being blocked (10% animal serum in PBS) for 1-hour at room temperature. Slides were then incubated overnight with primary antibody, diluted in block, at 4^{0}C. The following day slides we rested at room temperature for 10-minutes before 3 x 3-minute washes with Tris-buffered saline with

0.05% tween. Endogenous peroxidases were then quenched using 3% hydrogen peroxide in methanol for 30-minutes, followed by 3 x 3-minute washes in TBS with 0.05% tween. The sections were then incubated with a secondary antibody mix in 0.1% BSA TBST for 1-hour and 30-minutes, followed by 3 x 3-minute washes in TBS with 0.1% tween. The next steps made use of the Alexa Fluorophore-488 Superboost Kit Streptavidin kit (Thermofisher) and was conducted according to the manufacturer's instructions. Firstly, slides were incubated in tertiary antibody for 45-minutes followed by 3 x 3-minute washes with TBS containining 0.1% tween. Tyramide amplification was then achieved by mixing the 1x reaction buffer with 1x H_2O_2 solution and adding 100µl to each tissue section. The tyramide reaction was then stopped after 8-minutes of incubation by adding the stop solution, diluted 1:11 with PBS, for 1-minute. The slides were then washed in PBS before a second round of Tris-EDTA (pH9) antigen retrieval at 97.5^0C for 30-minutes. Following retrieval, the slides were left to cool at room temperature for 20-minutes before 3 x 3-minute washes in PBS, followed by incubation with blocking solution (10% animal serum in PBS) for 1-hour at room temperature. Slides were then incubated with primary antibody solution, diluted in PBS containing 10% normal animal serum, overnight at 4^0C. The next day, following a rest period of 10-minutes at room temperature, the slides were washed 3 x 3-minutes in PBS before incubation with a secondary antibody solution, diluted in PBS, for 1-hour at room temperature. The slides then underwent 3 x 3-minute washes in PBS before being mounted with fluorescence mounting medium (Agilent DAKO). Primary and secondary antibody details and concentrations can be found within Table 2.4.

2.12.4 Preparation for $Cx_3Cr_1^{eGFP}$ cell counts

Frozen sections were air dried for 10-minutes then washed in PBS for 2 x 5-minutes. Sections were then dehydrated through a series of ethanol washes; 70% for 2-minutes, 90% for 2-minutes, 100% for 5-minutes, and 100% for 10-minutes. Finally, sections are washed with xylene for 10-minutes. Sections were then rehydrated through washes with 100% ethanol for 10-minutes, 100% ethanol for 5-minutes, followed by 2 x 5-minute washes with PBS. Slides were then allowed to air dry for 10-minutes before mounting with Vectashield Hardset containing DAPI (Vector, UK).

2.12.5 Immunohistochemical staining controls

Prior to the full runs of immunohistochemical staining experiments, optimisations were run on small sample cohorts to ensure that antibody conditions and concentrations were optimised. To ensure for accurate staining, a section generated from a previous study with a known level

of staining was always included within optimisation runs alongside tissue taken from the present study cohorts. To ensure antibody specificity of staining, all immunohistochemical optimisations and full runs included a negative control, where the primary antibody was not applied but all other steps were consistent. Stained sections were only analysed if this negative control was clear. To prevent batch variation, which can occur between different experiments, all sections from one immunohistochemical analysis were stained within a single experiment.

2.13 Imaging acquisition and analysis of immunohistochemical staining

2.13.1 Imaging acquisition

DAB-labelled sections were imaged using an Axio Scan.Z1 slide scanner (x20, Ziess, Germany). Immunofluorescent labelling for Iba1/BrdU was imaged using a Zeiss 710 confocal microscope (x20 Zeiss, Germany), or a Leica TCS SP5 confocal microscope (x20 Leica Microsystems, Germany). Iba-1/Lamp2 staining was imaged using a Zeiss LSMZ10 confocal microscope (x20 Zeiss, Germany).

2.13.2 Image analysis

Image analysis for immunohistochemically stained sections was performed using ImageJ software (v1.46, NIH, Bethesda, MD, USA). Due to the large file sizes generated through slide scanner imaging, each slide scanned image was compressed by either 50 or 75% before analysis, to enable ImageJ to open the image. Iba-1 DAB, Iba-1/BrdU, Iba-1/Lamp2 and $Cx_3Cr_1^{eGFP}$ cell counts were all manually generated with the use of the CellCounter plugin. ROI placements can be seen in Figure 2.8, great care was taken to match regions as closely as possible between mice, with ROI areas also being kept as consistent as possible. Each ROI was manually positioned by the assessor, who was blind to surgical, genotype, and treatment status of the mice throughout. Corpus callosal and cortical ROIs were drawn manually using the straight-line tool, whereas consistently sized rectangles were used to assess all other regions. For percentage area of staining methods, a rolling 50-pixel background subtraction was applied. A manual threshold was then selected by the assessor for each individual brain region, and then applied to all images gathered from that region to generate a percentage value to reflect total area of positive staining. MAG-stained sections were graded subjectively on a scale from 0 to 3 depending on the extent of myelin debris. Sections were assessed manually through an Olympus BX51 microscope, Olympus, UK with grades from each side of the brain summated to give an overall value per brain region.

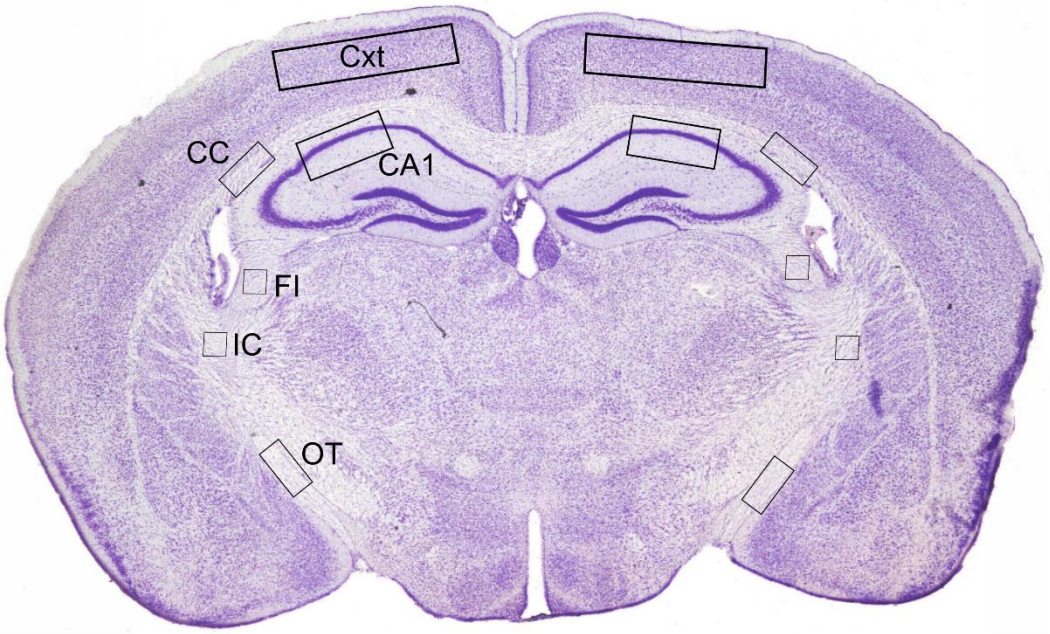

Figure 2.8 Regions of interest used for image analysis of immunohistochemical stains. Regions representing the cortex (Cxt), corpus callosum (CC), hippocampal CA1 (CA1), fimbria (FI), internal capsule (IC), and optic tract (OT) were all manually generated for both the left and right hemisphere using ImageJ software. Image represents figure 45, Bregma -1.70mm from the mouse atlas (Paxinos, 2001)

2.13.3 Exclusion criteria

Due to minor variation in the anatomical level of sections stained, some ROIs had to be slightly adjusted or images excluded entirely. Images were also excluded if excessive tissue damage or external debris was present leading to blocking of the antibody signal.

2.14 Statistical analysis

Statistical analysis was carried out using either SPSS (Version22, IBM corp) or Graphpad prism (v5, GraphPad Software Inc, La Jolla, USA) statistical software. Details of the specific statistical tests that were performed can be found within the methods section of the relevant chapter. Unless specifically stated otherwise, all data is presented as median±interquartile range and significance is gated at $p<0.05$.

Chapter 3

Investigating the role of microglial proliferation in the development of white matter damage and cognitive impairment following BCAS

3.1 Introduction

Chronic cerebral hypoperfusion has been shown to lead to diffuse white matter damage which is strongly correlated to cognitive decline. Despite these associative links, the pathological mechanisms by which chronic cerebral hypoperfusion leads to white matter damage and ultimately cognitive impairment remain largely unknown, evidence does however suggest that microglia and neuroinflammation may place a causal role. Chronic cerebral hypoperfusion, modelled in mice through bilateral common carotid artery stenosis (BCAS), leads to the progressive expansion of microglial cells within white matter regions (Coltman et al., 2011; Holland et al., 2015; Manso et al., 2017; Reimer et al., 2011). White matter microglial expansion was found to positively correlate with increased myelin pathology, diminished white matter signalling and impaired spatial learning and memory (Fowler et al., 2017; Kitamura et al., 2017; Manso et al., 2017). Treatment with broad acting anti-inflammatory drugs such as dimethyl fumarate, cilostazol and minocycline were found to rescue white matter signalling and cognitive impairments following BCAS (Fowler et al., 2017; Kitamura et al., 2017; Manso et al., 2017). Interestingly, despite varied mechanisms of action, reduced white matter microglia numbers was a common outcome of each anti-inflammatory treatment, correlating with improved functional and cognitive outcomes. Taken together these results led to the hypothesis that microglial expansion is a key pathological process driving white matter dysfunction and cognitive impairments following chronic cerebral hypoperfusion. To date, pharmacological interventions have only been able to demonstrate a correlation between reduced microglial number and improved functional outcomes. Therefore, to interrogate the role of microglial expansion following BCAS more specifically, the drug GW2580 was selected. GW2580 is an orally available inhibitor of cFMS receptor kinase, which is a fundamental mediator of colony-stimulating-factor-1 (CSF-1) signalling. CSF-1 signalling, through cFMS receptor kinase promotes the survival, proliferation, and differentiation of microglia (Conway et al., 2005). GW2580 treatment

allows for the specific and targeted blockade of microglial proliferation to accurately integrate its role in white matter damage and cognitive impairment following chronic cerebral hypoperfusion.

3.1.1 Hypothesis

This study tests the hypothesis that microglial proliferation leads to white matter damage and cognitive impairment following bilateral common carotid artery stenosis

3.1.2 Aims

Using a model of BCAS within wild-type, C57BL/6J mice, the studies aimed to:

1. Assess the effect of BCAS on temporal cortical blood flow changes following surgery
2. Investigate the response of white matter immune cell populations following 1-week of BCAS
3. Assess white and grey matter microglial expansion and proliferation, 1 and 6-weeks following BCAS
4. Investigate the impact of BCAS on the integrity of white matter regions, 6-weeks following surgery
5. Assess the effect of BCAS on spatial learning and memory, 6-weeks following surgery
6. Investigate the effect, on the above measures, of blocking microglial proliferation through chronic GW2580 treatment

3.2 Materials and Methods

3.2.1 Experimental Mice

Wild-type (C57BL/6J) (n=99) were purchased from Charles River Laboratories (JAX™-C57BL/6J) and used for all studies having been assigned to each experimental group at random. Mice, 3-4 months old, were studied at a short-term 1-week timepoint as well as a chronic 6-week timepoint following surgery. A total of 51 mice began the 1-week study and 48 the 6-week study. Details of group numbers and exclusions can be found in the relevant methods sections below, alternatively an overall summary can be found within Table 3.1.

Table 3.1 Number of mice within each experimental group with details of exclusions

Histology cohort 1-week study	Sham	BCAS	
Sham/BCAS surgery	*13*	*23*	
Exclusion criteria:			
Poor recovery following surgery	*0*	*3*	
<35% CBF reduction following BCAS surgery	*0*	*6*	
Final groups	*13*	*14*	
FACS cohort 1-week study	*Sham*	*BCAS*	
Sham/BCAS surgery	*4*	*11*	
Exclusion criteria:			
Poor recovery following surgery	*1*	*3*	
<35% CBF reduction following BCAS surgery	*0*	*2*	
Finals groups	*3*	*6*	
Chronic 6-week study	*sham*	*BCAS*	*BCAS+ GW2580*
Sham/BCAS surgery	*10*	*23*	*15*
Exclusion criteria:			
Poor recovery following surgery	*0*	*7*	*0*
<35% CBF reduction following BCAS surgery	*0*	*4*	*5*
Barnes maze trial completion <50%	*1*	*0*	*0*
Final groups	*9*	*12*	*10*

3.2.2 Bilateral common carotid artery stenosis

Bilateral common carotid artery stenosis (BCAS) surgery was performed as previously described (section 2.2). Micro-coils, of internal diameter 0.16mm and 0.18mm were applied to the left and right common carotid arteries, respectively. As a control, sham mice underwent the same procedure minus the application of micro-coils. Due to signs of poor health 3 mice from the 1-week histology cohort, 4 mice from the 1-week FACS cohort and 7 mice from the 6-week cohort were humanely culled and excluded from the study. More detailed information on exclusions following surgery are reported in Section 3.2.3 and detailed in Table 3.1.

3.2.3 Laser speckle imaging assessment of resting cortical blood flow

Laser speckle imaging was used to assess CBF within sham and BCAS mice following surgery as previously described (Section 2.3). For the short-term 1-week studies, blood flow responses were assessed prior to surgery (baseline) as well as 24-hours and 1-week following surgery. For the chronic 6-week study, CBF was analysed at baseline, 24-hours and 6-weeks following surgery. To enable stenosis mediated effects to be accurately assessed, a strict exclusion criterion was adopted by which 24-hour post-surgery blood flow reductions needed to exceed 35% for the mouse to be included in the study. This exclusion criteria was applied to both the short-term and chronic studies leading to the exclusion of 6 mice from the 1-week histology cohort, 2 mice from the 1-week FACS cohort and 9 from the 6-week study (detailed within Table 3.1)

3.2.4 GW2580 administration

GW2580 (LC Laboratories, PKC Pharmaceuticals Inc., USA) was delivered within the diet for the chronic 6-week study as previously described (Section 2.7.1). Food intake and animal weight were closely monitored throughout the study, with no group differences identified.

3.2.5 5-Bromo-2’-deoxyuridine (BrdU) administration

5-Bromo-2’-deoxyuridine (BrdU, B5002, Sigma-Aldrich) was administered via oval gavage once a day for the final 3-days of both the short-term and chronic study as previously described (Section 2.7.2).

3.2.6 Barnes maze behavioural testing

The Barnes maze is a test of visuo-spatial learning and memory and was carried out within the chronic 6-week study cohort, as previously described (Section 2.6). The training period commenced 4-weeks and ended 6-weeks following sham/BCAS surgery. An exclusion criterion based on maze exploration, as previously described (Section 2.6.8), was applied highlighting 1 mouse who was subsequently excluded from all studies (Table 3.1).

3.2.7 Tissue collection and processing

To collect tissue for histology, animals were sacrificed via cervical dislocation as previously described (Section 2.8.1). The tissue was then processed for paraffin embedding as previous described (Section 2.8.3). Tissue was then microtome sectioned in preparation for immunohistochemical staining (Section 2.8.4). For flow cytometry experiments, mice were transcardially perfused with ice cold PBS containing 0.1% heparin under deep isoflurane anaesthesia (Section 2.8.2). The white matter was then isolated as described within Section 2.9)

3.2.8 Flow cytometry and cell sorting

Isolated white matter tissue was processed into a single cell suspension as detailed within Section 2.9. Cells were then immunostained with primary antibodies directed against CD11b, CD45, Ly6C, and Ly6G at 1:200 (Ly6C) or 1:500 dilution for 30-minutes on ice. Cells were washed then analysed and sorted using a FACS Aria II (BD Biosciences). Cell sorting was performed by staff in the QMRI Flow Cytometry and Cell Sorting Facility (University of Edinburgh). Sorted cells were centrifuged at 6000 RPM for 5-minutes at 4˚C and then processed immediately for RNA extraction.

3.2.9 RNA extraction and cDNA synthesis

Sorted cells from isolated corpus callosum samples were processed for RNA extraction immediately post-sort using the High Pure RNA Isolation Kit (Roche) according to the manufacturer's instructions (as detailed within Section 2.10). RNA quantities were determined by Agilent 4200 Tapestation (Agilent Technologies). cDNA was synthesised from 1.5 ng RNA using the Superscript IV Reverse Transcriptase (Life Technologies), according to the manufacturer's instructions and used undiluted for qPCR reactions. cDNA samples were stored at -20ºC until use.

3.2.10 Quantitative (q)-PCR

cDNA libraries were analysed by qPCR using the DyNAmo ColorFlash SYBR Green kit (Thermo Scientific) according to the manufacturer's instructions (as described within Section 2.11). Briefly, the cDNA template was mixed with DyNAmo ColourFlash SYBR Green master mix (Fisher Scientific), nuclease-free H_2O and the following custom designed gene-specific primers (200 nM final concentration; Sigma Aldrich): CSF1R (forward: 5'-gaaggaaggccgaggctatg-3', reverse: 5'-gagaagccactgtccctgc-3') and Aif1 (forward: 5'-tggaggggatcaacaagcaa-3', reverse: 5'-tccatttccattcagatcaaatcc-3'). qPCR cycles were performed on a Bio-Rad CFX96 thermocycler (Bio-Rad Laboratories) as described previously (Section 2.11). Cycle threshold (Ct) values of target genes were normalized to Aif1, with data expressed as fold change relative to control group (shams) using the 2^ (−ΔΔCt) method.

3.2.11 Immunohistochemistry

Immunohistochemical staining was performed on 6μm paraffin embedded sections as previously described (Sections 2.12.1, 2.12.2, and 2.12.3). Tissue was stained with antibodies against Iba-1, BrdU, Lamp2 and MAG. Additional information on antibodies used can be found within Table 2.4.

3.2.12 Image acquisition and analysis

DAB-stained sections for Iba-1 and MAG quantification were imaged using an Axio ScanZ1 slide scanner (x20, Zeiss, Germany) as previously described (Section 2.13.1). Fluorescently stained sections for Iba1, BrdU and Lamp2 analysis were imaged using confocal microscopy, as previously described (Section 2.13.1). Cell count and percentage area per cell analysis was completed using the ImageJ software (v1.46, NIH, Bethesda, MD, USA) as previously described (Section 2.13.2). MAG staining was analysed semi-quantitatively using a 4-point scale, as previously described (Section 2.13.2).

3.2.13 Statistical analysis

Statistical analysis was performed using SPSS (v22, IBM Corp.) software. Repeated measures two-way ANOVA's were used to assess group differences in CBF as well as the Barnes maze measures of escape latency, movement distance and movement speed (training and reversal phases), with Bonferroni *post hoc* follow up analysis. Barnes maze training and reversal probe target zone preference were analysed using the Friedman test to determine differences in time spent within each quadrant. The Wilcoxon signed ranks *post hoc* test was

then applied to determine target zone preference. Independent samples Mann-Whitney U tests were used to analyse 1-week microglial DAB and microglial proliferation counts as well as FACS immune cell comparisons and CSF1R expression. Independent samples Kruskal-Wallis tests were used to analyse 6-week microglial DAB counts, microglial proliferation, Lamp2 and MAG analysis as well as Barnes maze training and reversal probe target zone comparisons, with Dunn's *post hoc* follow up analysis. Correlations were analysed using the Spearman's ranked correlation coefficient. For parametric statistical tests, data is presented as mean ± standard error of the mean (SEM) and for nonparametric testing, data is presented as median ± interquartile range (IQR) (specified in relevant figure legend). Statistical significance was determined at $p<0.05$.

3.2.14 Experimental contributions

The majority of experiments and analysis detailed within this chapter were conducted by myself. The studies, however, were also supported by Dr Emma Sigfridsson, Dr Jessica Duncombe, Dr Edel Hennessey, Dr Katie Askew, Dr Juraj Koudelka, Dr Stefan Szymkowiak and Professor Karen Horsburgh. I performed laser speckle imaging, behavioural testing, tissue processing and sectioning, immunohistochemical staining and slide scanner/confocal imaging of Iba-1 (DAB) and Lamp2 stains as well as all the data analysis presented within this chapter, with the exception of the 1-week FACs counts and 6-week MAG grading. Dr Emma Sigfridsson performed laser speckle imaging, behavioural testing, tissue processing/sectioning and stained/analysed MAG within the 6-week tissue. Dr Jessica Duncombe performed BCAS surgery, administered oral gavages, processed tissue, stained 6-week tissue for Iba-1/BrdU and imaged 1- and 6-week Iba-1/BrdU tissues. Dr Edel Hennessey administered oral gavages, collected/processed tissue and stained for Iba1/BrdU, all within the 1-week study. Dr Katie Askew performed the 1-week FACs isolation and quantification of immune cell populations and CSF1R expression. Dr Juraj Koudelka assisted with tissue collection at the 6-week time-point. Dr Stefan Szymkowiak optimised and assisted with tyramide Lamp2 staining. Professor Karen Horsburgh performed BCAS surgery for the 1-week FACS cohort.

3.3 Results

3.3.1 BCAS induces a significant and sustained reduction in cerebral blood flow

The first aim of this study was to assess the temporal profile of CBF changes up to 1-week post-BCAS. CBF was measured using laser speckle imaging at baseline (24-hours before surgery), 24-hours and 1-week following sham/BCAS surgery (Figure 3.1). Resting CBF was reported as percentage change from baseline flux (arbitrary unit). BCAS surgery on average elicited ≈60% reduction in CBF, which was maintained at 1-week following surgery, whereas sham mice displayed relatively stable blood flow measurements over the same period (Figure 3.1A). Statistical analysis revealed a significant overall effect of time ($F_{(1,20)}$ = 73.637, $p<0.001$) and surgery ($F_{(1,25)}$ = 142.847, $p<0.001$) as well as a significant time-surgery interaction ($F_{(2,50)}$ = 54.613, $p<0.001$). *Post hoc* analysis using the Bonferroni correction revealed that BCAS elicited a significant reduction in CBF at 24-hours (Sham; 103.4±4.6, BCAS; 41.92±4.5, $p<0.001$) and 1-week (Sham; 88.3±3.7, BCAS; 39.2±3.5, $p<0.001$) following surgery (Figure 3.1).

Overall, these data demonstrate that BCAS surgery elicits a significant reduction in CBF, which is maintained 1-week following surgery.

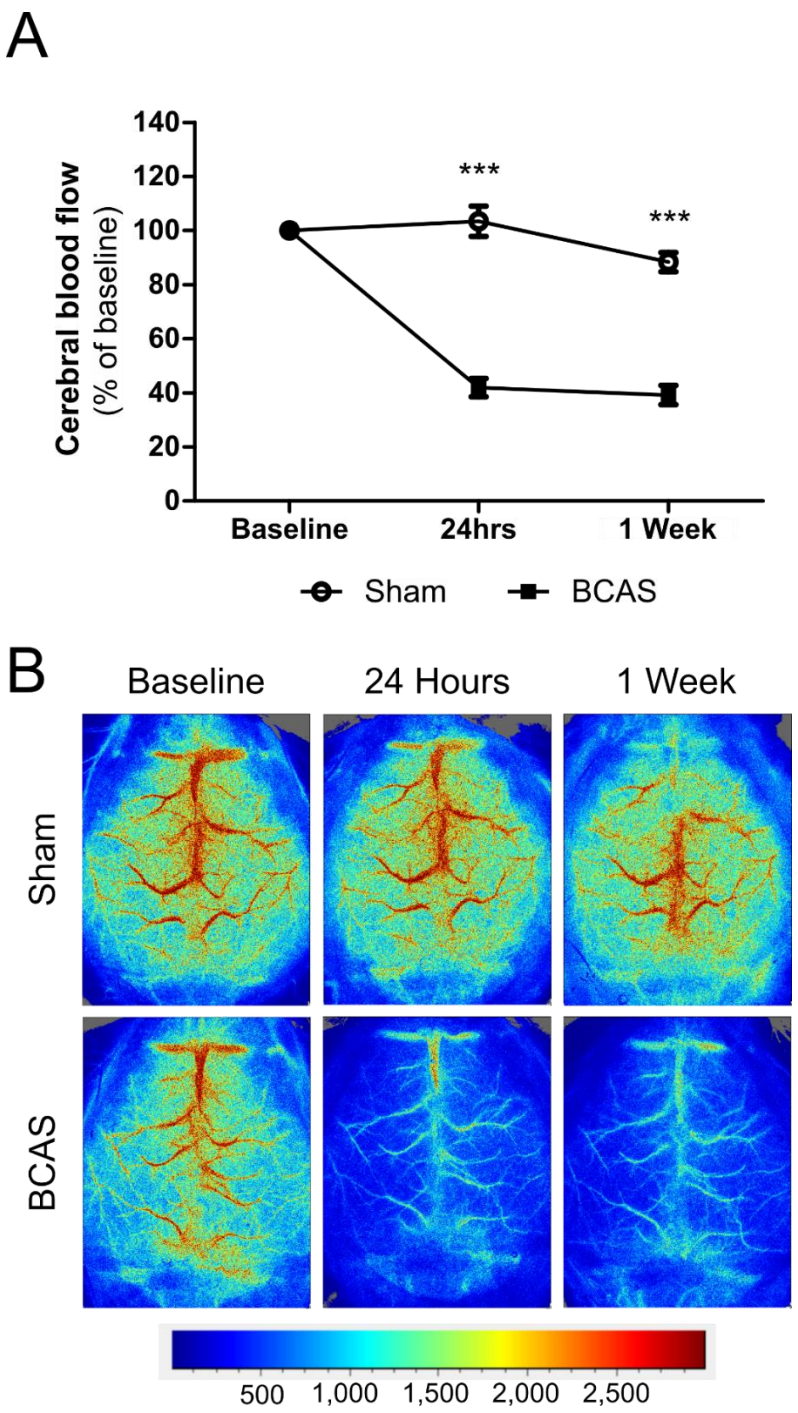

Figure 3.1 BCAS induces a sustained reduction in CBF. **(A)** BCAS surgery reduced CBF by ≈60%, in contrast sham mice showed stable blood flow over the same period. Data presented as Mean±SEM. ***p<0.001. **(B)** Representative images displaying laser speckle imaging of the cerebral vasculature within sham and BCAS mice at baseline, 24-hours and 1-week following surgery. Blue represents low and red represents high flow.

3.3.2 Microglial expansion dominates the early inflammatory response following BCAS

Previous research has demonstrated that BCAS leads to increased microglial numbers within specific white matter regions (Duncombe, Kitamura, et al., 2017; Fowler et al., 2017; Manso et al., 2017). Investigations into the effect of BCAS on the other immune cell populations within the white matter, however, has been limited. To accurately determine the contribution of other myeloid cell types to the inflammatory response following BCAS, flow cytometric quantification was carried out (Figure 3.2). Brain cell suspensions were prepared from the corpus callosum and stained with a panel of myeloid cell markers to enable cell populations of microglia, macrophages, neutrophils, and monocytes to be quantified 1-week following sham/BCAS surgery (Figure 3.2A). In agreement with previous immunohistochemical analysis, microglial numbers ($CD11b^{+}CD45^{low}$) were found to be significantly increased within the corpus callosum of BCAS mice (15,095±6,246) in comparison to shams (7518±3,451) ($U=18$, $p<0.05$) (Figure 3.2A). In respect to other myeloid cell populations, no significant difference in cell numbers were observed within macrophages ($CD11b^{+ve}CD45^{high}$), neutrophils ($Ly6G^{+ve}$) or monocytes ($Ly6C^{+ve}$) following BCAS (Figure 3.2A).

Taken together these data indicate that microglia are the principal mediators of the neuroinflammatory environment following BCAS, with little or no contribution of other myeloid cell populations.

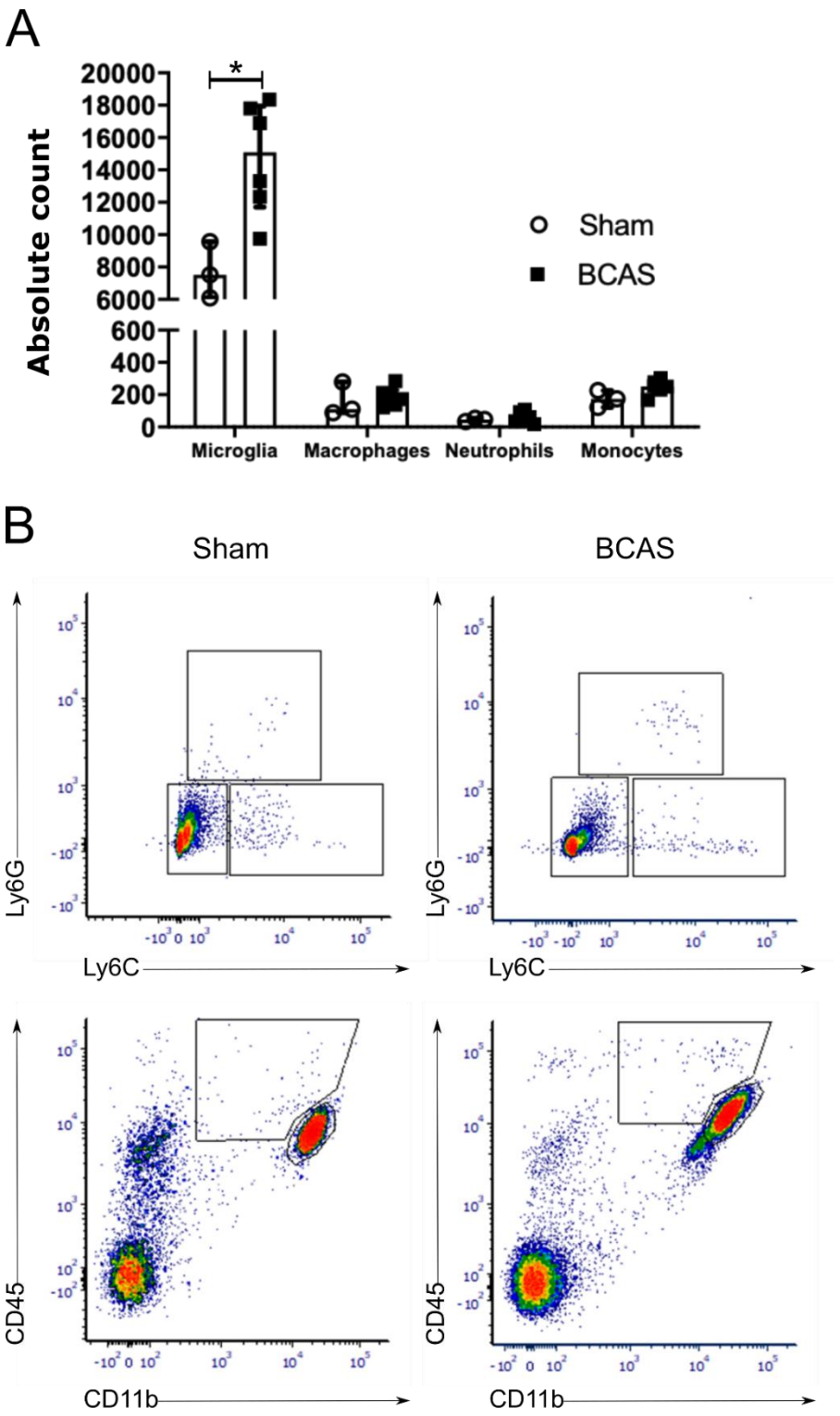

Figure 3.2 Microglial expansion dominates the early inflammatory response following BCAS. (A) Increased microglial cells within BCAS mice in comparison to shams, with no observed differences in macrophage, neutrophil or monocyte populations as measured by flow cytometry. Data presented as Median±IQR. $p<0.05$*. ***(B)*** Representative plots

displaying cell populations isolated, via flow cytometry, from the white matter of both sham and BCAS mice. Red indicates the highest density of cells with blue representing the lowest density.

3.3.3 BCAS induces microglial expansion following 1-week of reduced cerebral blood flow

Having demonstrated that microglial dominate the early neuroinflammatory response following BCAS surgery, the next aim was to determine if increased microglial numbers could be identified within regions important for learning and memory. Here, immunohistochemical DAB labelling using the pan myeloid cell marker Iba1 was used to determine if microglial expansion could be observed as early as 1-week following BCAS surgery, in both white and grey matter regions (Figure 3.3). Microglial expansion was calculated via cell counts per $0.1mm^2$, alongside percentage area measurements. Percentage area measurements, when normalised to total cell number, provide additional information relating to microglial activation state, as increased microglial surface area has been associated with microglial activation (B. M. Davis et al., 2017; Kozlowski & Weimer, 2012).

$Iba1^{+ve}$ cell counts within the hippocampus CA1 region, 1-week following surgery, identified a significant increase within BCAS mice (14.9±21.25) in comparison to shams (6.6±1.55) ($U=152$, $p<0.01$) (Figure 3.3A). Percentage area was then compared with values normalised to the total number of $Iba1^{+ve}$ cells. Percentage area of staining per $Iba1^{+ve}$ cell was found to be significantly increased within BCAS mice (0.23%±0.18) in comparison to shams (0.12%±0.05) ($U=152.5$, $p<0.01$) (Figure 3.3B). This analysis was then repeated within the corpus callosum to see if the white matter showed a similar response to that seen within the grey matter. Quantification of the total number of $Iba1^{+ve}$ cells showed a trend for increased cell numbers following surgery within BCAS mice (8.74±9.19) in comparison to shams (6.55±2.65) ($p=0.054$) (Figure 3.3C). The percentage area of staining per $Iba1^{+ve}$ cell showed a significant increase within BCAS mice (0.17%±0.07) compared to shams (0.14%±0.06) ($U=132.5$, $p<0.05$) (Figure 3.3D).

Overall, these data show evidence of not only microglial expansion, as early as 1-week following BCAS, but also increased cell size potentially indicating a structural conformational change indicative of an altered microglial phenotype.

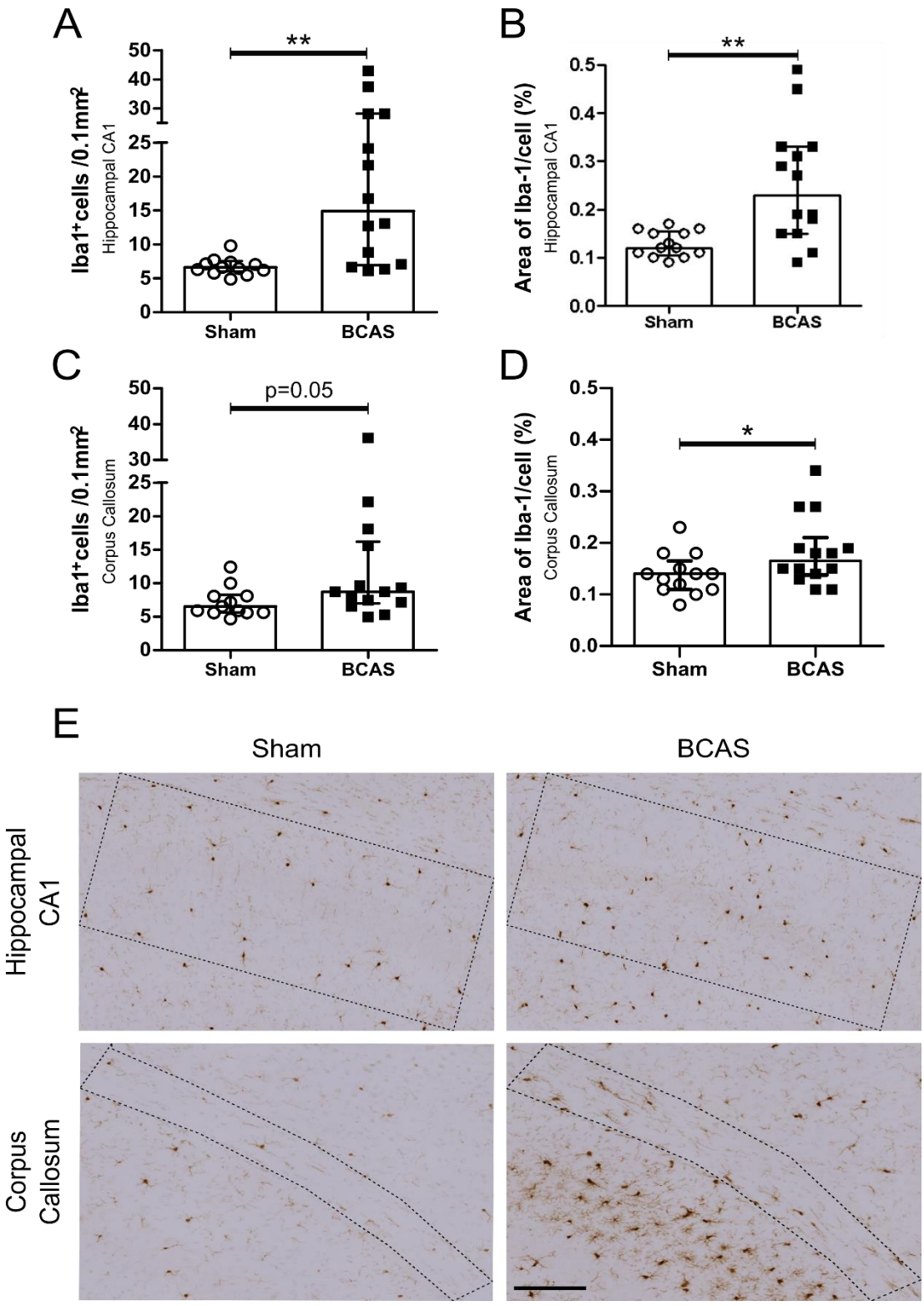

Figure 3.3 BCAS induces microglial expansion 1-week following surgery. **(A)** Iba1^{+ve} cell counts per 0.1mm^2 increased within the hippocampal CA1 region of BCAS mice compared to shams. **(B)** Iba1 area per cell showed a significant increase within the hippocampus of BCAS mice in comparison to shams. **(C)** A trend for increased Iba1^{+ve} cell counts within the

corpus callosum of BCAS mice compared to shams. **(D)** Significant increase in IBA1 area per cell within the corpus callosum of BCAS mice compared to shams. Data presented as Median±IQR. **(E)** Representative images of DAB Iba1 staining within the hippocampus CA1 and corpus callosum of sham and BCAS mice 1-week following surgery. Scale bar 50µm. Black dashed lines outline regions analysed.

3.3.4 Microglial expansion following BCAS is associated with a significant increase in local proliferation

To determine if the microglial expansion observed 1-week following BCAS could be attributed to increased local proliferation, the number of microglial cells co-expressing BrdU was evaluated 1-week following surgery (Figure 3.4). The total number of $Iba1^{+ve}BrdU^{+ve}$ cells increased within the hippocampus CA1 region of BCAS mice (5.95±15.46) when compared to shams (0±0) ($U=144.5$, $p<0.01$) (Figure 3.4A). To confirm that this observation was indeed an increase in proliferation rate and not simply due to increased total $iba1^{+ve}$ cells within BCAS mice, the percentage of $Iba1^{+ve}$ cells proliferating was also calculated (Figure 3.4B). A significant increase in the percentage of $Iba1^{+ve}$ cells proliferating was observed within BCAS mice (30.39%±53.31) in comparison to shams (0±0) ($U=144.5$, $p<0.01$) (Figure 3.4B). The total number of proliferating microglia was also found to be significantly increased 1-week following surgery, within the corpus callosum of BCAS mice (1.18±4.6) when compared to shams (0±0) ($U=161$, $p<0.001$) (Figure 3.4C). The same significant increase was observed when percentage of microglial cells proliferating was calculated, with BCAS mice (15.78±46.26) displaying a higher proportion when compared to shams (0±0) ($U=160$, $p<0.001$) (Figure 3.4D).

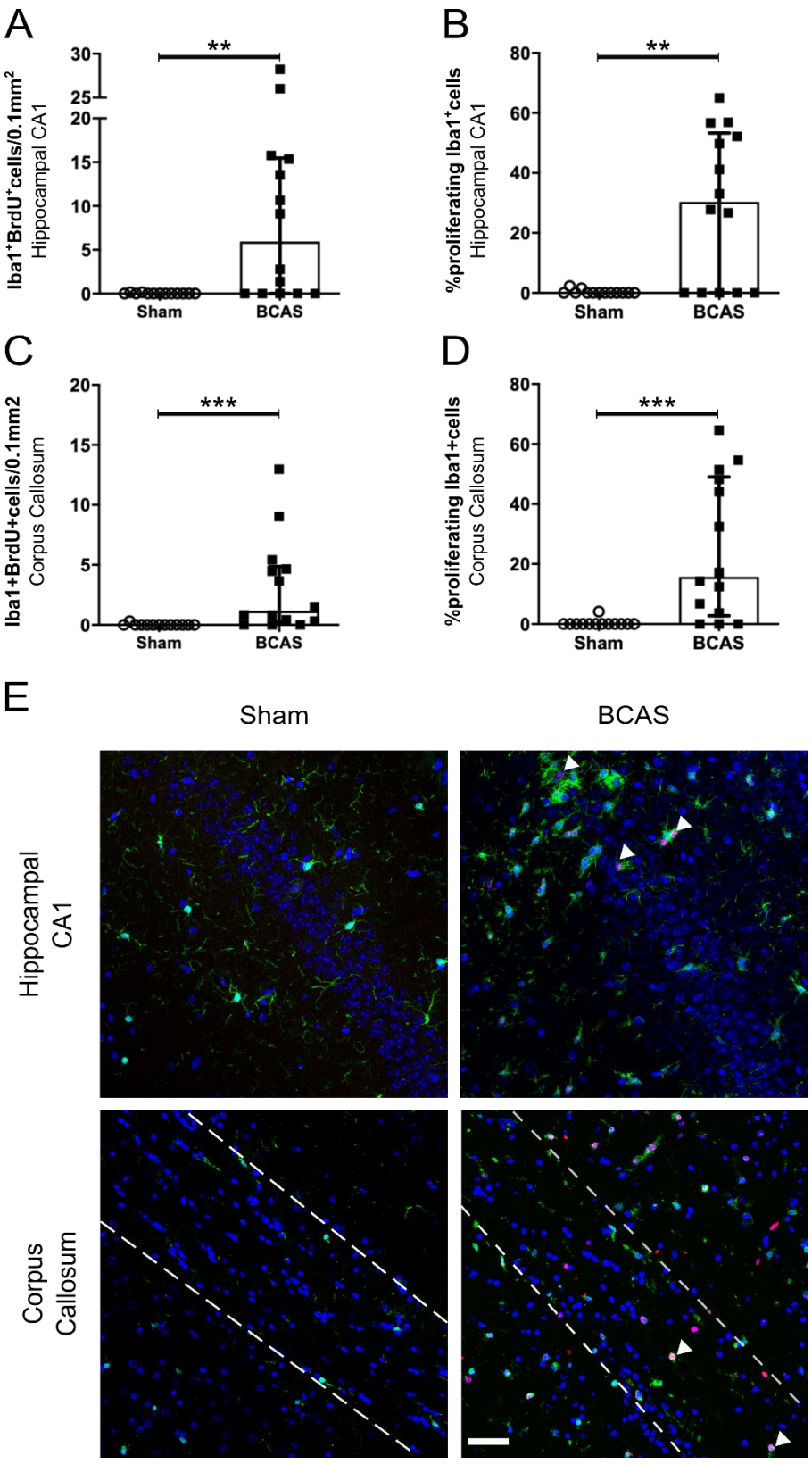

Figure 3.4 BCAS mediated microglial expansion is driven by local proliferation. **(A)** Increased number of proliferating Iba1^{+ve} cells within the hippocampal CA1 region of BCAS

mice in comparison to shams. **(B)** The percentage of proliferating Iba1^{+} cells were increased within BCAS mice when compared to shams. **(C)** Increased number of proliferating Iba1^{+ve} cells within the corpus callosum of BCAS mice in comparison to shams. **(D)** Increased percentage of proliferating Iba1^{+ve} cells within the corpus callosum of BCAS mice in comparison to shams. Data presented as Median±IQR. p<0.01**, p<0.001***. **(E)** Representative images of Iba1/BrdU/DAPI staining within the hippocampus CA1 and corpus callosum regions from sham and BCAS mice. Iba1-green, BrdU-red, and DAPI-blue. White arrowheads highlight proliferating microglial cells. Scale bar 50µm.

To determine if the proliferative response following BCAS is predominantly associated with microglial cells, the number of BrdU^{+ve}DAPI^{+ve} cells were also calculated (Figure 3.5). There was a significant increase in the proliferation of non-microglial cells within the hippocampus CA1 region of BCAS mice (1.25±5.26) in comparison to shams (0.14±0.28) (U=135, p<0.05) (Figure 3.5A). To determine the significance of this response in comparison to microglial proliferation, the percentage of proliferating cells that are Iba1^{+ve} was calculated. The results show that the majority of proliferating cells are Iba1^{+ve} within BCAS mice (78.55±85.60) and show a significantly greater proportion than that of shams (0±0) (U=144.5, p<0.01) (Figure 3.5B). In contrast, within the corpus callosum, there was no significant difference between the proliferation of non-microglial cells between BCAS (2.00±2.73) and sham mice (1.19±3.16) (p=0.943) (Figure 3.5C). Once again when the data is displayed as the percentage of proliferating cells that are Iba1^{+ve}, there is a clear significant increase within BCAS mice (43.80±50.71) in comparison to shams (0±0) (U=160, p<0.001) (Figure 3.5D).

Taken together these data indicate that the microglial expansion observed within white and grey matter regions 1-week following BCAS is driven by increased local proliferation. Furthermore, the proliferative response is predominantly microglial, with very little contribution of other cell types.

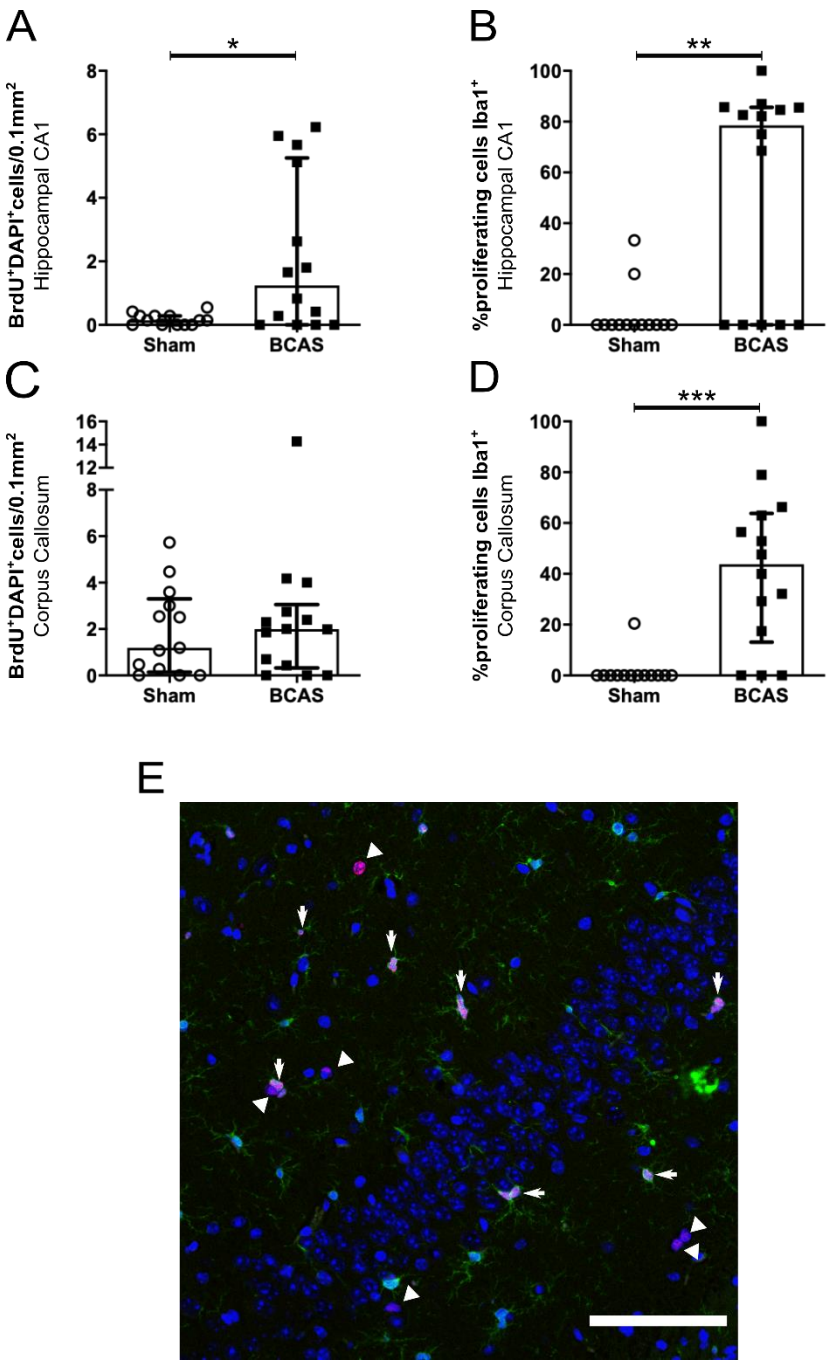

Figure 3.5 Proliferation following BCAS is predominantly microglial. **(A)** Proliferation of Iba1^{-ve} cells was increased within the hippocampus CA1 region of BCAS mice in comparison to shams. **(B)** Significant increase in the proportion of proliferating cells that are Iba1^{+ve} within the hippocampus of BCAS mice compared to shams. **(C)** No observed differences in Iba1^{-ve} cell proliferation within the corpus callosum of sham and BCAS following surgery. **(D)** Increased percentage of proliferating cells that are Iba1^{+ve} within the corpus callosum of BCAS mice when compared to shams. Data presented as Median±IQR. $p<0.05$*, $p<0.01$**, $p<0.001$***. **(E)** Representative image displaying BrdU^{+ve}DAPI^{+ve}Iba1^{-ve} cells (denoted by

white arrow heads) and $BrdU^{+ve}DAPI^{+ve}Iba1^{+ve}$ cells (denoted by white arrows) within the hippocampal CA1 region. Iba1-green, BrdU-red, DAPI-blue. Scale bar 50µm.

3.3.5 CSF1R inhibition has no impact on the magnitude of cerebral blood flow reductions following BCAS

The short-term study, described within sections 3.3.1-3.3.4, demonstrated that microglial expansion, driven by local proliferation, dominates the early neuroinflammatory response following BCAS. In attempt to uncover the pathway by which microglial proliferation is stimulated, microglial cells were isolated from the corpus callosum of sham and BCAS mice 1-week following surgery. A ≈3-fold increase in CSF1R expression was identified within BCAS mice (2.18±1.43) when compared to shams (1.01±0.18) ($U=21$, $p<0.05$), as measured by qPCR (Figure 3.6). CSF1R signalling has been highlighted as a key pathway promoting the survival, proliferation and differentiation of microglia (Conway et al., 2005). It was, therefore, hypothesised that this pathway is the most likely candidate driving microglial proliferation following BCAS. The oral inhibitor GW2580 has previously been shown, in models of chronic neurodegeneration, to effectively inhibit microglial proliferation without affecting cell survival, through the competitive inhibition of CSF1R (Adrian Olmos-Alonso et al., 2016b). To allow the effect of blocking microglial proliferation on pathological and cognitive outcomes to be assessed, GW2580 was administered within diet over a 6-week period following BCAS surgery.

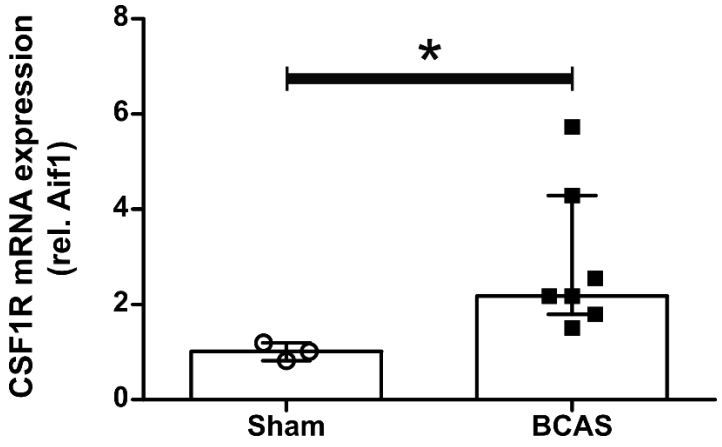

Figure 3.6 Increased microglial CSF1R expression following BCAS. **(A)** Increased CSF1R expression was identified within isolated corpus callosal microglial cells following BCAS. Data presented as Median±IQR. $p<0.05$*.

The first aim of the long-term study was to investigate the effect of GW2580 on cortical blood flow following BCAS, to determine if blocking CSF1R signalling had any impact on CBF reductions following BCAS surgery. Laser speckle imaging was utilised to assess CBF at baseline, 24-hours, and 6-weeks following sham/BCAS surgery (Figure 3.7). BCAS surgery elicited a ≈50% reduction in CBF which persisted at 6-weeks, whereas sham mice showed stable blood flow measurements over the same period (Figure 3.7A). Overall, there was a significant effect of group ($F_{(2,28)}$ = 107.243, p<0.001), time ($F_{(1.57, 43.97)}$ = 167.414, p<0.001) as well as a significant interaction between group and time ($F_{(3.14, 43.97)}$ = 30.90, p<0.001). Bonferroni *post hoc* analysis revealed a significant reduction in CBF 24-hours following surgery (sham; 97.06±5.82, BCAS; 52.24±9.65, p<0.001) which was persistent at 6-weeks (sham; 94.83±7.39, BCAS; 49.74±15.32, p<0.001) (Figure 3.7A). In contrast, no significant difference in blood flow reduction following GW2580 treatment was observed at 24-hours (sham; 97.06±5.82, BCAS+GW2580; 51.56±8.85, p<0.001) or 6-weeks (sham; 94.83±7.39, BCAS; 54.46±10.17, p<0.001) following surgery (Figure 3.7A).

These data illustrate that CBF is persistently reduced up to 6-weeks following BCAS. Furthermore, the extent and duration of CBF reductions following BCAS are unaffected by GW2580 treatment, and therefore any observed benefits cannot be explained by improvements in CBF.

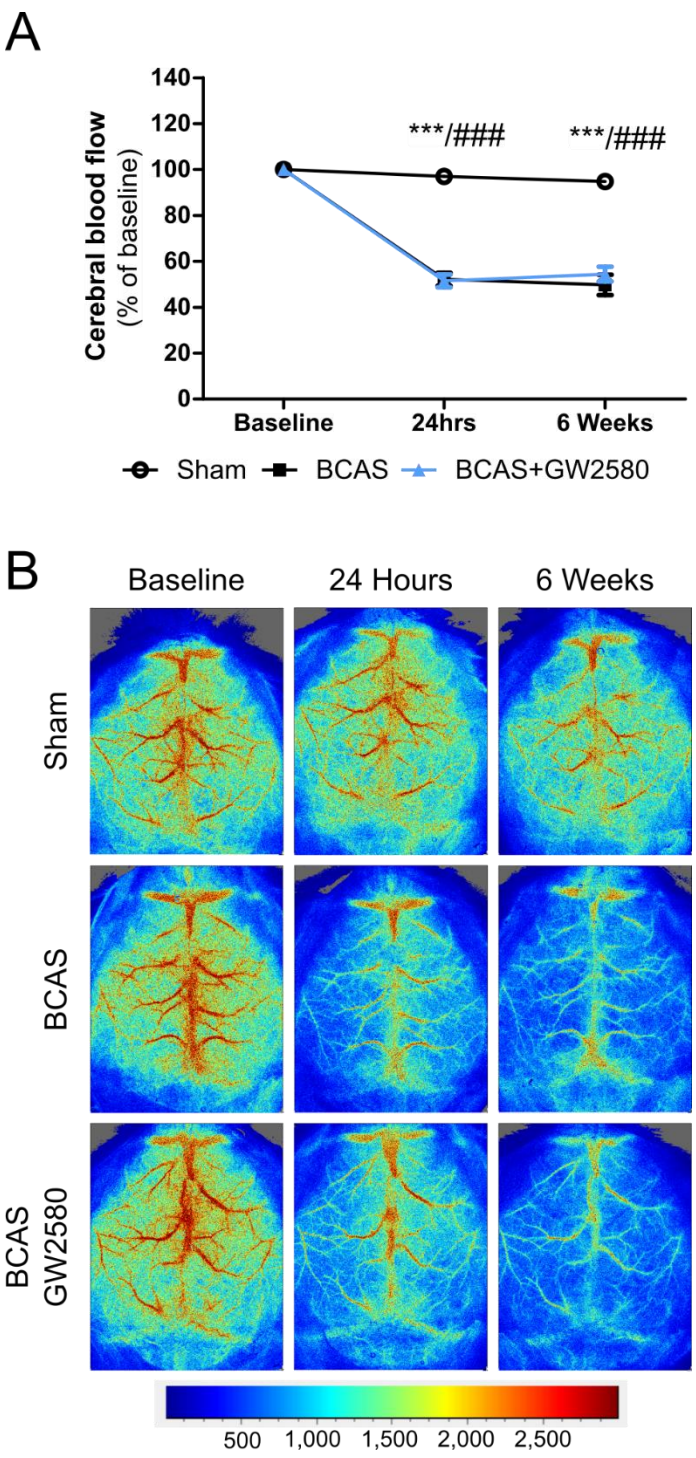

Figure 3.7 BCAS induces persistent reductions in CBF regardless of CSF1R inhibition. (A) BCAS induces a significant and persistent reduction in CBF within both the vehicle and GW2580 groups in comparison to shams. Data presented as Mean±SEM. $p<0.001$*** (* indicates post hoc analysis comparing sham to BCAS), $p<0.001^{\#\#\#}$ (# indicates post hoc analysis comparing BCAS to BCAS+GW2580). **(B)** Representative images of laser speckle imaging of cortical blood flow at baseline, 24-hours, and 6-weeks following surgery

within sham, BCAS and BCAS+GW2580 mice. Red indicates high and blue low blood flow (arbitrary flux units).

3.3.6 CSF1R inhibition following BCAS prevents microglial expansion

The next aim of the study was to assess changes in microglial numbers following long-term BCAS, and to determine if GW2580 can inhibit any observed increases. Immunohistochemical DAB staining of Iba1 was utilised to assess microglial expansion within the white matter regions; corpus callosum, internal capsule and fimbria as well as the grey matter region of the hippocampus (Figure 3.8 and Figure 3.9). Overall, there was a significant group effect on the number of Iba1 positive cells/0.1mm2 within the corpus callosum ($\chi 2_{(2)} = 15.255$, $p<0.001$), with post hoc analysis revealing significantly increased microglial numbers within BCAS (9.53±7.31) compared to BCAS+GW2580 mice (5.80±1.66) ($p<0.001$) (Figure 3.8A). Similarly, there were overall group differences within the internal capsule ($\chi 2_{(2)} = 10.386$, $p<0.01$) and fimbria ($\chi 2_{(2)} = 7.094$, $p<0.05$), with *post hoc* analysis revealing significant increases in microglial numbers within BCAS mice (IC; 8.25±6.29, F; 7.89±14.01) in comparison to BCAS+GW2580 mice (IC; 5.03±2.70, F; 6.10±1.89) ($p<0.01$, $p<0.05$ respectively) (Figure 3.8B/C).

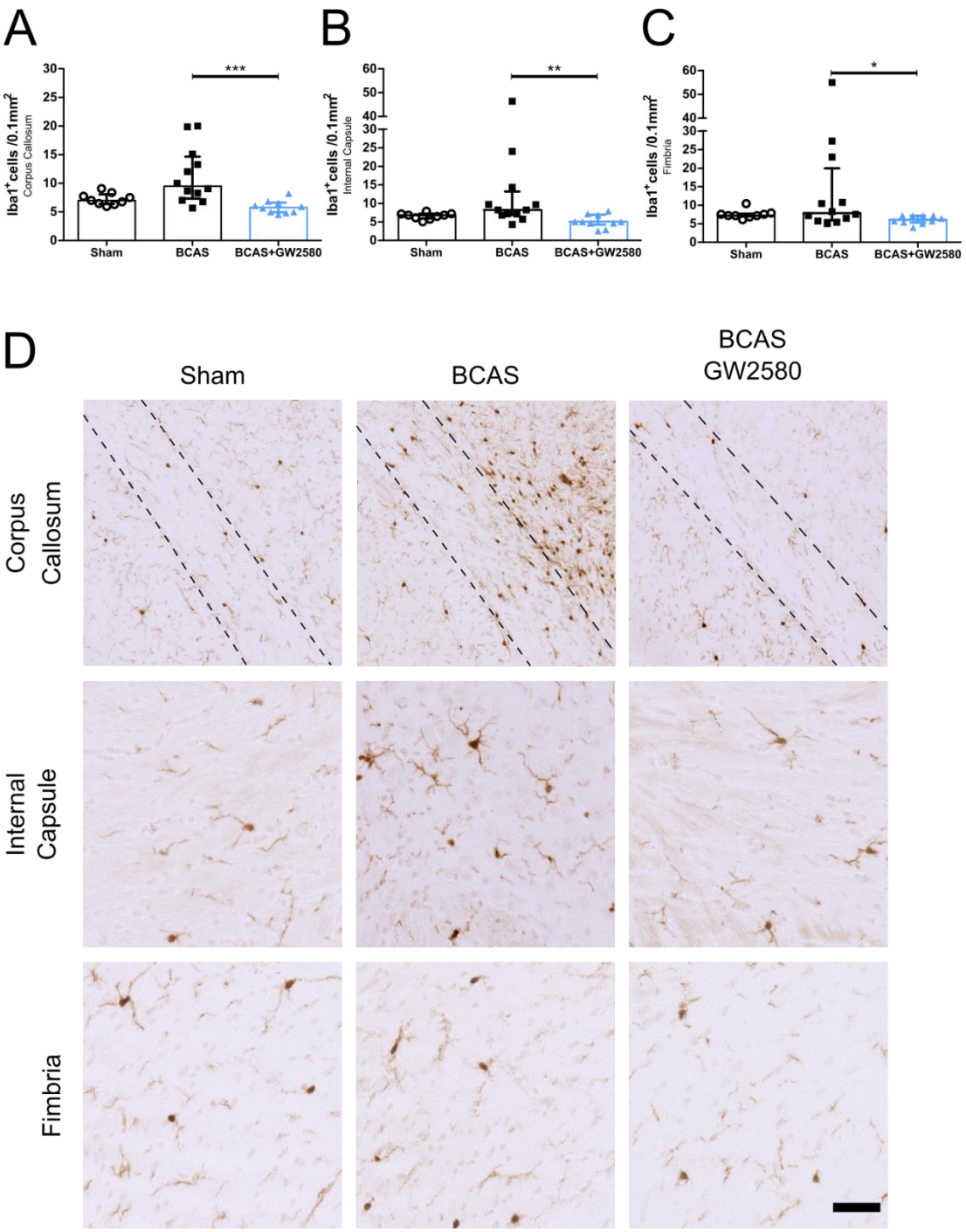

Figure 3.8 CSF1R inhibition prevents BCAS mediated white matter microglial expansion. Increased Iba1^{+ve} cells within BCAS but not BCAS+GW2580 mice 6-weeks following surgery within the corpus callosum **(A),** internal capsule **(B)** and fimbria **(C).** Data presented as Median±IQR. p<0.05*, p<0.01**, p<0.001***. **(D)** Representative images of DAB Iba1 staining within the corpus callosum, internal capsule and fimbria of sham, BCAS, and BCAS+GW25080 mice 6-weeks following surgery. Scale bar 50µm.

In respect to grey matter, the hippocampus CA1 region showed an overall group difference ($\chi 2_{(2)}$ = 15.679, p<0.001), with post hoc analysis revealing significantly increased microglial numbers within BCAS mice (7.08±1.40) in comparison to both sham (5.44±1.09) (p<0.05) and BCAS+GW2580 groups (5.24±1.26) (p<0.01) (Figure 3.9A).

Collectively, these results demonstrate widespread microglial expansion following 6-weeks of BCAS, which can be effectively blocked through GW2580 inhibition of the CSF1R pathway.

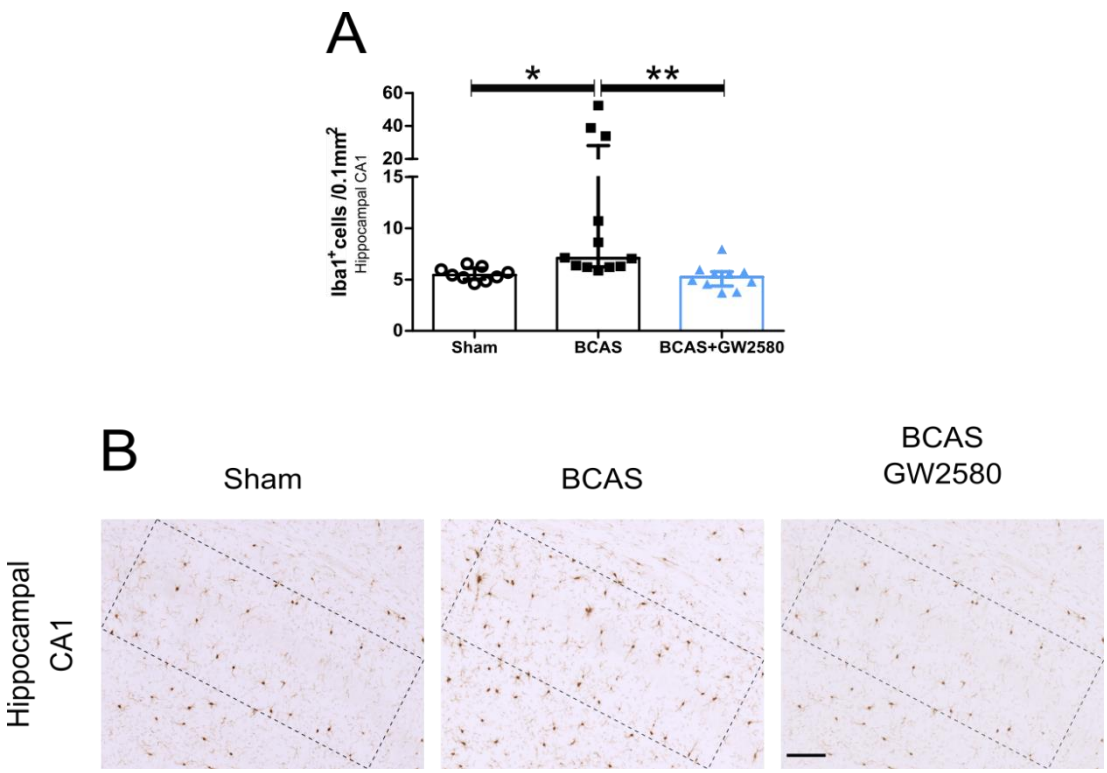

Figure 3.9 CSF1R inhibition prevents BCAS mediated hippocampal microglial expansion. **(A)** Increased Iba1^{+ve} cells within the hippocampus CA1 region of BCAS but not sham or BCAS+GW2580 mice 6-weeks following surgery. Data presented as Median±IQR. p<0.05*, p<0.01**. **(B)** Representative images of Iba1 DAB staining within the hippocampus CA1 region of sham, BCAS and, BCAS+GW2580 mice 6-weeks following surgery. Scale bar 50µm.

3.3.7 Modest levels of microglial proliferation at 6-weeks following BCAS blocked through CSF1R inhibition

Having demonstrated the effectiveness of GW2580 treatment in blocking microglial expansion following 6-weeks of BCAS, the next aim was to assess proliferation at this more chronic timepoint. Immunofluorescent staining using Iba1 and BrdU was once again employed to assess microglial proliferation within the hippocampus and corpus callosum 6-weeks following surgery (Figure 3.10). Within the hippocampus CA1 region a significant overall group effect was identified ($\chi 2_{(2)}$ = 6.815, $p<0.05$), with *post hoc* analysis demonstrating a significant increase in proliferating microglial cells within BCAS mice (0±0.15) in comparison to BCAS+GW2580 mice (0±0) ($p<0.05$) (Figure 3.10A). When the percentage of $Iba1^{+ve}$ cells proliferating was calculated an overall group effect was determined ($\chi 2_{(2)}$ = 6.191, $p<0.05$), with *post hoc* analysis revealing a strong trend for an increased proportion of proliferating microglia in BCAS mice (0±1.05) compared to BCAS+GW2580 mice (0±0) (p=0.051) (Figure 3.10B). Despite some evidence of proliferating microglia within the corpus callosum of a sub-set of BCAS mice, there were no significant group effects for the number of proliferating microglial cells (p=0.079) (Figure 3.10C) or the proportion of microglial cells proliferating (p=0.079) (Figure 3.10D).

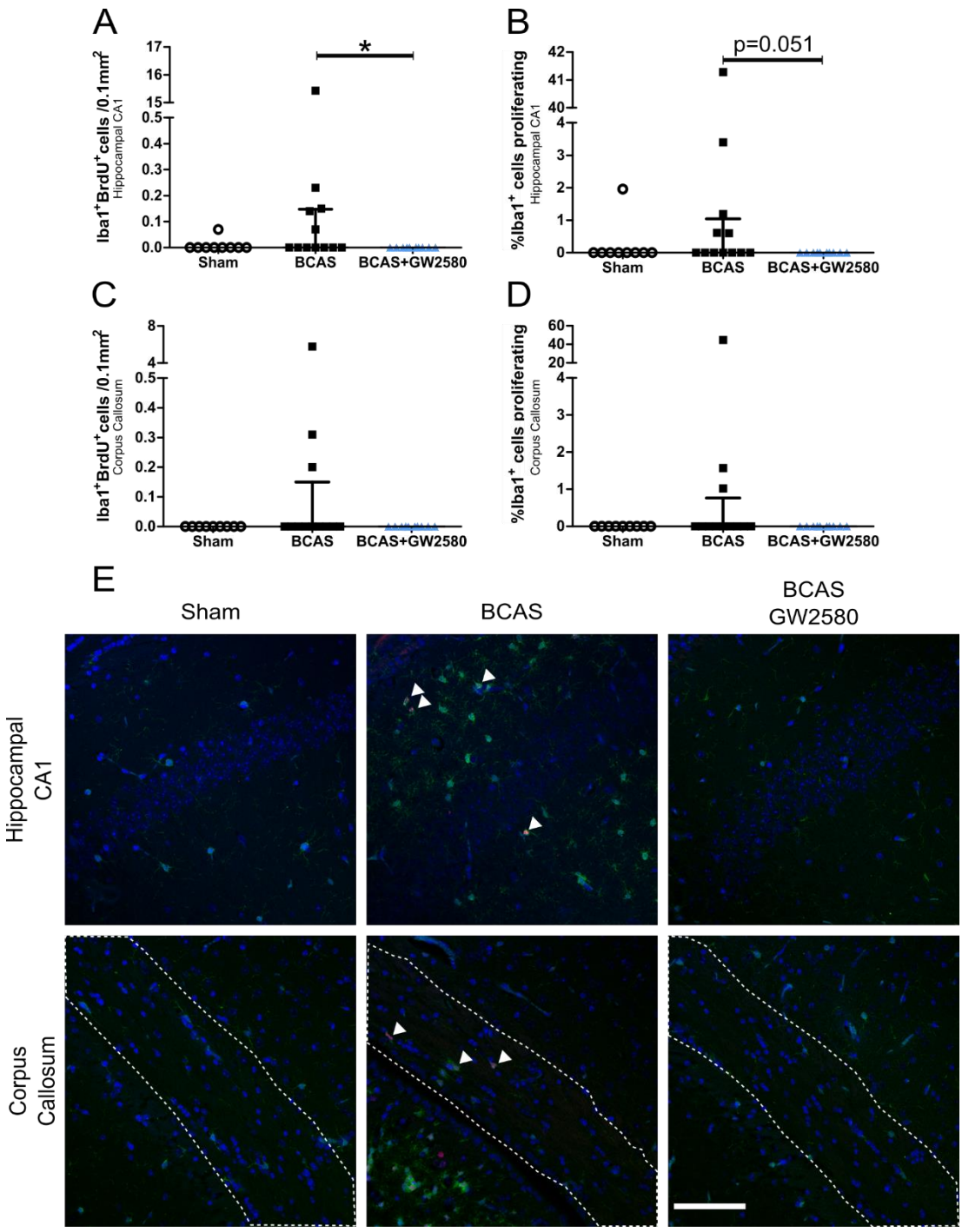

Figure 3.10 CSF1R inhibition prevents BCAS mediated hippocampal microglial proliferation. **(A)** Increased hippocampal CA1 microglial proliferation within BCAS but not sham or BCAS+GW2580 mice 6-weeks following surgery. **(B)** A trend for an increased percentage of microglial cells proliferating within the hippocampus of BCAS but not sham or BCAS+GW2580 mice. No significant difference in proliferating microglial cells **(C)** or percentage of microglial cells proliferating **(D)** within the corpus callosum across all groups. Data presented as Median±IQR. p<0.05*. Representative images of Iba1/Brdu/DAPI staining

within the hippocampus CA1 and corpus callosum of sham, BCAS, and BCAS+GW2580 mice 6-weeks following surgery. Iba1-green, BrdU-red, DAPI-blue. Scale bar 50µm.

Proliferation of non-microglial cells was limited at 6-weeks following surgery with no significant group differences observed within the hippocampus CA1 ($p=0.841$) (Figure 3.11A) or corpus callosum ($p=0.491$) (Figure 3.11C). When the percentage of cells proliferating that are microglial was calculated an overall significant group difference was observed within the hippocampus CA1 region ($\chi 2_{(2)} = 6.995$, $p<0.05$), however, *post hoc* analysis revealed no significant differences between groups (Figure 3.11B). No significant differences between the percentage of proliferating cells that are microglial was observed within the corpus callosum (0.079) (Figure 3.11D). The data does, however, once again clearly highlight that the majority of proliferation detected is microglial derived.

Overall, these data indicate that microglial proliferation, within the 3-days prior to the 6-week timepoint following BCAS, is limited. When microglial proliferation was present however, GW2580 treatment was found to successfully inhibit such responses.

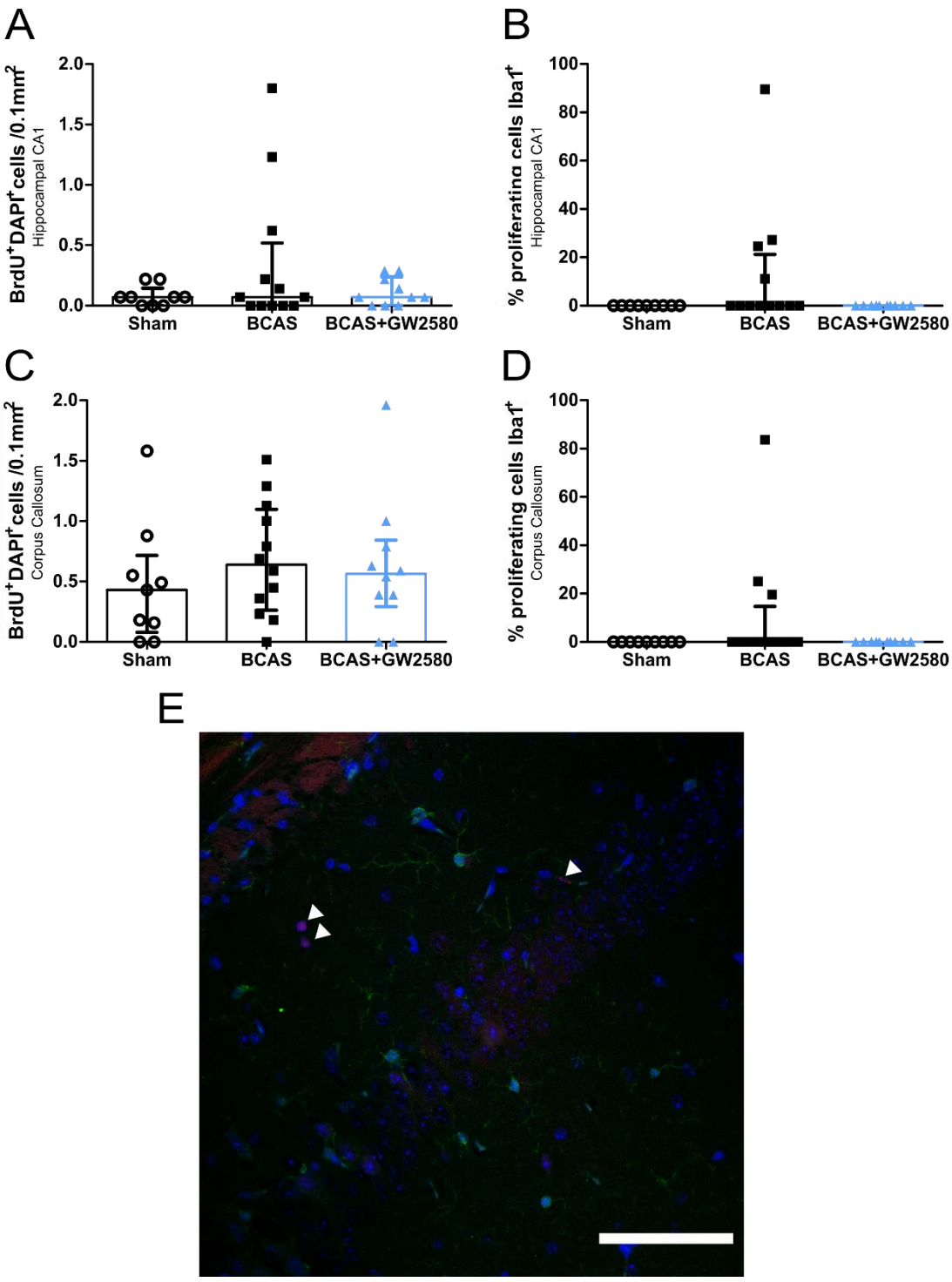

Figure 3.11 Limited proliferation of non-microglial cell types 6-weeks following BCAS surgery. Limited proliferation of Iba1^{-ve} cells across all 3 groups within the hippocampus CA1 region **(A)** and corpus callosum **(C)**. No significant difference in the percentage of proliferating cells that are microglial within the hippocampus **(B)** or corpus callosum **(D)** across all 3 groups. Data presented as Median±IQR. **(E)** Representative image displaying

$BrdU^{+ve}DAPI^{+ve}Iba1^{-ve}$ cells (denoted by white arrow heads) within the hippocampal CA1 region. Iba1-green, BrdU-red, DAPI-blue. Scale bar 50µm.

3.3.8 CSF1R inhibition protects against white matter damage following BCAS

Myelin associated glycoprotein (MAG) accumulation within white matter tracts is indicative of white matter damage and is associated with myelin damage and white matter dysfunction (Aboul-Enein et al., 2003; Barker, Wellington, Esiri, & Love, 2013). To investigate the integrity of white matter following BCAS, and the impact of CSF1R inhibition, MAG immunohistochemical staining was carried out and graded semi-quantitatively on a 4-point scale. MAG levels were assessed within the corpus callosum, internal capsule, and fimbria, with scores summated to generate an overall value representing white matter damage (Figure 3.12). Statistical analysis revealed a significant overall group effect ($\chi 2_{(2)} = 11.653$, $p<0.01$), with *post hoc* testing demonstrating a significant increase in MAG severity score within BCAS mice (2±5) in comparison to sham (0±0) ($p<0.01$) and BCAS+GW2580 groups (0±0.25) ($p<0.05$) (Figure 3.12A).

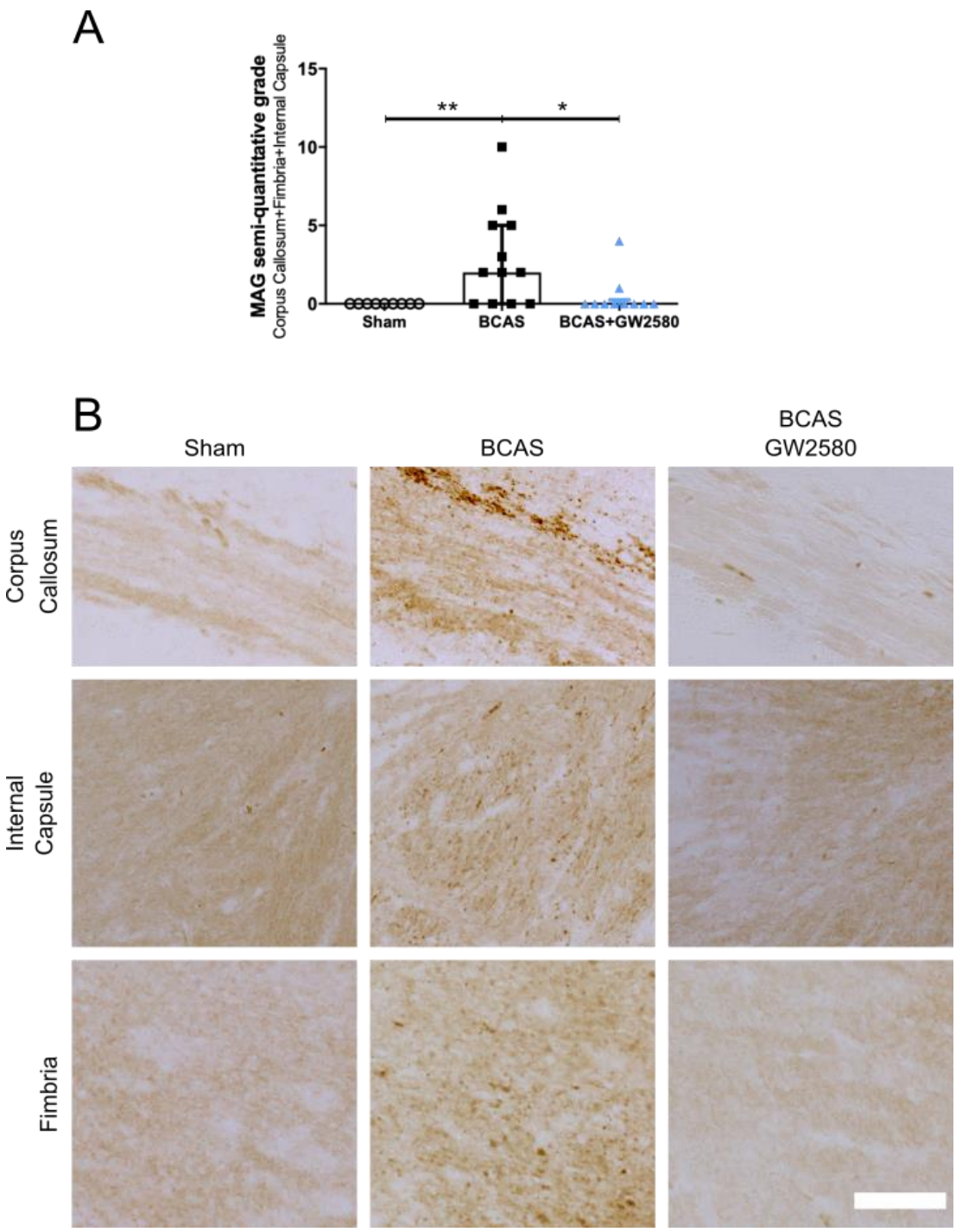

Figure 3.12 CSF1R inhibition prevents widespread white matter damage following BCAS. **(A)** Widespread white matter damage within the corpus callosum, internal capsule, and fimbria of BCAS mice but not within sham or BCAS+GW2580 groups. Data presented as Median±IQR. $p<0.05$*, $p<0.01$**. **(B)** Representative images of MAG DAB staining within the corpus callosum, internal capsule, and fimbria of sham, BCAS, and BCAS+GW2580 mice. Scale bar 50µm.

To determine if white matter microglial expansion is associated with increased white matter damage, MAG severity scores were correlated to microglial cell counts within the same areas (Figure 3.13). The extent of white matter damage was found to be positively correlated with the number of microglial cells within the same area ($r_{s(20)} = 0.644$, $p<0.01$) (Figure 3.13).

Collectively, these data illustrate that white matter damage following BCAS is correlated to microglial expansion and can be prevented through CSF1R inhibition.

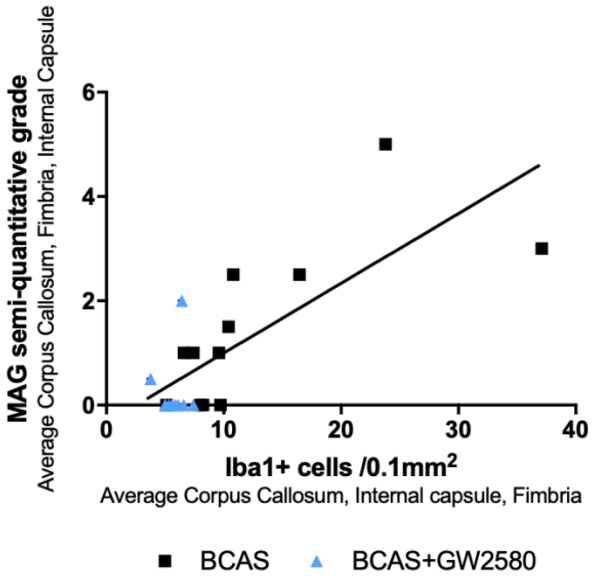

Figure 3.13 The severity of white matter damage is positively correlated to increased microglial numbers. The averaged white matter damage (MAG score) was positively correlated to the average Iba1^{+ve} cell number across a number of white matter regions (corpus callosum, internal capsule, and fimbria). As all sham mice showed 0 MAG grading scores, their data was omitted from the analysis. Data presented as Mean.

3.3.9 BCAS induced impairments in spatial learning are completely restored through CSF1R inhibition

The results presented within this chapter thus far demonstrate that chronic BCAS leads to both corpus callosum and hippocampal microglial expansion, alongside white matter damage. The corpus callosum and hippocampus represent important components of the frontal-subcortical circuitry that has been implicated in spatial learning the memory (Duncombe, Kitamura, et al., 2017). The next aim of the study, therefore, was to investigate the impact of

chronic BCAS on spatial learning and memory, as well as to determine if GW2580 treatment could rescue any observed deficits.

Spatial learning and memory as well as cognitive flexibility were assessed using the Barnes maze, which was carried out over 2 consecutive weeks, commencing 4-weeks following surgery. Spatial learning was assessed via escape latency measurements which reflect the time taken for each mouse to locate and enter the escape chamber. When escape latency was assessed, over the 6-day training period, a significant overall effect of time was observed ($F_{(3.340,93.507)} = 65.078$, $p<0.001$), indicating learning across trials (Figure 3.14A). An overall effect of group was also evident ($F_{(2,28)} = 13.116$, $p<0.001$). Although sham and BCAS performance is comparable at training day 1, *post hoc* analysis revealed a significant increase in BCAS escape latency across subsequent trails (T2; $p<0.05$, T3; $p<0.001$, T4; $p<0.01$), demonstrating impaired spatial learning compared to shams. Over the same training period, however BCAS+GW2580 mice showed escape latency times comparable to shams which were significantly different to that of the BCAS group (T3; $p<0.01$, T4; $p<0.05$, T6; $p<0.05$) (Figure 3.14A). Overall, these data illustrate that chronic BCAS leads to impaired spatial learning which can be rescued through the blockade of microglial expansion via CSF1R inhibition.

As an additional measure of spatial learning, total distance travelled during each trial was calculated (Figure 3.14B). Reduced travel distance over subsequent trails would be indicative of spatial learning as the mouse would be taking a more direct route to the escape chamber as the location is learnt. A significant overall effect of time was identified ($F_{(5,140)} = 31.972$, $p<0.001$), as well as an overall significant group difference ($F_{(2,28)} = 7.478$, $p<0.01$) with no interaction ($p=0.493$). *Post hoc* analysis revealed a significant increase in distance travelled, and therefore impaired spatial learning, within BCAS mice in comparison to shams across several trails (T2; $p<0.05$, T3; $p<0.01$, T4; $p<0.05$) (Figure 3.14B). Distance travelled within the BCAS+GW2580 mice was comparable to shams and significantly reduced in comparison to BCAS alone, although *post hoc* analysis revealed this difference was only statically significant at one timepoint (T2; $p<0.05$) (Figure 3.14B).

Due to the motile nature of the task, average speed measurements were gathered to ensure that mobility differences did not exist between groups. Overall a significant main effect of time was observed ($F_{(3.176,88.938)} = 11.322$, $p<0.001$). However, no significant effect of group was observed ($p=0.322$) as well as no significant interactions ($p=0.084$) indicating that escape latency can be used as a measure of learning without speed as a confounding factor (Figure 3.14C).

Following the spatial learning task, a probe trial was conducted, in which the escape chamber was removed, and the percentage of time spent within the quadrant previously home to the escape chamber was measured (Figure 3.14D). The probe trial was conducted 72-hours following the last training day and therefore represents a longer-term spatial reference memory assessment. Time spent within the target zone was compared across all 3 groups, with statistical analysis revealing a significant overall group difference ($\chi 2_{(2)} = 7.790$, $p<0.05$). *Post hoc* analysis demonstrated that sham mice spent significantly more time within their target quadrant (58.33±11.67) when compared to both BCAS (39.17 ±22.08) ($p<0.05$) and BCAS+GW2580 groups (35.83±20.83) ($p<0.05$). No significant difference between BCAS and BCAS+GW2580 groups was identified ($p=0.903$). In order that confirm that target quadrant times did indeed reflect a preference for that quadrant, time spent within all 4 quadrants was compared (Figure 3.14D). Sham mice showed an overall significant difference between time spent within each quadrant ($X^2_{(3)} = 18.506$, $p<0.001$), with *post hoc* analysis revealing a significant increase in time spent within the target zone compared to the other 3 zones (clockwise; $p<0.01$, opposite; $p<0.01$, counter-clockwise $p<0.01$). An overall difference in quadrant preference was also identified within the BCAS group ($X^2_{(3)} = 8.300$, $p<0.05$) however, *post hoc* analysis revealed a significant preference for the target quadrant over the opposite ($p<0.05$) and counter-clockwise ($p<0.05$) but not the clockwise ($p=0.07$) zone, indicating no target zone preference. Overall, BCAS+GW2580 mice showed no significant difference in time spent within each of the 4 quadrants ($p=0.07$) (Figure 3.14D).

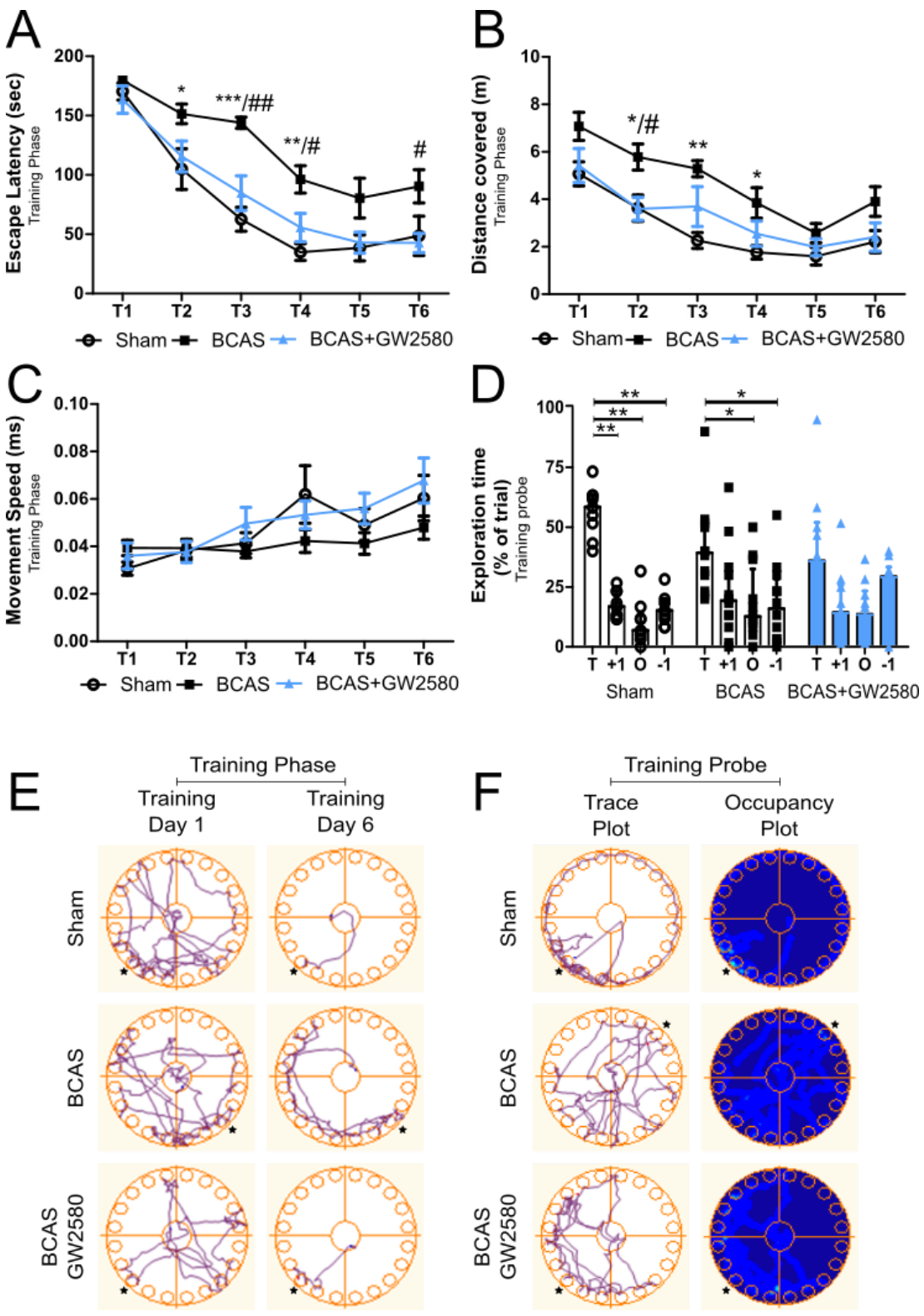

Figure 3.14 CSF1R inhibition restores BCAS mediated spatial learning impairments. **(A)** Increased escape latency within BCAS mice, indicative of impaired spatial learning, in comparison to both sham and BCAS+GW2580 groups which show comparable learning

profiles. **(B)** Increased distance travelled within BCAS mice indicates poorer spatial learning in comparison to sham and BCAS+GW2580 groups. **(C)** Comparable movement speed across all groups indicating that learning measures are not impacted by motility differences. Data presented as Mean±SEM. $p<0.05$*, $p<0.01$**, $p<0.001$*** (* indicates post hoc analysis comparing sham to BCAS), $p<0.05^{\#}$, $p<0.01^{\#\#}$ ($^{\#}$ indicates post hoc analysis comparing BCAS to BCAS+GW2580. **(D)** Sham mice demonstrate a target zone preference indicating intact spatial memory in contrast to BCAS and BCAS+GW2580 groups which show no preference for the target zone. Data presented as Median±IQR. $p<0.05$*, $p<0.01$**. **(E)** Representative movement traces during day 1 and 6 of the training period taken from sham, BCAS and BCAS+GW2580 groups. Stars indicate target hole. **(F)** Trace and occupancy plots gathered during probe trails of sham, BCAS, and BCAS+GW2580 mice. Stars indicate target hole; brighter colours indicate increased time spent in that area (occupancy plot only).

To determine if white matter microglial expansion is associated with impairments in spatial learning, average escape latency was correlated to microglial cell counts within the corpus callosum (Figure 3.15A). A significant positive correlation was identified ($r_{s(29)} = 0.522$, $p<0.01$), indicating that increased microglial numbers within the corpus callosum are linked to a poorer spatial learning performance (Figure 3.15A). Furthermore, to investigate the link between spatial learning impairments and white matter damage, MAG severity scores within the corpus callosum were correlated to average escape latency. Increased white matter damage was found to be positively correlated with a poorer spatial learning performance ($r_{s(20)} = 0.451$, $p<0.05$) (Figure 3.15B).

In conclusion, these data demonstrate that chronic BCAS leads to impairments in spatial learning and memory which are correlated to increased white matter microglial numbers and increased white matter damage. CSF1R inhibition, through GW2580 treatment, rescues deficits in spatial learning, but not memory, following 6-weeks of BCAS.

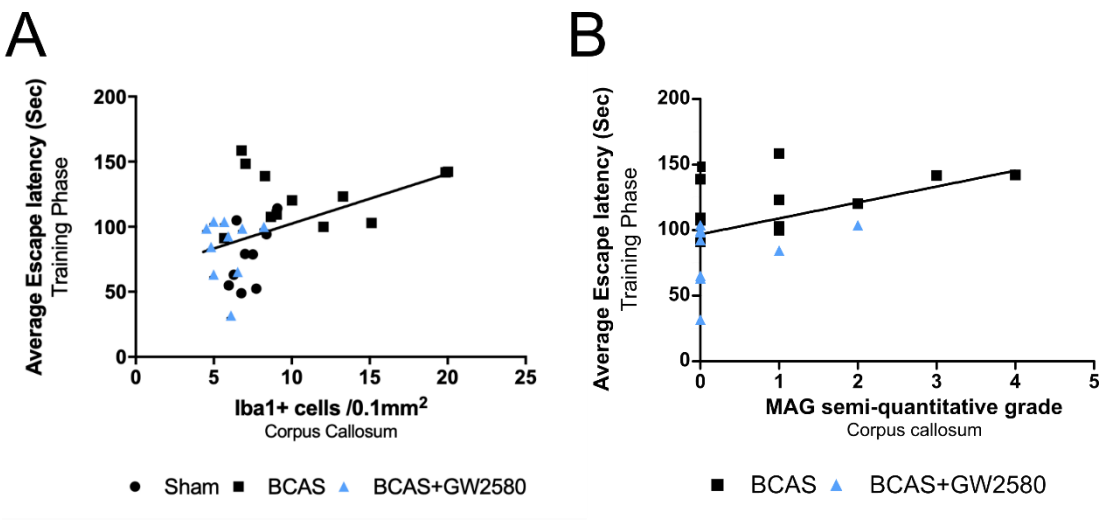

Figure 3.15 Increased average escape latency positively correlates with microglial numbers and MAG grading within the corpus callosum. Averaged escape latency (indicative of spatial learning) is positively correlated with the numbers of microglial cells **(A)** and MAG grading **(B)** within the corpus callosum. As all sham mice showed 0 MAG grading scores, their data was omitted from the analysis. Data presented as Mean.

3.3.10 Cognitive flexibility is unaltered following BCAS

To test cognitive flexibility an additional reversal training segment was completed within the Barnes maze following the reference memory probe (Figure 3.16). The reversal training phase, completed over 3 consecutive days, required mice to learn that their escape chamber had been relocated 180^0, to the other side of the maze. A significant overall effect of time was observed ($F_{(2,56)} = 31.975$, $p<0.001$) indicating learning over the reversal training phase (Figure 3.16A). Although the BCAS groups performance appeared poorer than both sham and BCAS+GW2580 groups, an overall group effect narrowly missed statistical significance ($p=0.053$) (Figure 3.16A). Distance travelled was also used as a measure of learning, as with escape latency a significant overall effect of time was observed ($F_{(2,56)} = 11.322$, $p<0.001$), with once again an overall group effect narrowly missing statistical significance ($p=0.053$) (Figure 3.16B). Once again speed was measured throughout the trails to determine if motility could influence the results. Overall, no significant effect of time ($p=0.06$) or group was observed ($p=0.12$), indicating that motility was comparable across groups (Figure 3.16C).

A probe trail was completed 72-hours following the last reversal training day to assess adaptive spatial memory (Figure 3.16D). Time spent within the target zone was compared across groups with no overall significant difference identified ($p>0.05$). When quadrant zone

preference within each group was analysed however, a significant difference between time spent within each quadrant was observed within sham mice ($X^2_{(3)} = 10.820$, $p<0.05$), with *post hoc* testing demonstrating a reversal target zone preference over the other quadrants (clockwise; $p<0.01$, opposite; $p<0.05$, counter-clockwise; $p<0.05$). Regarding BCAS and BCAS+GW2580 groups no significant differences between time spent within each quadrant were identified ($p=0.241$ and $p=0.113$ respectively) (Figure 3.16D).

Overall, these data indicate that BCAS leads to impairments in adaptive spatial memory, but not learning, 6-weeks following surgery with no beneficial impact of GW2580 treatment.

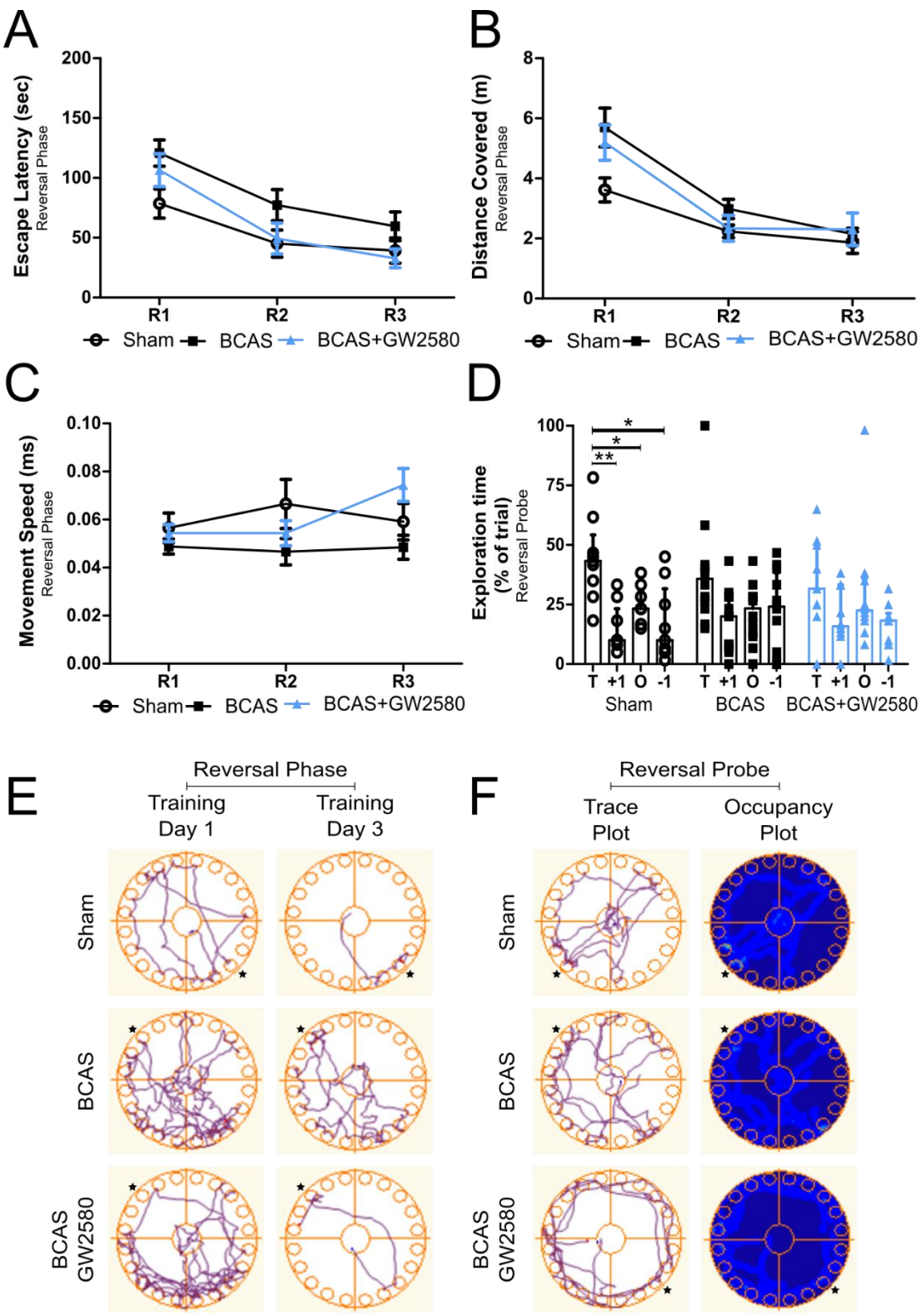

Figure 3.16 A trend for improved cognitive flexibility via CSF1R inhibition following BCAS. Overall, there was a significant effect of time indicating learning, with a trend for group differences when measured by escape latency **(A)** and total distance **(B)**. **(C)** Speed was found

to be comparable across all three groups. Data presented as Mean±SEM. **(D)** Sham mice demonstrate a target zone preference, whereas BCAS and BCAS+GW2580 groups show no preference for the target zone. Data presented as Median±IQR. $p<0.05$*, $p<0.01$**. **(E)** Representative movement traces during day 1 and 3 of the reversal training period taken from sham, BCAS, and BCAS+GW2580 groups. Stars indicate target hole. **(F)** Trace and occupancy plots gathered during reversal probe trails of sham, BCAS, and BCAS+GW2580 mice. Stars indicate target hole; brighter colours indicate increased time spent in that area (occupancy plot only).

3.3.11 CSF1R inhibition protects against increased microglial lysosomal expression following BCAS

The data so far has clearly demonstrated microglial expansion following BCAS, which can be successfully prevented through CSF1R inhibition. However, it is still unclear as to whether BCAS is impacting the phenotypic state of microglia, and therefore the link between microglial expansion and neuroinflammation is unclear. During the short-term study, microglial area per cell was found to be increased following BCAS (Figure 3.3), indicating a conformational change indicative of microglial activation. To assess the activation state of microglia following BCAS more directly, immunofluorescent staining using the lysosome-associated membrane protein 2 (Lamp2) was carried out within the corpus callosum, optic tract, and hippocampus CA1 region. Increased Lamp2 expression within microglia has been linked to increased phagocytic activity and is used more broadly as a marker of microglial activation (Kocur et al., 2015).

There was an overall group effect on the number of $Lamp2^{+ve}Iba1^{+ve}$ cells within the corpus callosum ($\chi2_{(2)} = 18.307$, $p<0.001$), with *post hoc* analysis revealing a significant increase within BCAS mice (2.50±3.43) in comparison to sham (0±0.5) ($p<0.01$) and BCAS+GW2580 groups (0±0.15) ($p<0.001$) (Figure 3.17A). In order rule out that this effect is simply driven by increased microglial number with the same $Lamp2^{+ve}$ cell occurrence, $Lamp2^{+ve}Iba1^{+ve}$ cell count was normalised to the number of $Iba1^{+ve}$ cells (Figure 3.17B). In agreement with previous data an overall group effect was identified ($\chi2_{(2)} = 18.273$, $p<0.001$), with *post hoc* analysis once again demonstrating a significant increase in BCAS mice (0.16±0.17) in comparison to sham (0±0.05) ($p<0.01$) and BCAS+GW2580 groups (0±0.02) ($p<0.001$) (Figure 3.17B). Within the optic tract there was a significant overall group effect ($\chi2_{(2)} = 15.559$, $p<0.001$) and *post hoc* analysis identified a significant increase in $Lamp2^{+ve}Iba1^{+ve}$ cells within BCAS mice (16.90±12.80) in comparison to shams (0±1.30) ($p<0.001$) (Figure 3.17C). In contrast to the corpus callosum however, BCAS+GW2580 mice were found to have

significantly higher Lamp2^{+ve}Iba1^{+ve} cells (13.35±15.90) in comparison to shams ($p<0.05$), with no significant difference when compared to BCAS mice ($p=0.571$) (Figure 3.17C). When the number of Lamp2^{+ve} microglial cells were normalised to total microglial numbers a similar trend was observed, with a significant overall effect ($\chi 2_{(2)} = 13.885$, $p<0.01$). *Post Hoc* analysis revealed once again a significant increase within BCAS (0.42±0.12) and BCAS+GW2580 mice (0.38±0.40) in comparison to shams (0±0.13) ($p<0.01$ and $p<0.05$ respectively), with no observed difference between BCAS groups ($p=1.000$) (Figure 3.17D). Despite a strong Lamp2^{+ve} microglial response within the white matter, the effect within the hippocampal grey matter region was muted. A strong Lamp2 response was observed in a subset of BCAS mice however this represented the minority of cases and therefore there was no overall difference between groups for cell counts ($p=0.334$) (Figure 3.17E) or counts normalised to total Iba1 numbers ($p=0.430$) (Figure 3.17F).

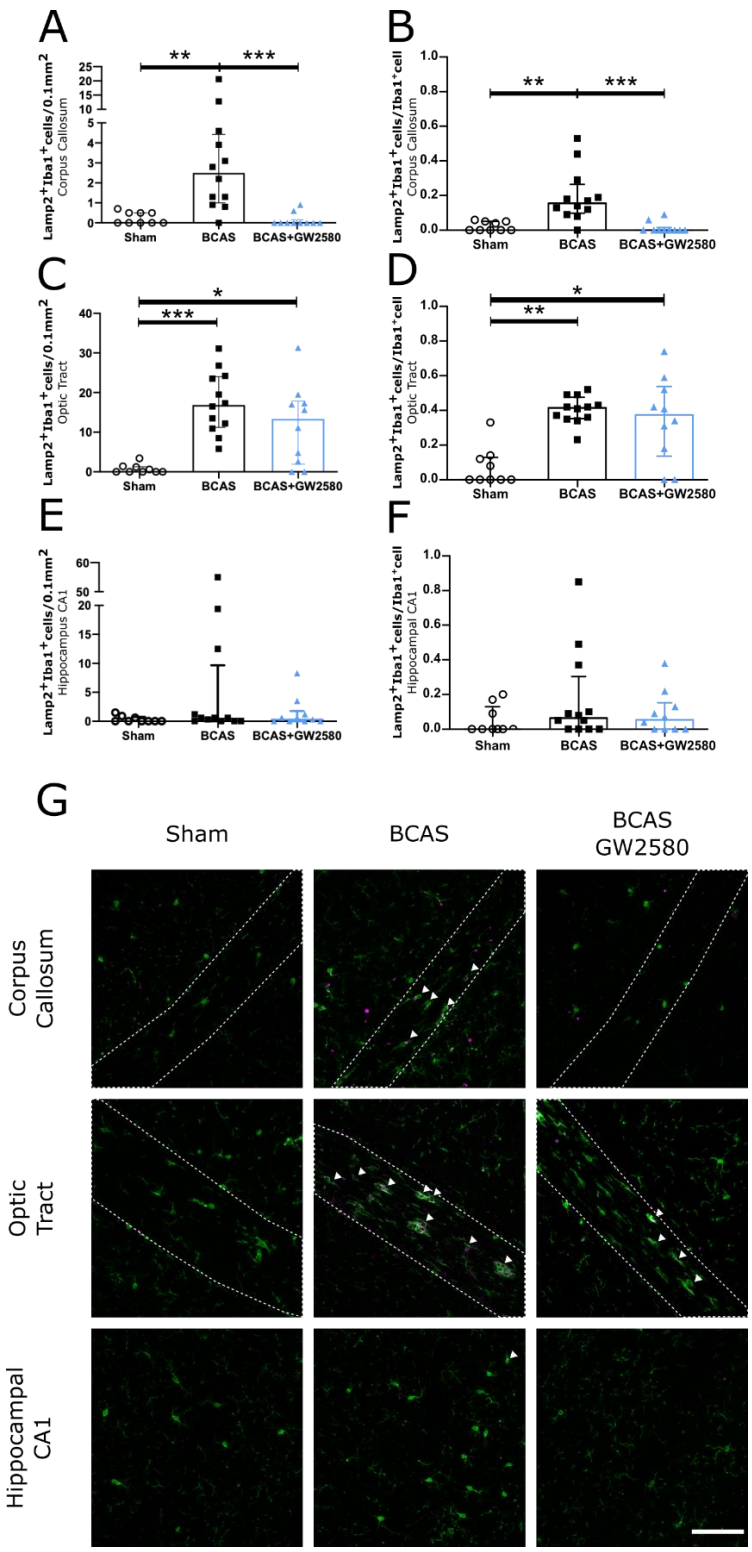

Figure 3.17 CSF1R inhibition protects against corpus callosum microglial activation following BCAS. **(A)** Increased Lamp2^{+ve}Iba1^{+ve} cells within the corpus callosum of BCAS mice but not sham or BCAS+GW2580 groups 6-weeks following surgery. **(B)** When normalised to number of Iba1^{+ve} cells, BCAS mice show significantly increased numbers of

Lamp2^{+ve} cells within the corpus callosum when compared to sham and BCAS+GW2580 groups. **(C)** Increased Lamp2^{+ve}Iba1^{+ve} cells within the optic tract of BCAS and BCAS+GW2580 mice compared to shams, 6-weeks following surgery. **(D)** When normalised to total Iba1^{+ve} cells, BCAS and BCAS+GW2580 mice show increased Lamp2^{+ve} cells compared to shams. Increased numbers of Lamp2^{+ve}Iba1^{+ve} cells within the hippocampal CA1 region of a subset of BCAS mice but overall, no group differences were detected for total Lamp2^{+ve} cells **(E)** or when normalised to total Iba1^{+ve} cells **(F)**. Data presented as Median±IQR. p<0.05*, p<0.01**, p<0.001***. **(G)** Representative images of Lamp2/Iba1 staining within the corpus callosum, optic tract, and hippocampus CA1 region taken from sham, BCAS, and BCAS+GW2580 mice. Iba1-green, Lamp2-megenta. White arrow heads represent Lamp2/Iba1 colocalised cells. Scale bar 50µm.

Having previously demonstrated that microglial expansion within the corpus callosum is positively correlated to increased white matter damage and spatial learning impairments, the next aim was to determine if increased Lamp2 expression was also involved. To determine if microglial Lamp2 expression is associated with increased white matter damage, MAG severity scores were correlated to microglial Lamp2^{+ve} cell counts within the corpus callosum (Figure 3.18A). The extent of white matter damage was found to be positively correlated to the number of Lamp2^{+ve} microglial cells within the corpus callosum ($r_{s(29)}$ = 0.655, p<0.001) (Figure 3.18A). Furthermore, to investigate the link between Lamp2 expression and impairments in spatial learning, average escape latency was correlated to Lamp2^{+ve} microglial cell counts within the corpus callosum (Figure 3.18B). A significant positive correlation was identified ($r_{s(29)}$ = 0.616, p<0.01), indicating that increased Lamp2^{+ve} microglial numbers are linked to a poorer spatial learning performance (Figure 3.18B).

Overall, these data indicate that chronic BCAS leads to increased microglial lysosomal expression within white matter regions, which is associated with increased white matter damage and impaired spatial learning. CSF1R inhibition, through GW2580 treatment, reduces white matter microglial Lamp2 expression, however this effect is region dependent.

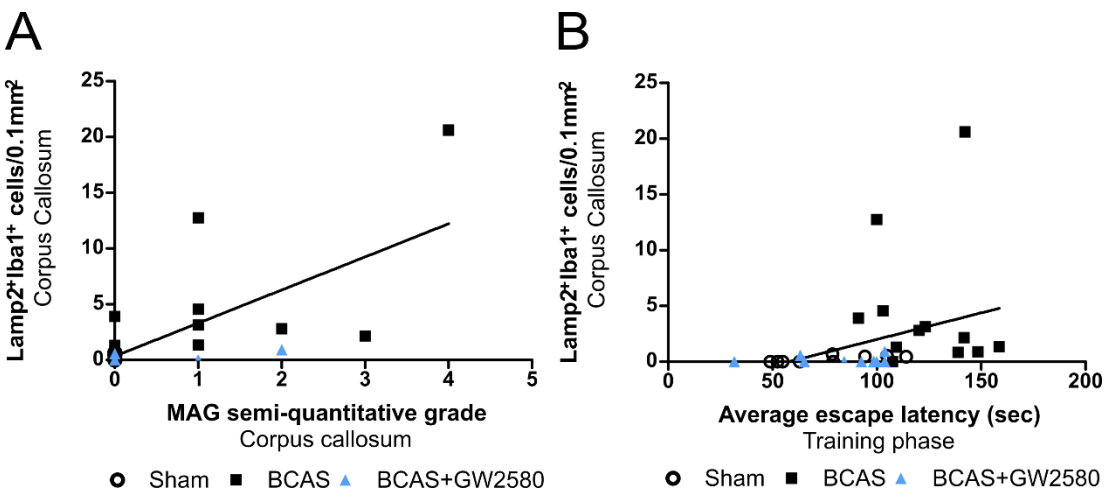

Figure 3.18 Lamp2 positive microglial cells are associated with increased white matter damage within the corpus callosum and impaired spatial learning. **(A)** $Lamp2^{+}Iba1^{+}$ cells positively correlate with increased MAG severity score within the corpus callosum. **(B)** $Lamp2^{+}Iba1^{+}$ cells positively correlate with increased escape latency times, indicative of a poorer Barnes maze performance. Data presented as Mean.

3.4 Discussion

The present study set out to investigate the role of microglial proliferation in the onset of white matter damage and cognitive impairment following BCAS. The results demonstrate that BCAS leads to both white and grey matter microglial proliferation, which is associated with increased white matter damage and impaired spatial learning. Blocking microglial proliferation through GW2580 treatment was found to prevent microglial expansion, preserve white matter integrity, and rescue spatial learning impairments following BCAS surgery.

3.4.1 Resting cerebral blood flow is significantly reduced following BCAS and unaltered by GW2580 treatment

The overall aim of this study was to investigate how sustained reductions in CBF leads to white matter damage and ultimately cognitive deficits. To achieve CBF reductions, the bilateral common carotid artery stenosis (BCAS) model was used. BCAS was found to lead to both short term and chronic reductions in CBF measured within the superficial cortex via laser speckle imaging. A ≈50-60% reduction in CBF was apparent 24-hours following BCAS surgery, which was maintained up to 6-weeks later with no obvious restoration. Such blood flow reductions were comparable to those previously reported within the literature (Fowler et al., 2017; Miki et al., 2009).

In the current study a mixed coil BCAS model was used, which applied 0.16mm and 0.18mm micro-coils to the common carotid arteries to reduced blood flow to the brain. The mixed coil model is a modification of the well-established 2x0.18mm BCAS model (Shibata et al., 2004) and was selected due to its ability to induce definite and reproducible white matter lesions which are associated with the early onset of neuropsychological deficits (Miki et al., 2009). This differs from the 2x0.18mm BCAS model which elicits a milder, ≈20-40%, reduction in CBF leading to a slower progressive onset of wide spread diffuse axonal damage, loss of white matter integrity and impairments in visuo-spatial learning and memory (Duncombe, Kitamura, et al., 2017).

In the present study blood flow was assessed via laser speckle analysis which allows repeated measurements, longitudinally, following surgery. Laser speckle analysis is however, restricted to the upper layers of the cortex and does not provide information on subcortical blood flow changes that might occur in response to BCAS surgery. Previous BCAS studies have demonstrated however, via MRI, that blood flow is affected throughout the brain, with significant reductions being evident in both cortical and sub-cortical regions (Boehm-Sturm et al., 2017; Hattori et al., 2016; Kitamura et al., 2017). Such data indicates that BCAS surgery effects blood flow throughout the brain, highlighting the importance of studying both cortical

and subcortical changes following surgery. It is important to note however, that both laser speckle and MRI analysis of CBF changes following BCAS are conducted under anaesthesia. Anaesthetics such as isoflurane have been shown to lead to vascular dilation and therefore blood flow may differ between anaesthetised and awake mice (Fan et al., 2016).

The BCAS procedure employed for the present study involved the application of a 0.16mm micro-coil to the right and a 0.18mm coil to the left common carotid arteries. Due to the difference in coil diameter, hemispheric disparities in blood flow were apparent early following surgery, however these did not persist long term (data not shown). As all measures were conducted at 1- or 6-weeks following surgery, when hemispheric blood flow had equalised, the hemispheric differences due to surgery were considered minimal. As an additional precaution, immunohistochemical analysis was completed on both hemispheres with values averaged.

C57/B6J mice were selected for studies as they have an incomplete circle of Willis, due to a lack of posterior cerebral arteries (G. Yang et al., 1997). Thus meaning that compensatory blood flow mechanisms are not sufficient to rescue blood flow reductions following BCAS surgery in C57/B6J mice (Qian et al., 2018). Despite this, a subset of mice showed resistance to BCAS surgery with little evidence of reduced CBF via laser speckle imaging. Through the injection of a fluorescently conjugated dextran, non-responding mice were found to have intact circle of Willis', with posterior cerebral arteries clearly visible leading to a conferred resistance to BCAS surgery (Figure 2.2). This therefore would indicate a level of genetic divergence within the C57/B6J mouse line. The present study aimed to investigate microglial responses to sustained CBF reductions. Therefore, to ensure that resilient mice did not compromise the study, strict exclusion criteria were established, such that mice needed to demonstrate at least a 35% reduction in CBF, 24-hours following BCAS surgery, to be included.

GW2580 treatment was shown to have no effect on blood flow reductions following BCAS surgery. Ensuring that any observed benefits to GW2580 treatment were independent of improved CBF following BCAS surgery.

3.4.2 Microglia dominate the early inflammatory response following BCAS

Microarray analysis conducted within the white matter 3-days following BCAS surgery identified alterations in pathways associated with neuroinflammation, cytokine-cytokine receptor interactions and cell proliferation (Reimer et al., 2011). Despite these findings' investigations assessing the profile of immune cells within the white matter following BCAS, have been limited (Duncombe, Kitamura, et al., 2017). To accurately assess such changes

white matter tissue taken from the corpus callosum was analysed via flow cytometry. Flow cytometric analysis revealed that BCAS surgery resulted in a 2-fold increase in microglial cells with macrophage, neutrophil and monocyte numbers unchanged. These findings are in agreement with previous investigations using the BCAS model which show, via immunohistochemistry, a robust increase in white matter microglial numbers following surgery (Coltman et al., 2011; Fowler et al., 2017; Holland et al., 2015; Kitamura et al., 2017; Manso et al., 2017; Reimer et al., 2011). A lack of macrophage response was also in agreement with previously published work, which demonstrated via Iba-1/TMEM119 co-labelling limited macrophage numbers within the corpus callosum in response to BCAS (Manso et al., 2017). Additionally, surgical techniques using bone marrow chimeric mice found no evidence of peripheral macrophages within the white matter following BCAS (Miyanohara et al., 2018).

Limited monocyte and neutrophil infiltration following BCAS, however, has not been shown previously and would suggest that the BBB is intact following 1-week of BCAS surgery. This is in agreement with previous findings which demonstrated that BBB disruption is not observed until 6-months following BCAS surgery, as detected by parenchymal fibrinogen and markedly reduced tight junction claudin-5 expression (Holland et al., 2015). Other groups however, have demonstrated cortical, hippocampal, and striatal BBB leakage through the quantification of Evans blue, as early as 14-days post-BCAS (J. M. Roberts et al., 2018). It could, therefore, be hypothesised that BBB leakage is brain region dependent with white matter regions showing increased resistance. However, additional investigations, focussing on BBB integrity within specific white matter regions would be required to confirm such a theory.

As a confirmation of microglial expansion following BCAS surgery, microglial numbers were calculated, via immunohistochemistry, 1-week following BCAS within both white and grey matter regions. Iba-1 cell counts demonstrated increased microglial numbers within the hippocampus following BCAS surgery, however, quantification within the corpus callosum only reported a strong trend for increased microglial numbers. Increased hippocampal microglial numbers is in agreement with previously published work assessing early neuroinflammatory changes following BCAS (J. M. Roberts et al., 2018). A lack of clear microglial expansion within the corpus callosum, however, does somewhat contradict flow cytometry results, which demonstrated a 2-fold microglial increase when compared to shams. This can however be attributed to the fact that immunohistochemical analysis is only assessing numbers within a subregion of the corpus callosum, from a 6µm section, whereas flow cytometry is analysing almost the entire corpus callosum and therefore can be deemed a more reliable assessment.

Despite only a trend for increased corpus callosum numbers, percentage area of Iba1 staining per cell was found to increase following BCAS, indicating enlarged microglial size. Previous studies have demonstrated that microglia undergo conformational changes when a switch from homeostatic to activated forms occurs (Karperien, Ahammer, & Jelinek, 2013). Increased microglial size has been reported after a number of inflammatory inducing insults such as LPS treatment, mechanical injury, and optic nerve crush injury (B. M. Davis et al., 2017; Kozlowski & Weimer, 2012; Stence, Waite M Fau - Dailey, & Dailey, 2001). Increased area of staining per cell does provide some data to illustrate altered microglial phenotype following surgery, however more advanced imaging techniques, such as multiphoton microscopy and 3-dimensional (3D) structural modelling, would be required to accurately confirm such a finding.

One important consideration for immunohistochemical analysis, is that Iba1 is a pan myeloid cell marker and therefore will be expressed on macrophages as well as microglia. Flow cytometry data, however, shows that the early neuroinflammatory response following BCAS is dominated by microglia. TMEM119 staining following BCAS also showed a 1 to 1 overlap with Iba-1, demonstrating microglial specific expansion following BCAS (Manso et al., 2017). Therefore, the contribution of macrophages to Iba1 cell counts is likely to be minimal.

3.4.3 Microglial expansion following BCAS is driven by local proliferation

To determine if microglial expansion is driven by the local proliferation of endogenous microglial following BCAS, BrdU was administered over the last 3-days prior to the 1-week timepoint. BrdU incorporates into the DNA of actively dividing cells, allowing proliferating cells to be identified via immunohistochemistry. Iba1-BrdU co-staining demonstrated significantly increased levels of microglial proliferation within both white and grey matter regions, 1-week following BCAS surgery. These findings are in agreement with previous literature, which reported increased white matter microglial numbers associated with local proliferation, following 10-weeks of BCAS (Manso et al., 2017). However, the present study provides the first evidence to demonstrate early microglial proliferation in response to BCAS. This finding however is supported by previous literature that demonstrated significant alterations in 15 genes associated with the regulation of cell proliferation, through microarray analysis completed on white matter tissue samples taken 3-days following BCAS (Reimer et al., 2011).

Such findings also align with recent clinical evidence which identified 5 risk loci, through GWAS, associated with neuroimaging markers of white matter dysfunction that were all highly expressed by microglial/macrophages populations (Armstrong et al., 2020; Persyn et al., 2020). Furthermore, increased microglial number is a frequently observed feature, at *post mortem*, within human VCI cases (Simpson, Fernando Ms Fau - Clark, et al., 2007; Simpson, Ince Pg Fau - Higham, et al., 2007).

Under normal homeostatic conditions microglial proliferation is matched to apoptosis to maintain a stable population of microglial cells throughout the brain. The balance between microglial proliferation and apoptosis has be shown to become disrupted in neurodegenerative conditions leading to excessive microglial proliferation (Diego Gomez-Nicola & V. Hugh Perry, 2015). Taken together these findings therefore provide strong evidence to demonstrate that microglial expansion occurs early, following BCAS surgery, within both white and grey matter regions and is driven by local proliferation.

Alongside the quantification of proliferating microglial cells, the number of non-microglial proliferating cells was also calculated. Analysis of non-microglial cell proliferation showed significant increases within the hippocampus, but not the corpus callosum, following BCAS. Flow cytometry data demonstrated no change in the numbers of macrophages, neutrophils, or monocytes following BCAS, suggesting that these non-microglial proliferating cells are unlikely to be immune related. Although, flow cytometry was completed within the corpus callosum and therefore it is possible that the immune cell profile may differ within the hippocampus. It has been shown however, that astrogliosis occurs in response to BCAS (Kitamura et al., 2017), with changes observed subsequent to microglial alterations (Holland et al., 2015). Consistent with these findings, the release of microglial cytokines has been identified as a key mechanism triggering astrogliosis (Liddelow et al., 2017). Increased GFAP, a marker of astrogliosis, has also been demonstrated within hippocampus, cortex, and striatum at early timepoints following BCAS (J. M. Roberts et al., 2018). Therefore, astrocytic proliferation is a likely candidate for the non-microglial proliferation observed within the hippocampus.

Endothelial cell proliferation is another possible candidate for the non-microglial proliferation occurring within the hippocampus following BCAS. As angiogenesis has been a proposed mechanism by which the cerebral vasculature may attempt to counteract the detrimental effects of BCAS. Previous studies, however, using Ki67 as a marker of proliferation, identified only 6.8% co-localisation with the endothelial marker PECAM-1 within the hippocampus and striatum of mice following BCAS (J. M. Roberts et al., 2018). The authors then went on to demonstrate, within the grey matter, 71.8% co-localisation of

Ki67 with the microglial marker CD11b, 55.1% with the astrocytic marker GFAP and 30.8% with the oligodendrocyte marker OSP (J. M. Roberts et al., 2018). Further, supporting the present findings of microglial proliferation early following BCAS and highlighting astrocytes and oligodendrocytes as the most likely candidates for the non-microglial proliferation observed. In the present study, however, non-microglial proliferation is proportionally seen to be minimal when compared to microglial proliferation, which clearly dominates the early neuroinflammatory response following BCAS.

3.4.4 GW2580 treatment prevents microglial expansion following BCAS

As mentioned previously, robust increases in white matter microglial numbers have been consistently demonstrated following BCAS surgery (Coltman et al., 2011; Fowler et al., 2017; Holland et al., 2015; Kitamura et al., 2017; Manso et al., 2017; Reimer et al., 2011). The present study, however, was the first evidence to clearly show that local microglial proliferation dominates the early neuroinflammatory response following BCAS. This therefore led to the hypothesis that the blockade of microglial proliferation could have a beneficial impact on downstream white matter impairment and cognitive dysfunction.

A key mechanism by which microglial proliferation is regulated is through the colony-stimulating factor 1 receptor (CSF1R) (Raivich et al., 1998). The ligands CSF-1 (also known as M-CSF) and interleukin-34 (IL-34) bind to the CSF1R leading to downstream signalling promoting the survival, differentiation, and proliferation of mononuclear phagocytes, with the most notable of these being microglial cells (Hume & MacDonald, 2012). In the present study, white matter microglia were found to have a ≈3-fold increase in CSF1R expression following short-term BCAS, thus highlighting CSF1R signalling as the likely mechanism underlying microglial proliferation. GW2580 is an orally available inhibitor of CSF1R and therefore provided a specific method by which microglial proliferation could be blocked following BCAS (Conway et al., 2005).

In the present study, chronic treatment with the competitive CSF1R antagonist GW2580 was found to successfully inhibit microglial expansion within white and grey matter regions, following BCAS. Previous research using the same 75mg/kg GW2580 dosing regime, reported ≈50% reduction in microglial proliferation in models of prion disease (Gomez-Nicola et al., 2013) and Alzheimer's disease (Adrian Olmos-Alonso et al., 2016b). Here we report almost a complete inhibition of microglial proliferation, with BCAS+GW2580 mice even showing a slight dip in microglial numbers below that of shams. The difference in GW2580 effectiveness within the present study is likely due to the severity of disease models being assessed. Prion

and AD models elicit a robust and chronic neuroinflammatory response, characterised by increased pro-inflammatory genes such as IL-1β, CSF1, and IL-34, observed as late as 18-weeks following prion inoculation (Gomez-Nicola et al., 2013) and 9-months within AD mice (A. Olmos-Alonso et al., 2016). BCAS in contrast, leads to more subtle inflammatory responses, with microarray analysis demonstrating increased pro-inflammatory gene expression 3-days following surgery (Reimer et al., 2011), with only very subtle changes detected 6-weeks later (Manso et al., 2017). GW2580 acts as a competitive antagonist at the intracellular tyrosine kinase domain of the CSF1 receptor (Dai et al., 2002), and therefore under extremely high levels of proliferation, GW2580 may be out-competed for binding by the endogenous ligands CSF1 and IL-34. Therefore, the almost complete blockade in microglial proliferation observed following BCAS likely reflects a proliferation rate at which GW2580 can successfully outcompete endogenous CSF1 and IL-34 ligands. However, to accurately assess this, CSF1 and IL-34 ligand expression within BCAS mice with and without GW2580 treatment would need to be quantified.

In the present study microglial numbers within BCAS mice, following GW2580 treatment, were found to be lower than that of shams. One explanation for this could be that GW2580 treatment, alongside blocking BCAS mediated proliferation, is also preventing normal homeostatic microglial proliferation. Longitudinal fate mapping studies, however, demonstrate that microglial proliferation within the mouse neocortex is a rather deactivated process, with ≈50% of all microglial cells persisting until the end of the mouse's lifespan (Fuger et al., 2017). Thus, indicating that microglial homeostatic proliferation rates are low and therefore unlikely to account for such a difference in microglial numbers (Askew et al., 2017). An alternative explanation is that BCAS results in microglial apoptosis which would account for the dip in microglial numbers within BCAS mice following GW2580 treatment. Such an effect would not be as easily observed within the BCAS group due to a prominent microglial proliferative response. Previous studies, however, found no increase in numbers of apoptotic cells within the white matter, 3-days or 1-month following BCAS (Reimer et al., 2011). Although, this might not be the case in the present study which utilised a mixed coil BCAS model with assessments at a more chronic timepoint. It could, therefore, be the case that modest levels of apoptosis, coupled to a blockade of homeostatic proliferation, coincide to lead to an overall dip in microglial numbers following GW2580 treatment. To confirm this, additional experiments would be required using apoptotic markers or fate mapping technologies, alongside sham groups treated with GW2580.

To assess microglial proliferation at a chronic timepoint following BCAS, BrdU was administered for the 3-days prior to the 6-week timepoint. Immunohistochemical analysis

revealed very little evidence of microglial proliferation 6-weeks following surgery. The same BrdU treatment regime was used for both short-term and chronic studies. This suggests that microglial proliferation rates are higher at 1-week compared to 6-weeks following BCAS. As evidenced in the present study, CBF reductions are apparent 24-hours following surgery and maintained consistently up to 6-weeks later. Previous studies have also demonstrated that reduced white matter oxygen tension can be detected 3-days following BCAS and was maintained at hypoxic levels when assessed 1- and 6-weeks following surgery (Duncombe, Kitamura, et al., 2017). Despite persistent cerebral hypoperfusion and white matter hypoxia, microglial proliferation rates in the present study were found to be higher when assessed at 1-week compared to 6-weeks. Thus, indicating that signalling mechanisms, triggering the proliferation of microglial, occur early following BCAS and do not persist at later timepoints. In support of this, previous microarray analysis demonstrated increased endothelial related gene expression, alongside of a battery of proinflammatory genes, acutely following BCAS (3-days) (Reimer et al., 2011). Such responses, however, were difficult to detect when assessed chronically (6-weeks) following surgery (Manso et al., 2017). However, it is important to note that 3 BrdU doses would be unlikely to capture all the proliferation ongoing at either timepoint. Therefore, to assess microglial proliferation more comprehensively, chronic BrdU dosing would be required.

3.4.5 GW2580 treatment prevents white matter integrity disruption following BCAS

In agreement with previous studies (Coltman et al., 2011; Kitamura et al., 2017; McQueen et al., 2014; Reimer et al., 2011) white matter damage was found to be widespread with increased MAG accumulations identified within the corpus callosum, fimbria, and internal capsule following chronic BCAS. White matter damage was also found to positively correlate with increased microglial number within all white matter regions analysed.

GW2580 treatment was found to ameliorate white matter damage through the blockade of microglial proliferation across white matter regions. BCAS studies have previously reported a close association between microglial number and impairments in white matter function (Fowler et al., 2017; Kitamura et al., 2017; Manso et al., 2017). Additional, broad spectrum anti-inflammatory pharmacological approaches, linked to reduced microglial number, have demonstrated reductions in white matter damage and improvements in white matter function following BCAS (Fowler et al., 2017; Manso et al., 2017; Miyanohara et al., 2018). The present study, however, provides the first direct evidence to demonstrate that microglial proliferation is crucial to white matter damage, following BCAS.

Microglia are proposed to be detrimental to both the white matter and oligodendrocytes through the chronic release of free radicals and cytokines following sustained neuroinflammation (Howell et al., 2010). Increased Lamp2 expression within the corpus callosum also demonstrates that microglial proliferation is accompanied by increased microglial activation, likely leading to the release of pro-inflammatory cytokines driving further damage. Increased lamp2 expression is indicative of lysosomal activity which would suggest increased microglial phagocytic activity. Whether microglia are indeed phagocytosing material within the white matter tracts is currently unknown. However, it would suggest that damage is occurring within these regions leading to increased debris, triggering clearance pathways. In agreement with the role of microglia in white matter damage, previous studies using the anti-convulsant levetiracetam, showed that white matter damage and cognitive impairment were reversed due to reduced microglial activity. Inhibition of microglial activity was also found to be associated with reduced oligodendrocyte cell death within the cerebral white matter (Inaba et al., 2019). Additional experiments using more detailed imaging approaches, such as electron microscopy, would be required to definitively prove that microglial are indeed phagocytosing debris within white matter tracts following BCAS. However, the present study does clearly demonstrate that microglial proliferation is a fundamental step in the onset of white matter damage following BCAS.

In support of our present findings, previous studies using GW2580 treatment have demonstrated improved white matter integrity and function in mouse models of multiple sclerosis (Crespo et al., 2011) and spinal cord injury (Gerber et al., 2018). Furthermore, approaches to deplete microglia have shown promise in the reversal of white matter damage. For example, treatment with the CSF1R inhibitor PLX5622, in an experimental autoimmune encephalomyelitis mouse model of multiple sclerosis, demonstrated reduced demyelination, immune cell activation, and preserved mature myelinating oligodendrocytes within white matter lesion areas (Nissen, Thompson, West, & Tsirka, 2018). The pharmacological or genetic depletion of microglia has also been shown to have a beneficial impact on white matter pathology within a range of neurodegenerative disease models (Garcia-Agudo et al., 2019; Janova et al., 2018; Klein et al., 2015), including chronic stroke (Jackson, Dumanli, Johnson, Fagan, & Ergul, 2020).

Interestingly however, human loss of function mutations within the CSF1R gene have been identified and lead to the onset of hereditary diffuse leukoencephalopathy with spheroids (Rademakers et al., 2011). CSF1R-related leukoencephalopathy patients typically present with frontotemporal dementia-like cognitive phenotypes with neuroimaging evidence of white matter abnormalities, thinning of the corpus callosum, diffusion-restricted lesions in the white

matter, and brain calcifications (Konno, Kasanuki, Ikeuchi, Dickson, & Wszolek, 2018). Thus, highlighting that long-term inhibition of CSF1R signalling is likely to be harmful to the white matter and therefore further research is required to elucidate the beneficial timing of such pharmacological interventions.

3.4.6 GW2580 treatment rescues spatial learning impairments following BCAS

The corpus callosum and hippocampus represent important components of the frontal-subcortical circuitry that has been implicated in spatial learning the memory (Duncombe, Kitamura, et al., 2017). Previous studies have also demonstrated a close relationship between white matter damage and cognitive impairments following BCAS (Ben-Ari et al., 2019; Coltman et al., 2011; Holland et al., 2015; Nishio et al., 2010; Shibata et al., 2007), with some evidence of improvements following broad acting anti-inflammatory interventions (Miyanohara et al., 2018; C. Qin et al., 2017). To date however the direct relationship between microglial proliferation and cognitive impairment has not been reported.

Here, the assessment of spatial learning and memory, via the Barnes maze, identified significant impairments 6-weeks following BCAS surgery. These findings are in agreement with previous studies which report spatial learning deficits following BCAS, using a conventional 8-arm radial maze or Y-maze tests (Maki et al., 2011; Shibata et al., 2007; Washida et al., 2010). Previous experiments using the Barnes maze however, were only able to detect spatial learning impairments 5-6 months following BCAS (Holland et al., 2015; Nishio et al., 2010). The accelerated onset of Barnes maze cognitive impairment in the present study is likely a reflection of the more severe blood flow reductions achieved here (50-60%) when compared to the previous BCAS studies (20-40%) (Holland et al., 2015; Nishio et al., 2010).

Chronic GW2580 treatment was found to preserve spatial learning, following BCAS, which was associated with reduced white matter microglial numbers and white matter damage. In agreement with these findings, the pharmacological ablation of microglia prior to BCAS surgery, through PLX3397 treatment, was found to supress white matter damage and restore cognitive abilities (Kakae et al., 2019a). Disruption of white matter tracts, especially within the prefrontal cortex, has been suggested as a mechanism underpinning spatial learning deficits following BCAS (Burton et al., 2004; Shibata et al., 2007). Furthermore, ischemic disruption of the prefrontal cortical-subcortical circuits has been implicated in the cognitive and mood-behaviour abnormalities seen in human VCI (Bonelli & Cummings, 2007; Lanza et al., 2017). Due to the significant white matter integrity improvement following GW2580 treatment, it can

therefore be inferred that rescued white matter integrity culminates in preserved spatial learning, following BCAS. Indeed, it has been suggested that spatial learning is dependent on white matter circuitry which allows for efficient communication between brain regions (Coltman et al., 2011; Shibata et al., 2007). This is in agreement with previous research which demonstrated that disruption of axon-glial integrity and microglial expansion were associated with impairments in spatial learning (Kitamura et al., 2017).

Despite significant improvements in spatial learning, GW2580 treatment was found to only display modest restorative effects on spatial memory. Spatial memory has been proposed to be related to cognitive domains that are reliant on an intact hippocampus, as well as effective hippocampal signalling through frontal-subcortical circuitry (Nishio et al., 2010; Sharma, Rakoczy, & Brown-Borg, 2010). In agreement with this, milder models of BCAS, absent of hippocampal inflammatory responses and pathology, display spatial learning but not spatial memory impairments (Shibata et al., 2007). In the present study we observe a significant proliferative microglial response within the CA1 region of the hippocampus following BCAS surgery. Even though chronic GW2580 treatment was found to successfully inhibit this microglial expansion, no spatial memory improvements were observed. This may reflect the fact that GW2580 is unable to prevent damage to other cell types within the hippocampus, most namely neurons and synapses which could be significantly impacted following BCAS leading to memory impairments. Thus, indicating that damage may occur through microglial-independent processes. It could also be the case that GW2580 treatment, restores frontal-subcortical circuitry to such an extent that spatial learning is maintained, however, damage may persist and thus sustain deficits in spatial memory.

Following the training phase, the escape chamber was relocated 180^0 to the other side of the maze and visuo-spatial learning and memory of this new location was assessed (Pompl, Mullan Mj Fau - Bjugstad, Bjugstad K Fau - Arendash, & Arendash, 1999). A slight trend for worsened reversal learning was apparent following BCAS with a slight improvement in response to GW2580 treatment. Sham mice, however, were the only group able to demonstrate intact memory for the target zone during probe trails. Reversal learning within the BCAS group did appear to show a slower rate of learning in comparison to both sham and BCAS+GW2580 groups. This contrasts with the clear learning impairment observed within BCAS mice during the training phase in comparison to sham and BCAS+GW2580 groups. This may reflect the fact that the reversal phase is much shorter than the training phase, and therefore sham and BCAS+GW2580 groups might not have had sufficient time to clearly outperform the BCAS group (O'Leary & Brown, 2009).

Throughout both standard and reversal training phases escape latency was used as the outcome measure of performance. Escape latency refers to the time taken for the mouse to locate and enter the escape chamber, which can be highly influenced by movement speed. To ensure that mobility differences between groups were not influencing learning outcomes, movement speed was compared across groups. Movement speed, during both training and reversal phases, was found to be comparable across all groups, and therefore had no influence on learning outcomes in the present study.

Across both training and reversal phases, GW2580 treatment showed some benefit to learning outcomes with no observed improvement in long-term memory impairments following BCAS. This is an important distinction, as blocking microglial proliferation appears to selectively rescue learning but not memory deficits following BCAS. Human VCI is characterised by impairments in cognitive functions important for executive functioning and speed of processing, which are reliant of healthy white matter (de Groot et al., 2000). In later stages of disease processes, severe memory impairments become apparent which are associated with increased severity of SVD pathology (Smallwood et al., 2012). Furthermore, a common finding within patients showing vascular brain lesions as a result of cerebrovascular disease are impairments in executive functions, such as cognitive flexibility, as well as processing speed (Looi & Sachdev, 1999). This therefore indicates that CSF1R inhibition alone is not sufficient to rescue both learning and memory impairments following BCAS, indicating additional mechanism effecting cognition beyond white matter damage, or simply that restoration of frontal-subcortical circuitry is not sufficient to restore spatial memory.

Overall, this data provides the first evidence to demonstrate that microglial proliferation significantly contributes to white matter damage and spatial learning impairments following BCAS.

3.4.7 GW2580 treatment prevents BCAS mediated increases in microglial lysosomal expression within the corpus callosum

Lamp2 expression has been shown to be required for the fusion of lysosomes and phagosomes within microglial cells (Huynh et al., 2007). Therefore, increased lamp2 expression can be considered a marker of increased microglial phagocytic activity as well as a general indicator of microglial activation (Kocur et al., 2015). In the present study, increased lamp2 expression was observed within white but not grey matter regions following BCAS. This may reflect increased myelin debris within white matter regions causing an increased need for phagocytic activity to facilitate clearance. In support of this a recent study identified, using CLARITY imaging, that spatial learning and memory deficits as well as white matter

damage following BCAS, were associated with microglial activation and an increase in the number of reactive microglia adhering to and phagocytosing myelin (Zhang et al., 2020). Thus, demonstrating that microglia are directly damaging myelinated axons. Myelin phagocytosis was found to be associated with an upregulation in the expression of complement C3 and its receptor C3aR (Zhang et al., 2020). Furthermore, human *post mortem* neuropathological investigations have highlighted increased $CD68^{+ve}$ microglia, indicative of increased phagocytic activity, as a prominent feature of deep subcortical lesions within an ageing population (Waller et al., 2019). Additionally, the increased production of myelin fragments released from aging myelin sheaths has been shown to lead to the formation of insoluble, lipofuscin-like lysosomal inclusion within microglia. Over-time such insoluble inclusions overwhelm the lysosomal capacity of microglial cells resulting in microglial senescence and immune dysfunction in ageing (Safaiyan et al., 2016).

Increased white matter, but not grey matter, lysosomal activity may indicate that the level of damage within white matter areas exceeds that of the hippocampus leading to an increased need for phagocytic processes. Indeed, white matter regions have been shown to be particularly vulnerable to vascular disruption (Black, Gao F Fau - Bilbao, & Bilbao, 2009; Iadecola, 2013), which has been attributed to the relative scarcity of collateral blood flow in deep white matter regions (Iadecola, Park, & Capone, 2009). Furthermore, ageing has been demonstrated to reveal brain region specific differences in microglial phenotype, with white matter microglia displaying increased levels of the phagocytic related marker CD68 (Hart, Wyttenbach, Perry, & Teeling, 2012).

In response GW2580 treatment, microglial lamp2 expression within the corpus callosum was found to be significantly reduced to sham levels. When lamp2 expression was normalised to the total number of microglial cells, BCAS+GW2580 mice still demonstrated very low numbers of lamp2 expressing microglia within the corpus callosum. Previous studies have suggested that GW2580 leads to an overall shift of inflammatory profile from pro- to anti-inflammatory (Gomez-Nicola et al., 2013; A. Olmos-Alonso et al., 2016). In support of this, work using cultured human microglia has demonstrated that increased CSF1R signalling leads to the production of pro-inflammatory cytokines (Walker, Tang, & Lue, 2017). Reduced lamp2 expression could therefore indicate that GW2580 treatment is not only blocking microglial proliferation but is also causing a switch to a more anti-inflammatory microglial phenotype following BCAS. In agreement with this explanation, GW2580 treatment in a mouse model of Parkinson's disease was observed to block microglial proliferation, leading to reduced mRNA expression of pro-inflammatory markers, with no effect on anti-inflammatory markers (Neal et al., 2020).

Alternatively, another explanation could be that early microglial proliferation leads to the release of harmful pro-inflammatory cytokines resulting in myelin and axonal damage within the white matter. Over more chronic time periods cellular debris collects leading to increased lysosomal activity within microglial cells, to enable debris to be phagocytosed and cleared. GW2580 would therefore act to block microglial proliferation, significantly reducing neuroinflammation, and thus preventing white matter damage and the need for phagocytic processes. In support of this, research within a rat MCCAO model, demonstrated that microglial were activated via complement 3 receptor signalling, leading to microglial adhering to and phagocytosing myelin. Genetic deletion of the complement 3 receptor was then found to limit microglial activation and attenuate white matter injury and cognitive deficits following hypoperfusion (Zhang et al., 2020). Increased microglial activation and proliferation has also been identified within the white matter of ageing human brains, being identified not only within lesioned areas but also within the non-lesioned white matter (Simpson, Ince Pg Fau - Higham, et al., 2007). Further investigations therefore are required to shed light on these process by looking at lamp2 activity acutely following BCAS.

GW2580 treatment was found to have no positive effect on lamp2 expression within the optic tract, which could indicate that this region is particularly susceptible leading to a more significant response. Iba1 cell counts within the optic tract during the lamp2 analysis revealed a big increase following BCAS with only a modest, non-significant, reduction following GW2580 treatment (data not included). Indicating that GW2580 treatment was ineffective within this area. This regional effect might reflect a magnitude of proliferative response within the optic tract that the current dose of GW2580 is unable to compete with and therefore cannot completely block. GW2580 acts as a competitive antagonist at the intracellular tyrosine kinase domain of the CSF1 receptor (Dai et al., 2002), and therefore under extremely high levels of proliferation GW2580 may be out-competed for binding by the endogenous ligands CSF1 and IL-34. Thus, microglia are still proliferating within this area and increased phagocytic activity is still present. Indeed, microglial numbers within the optic tract were shown to only be reduced by ≈35% following GW2580 treatment. This explanation is supported by previous investigations using the same 75mg/kg GW2580 dose in more severe disease models, that were able to achieve only a 50% reduction in microglial proliferation (Gerber et al., 2018; Gomez-Nicola et al., 2013; Martínez-Muriana et al., 2016; A. Olmos-Alonso et al., 2016).

3.4.8 Study limitations and future directions

In the present study, despite clear evidence of microglial proliferation contributing to white matter damage and cognitive impairment, data relating to the behaviour and activation state of

microglia in response to BCAS is lacking. In recent years significant advancements in intravital imaging approaches, alongside transgenic microglial reporter lines, have been made providing unprecedented access to the assessment of microglial behaviour *in vivo*. For example, multiphoton microscopy, alongside microglial reporter mice, can be used to 3D reconstruct individual microglial cells through which microglial activation state can be determined by the assessment of structural parameters (B. M. Davis et al., 2017; Kozlowski & Weimer, 2012). Microglial process motility has also be demonstrated to be dynamic and alter under disease conditions (Nimmerjahn et al., 2005). The aim, therefore, in chapter 4 was to utilise these state-of-the-art methods to allow for a more in-depth assessment of microglial structure and function following BCAS.

A key indication of microglial activation state, determined from the present study, was the observation of white matter microglial proliferation associated with increased lysosomal activity. However, an investigation into the lysosomal activity of microglial within white matter tracts, as well as a determination of what debris might be stimulating such as response, was not in the scope of the present study. Future studies, however, could make use of 3D electron microscopy to clearly demonstrate phagocytosing microglial following BCAS (Tremblay, Lowery, & Majewska, 2010). Alternatively, confocal microscopy and immunofluorescence has been shown to be a powerful method to assess phagocytosis, through the observation of 3D poches within terminal microglial branches that completely surround apoptotic cells (Sierra et al., 2010).

In the current study evidence of microglial activation was presented through an increase in microglial size 1-week following BCAS, as well as increased lysosomal activity 6-weeks following surgery. These data, although inferring microglial activation, do not provide clear evidence that microglial are actively contributing to neuroinflammation following BCAS. Therefore, in future studies it will be important to show such changes more comprehensively, to help clearly demonstrate that microglial are actively contributing to neuroinflammatory mediated damage. For example, white matter microglial could be isolated through flow cytometry and qPCR carried out to highlight increased expression of pro-inflammatory cytokines such as TNF-α, IL-1 and IL-6 (J. A. Smith, Das A Fau - Ray, Ray Sk Fau - Banik, & Banik, 2012). The present study also lacked the evaluation of perivascular macrophages which are likely to be impacted following BCAS due to their proximity to the vasculature. Furthermore, CSF1R signalling is important for the proliferation of perivascular macrophages and therefore the effects of GW2580 treatment currently cannot be solely attributed to microglial cells (Miron & Priller, 2020). Future studies should, therefore, look to delineate perivascular macrophages more comprehensively from microglial cells to determine the true

contribution of each to pathology following BCAS surgery, as well as uncover their individual responses to GW2580 treatment.

A key limitation of the present study is the lack of understanding as to what signalling mechanisms drive microglial proliferation following BCAS. Previous studies, through the implantation of fibre-optic oxygen sensors within the corpus callosum, demonstrated reduced PO_2 levels following BCAS. PO_2 levels were shown to dramatically reduced to hypoxic levels within 24-hours, and remain reduced when assessed 1- and 6-weeks later (Duncombe, Kitamura, et al., 2017). It has been shown that injured neurons produce increased amounts of CSF1 leading to microglial proliferation and activation (Guan et al., 2016). Therefore, hypoxia could be the mechanism by which neurons produce CSF1 triggering increased microglial proliferation following BCAS. Additional studies are however required to clearly prove such a mechanistic link. For example, correlating increased hypoxia within white matter regions to increased CSF1 production would help delineate such a mechanism. Additionally, microarray analysis conducted 3-days following BCAS demonstrated endothelial related gene changes occurring alongside inflammatory associated genes (Reimer et al., 2011). Thus, providing some evidence to suggest that the endothelium may be one of the earliest responders to hypoxia following BCAS surgery. In future studies it would be important to investigate endothelial related changes to determine if signalling from endothelial cells to microglial could be the first mechanism triggering harmful microglial proliferation following BCAS.

Interestingly, GW2580 treatment here was found to preserve spatial learning but not memory following BCAS. A limitation of the present study is the lack of mechanistic insight as to why memory impairments could not be rescued. The hippocampus is a region heavily implicated in the formation of spatial memory (Nishio et al., 2010; Sharma et al., 2010). Here, despite no memory improvement, increased microglial proliferation within the CA1 region following BCAS was found to be successfully blocked through GW2580 treatment. In future experiments it would be important to assess hippocampal neuronal apoptosis, through caspase-3 immunohistochemistry, to help determine if such changes are underpinning memory deficits, even in the absence of microglial proliferation. Additionally, GW2580 treatment may not fully repair the frontal-subcortical circuitry damage following BCAS, thus restoring spatial learning but not memory. Future electrophysiological experiments testing hippocampal communication with other brain regions, such as the prefrontal cortex, would help delineate the underlying mechanisms impairing spatial memory following BCAS.

The observation of impaired spatial memory in absence of microglial proliferation indicates that non-microglial related damage could still be occurring. Increased reactive oxygen species production could be one mechanism by which spatial memory is impaired in the absence of

microglial expansion (H. A. Kim et al., 2012). Additional experiments targeting NADPH oxidase could help elucidate such mechanisms. For example, a combination therapy approach with GW2580 and the NADPH oxidase inhibitor apocynin could be used to see if both spatial learning and memory impairments could be rescued following BCAS (Y. Y. Qin et al., 2017). Alternatively, for a more targeted approach, NADPH oxidases knockout transgenic mice could be used to study the implications of Nox signalling on spatial memory impairments following BCAS (Buvelot, Jaquet, & Krause, 2019).

In the current study microglial proliferation, in response to BCAS, was found to be key to the development of white matter damage and cognitive impairment. What remains unclear, however, is the mechanisms by which microglia can cause such damage. In an attempt to uncover such mechanisms, a bulk transcriptome study of isolated white matter has been undertaken since the completion of this study. A key outcome of the RNA sequencing analysis was the identification of microglial, as well as endothelial enriched gene sets, which were found to be significantly increased following BCAS and subsequently modified following GW2580 treatment. Endothelial dysfunction, through both clinical and pre-clinical studies, has been identified as a key early initiator of cerebrovascular disease (Iadecola et al., 2019; Rajani & Williams, 2017; F. Wang et al., 2018; J. M. Wardlaw et al., 2019). The role of endothelial dysfunction following BCAS, was investigated within chapter 5, through *in vivo* intravital imaging.

In the present study we have demonstrated that the blockade of microglial proliferation is able to attenuate damage and cognitive impairment following BCAS. The view, however, that all microglia are bad in the context of BCAS and removing them is advantageous is very simplistic. The recent advancement of single-cell RNA sequencing methods has allowed microglia to be studied on an individual basis, across the mouse lifespan, as well as in the context of disease. Such studies have demonstrated a very complex picture, demonstrating that microglia are a very heterogenous population in which gene expression can vary even in the same brain region (Hammond et al., 2019; Stratoulias, Venero, Tremblay, & Joseph, 2019; Tan, Yuan, & Tian, 2020). Therefore, future studies will need to make use of such sequencing technologies to enable a complete picture of microglial changes, following BCAS with and without GW2580 treatment, to be determined.

3.5 Conclusion

In conclusion, the data presented within this chapter provides the first conclusive evidence that white matter microglial proliferation is fundamental to white matter damage following BCAS. Furthermore, specific blockade of microglial proliferation, through competitive inhibition of CSF1R signalling, can restore white matter integrity and rescue impairments in spatial learning following BCAS.

Chapter 4

Investigating structural and functional microglial changes in response to BCAS with the use of intravital imaging

4.1 Introduction

The studies in the previous chapter, demonstrated that microglial proliferation following BCAS is associated with both white matter damage and cognitive impairments. These studies, however, were limited by the fact that all investigations were conducted *post mortem*. Thus, preventing any inference on microglial phenotype that can be determined through alterations in both shape and dynamic process movement. The next aim, therefore, was to further characterise microglial responses to BCAS through, *in vivo*, structural, and functional evaluations.

Under normal homeostatic conditions, microglia display a characteristic morphology with a small spherical cell soma surrounded by highly ramified flopodia-like processes. In homeostatic 'resting' states, microglial processes are highly motile, extending and retracting continuously in order to sample their local environment and contact neighbouring cells (Nimmerjahn et al., 2005). In response to injury or infection however, homeostatic microglia undergo dynamic, multi-step, conformational changes culminating in the retraction of processes leading to a more amoeboid appearance, characteristic of microglial activation (M. A.-O. Kluge et al., 2017; Stence et al., 2001).

The development of intravital imaging approaches, alongside genetic labelling tools, has led to a greater understanding of dynamic microglial behaviours in the context of both homeostasis and disease (Wieghofer, Knobeloch Kp Fau - Prinz, & Prinz, 2015). Through the replacement of the Cx_3Cr_1 gene with a green florescent protein (eGFP), transgenic reporter mice were developed allowing the visualisation of microglia as well as monocytes, subsets of natural killer cells and dendritic cells (Jung, Aliberti J Fau - Graemmel, et al., 2000). Heterozygous $Cx_3Cr_1^{eGFP/+}$ mice have been extensively used in the field of neuroinflammation, due to their ability to accurately target microglia with a high degree of specificity (Nimmerjahn et al., 2005; Wieghofer et al., 2015). Previous studies employing genetic labelling and intravital imaging, demonstrated that the quantification of microglial morphological

parameters, such as soma size and sphericity, can accurately distinguish between resting and activated microglial populations (B. M. Davis et al., 2017; Kozlowski & Weimer, 2012). Such morphological changes were also observed alongside increased expression of markers of microglial activation such as CD68 and MHC11 (Kettenmann et al., 2011; Lartey et al., 2014). Microglial process movements have also been shown to be highly dynamic and accurately reflect microglial responses to damage and disease. As part of normal homeostatic functioning microglia extend and retract processes continuously to sample their local environment. These process behaviours can change under disease conditions, indicating altered microglial functions, even in the absence of gross structural changes (Kluge et al., 2018; M. G. A.-O. h. o. o. Kluge et al., 2017). To date, such detailed phenotypical microglial evaluations have not been carried out within the context of BCAS.

It is being increasingly recognised that dementia syndromes rarely exist in isolation, with reports suggesting that neurovascular pathology is present in up to 80% of sporadic late-onset AD patients (Toledo et al., 2013). It is therefore, becoming ever more apparent that pathological causes of dementia need to be assessed in combination to fully uncover the common mechanisms leading to neuroinflammation, neuro-glial-vascular unit dysfunction and ultimately cognitive impairment.

App23 mice have been engineered to overexpress human APP containing the Swedish (KM670/671NL) mutation driven by a Thy1 promoter. App23 mice progressively develop both meningeal and parenchymal amyloid deposits and display pathological, cognitive, and behavioural alterations common to Alzheimer's disease (AD) (Shang J Fau - Yamashita et al., 2016; Sturchler-Pierrat et al., 1997). Previous studies using co-morbid constructs of App23 and BCAS show exacerbated neuronal loss, BBB leakage, and demonstrate exacerbated AD pathology including neurovascular unit disruption, loss of axon-glial integrity, and cerebrovascular remodelling (Shang J Fau - Yamashita et al., 2016; Zhai Y Fau - Yamashita, Yamashita T Fau - Nakano, Nakano Y Fau - Sun, Sun Z Fau - Morihara, et al., 2016). The effect of amyloidosis and BCAS on the microglial population, however, has not been extensively analysed.

In the present study, $Cx_3Cr_1^{eGFP/+}$ microglial reporter mice were used alongside multiphoton microscopy to allow structural and functional microglial changes to be evaluated following BCAS. Furthermore, microglial responses will be assessed in conjunction with neurovascular and cognitive functional evaluations. Additionally, the effect of amyloidosis will be assessed, alongside BCAS, to determine if microglial responses as well as neurovascular and cognitive functional deficits are exacerbated in the context of co-morbidities.

4.1.1 Hypothesis

This study set out to test the hypothesis that phenotypic alterations in microglia occur in response to BCAS leading to neuro-glial-vascular unit dysfunction and cognitive impairment, which is further exacerbated in the presence of increased amyloid.

4.1.2 Aims

Using a model of BCAS, within $Cx_3Cr_1^{eGFP/+}$ microglial reporter mice, the studies aimed to:

1. Assess the temporal profile of cortical CBF changes following BCAS
2. Investigate microglial structural alterations in response to BCAS, 1-week following surgery
3. To assess microglial process dynamics in response to BCAS, 1-week following surgery
4. To investigate microglial expansion within white and grey matter regions in response to BCAS, 3-months following surgery
5. To investigate neurovascular coupling mechanisms in response to BCAS, 3-months following surgery
6. To investigate spatial learning and memory in response to BCAS, 3-months following surgery
7. To determine the effect of amyloidosis and BCAS on microglial responses, neurovascular coupling mechanisms, and spatial learning and memory 3-months following surgery.

4.2 Materials and Methods

4.2.1 Experimental mice

$Cx_3Cr_1^{eGFP/eGFP}$ mice were acquired as a generous gift from Professor Jeffrey Pollard and cross-bred with App23 heterozygous mice to generate $Cx_3Cr_1^{eGFP/+}App23^{+/-}$ and $Cx_3Cr_1^{eGFP/+}App23^{-/-}$ mice. All mice were assigned to surgical groups at random. Mice, 7-9 months old, were studied at a short-term 1-week timepoint as well as a chronic 3-month timepoint following surgery. A total of 19 mice began the 1-week study and 36 the 3-month study. Details of group numbers and exclusions can be found in the relevant methods sections below, alternatively an overall summary can be found within Table 4.1.

Table 4.1 Number of mice within each experimental group with details of exclusions

Short-term 1-week study	$Cx_3Cr_1^{eGFP/+}$ Sham	$Cx_3Cr_1^{eGFP/+}$ BCAS	$Cx_3Cr_1^{eGFP/+}$ App23 Sham	$Cx_3Cr_1^{eGFP/+}$ App23 BCAS
Sham/BCAS surgery	*5*	*6*	*4*	*4*
Exclusion criteria:				
<25% CBF reduction following BCAS surgery	*0*	*1*	*0*	*0*
Final groups	*5*	*5*	*4*	*4*
Chronic 3-month study	$Cx_3Cr_1^{eGFP/+}$ Sham	$Cx_3Cr_1^{eGFP/+}$ BCAS	$Cx_3Cr_1^{eGFP/+}$ App23 Sham	$Cx_3Cr_1^{eGFP/+}$ App23 BCAS
Sham/BCAS surgery	*9*	*8*	*9*	*10*
Exclusion criteria:				
Poor recovery following surgery	*0*	*0*	*1*	*1*
<25% CBF reduction following BCAS surgery	*0*	*1*	*0*	*0*
Finals groups for NVC assessment	*9*	*7*	*8*	*9*
Barnes maze exclusion criteria:				
Lack of maze exploration	*3*	*2*	*1*	*2*
Final groups for Barnes maze assessment	*6*	*5*	*7*	*7*
Immunohistochemical analysis exclusion criteria:				
Poor recovery following NVC	*0*	*0*	*0*	*1*
Final groups for immunohistochemical analysis	*9*	*7*	*8*	*8*

4.2.2 Bilateral common carotid artery stenosis

Bilateral common carotid artery stenosis (BCAS) surgery was performed according the method previously described (Section 2.2). For the present study, a milder form of BCAS was achieved through the application of 0.18mm diameter micro-coils to both the left and right common carotid arteries. As a control for all experiments sham mice underwent an identical procedure with the only exception being the application of micro-coils. For the 1-week multiphoton imaging study all mice recovered well following surgery. For the 3-month study 1 $Cx_3Cr_1^{eGFP/+}$App23 sham and 1 $Cx_3Cr_1^{eGFP/+}$App23 BCAS mouse recovered poorly following surgery and therefore were humanely culled and excluded from the study (Table 4.1).

4.2.3 Craniotomy and cranial window surgery in preparation for multiphoton microscopy

Cranial window surgery was carried out 4-weeks prior to multiphoton microscopy according to the method outlined within Section 2.4. Strict exclusion criteria were applied to minimise any effect of cranial window implantation on the neuro-inflammatory response, details found within Section 2.4. No mice were excluded from the study based on these exclusion criteria.

4.2.4 Laser speckle imaging assessment of resting cortical blood flow

Laser speckle imaging was used to assess cortical CBF within both sham and BCAS mice as previously described (Section 2.3). For the multiphoton imaging, 1-week, study CBF was assessed at baseline and 24-hours following surgery. For the 3-month study blood flow was assessed at baseline, 24-hours, 1-month, and 3-months following surgery. Due to the milder nature of BCAS surgery, blood flow reductions needed to exceed 25% for the mouse to be included within the study. According to this criteria, 1 $Cx_3Cr_1^{eGFP/+}$ BCAS mouse from the 1-week study and 1 $Cx_3Cr_1^{eGFP/+}$ BCAS mouse from the 3-month study were excluded (Table 4.1).

4.2.5 Laser speckle assessment of neurovascular coupling responses

Neurovascular coupling responses were assessed 3-months following sham/BCAS surgery. A detailed method for neurovascular coupling measurements can be found within Section 2.3.2. Stimulation recordings were excluded if baseline blood flow fluctuated during the

assessment window or if operator error led to non-physiological responses. According to these criteria 1 $Cx_3Cr_1^{eGFP/+}$ sham and 1 $Cx_3Cr_1^{eGFP/+}$App23 BCAS stimulations were excluded resulting in an average value of 3 measurements for these mice.

4.2.6 Multiphoton microscopy

Multiphoton microscopy was carried out using the set-up and parameters detailed within Section 2.5. Approximately 30-minutes prior to imaging, mice receive a tail vein injection of 100µl Rhodamine B (15mg/ml) (Table 2.2), to allow the vasculature to be readily visualised. Microglial were readily visible due to the genetic eGFP tag attached to the Cx_3Cr_1 receptor.

4.2.7 *In vivo* assessment of microglial structure

Detailed methods for microglial structural evaluations can be found within Section 2.5.1. In brief, 3 z-stacks were acquired within the cerebral cortex of each mouse. Z-stacks were then processed using the IMARIS software to generate 'surface casts' of each microglial cell (Figure 2.4). Exclusion parameters were implemented so that a microglial cell was only analysed if its full form was visible within the field of view. Surface casts were generated of each cell soma within the field of view and used to generate values for area, volume, and sphericity.

4.2.8 *In vivo* assessment of microglial process dynamics

To capture dynamic microglial process movements in real time, *in* vivo, repeated z-stacks were gathered consecutively over a 15-minute period via multiphoton microscopy, according to the method detailed within Section 2.5.2. Microglial process motility was analysed by calculating the pixel differences between consecutive maximum intensity images. To calculate microglial process coverage (surveillance measurement), the percentage area of microglial pixels within maximum intensity images was calculated. The coverage value represents the surveillance ratio which is defined as the ratio of microglia-occupied pixels as a proportion of the total pixels within the field of view.

4.2.9 Barnes maze behavioural testing

The Barnes maze is a test of visuo-spatial learning and memory and was carried out as previously described within Section 2.6. The training period commenced 10-weeks and ended 12-weeks following sham/BCAS surgery. An exclusion criterion based on maze exploration, previously described (Section 2.6.8), was applied highlighting 3 $Cx_3Cr_1^{eGFP/+}$ sham, 2

$Cx_3Cr_1^{eGFP/+}$ BCAS, 1 $Cx_3Cr_1^{eGFP/+}$App23 sham and 2 $Cx_3Cr_1^{eGFP/+}$App23 BCAS mice for exclusion (Table 4.1).

4.2.10 Tissue collection and processing

For the behavioural cohort, animals were sacrificed 3-months post sham/BCAS surgery via transcardial perfusion, and the brains extracted, and flash frozen in liquid nitrogen as previously described within Section 2.8.2. The tissue was then cut into 12μm coronal sections using a cryostat, as previously described (Section 2.8.5). For flow cytometry experiments, mice were transcardially perfused with ice cold PBS containing 0.1% heparin under deep isoflurane anaesthesia (Section 2.8.2). The brain was then swiftly extracted and dissected into 2 hemibrains.

4.2.11 Flow cytometry and cell sorting

Isolated hemibrains were processed into a single cell suspension as detailed within Section 2.9. Cells were then immunostained with primary antibodies directed against CD11b, CD45, Ly6C, and Ly6G at 1:200 (Ly6C) or 1:500 dilution for 30-minutes on ice. Cells were washed then analysed and sorted using a FACS Aria II (BD Biosciences). Cell sorting was performed by staff in the QMRI Flow Cytometry and Cell Sorting Facility (University of Edinburgh). Sorted cells were centrifuged at 6000 RPM for 5-minutes at 4˚C and then stored at -80^0C.

4.2.12 RNA extraction and cDNA synthesis

Sorted cells in RLT Buffer were defrosted and vortexed for 1-minute to homogenise cells and RNA was extracted using the AllPrep DNA/RNA/miRNA Universal Kit (Qiagen) according to the manufacturer's instructions (Section 2.10). Sorted cells were processed immediately post-sort and RNA was extracted using the High Pure RNA Isolation Kit (Roche) according to the manufacturer's instructions. RNA quantities were determined by Agilent 4200 Tapestation (Agilent Technologies). cDNA was synthesised from 15 ng RNA using the Superscript IV Reverse Transcriptase (Life Technologies), according to the manufacturer's instructions and used undiluted for qPCR reactions. cDNA samples were stored at -20ºC until use.

4.2.13 Quantitative (q)-PCR

cDNA libraries were analysed by qPCR using the DyNAmo ColorFlash SYBR Green kit (Thermo Scientific) according to the manufacturer's instructions (Section 2.11). Briefly, the

cDNA template was mixed with DyNAmo ColourFlash SYBR Green master mix (Fisher Scientific), nuclease-free H_2O and the following custom designed gene-specific primers (200 nM final concentration; Sigma Aldrich): *18s* (forward: 5'-cccagtaagtgcgggtcat-'3, reverse: 5'-ccgagggcctcactaaacc-3') and *Cx_3Cr_1* (forward: 5'-gccaactccatgaacaaccg-3', reverse: 5'-ttgacttccgagttgcggag-3'). qPCR cycles were performed on a Bio-Rad CFX96 thermocycler (Bio-Rad Laboratories) as described previously within Section 2.11. Cycle threshold (Ct) values of target genes were normalized to *18S*, with data expressed as fold change relative to control group (wild-type) using the 2^ (−ΔΔCt) method.

4.2.14 Image acquisition and analysis

For detailed information on multiphoton image capture and analysis please refer to Sections 2.5, 2.5.1 and 2.5.2. To allow for $Cx_3Cr_1^{eGFP}$ positive cell number to be quantified, coronal 12 μ*m* sections were cover-slipped with vectashield containing DAPI (Section 2.12.4). Images for $Cx_3Cr_1^{eGFP}$/DAPI sections were acquired on an Axio ScanZ1 slide scanner (x20, Zeiss, Germany) as previously described within Section 2.13.1. Cell count analysis was completed using the ImageJ software (v1.46, NIH, Bethesda, MD, USA), with use of the cell counter plugin, as previously described within Section 2.13.2.

4.2.15 Statistical analysis

Statistical analysis was performed using SPSS (v22, IBM Corp.) and Prism (v8, GraphPad Software Inc, La Jolla, USA) software packages. Multiphoton cell counts, process motility and coverage, immunohistochemical cell counts, neurovascular coupling and Barnes maze learning profile comparisons were analysed using independent samples Mann Whitney U tests. Repeated measures two-way ANOVA's were used to assess group differences in CBF as well as the Barnes maze measures of escape latency, movement distance, and movement speed (training and reversal phases), with Bonferroni *post hoc* follow up analysis. Barnes maze training and reversal probe data were analysed using the Friedman test to determine differences in time spent within each quadrant. The Wilcoxon signed ranks *post hoc* test was then applied to determine target zone preference. Measures of microglial structure (soma area, volume, and sphericity) were analysed using nested t-tests. Cx_3Cr_1 receptor expression was analysed with the use of an independent samples t-test. All statistical analysis was completed within SPSS, except for microglial structural analysis, which were analysed using the Prism software. For parametric statistical tests, data is presented as mean ± standard error of the mean (SEM) and for nonparametric testing data is presented as median ± interquartile range (IQR) (specified in relevant figure legend). Statistical significance was determined at $p<0.05$.

4.2.16 Experimental contributions

The majority of experiments and analysis detailed within this chapter were conducted by myself. The studies, however, were also supported by Dr Juraj Koudelka, Dr Katie Askew, Dr Gaia Brezzo, and Professor Karen Horsburgh. I performed multiphoton imaging, laser speckle imaging, neurovascular coupling measurements, behavioural testing, tissue collection and processing, immunohistochemical staining and imaging as well as all the data analysis presented. Dr Juraj Koudelka performed cranial window surgery, operated the software for image capture during multiphoton imaging and assisted with tissue collection and processing. Dr Katie Askew completed flow cytometry and qPCR as well as assisting with laser speckle imaging, neurovascular coupling assessments, behavioural testing, and tissue collection and processing. Dr Gaia Brezzo assisted with neurovascular coupling assessments. Professor Karen Horsburgh carried out sham/BCAS surgery on all mice.

4.3 Results

4.3.1 BCAS induces a significant and sustained reduction in cerebral blood flow within $Cx_3Cr_1^{eGFP/+}$ mice

Having demonstrated previously that genetic diversity, within C57BL/6J mice, can confer resistance to BCAS surgery (Figure 2.2). The first aim of this study was to confirm that BCAS surgery can elicit significant and sustained reductions in CBF within $Cx_3Cr_1^{eGFP/+}$ mice. Laser speckle imaging was employed to assess CBF at baseline, 24-hours, 1-month, and 3-months following sham/BCAS surgery (Figure 4.1). BCAS surgery using 2x0.18mm micro-coils elicited a CBF reduction of ≈26% at 24-hours, which progressed to a reduction of ≈30% at 3-months (Figure 4.1A). Statistical analysis demonstrated a significant overall effect of time ($F_{(1.33,18.64)} = 10.83$, $p<0.01$), group ($F_{(1,14)} = 51.38$, $p<0.001$) as well as a significant time-group interaction ($F_{(1.33,18.64)} = 8.84$, $p<0.01$). Bonferroni *post hoc* analysis revealed a significant CBF reduction in BCAS mice when compared to shams, at 24-hours (sham: 111.1±2.39, BCAS: 73.5±5.07, $p<0.001$), 1-month (sham: 93.9±2.87, BCAS: 80.1±3.44, $p<0.01$) and 3-months (sham: 95.2±3.11, BCAS: 69.8±4.87, $p<0.01$) following surgery (Figure 4.1A).

Overall, these data demonstrate that BCAS surgery, within $Cx_3Cr_1^{eGFP/+}$ mice, leads to a significant and sustained reduction in CBF.

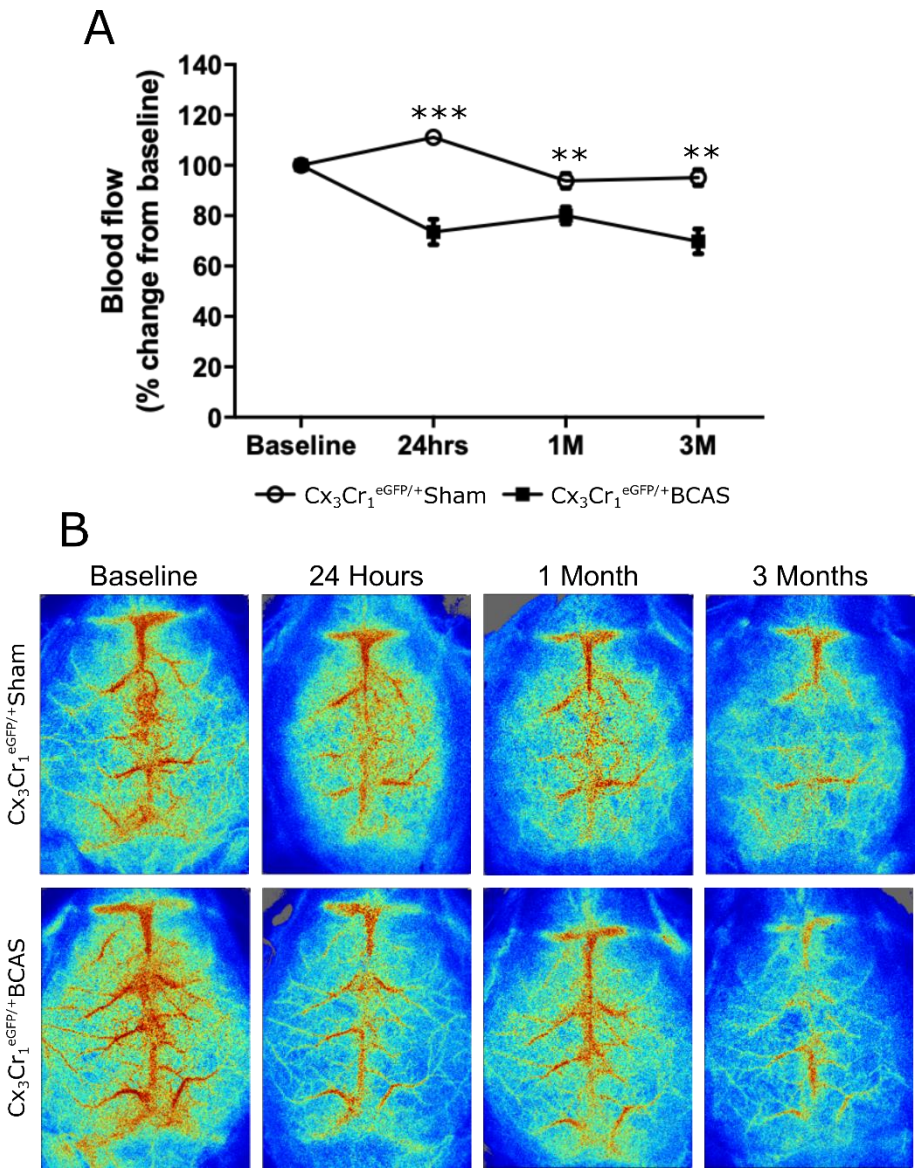

Figure 4.1 BCAS elicits a significant and sustained reduction in CBF within $Cx_3Cr_1^{eGFP/+}$ mice. **(A)** Laser speckle imaging shows a significant reduction in CBF following BCAS surgery, with an ≈26% reduction at 24-hours which was sustained leading to a reduction of ≈30% at 3-months. **(B)** Representative images of CBF recordings of sham/BCAS mice at baseline, 24-hours, 1-month, and 3-months following surgery. Blue represents the lowest blood flow with red representing high blood flow levels.

4.3.2 Microglial structure is unaltered following BCAS within $Cx_3Cr_1^{eGFP/+}$ mice

The next aim of this study was to determine if BCAS leads to microglial conformational changes indicative of microglial activation. $Cx_3Cr_1^{eGFP/+}$ mice alongside multiphoton

microscopy were employed to assess changes in microglial structure, *in vivo*, 1-week following BCAS (Figure 4.2). Multiple z-stacks were gathered from the cerebral cortex and reconstructed to capture the structure of individual microglial cells in 3D (Figure 4.2). Analysis of soma area as well as soma volume revealed no significant difference between sham (area: 32340μm^2±76, volume: 12586μm^3±407) or BCAS groups (area: 3568μm^2±106, volume: 13589μm^3±452.79) 1-week following surgery (p=0.27 and p=0.40 respectively) (Figure 4.2A/B). Microglial soma sphericity was also found to be unaltered within BCAS mice (0.78±0.01) in comparison to shams (0.80±0.01, p=0.50) (Figure 4.2C). To determine if microglial expansion could be detected, irrespective of structural changes, the total number of $Cx_3Cr_1^{+ve}$ cells present within each z-stack was quantified (Figure 4.2D). Statistical analysis revealed no significant difference between the number of $Cx_3Cr_1^{+ve}$ microglial cells within BCAS mice (10.15±1.77) when compared to shams (11.43±4.11, p=0.15) (Figure 4.2D).

Overall, these data show no evidence of microglial structural or density changes, within the cerebral cortex of $Cx_3Cr_1^{eGFP/+}$ mice, 1-week following BCAS.

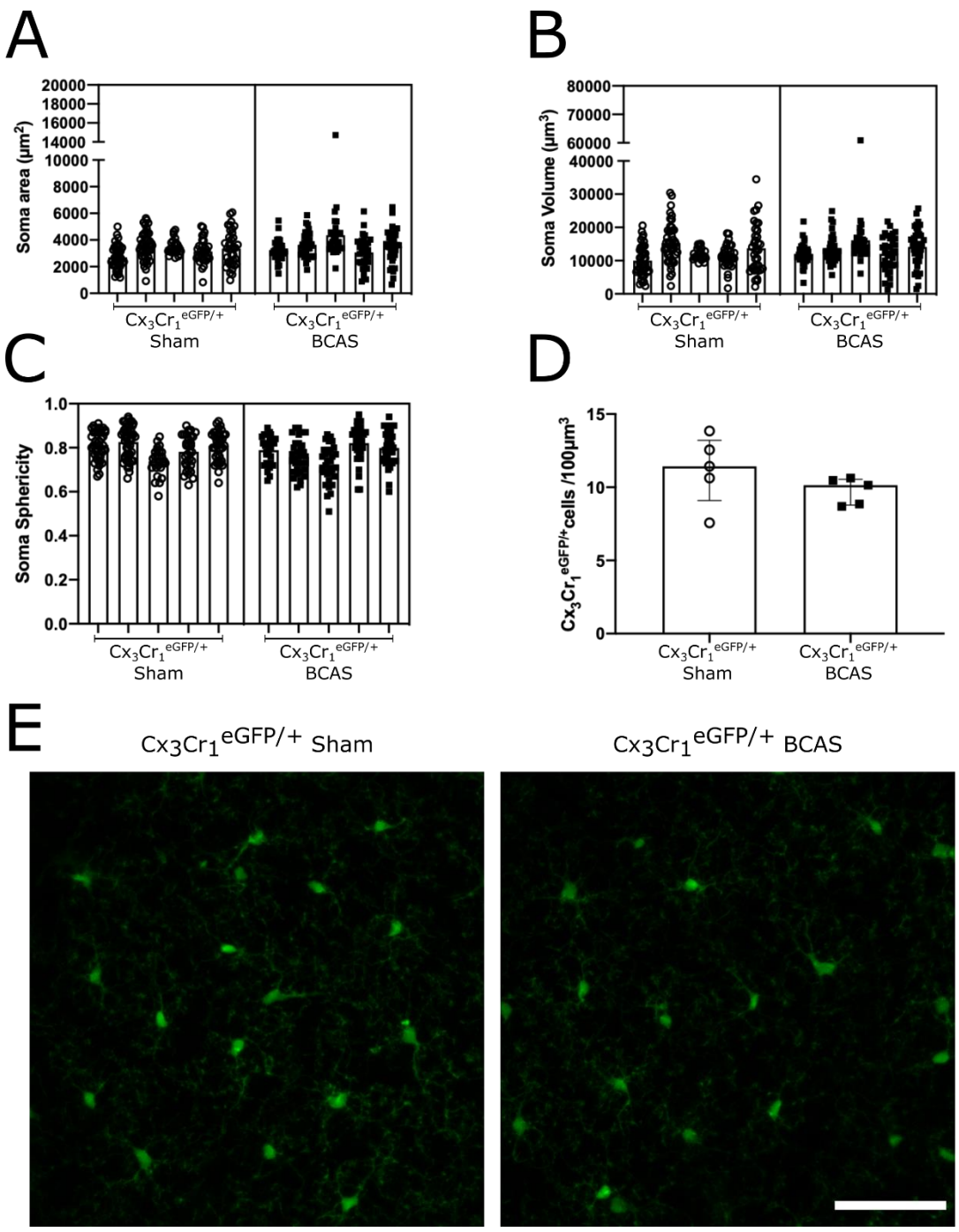

Figure 4.2 Microglial structure unaltered in $Cx_3Cr_1^{eGFP/+}$ mice following BCAS. Microglial structure was analysed using reconstructed z-stacks taken from the cerebral cortex via multiphoton microscopy. Soma area **(A)**, volume **(B)** and sphericity **(C)** were found to be unaltered following BCAS surgery. Data presented as Mean±SEM. **(D)** No significant difference between the total number of microglial cells within each cortical field of view was identified following BCAS. Data presented as Median±IQR. **(E)** Representative images of 2D

summated stacks generated from the 3D z-stacks used for structural analysis. Scale bar 50µm.

4.3.3 Microglial process dynamics are unaltered following BCAS within $Cx_3Cr_1^{eGFP/+}$ mice

Although no microglial structural changes were observed 1-week following BCAS, we wondered whether, more subtle, dynamic changes were occurring. Previous studies have demonstrated that microglial process movement can be altered in disease conditions, indicative of altered microglial functions, despite the absence of gross structural changes (Kluge et al., 2018; M. G. A.-O. h. o. o. Kluge et al., 2017). Microglial process motility was captured *in vivo* via repeated z-stacks taken from the cortex of $Cx_3Cr_1^{eGFP/+}$ mice with the use of multiphoton microscopy. Both extension and retraction of processes were assessed by calculating pixel differences between 2 consecutive z-stacks gathered ≈48 seconds apart. Pixel differences are calculated as a percentage change from 1 z-stack to the next. These values are then averaged across all z-stacks gathered to give a motility index value representing 15-minutes of recording (Figure 4.3A/C). Statistical analysis revealed no difference in process motility between sham (50.99%±21.09) and BCAS groups (55.52%±14.95) 1-week following surgery ($p=0.421$) (Figure 4.3A). As an additional measure of process motility, process coverage was calculated (Figure 4.3B/D). Process coverage refers to the percentage of the total imaging field that is contacted by microglial processes during a 15-minute recording. No significant difference in process coverage was identified between sham (68.83%±4.23) and BCAS (67.69%±4.46) mice, 1-week following surgery ($p=0.0.39$) (Figure 4.3B).

Overall, these data indicate that microglial process dynamics are unaltered within $Cx_3Cr_1^{eGFP/+}$ mice 1-week following BCAS.

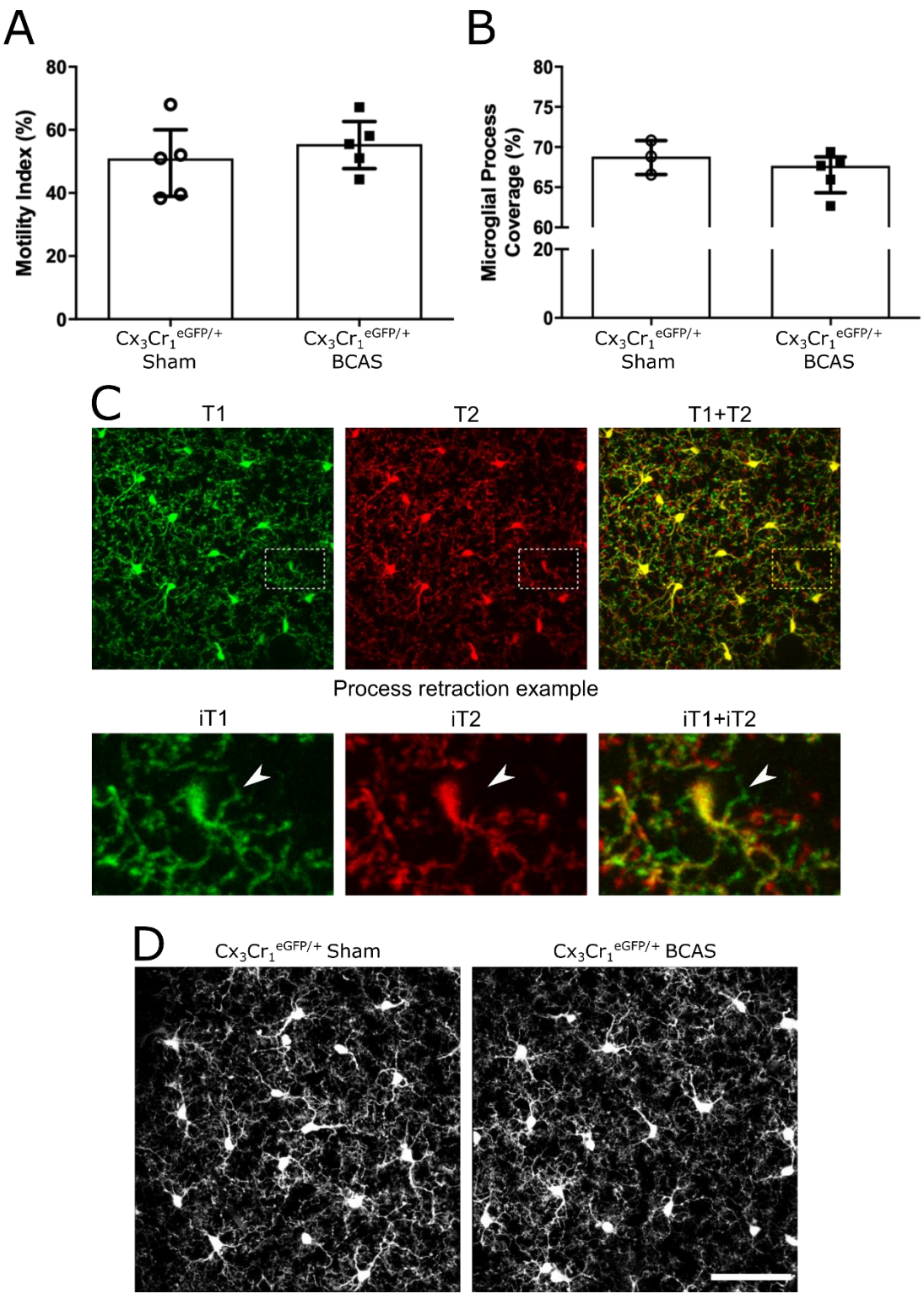

Figure 4.3 Microglial surveillance functions are unaltered within $Cx_3Cr_1^{eGFP/+}$ mice following BCAS. **(A)** Microglial motility measured over a consecutive 15-minute imaging period, was found to be unaltered following BCAS surgery. **(B)** Microglial process coverage was assessed over the same 15-minute imaging period and was also found to be unaltered 1-

week following BCAS surgery. Data presented as median±IQR. **(C)** Images to demonstrate dynamic microglial process movement. T1 (green) is a 2D summated version of the first 3D z-stack acquired. T2 (red) represents a z-stack gathered ≈48 seconds later, with T1+T2 showing a merge of the 2 images. The hashed square represents the inserts (i) that are shown below, with the white arrowhead highlighting an example of process retraction. **(D)** Representative images of a summated projection of all z-stacks gathered over the 15-minute imaging period to enable total process coverage to be calculated with $Cx_3Cr_1^{eGFP/+}$ sham and $Cx_3Cr_1^{eGFP/+}$ BCAS mice. Scale bar 50μm.

4.3.4 Microglial density is unaltered following BCAS within $Cx_3Cr_1^{eGFP/+}$ mice

The lack of any phenotypical changes within microglial cells was surprising given the clear microglial response following BCAS observed within chapter 3. Multiphoton microscopy, in our hands, is restricted to the upper layers of the cortex. Therefore, to determine if the lack of microglial response was due to a cortical resistance, more widespread microglial counts were carried out 3-months following BCAS surgery. $Cx_3Cr_1^{eGFP/+}DAPI^{+ve}$ cell counts were carried out, *post mortem*, within the corpus callosum and hippocampus CA1, due to the fact that these regions had previously shown a strong microglial response following BCAS (Figure 4.4). A larger region of interest was also used to quantify microglia within the cortex, to determine if the muted cortical response is limited to superficial regions (<200μm). Statistical analysis revealed no significant differences between microglial numbers within the cortex (p=1.00), corpus callosum (p=1.00) or hippocampus CA1 region (p=0.252) of BCAS mice (cortex: 13.31±3.26, corpus callosum: 12.47±2.94, CA1: 11.93±2.0) in comparison to shams (cortex: 12.62±2.12, corpus callosum: 12.02±2.67, CA1: 11.12±1.59) 3-months following surgery (Figure 4.4A/B/C). The percentage area of Cx_3Cr_1 florescence per cell was also calculated to give an indication of microglial structural changes 3-months following BCAS. The area of Cx_3Cr_1 expression per cell was not significantly different within the cortex (p=0.47), corpus callosum (p=0.30), or hippocampal CA1 region (p=0.61) of BCAS mice (cortex: 0.73±0.3, corpus callosum: 0.43±0.16, CA1: 0.86±0.52) when compared to shams (cortex: 0.85±0.09, corpus callosum: 0.49±0.12, CA1: 0.92±0.17) (Figure 4.4D/E/F).

Taken together these data show no evidence of microglial expansion, within $Cx_3Cr_1^{eGFP/+}$ mice, following 3-months of BCAS.

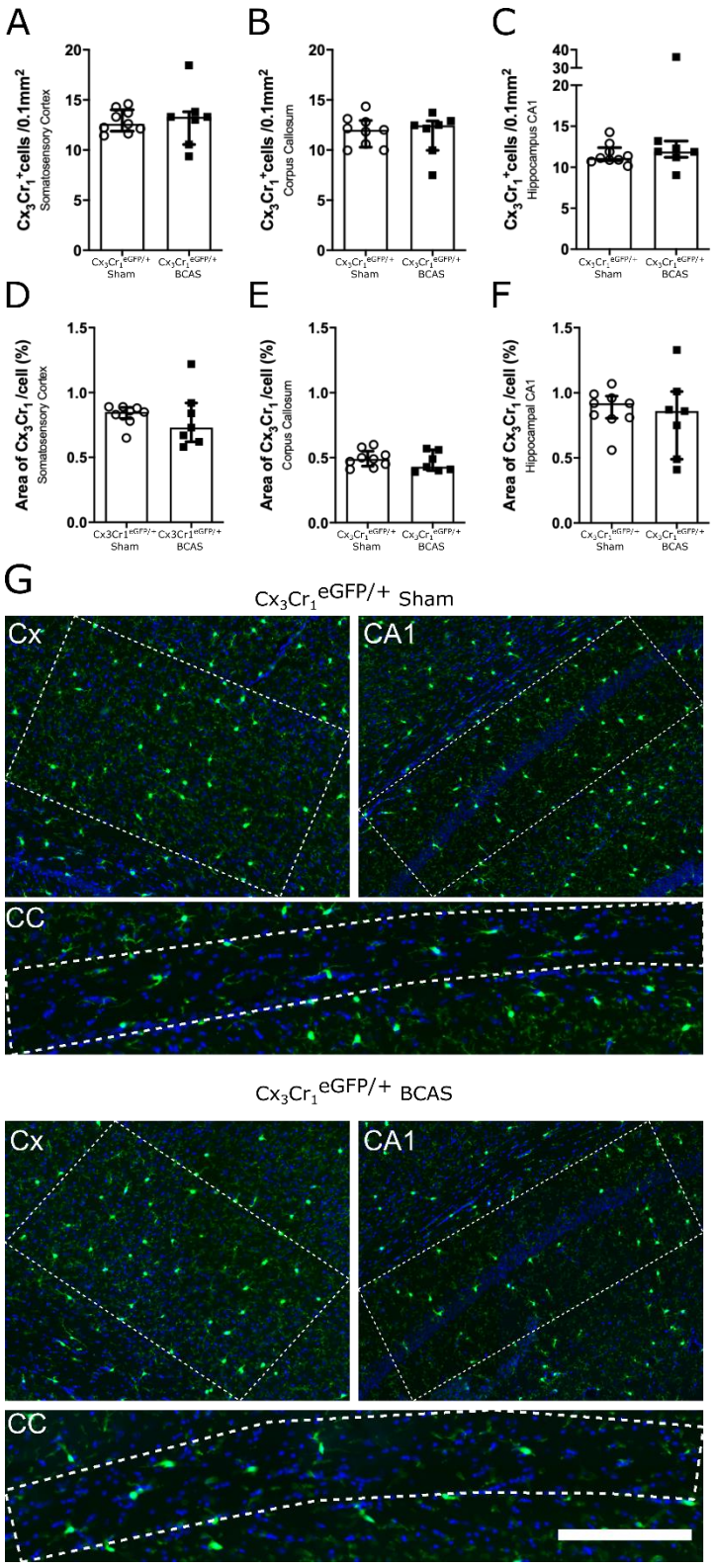

Figure 4.4 Microglial density is unaltered 3-months following BCAS in $Cx_3Cr_1^{eGFP/+}$ mice. $Cx_3Cr_1^{eGFP/+}$ cell counts per 0.1mm^2 were found to be unaltered 3-months following BCAS surgery within the somatosensory cortex **(A)**, corpus callosum **(B)** and the hippocampal

CA1 region **(C)**. As an indication of altered microglial structure, the area of $Cx_3Cr_1^{eGFP/+}$ florescence per cell was calculated and found to be unaltered 3-months following BCAS within the somatosensory cortex **(D)**, corpus callosum **(E)**, and the hippocampal CA1 region **(F)**. Data presented as median±IQR. **(G)** Representative images of $Cx_3Cr_1^{eGFP/+}$/DAPI staining within $Cx_3Cr_1^{eGFP/+}$ sham and $Cx_3Cr_1^{eGFP/+}$ BCAS mice 3-months following surgery within the somatosensory cortex (Cx), corpus callosum (CC), and hippocampal CA1 region (CA1). Regions of interest for cell counts are represented by the dotted white lines. Scale bar 50µm.

4.3.5 Neurovascular coupling responses are unaltered following BCAS within $Cx_3Cr_1^{eGFP/+}$ mice

Vascular haemodynamic responses are crucial to help match blood flow to energy consumption within the brain. Previous studies have demonstrated a significant impairment in neurovascular coupling responses following BCAS (Duncombe, Kitamura, et al., 2017). The next aim therefore was to test neurovascular coupling responses within $Cx_3Cr_1^{eGFP/+}$ mice following 3-months of BCAS. Laser speckle imaging was used to detect blood flow changes within the barrel cortex following unilateral whisker stimulation (Figure 4.5). No significant difference in blood flow response to whisker stimulation was detected within BCAS mice (22.47±16.48) when compared to shams (18.06±14.49), 3-months following surgery ($p=0.606$) (Figure 4.5A).

Overall, these data indicate that neurovascular coupling responses are unaltered within $Cx_3Cr_1^{eGFP/+}$ mice following 3-months of BCAS.

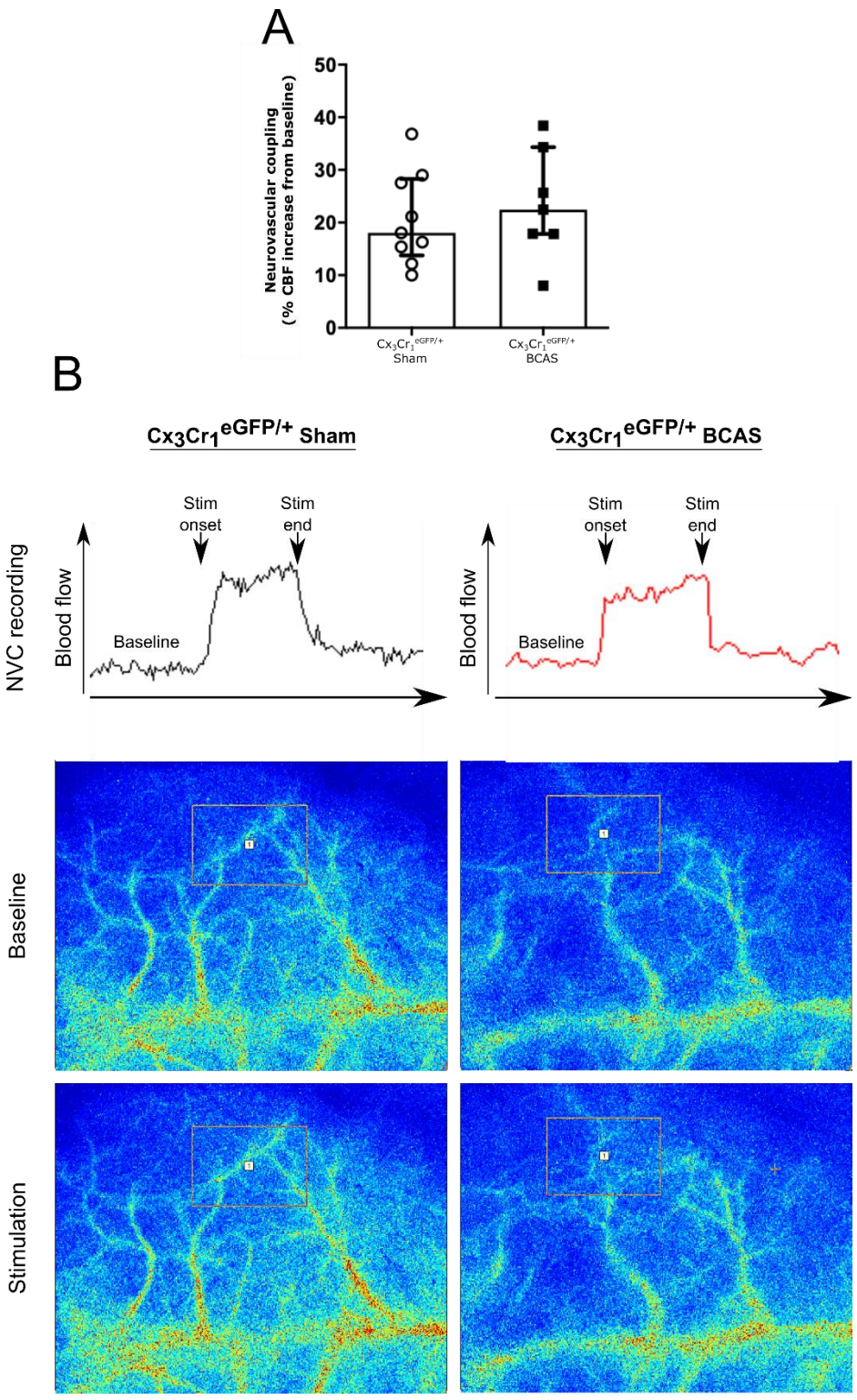

Figure 4.5 Neurovascular coupling responses are unaltered following BCAS within $Cx_3Cr_1^{eGFP/+}$ mice. **(A)** Blood flow responses within the barrel cortex following whisker stimulation were found to be unaltered following BCAS surgery. Data presented as median±IQR. **(B)** Representative images displaying blood flow recordings before, during, and

after whisker stimulation within both $Cx_3Cr_1^{eGFP/+}$ sham and $Cx_3Cr_1^{eGFP/+}$ BCAS mice. Accompanied by images of CBF, as measured by laser speckle, at baseline and during whisker stimulation. The box on each image indicates the region measured within the somatosensory cortex.

4.3.6 Spatial memory is impaired following BCAS within $Cx_3Cr_1^{eGFP/+}$ mice

The next aim of the study was to assess spatial learning and memory, within $Cx_3Cr_1^{eGFP/+}$ mice following 3-months of BCAS. As in chapter 3, the Barnes maze was used to test visuo-spatial learning and memory over a 2-week period. Spatial learning was assessed over 6 consecutive days, with the time taken for mice to locate and enter the escape chamber (escape latency) used as a measure of learning (Figure 4.6). Statistical analysis, over all 6 trainings days, reported an overall main effect of time ($F_{(5,45)} = 20.260$, $p<0.001$) indicating learning across training days. However, no effect of group ($p=0.187$) or significant interaction ($p=0.792$) were identified (Figure 4.6A). As an additional measure of spatial learning movement distance per trial was compared, once again an overall main effect of time was identified ($F_{(5,45)} = 9.962$, $p<0.001$) with no significant group differences ($p=0.472$) or interactions ($p=0.777$) (Figure 4.6B). Thus, indicating that spatial learning was unaffected following BCAS within $Cx_3Cr_1^{eGFP/+}$ mice. To ensure that movement speed was not influencing results, average speed per trial was assessed and compared between groups. An overall main effect of time was observed ($F_{(5,45)} = 7.811$, $p<0.001$) with no main effect of group ($p=0.104$) or interaction ($p=0.284$), indicating that movement speed was comparable between groups and therefore had no impact on learning (Figure 4.6C).

Following the spatial learning task, a reference memory probe trial was conducted, in which the escape chamber was removed, and the percentage of time spent within the quadrant previously home to the escape chamber was measured (Figure 4.6D). The probe trial was conducted 72-hours following the last training day to allow longer-term spatial memory to be assessed. Statistical analysis revealed no significant difference in the time spent within the target zone of $Cx_3Cr_1^{eGFP/+}$ sham (69.17%±25) when compared to BCAS mice (95%±56.7) ($U = 15$, $p>0.05$). To confirm that target quadrant times did indeed reflect a preference for that quadrant, time spent within all 4 quadrants were compared. Within $Cx_3Cr_1^{eGFP/+}$ sham mice, a significant difference between time spent within each quadrant was identified ($X^2_{(3)} = 11.945$, $p<0.01$), with *post hoc* analysis revealing a significant increase in time spent within the target zone compared to all other zones (clockwise; $p<0.05$, opposite; $p<0.05$, counter-clockwise

p<0.05) (Figure 4.6D). Within $Cx_3Cr_1^{eGFP/+}$ BCAS mice, however, no significant difference between time spent within each quadrant was reported (p=0.224) indicating no significant preference for the target zone (Figure 4.6D).

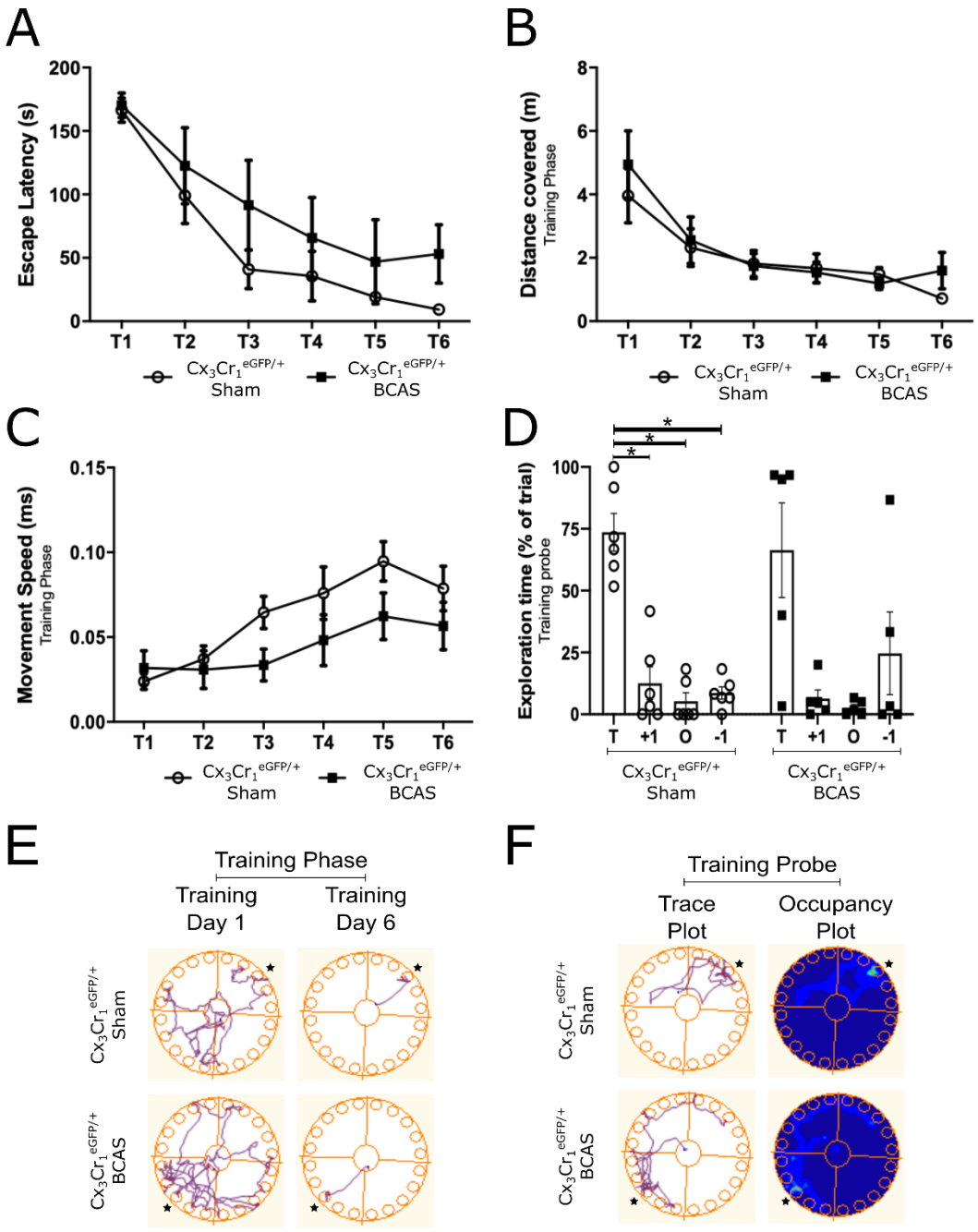

Figure 4.6 Spatial memory, but not learning, is impaired following BCAS within $Cx_3Cr_1^{eGFP/+}$ mice. **(A)** An overall effect of time demonstrates learning within both groups. Escape latency was found to be comparable across the 6 training days, indicating no spatial

learning impairment following BCAS. **(B)** Movement distance throughout each trial revealed a similar pattern to escape latency, with an overall effect of time and no group differences. **(C)** Although movement speed was found to be significantly affected by time, with no group differences identified. Data presented as mean±SEM. **(D)** Sham mice demonstrated a preference for the target quadrant indicating an intact memory of the target hole location. BCAS mice showed no preference for any quadrant. Data presented as median±IQR. *p<0.05. **(E)** Representative movement traces during day 1 and 6 of the training period taken from $Cx_3Cr_1^{eGFP/+}$ sham and $Cx_3Cr_1^{eGFP/+}$ BCAS groups. Stars indicate target hole. **(F)** Trace and occupancy plots gathered during probe trails of $Cx_3Cr_1^{eGFP/+}$ sham and $Cx_3Cr_1^{eGFP/+}$ BCAS mice. Stars indicate target hole; brighter colours indicate increased time spent in that area (occupancy plot only).

To test cognitive flexibility, an additional reversal training segment was completed within the Barnes maze following the reference memory probe (Figure 4.7). The reversal training phase, completed over 3 consecutive days, required mice to learn that their escape chamber had been relocated, 180^0, to the other side of the maze. Across the 3 reversal training days an overall main effect of time was observed ($F_{(2,18)} = 33.737$, $p<0.001$) indicting learning within both groups (Figure 4.7A). No overall group effect was reported ($p=0.303$) as well as no significant interaction ($p=0.649$) indicating a comparable performance across both groups (Figure 4.7A). A similar pattern was also observed with movement distance, which was shown to be significantly reduced over time ($F_{(1.2,10.796)} = 22.910$, $p<0.001$), with no significant group differences ($p=0.233$) or interactions ($p=0.310$) (Figure 4.7B). Movement speed was also found to be effected overall by time ($F_{(1.28,11.49)} = 5.448$, $p<0.05$) with no significant group effects ($p=0.738$) or interactions identified ($p=0.678$) (Figure 4.7C). Thus, indicating that reversal learning was unaffected following chronic BCAS within $Cx_3Cr_1^{eGFP/+}$ mice.

To assess adaptive memory, a reversal memory probe was carried out 72-hours following the final reversal training day (Figure 4.7D). A comparison between time spent within the target quadrant revealed no significant difference between $Cx_3Cr_1^{eGFP/+}$ BCAS mice (36.67%±45) when compared to shams (48.33%±19.6) ($U = 14$, $p>0.05$). To confirm that target quadrant times did indeed reflect a preference for that quadrant, time spent within all 4 quadrants were compared (Figure 4.7D). Within $Cx_3Cr_1^{eGFP/+}$ sham mice a significant difference in the time spent within each of the 4 quadrants was identified ($X^2_{(3)} = 8.069$, $p<0.05$), with *post hoc* analysis demonstrating a preference for the target quadrant over all others (clockwise $p<0.05$, opposite $p<0.05$, counter-clockwise $p<0.05$) (Figure 4.7D). Likewise, $Cx_3Cr_1^{eGFP/+}$ BCAS showed a significant difference between the time spent within each quadrant ($X^2_{(3)} = 10.188$, $p<0.05$). However, *post hoc* analysis demonstrated a preference

for the target zone over the clockwise ($p<0.05$) and counter-clockwise ($p<0.05$) zones but not the opposite zone ($p=0.273$) (Figure 4.7D). Therefore, no clear preference for the target zone was identified indicating impaired reversal memory within $Cx_3Cr_1^{eGFP/+}$ BCAS following 3-months of BCAS.

In conclusion these data illustrate impairments in visuo-spatial memory, but not learning, within $Cx_3Cr_1^{eGFP/+}$ mice following chronic BCAS.

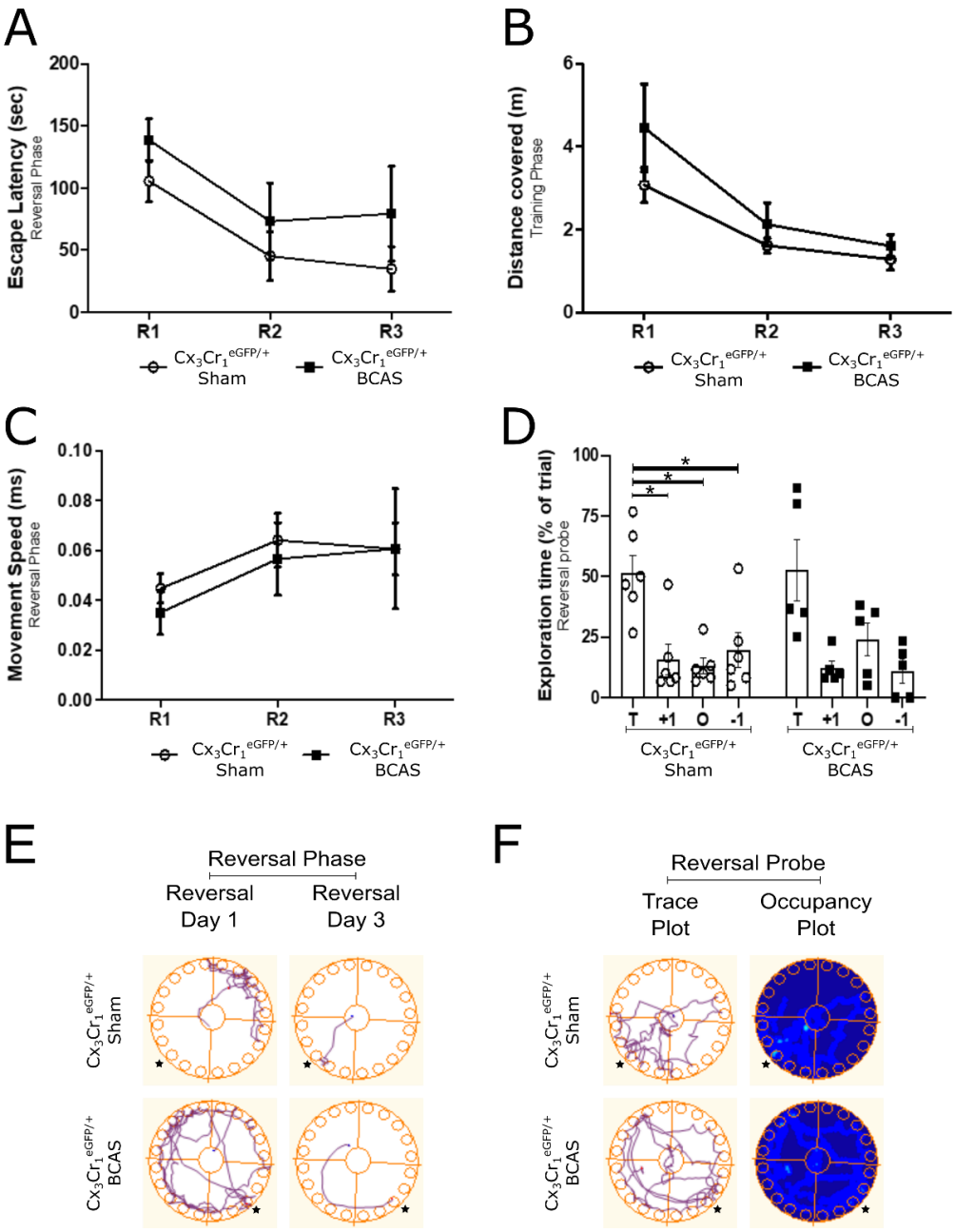

Figure 4.7 Reversal memory, but not learning, is impaired following BCAS within $Cx_3Cr_1^{eGFP/+}$ mice. **(A)** An overall effect of time demonstrates learning within both groups.

Escape latency was found to be comparable across the 3 reversal training days indicating no spatial learning impairment following BCAS. **(B)** Movement distance throughout each trial revealed a similar pattern to escape latency with an overall effect of time and no group differences. **(C)** Although movement speed was found to be significantly affected by time, no group differences were identified. Data presented as mean±SEM. **(D)** Sham mice demonstrated a preference for the target quadrant, indicating an intact memory of the target hole location. BCAS mice showed a target zone preference when compared to clockwise and counter-clockwise but not opposite quadrants, indicating no preference for the target zone and therefore impaired adaptive memory. Data presented as median±IQR. *p<0.05. **(E)** Representative movement traces during day 1 and 3 of the reversal training period taken from $Cx_3Cr_1^{eGFP/+}$ sham and $Cx_3Cr_1^{eGFP/+}$ BCAS groups. Stars indicate target hole. **(F)** Trace and occupancy plots gathered during probe trails of $Cx_3Cr_1^{eGFP/+}$ sham and $Cx_3Cr_1^{eGFP/+}$ BCAS mice. Stars indicate target hole; brighter colours indicate increased time spent in that area (occupancy plot only).

4.3.7 Microglial density remains unaltered following BCAS within $Cx_3Cr_1^{eGFP/+}$App23 mice

Previous studies using co-morbid constructs of App23 and BCAS show exacerbated cerebrovascular pathology associated with more severe functional and cognitive outcomes (Shang J Fau - Yamashita et al., 2016). The effect of a co-morbid App23 and BCAS construct on microglial populations, however, has not been extensively analysed. The next aim of the study, therefore, was to carry out a detailed phenotypical analysis of microglia within $Cx_3Cr_1^{eGFP/+}$App23 mice following sham/BCAS surgery.

The first aim was to evaluate microglial density within $Cx_3Cr_1^{eGFP/+}$App23 mice following 3-months of sham/BCAS surgery. $Cx_3Cr_1^{eGFP/+}DAPI^{+ve}$ cell counts were carried out within the cortex, corpus callosum, and hippocampal CA1 region (Figure 4.8). Statistical analysis revealed no significant differences between microglial numbers within the cortex (p=0.916), corpus callosum (p=0.713) or hippocampus CA1 region (p=0.598) of BCAS mice (cortex: 14.35±4.43, corpus callosum: 12.46±4.23, CA1: 12.29±1.78) in comparison to shams (cortex: 13.95±3.16, corpus callosum: 13.40±3.83, CA1: 12.00±2.64) (Figure 4.8A/B/C). Percentage area of Cx_3Cr_1 eGFP florescence per cell was also calculated as an indication of altered structure. The area of Cx_3Cr_1 expression per cell was found to be unaltered within the cortex (p=0.834), corpus callosum (p=0.916) and hippocampal CA1 region (p=0.189) of BCAS mice (cortex: 0.74±0.25, corpus callosum: 0.455±0.12, CA1: 0.81±0.105) when compared to shams (cortex: 0.72±0.095, corpus callosum: 0.43±0.085, CA1: 0.855±0.093) (Figure 4.8D/E/F).

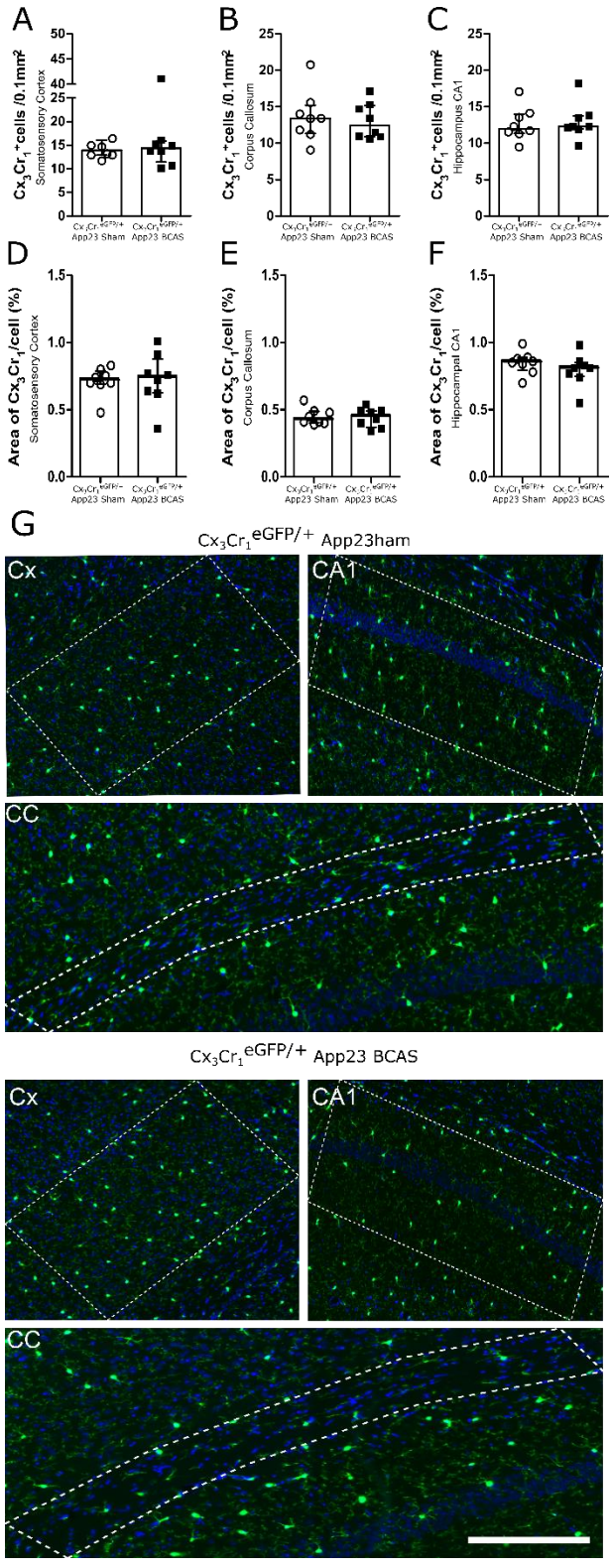

Figure 4.8 Microglial density is unaltered 3-months following BCAS within $Cx_3Cr_1^{eGFP/+}$App23 mice. $Cx_3Cr_1^{eGFP/+}$ cell counts per 0.1mm^2 within $Cx_3Cr_1^{eGFP/+}$App23 mice

were found to be unaltered 3-months following BCAS surgery within the somatosensory cortex **(A)**, corpus callosum **(B)**, and the hippocampal CA1 region **(C)**. As an indication of altered microglial structure, the area of $Cx_3Cr_1^{eGFP/+}$ florescence per cell was calculated and found to be unaltered 3-months following BCAS within the somatosensory cortex **(D)**, corpus callosum **(E)** and the hippocampal CA1 region **(F)**. Data presented as median±IQR. **(G)** Representative images of $Cx_3Cr_1^{eGFP/+}$DAPI staining within $Cx_3Cr_1^{eGFP/+}$App23 sham and BCAS mice, taken from the somatosensory cortex (Cx), hippocampal CA1 region (CA1), and corpus callosum (cc), 3-months following surgery. Scale bar 50µm.

To assess the effect on microglial populations of increased amyloid alone, microglial counts within $Cx_3Cr_1^{eGFP/+}$App23 sham mice were compared to $Cx_3Cr_1^{eGFP/+}$ shams (Figure 4.9). No significant alterations in microglial numbers were identified within the cortex ($p=0.114$), corpus callosum ($p=0.277$) or hippocampal CA1 region ($p=0.236$) of $Cx_3Cr_1^{eGFP/+}$App23 sham mice (cortex: 13.95±3.16, corpus callosum: 13.40±3.83, hippocampal CA1: 12.00±2.64) in comparison to $Cx_3Cr_1^{eGFP/+}$ shams (cortex: 12.62±2.12, corpus callosum: 12.02±2.67, hippocampal CA1: 11.12±1.59) (Figure 4.9A/B/C). Cx_3Cr_1 eGFP expression per cell quantification also revealed no significant differences within the corpus callosum ($p=0.114$) or hippocampal CA1 region ($p=0.541$) of $Cx_3Cr_1^{eGFP/+}$App23 sham mice (corpus callosum: 0.43±0.09, hippocampal CA1: 0.86±0.09) in comparison to $Cx_3Cr_1^{eGFP/+}$ shams (corpus callosum: 0.49±0.12, hippocampal CA1: 0.92±0.17) (Figure 4.9E/F).Within the cortex however, $Cx_3Cr_1^{eGFP/+}$App23 sham mice showed a significant reduction in $Cx_3Cr_1^{eGFP}$ expression per cell (0.72±0.10) when compared to $Cx_3Cr_1^{eGFP/+}$ shams (0.85±0.09, $p<0.05$), indicating a reduced in microglial size (Figure 4.9D).

Together these data show no evidence of microglial expansion within $Cx_3Cr_1^{eGFP/+}$ sham mice, even when subjected to both BCAS and increased amyloid.

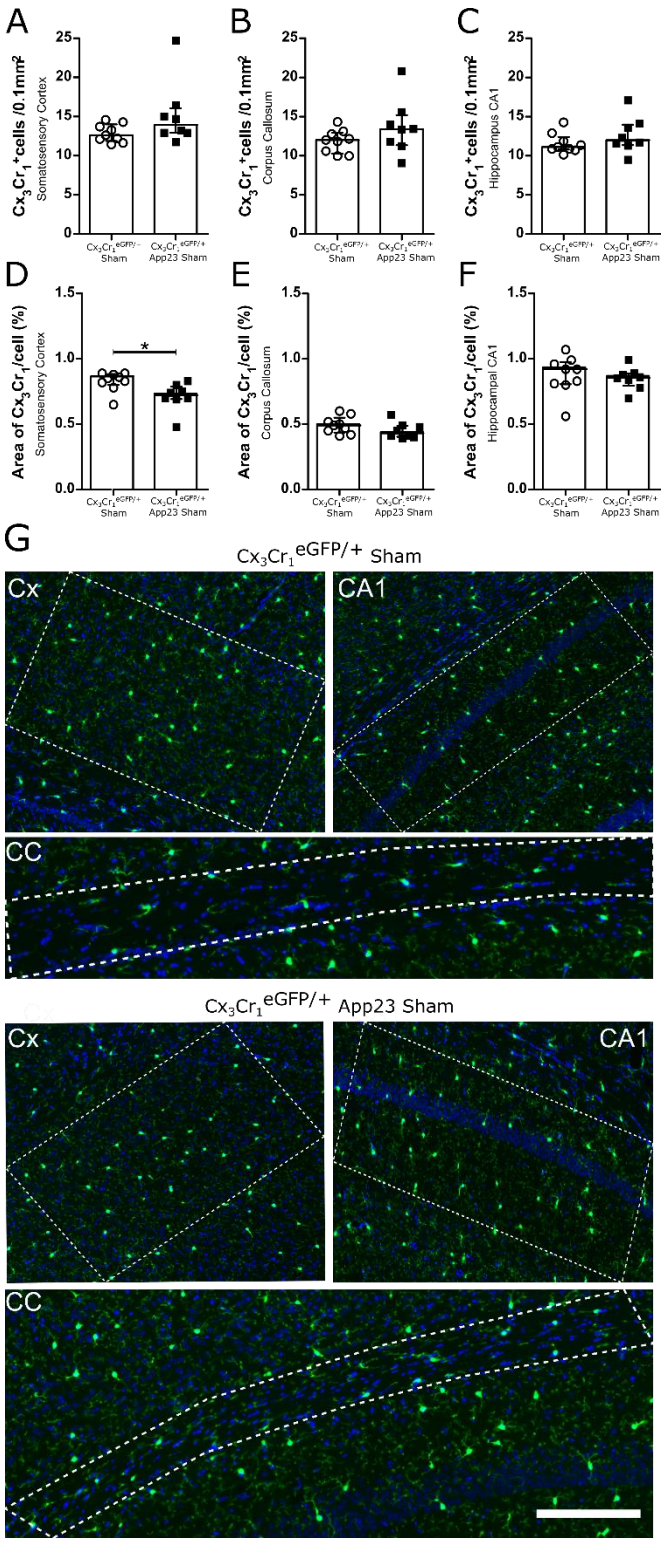

Figure 4.9 Microglial density is unaltered within $Cx_3Cr_1^{eGFP/+}$ mice in response to APP overexpression alone. $Cx_3Cr_1^{eGFP/+}$ cell counts per 0.1mm^2 within $Cx_3Cr_1^{eGFP/+}$App23 sham mice were found to be comparable to $Cx_3Cr_1^{eGFP/+}$ shams within the somatosensory cortex **(A)**, corpus callosum **(B)** and the hippocampal CA1 region **(C)**. As an indication of altered microglial

structure, the area of $Cx_3Cr_1^{eGFP/+}$ florescence per cell was calculated and found to be unaltered in $Cx_3Cr_1^{eGFP/+}$App23 sham when compared to $Cx_3Cr_1^{eGFP/+}$ sham mice within the corpus callosum **(E)** and the hippocampal CA1 region **(F)**. $Cx_3Cr_1^{eGFP/+}$ florescence per cell, however, was found to be reduced within $Cx_3Cr_1^{eGFP/+}$App23 sham mice when compared to $Cx_3Cr_1^{eGFP/+}$ shams **(D)**. Data presented as median±IQR. $^{*}p<0.05$. **(G)** Representative images of $Cx_3Cr_1^{eGFP/+}$DAPI staining within $Cx_3Cr_1^{eGFP/+}$App23 sham and $Cx_3Cr_1^{eGFP/+}$ sham mice, within the somatosensory cortex (Cx), hippocampal CA1 region (CA1), and corpus callosum (cc), 3-months following surgery. Scale bar 50µm.

4.3.8 Neurovascular coupling responses are impaired following BCAS within $Cx_3Cr_1^{eGFP/+}$App23 mice

Having previously demonstrated that BCAS had no impact on neurovascular coupling responses 3-months following surgery within $Cx_3Cr_1^{eGFP/+}$ mice, the next aim was to determine if deficits were apparent when BCAS was coupled to increased amyloid. Neurovascular coupling following whisker stimulation was measured within $Cx_3Cr_1^{eGFP/+ve}$App23 sham/BCAS mice 3-months following surgery (Figure 4.10A). Blood flow responses following stimulation were found to be significantly reduced within BCAS mice (10.69±6.99) in comparison to shams (22.77±16.9, $p<0.01$) (Figure 4.10A), indicating impaired neurovascular coupling responses. To determine if this impairment is mediated solely by increased amyloid, neurovascular coupling measurements from $Cx_3Cr_1^{eGFP/+}$App23 sham mice were compared to $Cx_3Cr_1^{eGFP/+}$ shams (Figure 4.10B). No significant difference between blood flow response to stimulation was identified ($p=0.277$) indicating comparable responses within $Cx_3Cr_1^{eGFP/+}$App23 sham (22.77±16.9) and $Cx_3Cr_1^{eGFP/+}$ sham mice (18.06±14.49) (Figure 4.10B).

Overall, these data illustrate that BCAS coupled to increased amyloid leads to neurovascular coupling deficits, which are not apparent when mice are subjected to BCAS or increased amyloid alone.

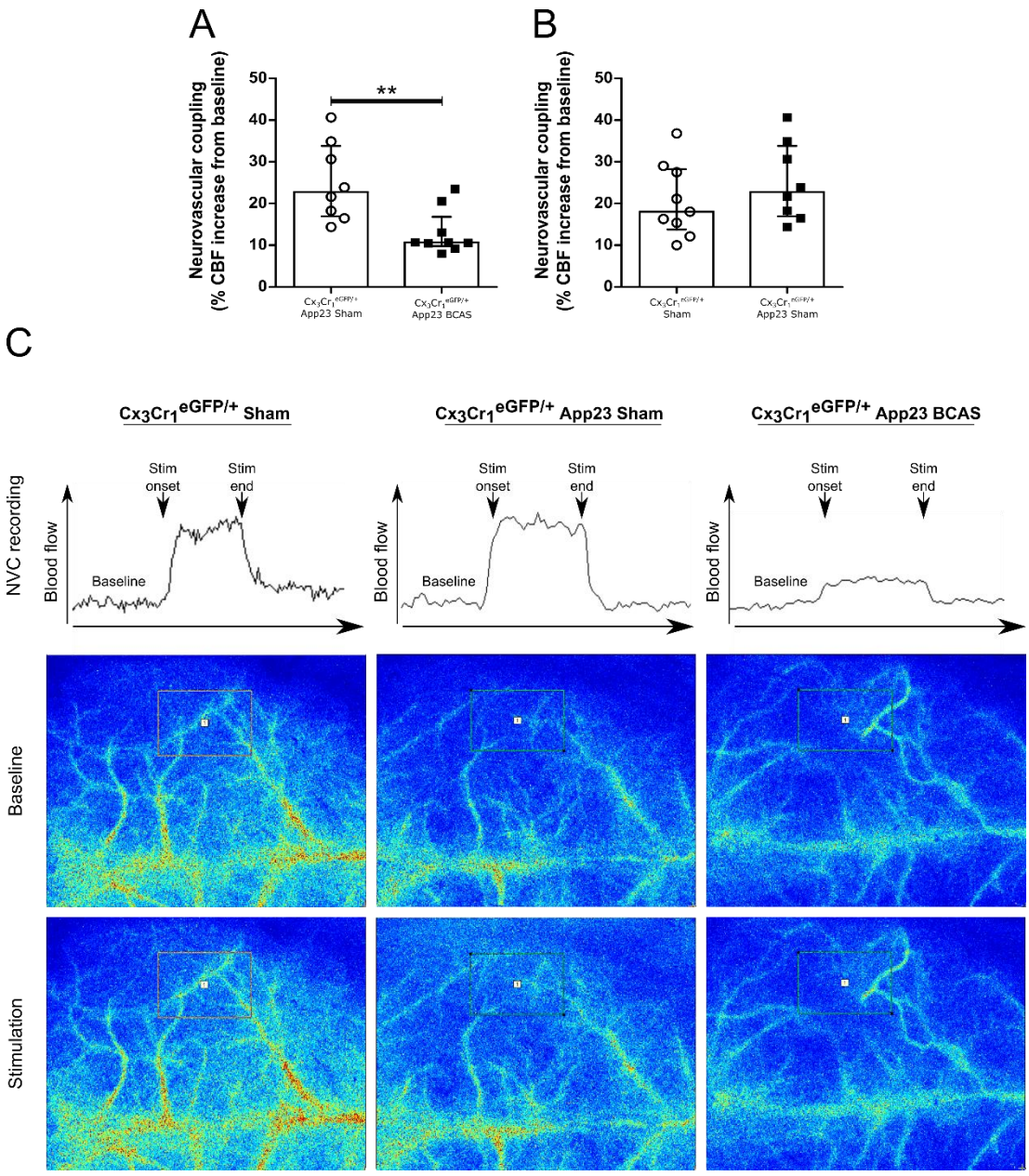

Figure 4.10 Neurovascular coupling responses are significantly impaired within $Cx_3Cr_1^{eGFP/+}$ App23 mice following BCAS. **(A)** Blood flow responses within the barrel cortex following whisker stimulation were found to be significantly reduced within $Cx_3Cr_1^{eGFP/+}$App23 BCAS mice in comparison to $Cx_3Cr_1^{eGFP/+}$App23 shams. $^{**}p<0.01$. **(B)** Neurovascular coupling responses were found to be comparable between $Cx_3Cr_1^{eGFP/+}$ sham and $Cx_3Cr_1^{eGFP/+}$App23 sham mice. Data presented as median±IQR **(C)** Representative images displaying blood flow recordings before, during, and after whisker stimulation within $Cx_3Cr_1^{eGFP/+}$ sham mice, as well as $Cx_3Cr_1^{eGFP/+}$ App23 sham and BCAS mice. Accompanied by images of CBF, as measured by laser speckle, at baseline and during whisker stimulation. The box on each image indicates the region measured within the somatosensory cortex.

4.3.9 Microglial structure and process motility are unaffected within $Cx_3Cr_1^{eGFP/+}$App23 mice following BCAS

Having demonstrated neurovascular coupling impairments within $Cx_3Cr_1^{eGFP/+}$App23 mice following 3-months of BCAS, in the absence of microglial expansion, we wondered whether microglia may still play a role in this dysfunction through altered function. A switch to a more activated pro-inflammatory microglial phenotype could, in the absence of expansion, still be a mechanism by which the neuro-glial-vascular unit becomes dysfunctional. To investigate this, multiphoton microscopy was utilised to assess microglial structure and process dynamics 1-week following sham/BCAS surgery in $Cx_3Cr_1^{eGFP/+}$App23 mice (Figure 4.11). No significant differences were identified for soma area ($p=0.27$), volume ($p=0.29$) or sphericity ($p=0.51$) within $Cx_3Cr_1^{eGFP/+}$App23 BCAS mice (area: 2439μm^2±70, volume: 8444μm^3±304, sphericity: 0.82±0.01) when compared to $Cx_3Cr_1^{eGFP/+}$App23 shams (area: 2607μm^2±100, volume: 9073μm^3±496, sphericity: 0.80±0.01) (Figure 4.11A/B/C).

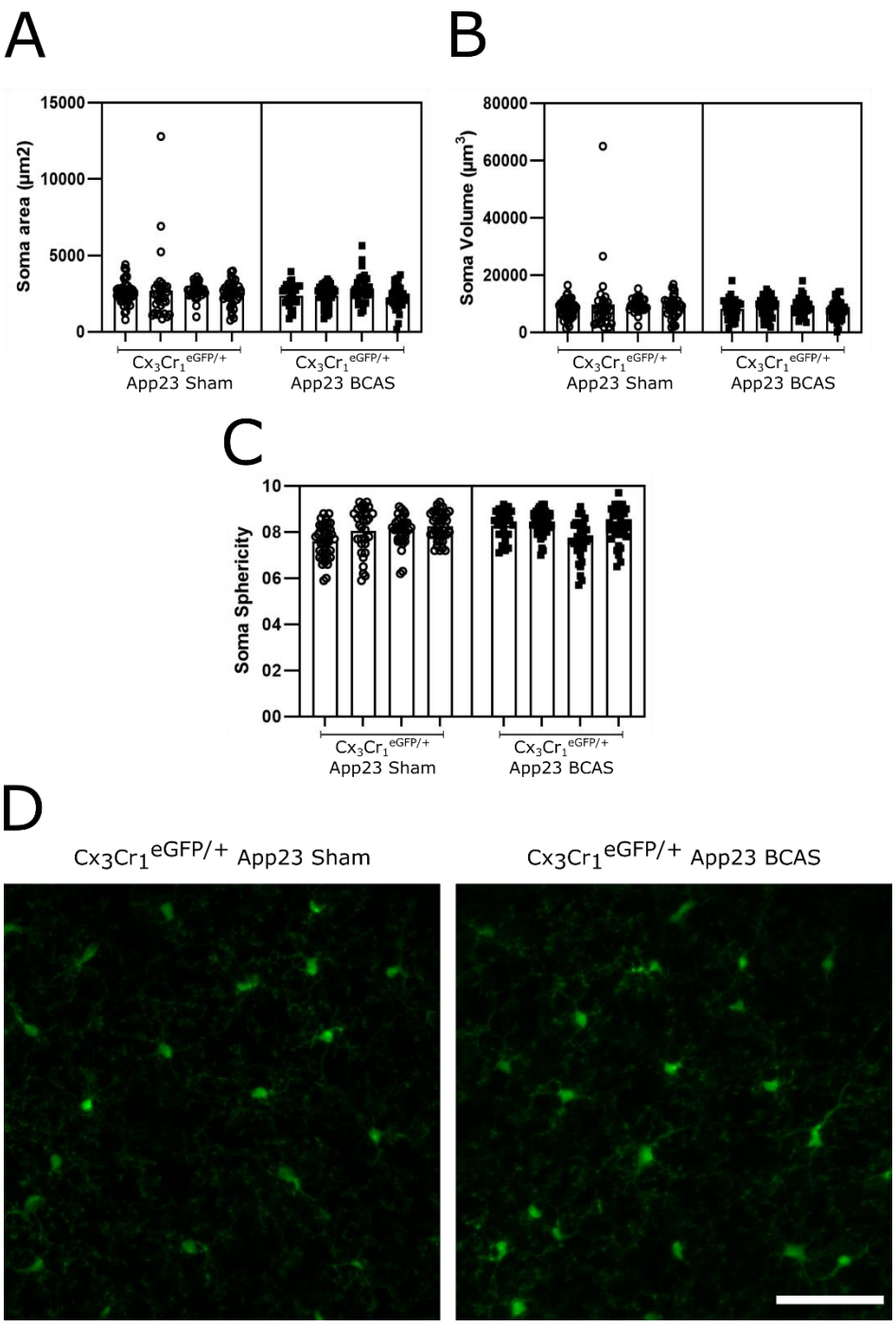

Figure 4.11 Microglial structure is unaltered within $Cx_3Cr_1^{eGFP/+}$App23 mice following BCAS. Microglial structure was analysed using reconstructed z-stacks taken from the cerebral cortex via multiphoton microscopy. Soma area **(A)**, volume **(B)** and sphericity **(C)** were found to unaltered following BCAS surgery. Data presented as Mean±SEM. (D) Representative images of 2D summated stacks generated from the 3D z-stacks used for structural analysis. Scale bar 50µm.

Process motility and coverage were also found to be unaltered, 1-week following surgery, within $Cx_3Cr_1^{eGFP/+}$App23 BCAS mice (motility: 56.65±15.51, coverage: 69.18±13.41) when compared to $Cx_3Cr_1^{eGFP/+}$App23 sham mice (motility: 54.73±4.0, coverage: 70.80±2.08) (p=0.343 and p=1.00 respectively) (Figure 4.12A/B).

Taken together, these data demonstrate an absence of both microglial structural and functional changes 1-week following BCAS within $Cx_3Cr_1^{eGFP/+}$App23 mice.

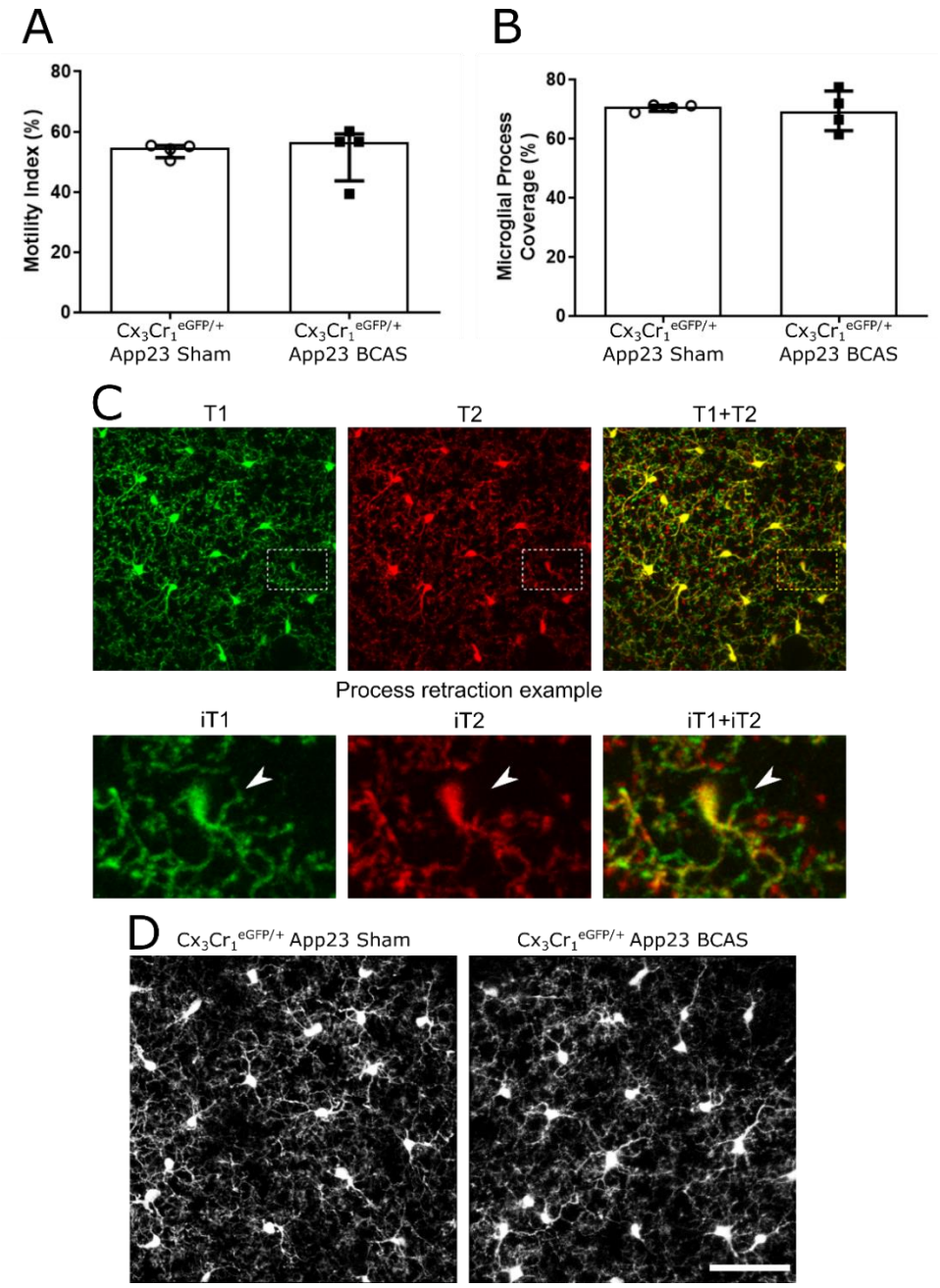

Figure 4.12 Microglial surveillance functions are unaltered within $Cx_3Cr_1^{eGFP/+}$App23 mice following BCAS. **(A)** Microglial motility measured over a consecutive 15-minute imaging

period, was found to be unaltered within $Cx_3Cr_1^{eGFP/+}$App23 mice 1-week following BCAS surgery. **(B)** Microglial process coverage was assessed over the same 15-minute imaging period and was also found to be unaltered 1-week following BCAS surgery. Data presented as median±IQR. **(C)** Images to demonstrate dynamic microglial process movement. T1 (green) is a 2D summated version of the first 3D z-stack acquired. T2 (red) represents a z-stack gathered ≈48 seconds later, with T1+T2 showing a merge of the 2 images. The hashed square represents the inserts (i) that are shown below, with the white arrowhead highlighting an example of process retraction. **(D)** Representative images of a summated projection of all z-stacks gathered over the 15-minute imaging period to enable total process coverage to be calculated within $Cx_3Cr_1^{eGFP/+}$ App23 sham and $Cx_3Cr_1^{eGFP/+}$ App23 BCAS mice. Scale bar 50µm.

4.3.10 Spatial learning and memory are impaired within $Cx_3Cr_1^{eGFP/+}$App23 mice, with no additional BCAS mediated deficit

Having demonstrated spatial memory, but not learning, impairments within $Cx_3Cr_1^{eGFP/+}$ mice following 3-months of BCAS, the next aim was to determine if additional deficits were apparent when BCAS was coupled to increased amyloid. The Barnes maze was carried out on $Cx_3Cr_1^{eGFP/+}$App23 mice 3-months following sham/BCAS surgery (Figure 4.13). During the training phase, an overall effect of time was observed ($F_{(5,60)} = 4.415$, $p<0.01$) indicating a degree of learning across the 6 training days. No significant group ($F_{(1,12)} = 0.110$, $p=0.745$) or interaction effects ($F_{(5,60)} = 0.440$, $p=0.819$) were identified (Figure 4.13A). Movement distance demonstrated the same trend with an overall effect of time ($F_{(2.66,31.93)} = 5.555$, $p<0.01$) with no significant effects of group ($F_{(1,12)} = 0.000$, $p=0.997$) or interaction ($F_{(2.66,31.93)} = 1.385$, $p=0.266$) (Figure 4.13B). Analysis of movement speed throughout the training days revealed no significant effects of time ($F_{(2.71,32.50)} = 1.815$, $p=0.168$), group ($F_{(1,12)} = 0.236$, $p=0.636$) or interactions ($F_{(2.71,32.50)} = 0.990$, $p=0.403$) (Figure 4.13C).

Overall, these data demonstrate learning within each group with no effect of BCAS surgery. The learning profile across the 6 training days, however, was very flat and not the usual steep learning profile that is apparent within sham mice (Figure 4.6A). To determine if increased amyloid alone resulted in an impairment in spatial learning, the learning profiles of $Cx_3Cr_1^{eGFP/+}$App23 sham mice were compared to $Cx_3Cr_1^{eGFP/+}$ shams (Figure 4.13E). Analysis of the learning slope across the 6 training days revealed a significant increase in $Cx_3Cr_1^{eGFP/+}$App23 sham mice (-23.26±28.0) when compared to $Cx_3Cr_1^{eGFP/+}$ shams (-33.96±6.9) ($p<0.05$) indicative of a slower rate of spatial learning (Figure 4.13E). Taken

together these data indicate impaired spatial learning within $Cx_3Cr_1^{eGFP/+}$App23 mice, with no additional deficit apparent following BCAS.

As a test of spatial memory, a probe trial was carried out within $Cx_3Cr_1^{eGFP/+}$App23 sham and BCAS mice, 72-hours following the last training day (Figure 4.13D). Statistical analysis revealed no significant difference in the time spent within the target zone of $Cx_3Cr_1^{eGFP/+}$App23 sham (65%±56.67) when compared to BCAS mice (22.5%±66.25) ($U = 17.5$, $p>0.05$). To confirm that target quadrant times did indeed reflect a preference for that quadrant, time spent within all 4 quadrants were compared. $Cx_3Cr_1^{eGFP/+}$App23 sham mice showed a significant difference in the time spent within each quadrant ($X^2_{(3)} = 8.492$, $p<0.05$). *Post hoc* analysis revealed a target zone preference over the clockwise ($p<0.05$) and opposite ($p<0.05$) zones, but not the counter-clockwise zone ($p=0.672$) demonstrating no preference for the target quadrant (Figure 4.13D). $Cx_3Cr_1^{eGFP/+}$App23 BCAS mice demonstrated no difference in the time spent within either quadrant ($X^2_{(3)} = 1.868$, $p=0.60$) (Figure 4.13D).

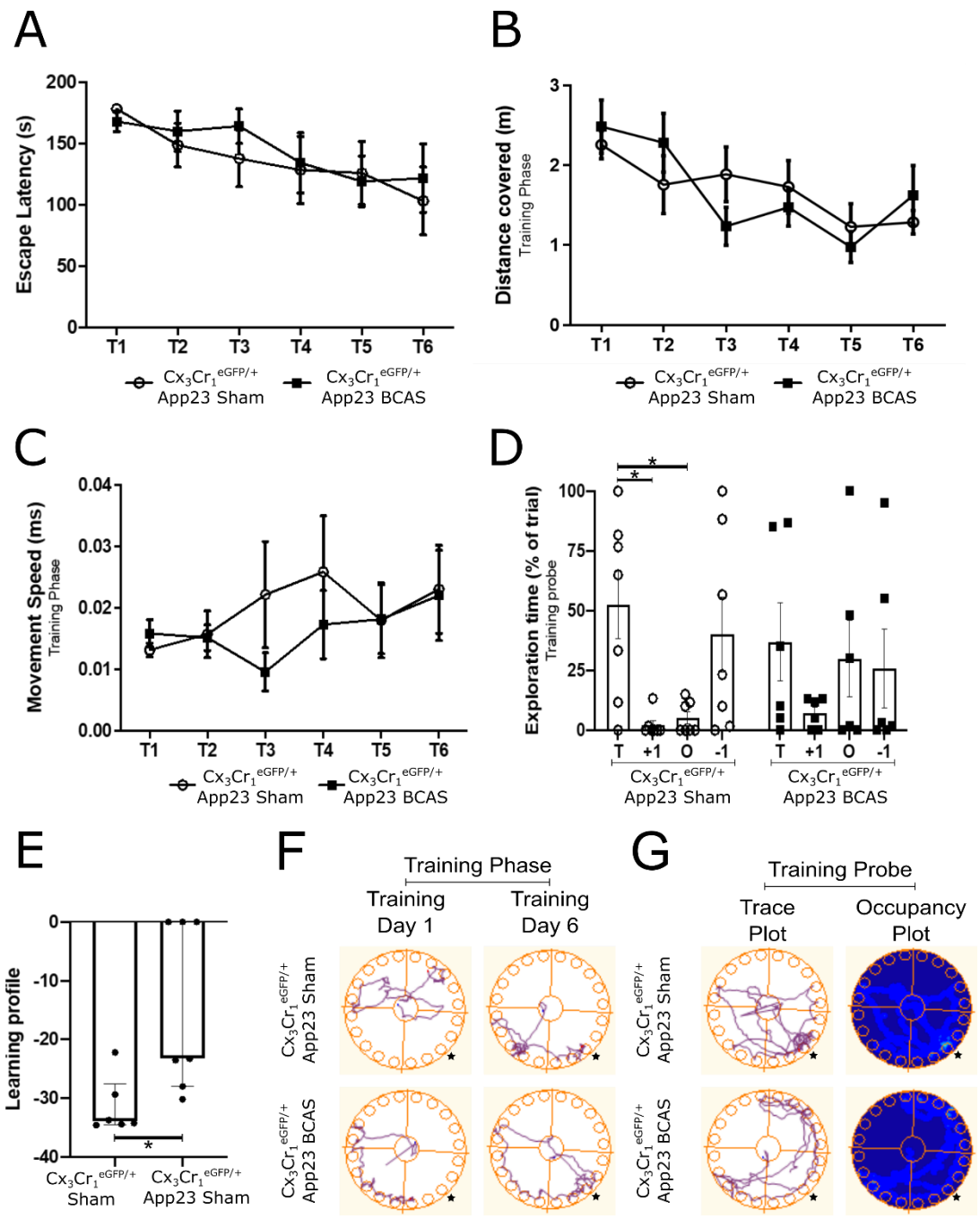

Figure 4.13 Spatial learning and memory are impaired within $Cx_3Cr_1^{eGFP/+}$App23 mice, with no additional BCAS mediated deficit. **(A)** An overall effect of time demonstrates learning within both groups. Escape latency was found to be comparable across the 6 training days indicating no additional spatial learning deficit following BCAS. **(B)** Movement distance throughout each trial revealed a similar pattern to escape latency with an overall effect of time and no group differences. **(C)** Movement speed across the 6 training days revealed no significant overall effects of time or group as well as no interactions. Data presented as

mean±SEM. **(D)** $Cx_3Cr_1^{eGFP/+}$App23 sham mice demonstrated a preference for the target quadrant over clockwise and opposite but not counter-clockwise zones, indicating no memory for the target hole. $Cx_3Cr_1^{eGFP/+}$App23 BCAS mice showed no preference for any quadrant. Data presented as median±IQR. *p<0.05. **(E)** A significant increase in learning profile within $Cx_3Cr_1^{eGFP/+}$App23 sham mice, indicative of a slower rate of spatial learning, was identified when compared to $Cx_3Cr_1^{eGFP/+}$ shams. *p<0.05 **(F)** Representative movement traces during day 1 and 6 of the training period taken from $Cx_3Cr_1^{eGFP/+}$App23 sham and $Cx_3Cr_1^{eGFP/+}$App23 BCAS groups. Stars indicate target hole. **(G)** Trace and occupancy plots gathered during probe trails of $Cx_3Cr_1^{eGFP/+}$App23 sham and $Cx_3Cr_1^{eGFP/+}$App23 BCAS mice. Stars indicate target hole; brighter colours indicate increased time spent within that area (occupancy plot only).

Having demonstrated impairments in spatial memory within $Cx_3Cr_1^{eGFP/+}$App23 mice the next aim was to assess cognitive flexibility (Figure 4.14). $Cx_3Cr_1^{eGFP/+}$App23 sham and BCAS mice underwent reversal training across 3 consecutive days. Statistical analysis revealed an overall effect of time ($F_{(2,24)} = 4.290$, $p<0.05$) with no significant effects of group ($F_{(1,12)} = 0.369$, $p=0.56$) or interaction ($F_{(2,24)} = 1.558$, $p=0.231$) (Figure 4.14A). Movement distance displayed the same pattern with an overall effect of time ($F_{(2,24)} = 4.783$, $p<0.05$), with no significant group ($F_{(1,12)} = 0.738$, $p=0.407$) or interaction effect ($F_{(2,24)} = 0.360$, $p=0.701$) (Figure 4.14B). Movement speed across reversal training reported no significant effects of time ($F_{(2,24)} = 0.324$, $p=0.727$), group ($F_{(1,12)} = 0.000$, $p=1.000$) or interactions ($F_{(2,24)} = 0.224$, $p=0.801$) (Figure 4.14C).

As with the training phase, although an improvement in escape latency and movement distance over time was apparent, the learning prolife appeared flatter in comparison to $Cx_3Cr_1^{eGFP/+}$ sham mice (Figure 4.7). Therefore, learning profiles of $Cx_3Cr_1^{eGFP/+}$App23 sham and $Cx_3Cr_1^{eGFP/+}$sham mice were compared. $Cx_3Cr_1^{eGFP/+}$App23 sham mice displayed a significant reduced learning slope over the reversal training phase (-0.28±14.13) when compared to $Cx_3Cr_1^{eGFP/+}$ sham mice (-36.95±17.94) ($p<0.05$) (Figure 4.14E).

Adaptive memory was then assessed with a reversal probe completed 72-hours following the final reversal training day (Figure 4.14D). Statistical analysis revealed no significant difference in the time spent within the target zone of $Cx_3Cr_1^{eGFP/+}$App23 sham (25%±63.33) when compared to BCAS mice (35.83%±35.83) ($U = 20$, $p>0.05$). When time spent within the target quadrant was compared to the other 3 quadrants, both $Cx_3Cr_1^{eGFP/+}$App23 sham and BCAS mice showed no significant difference in the time spent within each quadrant ($X^2_{(3)} =$

1.000, p=0.80, and $X^2_{(3)}$ = 5.722, p=0.13 respectively), indicating no memory for the target zone (Figure 4.14D).

Taken together these data illustrate an impairment in spatial learning and memory as well as cognitive flexibility and adaptive memory within $Cx_3Cr_1^{eGFP/+}$App23 mice, with no additional detrimental effect of BCAS.

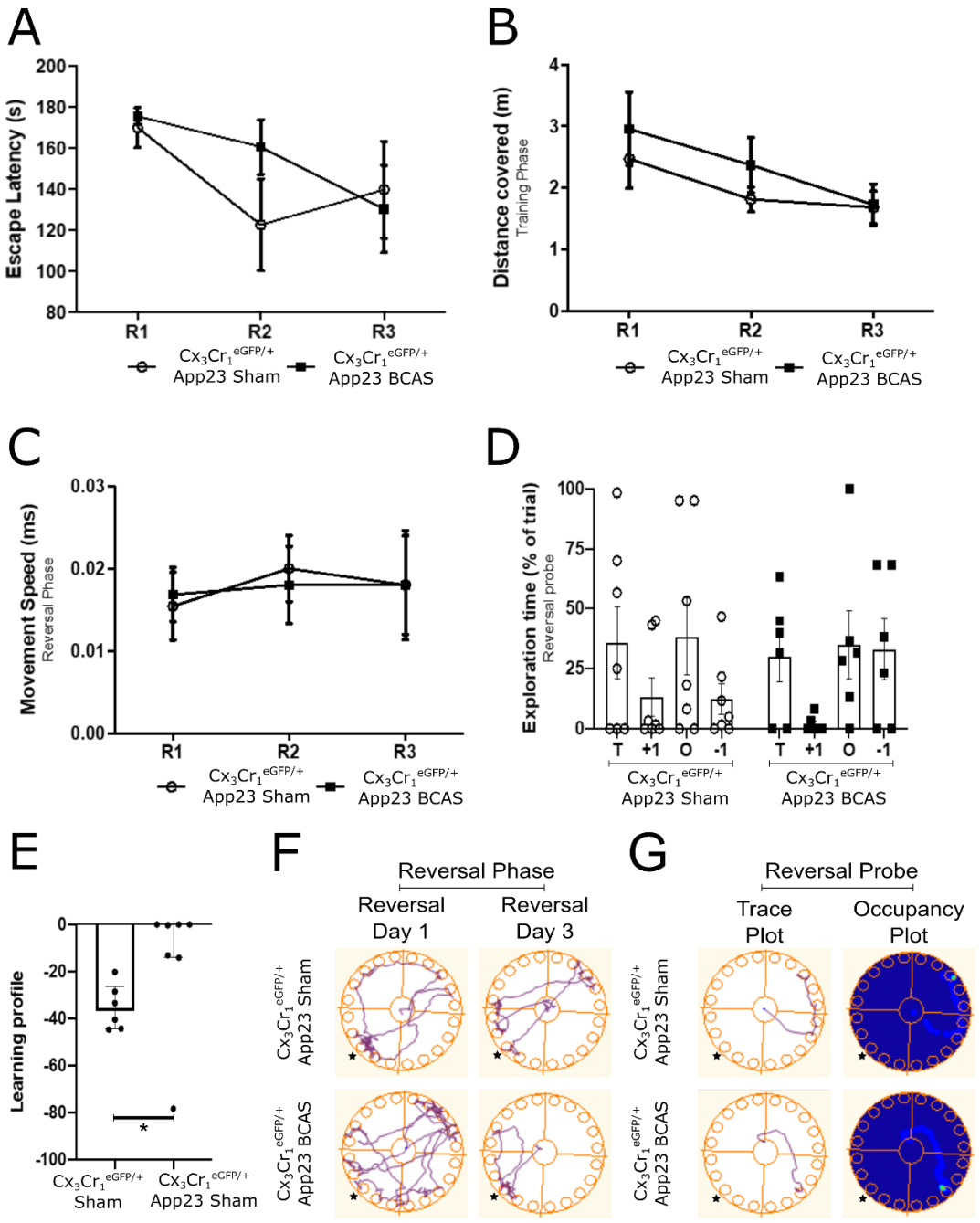

Figure 4.14 Cognitive flexibility and adaptive memory are impaired within $Cx_3Cr_1^{eGFP/+}$App23 mice, with no additional BCAS mediated deficit. **(A)** An overall effect

of time demonstrates learning within both groups. Escape latency was found to be comparable across the 3 reversal training days indicating no additional deficit following BCAS. **(B)** Movement distance throughout each trial revealed a similar pattern to escape latency with an overall effect of time and no group differences. **(C)** Movement speed across the 3 reversal training days revealed no significant overall effects of time or group as well as no interactions. Data presented as mean±SEM. **(D)** $Cx_3Cr_1^{eGFP/+}$App23 sham and BCAS mice showed no preference for any quadrant during probe trials, indicative of impaired adaptive memory. Data presented as median±IQR. **(E)** A significant increase in learning profile within $Cx_3Cr_1^{eGFP/+}$App23 sham mice, indicative of a slower rate of cognitive flexibility, was identified when compared to $Cx_3Cr_1^{eGFP/+}$ shams. Data presented as median±IQR. *p<0.05 **(F)** Representative movement traces during day 1 and 3 of the reversal training period taken from $Cx_3Cr_1^{eGFP/+}$App23 sham and $Cx_3Cr_1^{eGFP/+}$App23 BCAS groups. Stars indicate target hole. **(G)** Trace and occupancy plots gathered during probe trails of $Cx_3Cr_1^{eGFP/+}$App23 sham and $Cx_3Cr_1^{eGFP/+}$App23 BCAS mice. Stars indicate target hole; brighter colours indicate increased time spent in that area (occupancy plot only).

4.3.11 eGFP insertion leads to reduced Cx_3Cr_1 receptor expression within $Cx_3Cr_1^{eGFP/+}$ mice

The data presented within the chapter thus far has demonstrated an absence of microglial response, in terms of structure, expansion and function, following both BCAS and BCAS coupled with increased amyloid. A lack of microglial response is surprising, particularly given the significant microglial response observed following BCAS within chapter 3. Through the generation of the $Cx_3Cr_1^{eGFP/+}$ microglial reporter mouse, 1 copy of the Cx_3Cr_1 receptor is replaced with the gene encoding green florescent protein (eGFP). The Cx_3Cr_1 receptor allows for neuronal-microglial communication and its signalling is suggested to be responsible for sustaining normal microglial activity (Biber, Neumann H Fau - Inoue, Inoue K Fau - Boddeke, & Boddeke, 2007; U.-K. Hanisch & H. Kettenmann, 2007). Therefore, the next aim was to determine if the loss of Cx_3Cr_1 receptor signalling could be an explanation for the lack of microglial response observed following BCAS. Flow cytometry was used to isolate microglial cells from $Cx_3Cr_1^{eGFP/+}$ and wild-type C57BL/6J mice. Cx_3Cr_1 receptor expression was then quantified through qPCR and compared between groups (Figure 4.15). Statistical analysis revealed a significant, ≈5-fold, reduction in Cx_3Cr_1 receptor expression within $Cx_3Cr_1^{eGFP/+}$ mice (0.22±0.07) when compared to wild-type C56BL/6J mice (1.08±0.38) ($t(4) = 3.131$, $p<0.05$) (Figure 4.15).

Overall, these data demonstrate that Cx_3Cr_1 receptor expression is significantly reduced following eGFP insertion within $Cx_3Cr_1^{eGFP/+}$ mice.

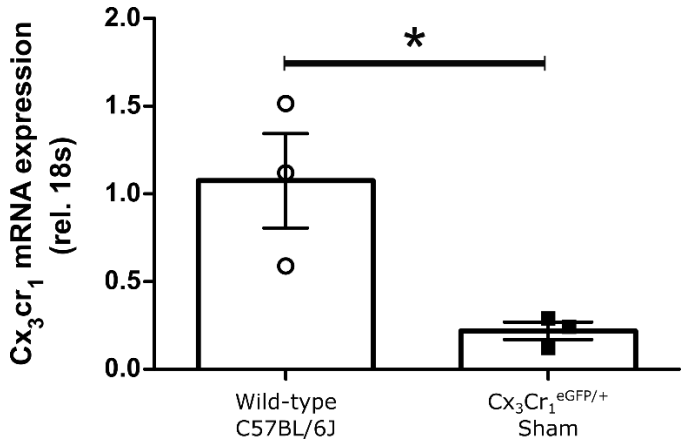

Figure 4.15 Cx_3Cr_1 receptor expression is significantly reduced within $Cx_3Cr_1^{eGFP/+}$ mice. Cx_3Cr_1 receptor expression within microglial cells was found to be significantly reduced, *≈5-fold,* within $Cx_3Cr_1^{eGFP/+}$ mice in comparison to wild-type C57BL/6J mice. Data presented a mean±SEM. $^{*}p<0.05$.

4.4 Discussion

The present study set out to investigate structural and functional alterations within microglial cells following BCAS, and to discover how these may change when coupled with a model of amyloidosis. The results show, following BCAS alone, no alterations within microglial structure, function, or density alongside unimpaired neurovascular coupling responses and visuospatial learning. Spatial memory, however, was found to be impaired following BCAS despite the absence of a clear microglial response. When BCAS was coupled to a model of amyloidosis, microglial structure, function, and density were once again found to be unaltered. In contrast, neurovascular coupling responses were found to be impaired when BCAS and increased amyloid were present together. Visuospatial learning and memory, however, were found to be impaired within App23 mice alone, with no additional deficits apparent following BCAS surgery. Cx_3Cr_1 receptor heterozygous mice were used for all experiments, with qPCR analysis revealing a ≈5-fold reduction in Cx_3Cr_1 receptor expression. The interruption of normal Cx_3Cr_1 receptor signalling, therefore, could be an explanation as to the lack of microglial responses observed here following BCAS, even in the presence of increased amyloid.

4.4.1 Microglial density is unaltered following BCAS within $Cx_3Cr_1^{eGFP/+}$ mice

To allow microglia to be readily visualised the $Cx_3Cr_1^{eGFP/+}$ transgenic mouse line, in which one allele of the Cx_3Cr_1R gene is replaced with the gene encoding enhanced green fluorescent protein (eGFP), was used. This insertion results in the expression of eGFP within $Cx_3Cr_1^{+}$ cells, which include microglia, dendritic cells, and activated endothelial cells (Jung S, 2000). The original aim was to use this microglial reporter line to allow dynamic microglial mechanisms to be evaluated following BCAS. Initial investigations however, demonstrated an absence of microglial expansion following both short-term and chronic BCAS.

These results are surprising given the substantial microglial proliferative response observed in chapter 3. In the present study, however, 0.18mm micro-coils were applied to the left and right common carotid arteries, resulting in a CBF reduction of ≈30%. This contrasts with the BCAS procedure within chapter 3, that used a mixed-coil approach achieving a slightly more severe blood flow reduction of ≈50%. Microglial density in the present study, was also assessed at a more chronic 3-month time-point following surgery, in contrast to the 6-week evaluation that was carried out previously. Despite these experimental differences, the lack of microglial expansion was still unexpected as previous experiments, using the same milder BCAS model, consistently report white matter microglial expansion following BCAS

(Coltman et al., 2011; Duncombe, Kitamura, et al., 2017; Fowler et al., 2017; Holland et al., 2015; Kitamura et al., 2017; Manso et al., 2017; Reimer et al., 2011). A key difference between the present study and the previous BCAS literature is the use of the $Cx_3Cr_1^{eGFP/+}$ transgenic mouse line. Therefore, the loss of 1 gene encoding the Cx_3Cr_1 receptor could be impacting on microglial responses following BCAS.

Despite heterozygous Cx_3Cr_1 receptor mice being routinely used for multiphoton experiments, with the assumption of no adverse microglial effects, signalling between the chemokine receptor Cx_3Cr_1 and its sole ligand Cx_3CL_1 (Fractalkine) has been identified as a prominent regulator of microglial activation (Jeffrey K. Harrison et al., 1998; Nishiyori et al., 1998). Studies on the consequence of a total loss of Cx_3Cr_1 receptor expression are mixed. Initially, no evidence of altered phenotype was observed in either CNS or peripheral immune responses (Jung, Aliberti, et al., 2000). However, additional investigations reported the activation of microglia towards a neurotoxic profile in the absence of Cx_3Cr_1 receptor signalling (Cardona et al., 2006; Fumagalli, Perego C Fau - Ortolano, Ortolano F Fau - De Simoni, & De Simoni, 2013). One study suggested that deficiency is protective against ischemic stroke (Tang Z Fau - Gan et al., 2014), whereas others have shown that the downregulation of Cx_3CL_1 by neurons leads to microglial neurotoxicity after ischemic stroke (He, Ren, Guo, & Deng, 2019). Mixed neuron-glial cultures, prepared from Cx_3Cr_1 KO mice stimulated with LPS, also showed reduced microglial activation with the lessened release of the pro-inflammatory cytokines TNF-alpha, NO, and superoxide from microglial cells (Mattison et al., 2013).

Heterozygous $Cx_3Cr_1^{eGFP/+}$ mice, in contrast, have been considered to have normal microglial behaviours following eGFP insertion and therefore are widely used in neuroimaging studies (Nimmerjahn et al., 2005; Wieghofer et al., 2015). For example, it has been reported that infarctions within $Cx_3Cr_1^{eGFP/+}$ mice were similar to wild-type controls after MCAO (Fumagalli et al., 2013). However, there is now growing evidence to suggest, under certain experimental conditions, that Cx_3Cr_1 receptor heterozygosity leads to abnormal microglial responses (Poniatowski et al., 2017; Wieghofer et al., 2015). In support of our findings, research in a model of ischemic preconditioning (IPC), demonstrated that microglial expansion following IPC was prevented within Cx_3Cr_1 receptor heterozygous mice (A. A.-O. McDonough et al., 2019). Pharmacological inhibition of Cx_3Cr_1 receptor signalling, within a rat model of hypertension, was also found to prevent microglial activation, reduced pro-inflammatory cytokines, and restore systolic blood pressure (Ho et al., 2020). A role for fractalkine signalling in microglial proliferation has also been demonstrated in cultured human microglia (Hatori, Nagai A Fau - Heisel, Heisel R Fau - Ryu, Ryu Jk Fau - Kim, & Kim, 2002).

Furthermore, in a model of ischemia stroke, neuronal autophagy was shown to result in decreased neuronal Cx_3CL_1 expression leading to microglial activation (He et al., 2019).

Such findings are interesting given the fact that Cx_3Cl_1-Cx_3Cr_1 signalling has been proposed as a constitutive signalling with a calming influence limiting microglial activation (Cardona et al., 2006). However, the evidence for such a role comes from Cx_3Cr_1 knockout experiments and therefore it could be the case that reducing, but not completely blocking, Cx_3CL_1-Cx_3Cr_1 signalling is having an alternative effect of microglial responses. Additional studies within Cx_3Cr_1 heterozygous mice assessing Cx_3CL_1-Cx_3Cr_1 signalling under normal and disease conditions, therefore, would be required to prove such a theory.

Taken together, the evidence from previous studies alongside our own findings suggests that fractalkine signalling is an important pathway by which microglial proliferation and activation can be initiated in response to certain stimuli, and that even small perturbations in receptor levels has the potential to attenuate microglial responses.

4.4.2 Microglial structure and surveillance functions are unaltered following BCAS within $Cx_3Cr_1^{eGFP/+}$ mice

The advancement of microglial reporter lines alongside neuroimaging studies have allowed single microglial cells to be tracked over-time in both homeostatic and pathological conditions. Such investigations have allowed microglial structural transformations to be observed and tracked within changing environments. Under normal homeostatic conditions, microglia adopt a characteristic morphology, consisting of a small spherical cell soma surrounded by highly ramified flopodia-like processes. (Nimmerjahn et al., 2005). In the presence of damage or infection, homeostatic microglia undergo dynamic structural changes, ultimately forming an amoeboid-like appearance (M. A.-O. Kluge et al., 2017; Stence et al., 2001). Amoeboid-like microglial confirmations are indicative of an activated microglial state and are associated with the upregulation of inflammatory related markers such as CD68 and MHC11 (Kettenmann et al., 2011; Lartey et al., 2014). Multiphoton imaging has allowed such morphological changes, within individual microglial cells, to be quantified. Structural parameters, such as soma size and sphericity, can accurately distinguish between activated and resting microglial populations, as amoeboid conformations are associated with the increased release of pro-inflammatory cytokines (B. M. Davis et al., 2017; Kozlowski & Weimer, 2012).

To date detailed phenotypical evaluations of microglial structure have not been carried out within the context of BCAS. Therefore, in the present study, the aim was to determine if microglial conformational changes could be identified following short-term BCAS. Such an observation would help build on the pathogenic understanding of the previous chapter, by

illustrating the presence of microglial activation alongside extensive proliferation in response to BCAS.

$Cx_3Cr_1^{eGFP/+}$ mice were used to allow microglial cells within the cerebral cortex to be readily visualised via multiphoton microscopy. Previous neuroimaging studies have demonstrated that in response to various insults such as ischemic stroke, Aβ deposition (Lull & Block, 2010) and probe implantation (Kozai, Vazquez, Weaver, Kim, & Cui, 2012), microglial conformationally change to more amoeboid forms leading to neuroinflammation. In the present study, cortical z-stacks were acquired to allow the structural evaluation of individual microglial cells, *in vivo*, 1-week following BCAS surgery. Soma area, volume and sphericity were found to be unaltered following BCAS. This result is difficult to contextualise due to the previous observation of a lack of BCAS mediated microglial expansion within $Cx_3Cr_1^{eGFP/+}$ mice. One explanation is that no structural alterations are occurring following BCAS since Cx_3Cr_1 receptor heterozygosity is preventing the microglial response. Alternatively, it could be the case that 1-week of BCAS does not lead to such structural changes and is not associated with microglial activation. Previous work using a photothrombotic occlusion model used multiphoton microscopy and $Cx_3Cr_1^{eGFP/+}$ mice to demonstrate increased microglial soma size, indicative of microglial activation within both the peri-infarct and sites of secondary neurodegeneration (Kluge et al., 2018). Microglial structural changes observed within the peri-infarct region and sites of secondary neurodegeneration also showed increased expression of markers associated with microglial activation such as CD68 and CD11b (M. A.-O. Kluge et al., 2017). However, these observations are in the context of more severe blood flow reductions. Therefore, without a clear wild-type comparison, it is difficult to determine if microglial structural changes are occurring following short-term BCAS. In the previous chapter microglial area per cell was found to be increased through immunohistochemical staining of Iba-1. However, such an evaluation is limited and does not compare to the accuracy of the structural evaluation methods used here. It would therefore be necessary for additional experiments to be conducted to help elucidate microglial structural changes following BCAS in the absence of Cx_3Cr_1 receptor heterozygosity. Cx_3Cr_1 receptor antibodies are available which would allow microglial structure within wild-type mice to be compared to $Cx_3Cr_1^{eGFP/+}$ mice through structural evaluation of z-stacks taken from thick cortical tissue sections. Such a comparison would help determine if microglial structure is altered following BCAS and whether such changes are prevented by Cx_3Cr_1 heterozygosity.

In conjunction with morphological changes, microglial process dynamics have also been shown to infer altered phenotypic state following insult. In homeostatic ‘resting’ states, microglial processes are highly dynamic and function to sample their local environment,

including making contact with other cells within their vicinity (Nimmerjahn et al., 2005). Rapid extension and retraction of process has been shown to be an important step in the sequence of structural changes leading to microglial activation (Stence et al., 2001). Microglial process movement has also been shown to reflect response to areas of damage. For example, following a laser ablation injury, microglial processes were found to extend towards the injured area (Davalos et al., 2005). The absence of microglial process movement towards areas of injury can also reflect dysfunctional responses. For example, in an experimental stroke model, process extension to areas of laser injury was found to be impaired within sites of secondary neurodegeneration (Kluge et al., 2018). To date microglial process dynamics have not been evaluated within the context of BCAS. In present study repeated z-stacks of the cerebral cortex were gather, over 15 consecutive minutes, to allow microglial process dynamics to be evaluated 1-week following BCAS surgery. Process motility as well as coverage were found to be unaffected following BCAS surgery. As with structural changes, it is once again difficult to draw conclusive conclusions from these findings due to the confound of Cx_3Cr_1 receptor heterozygosity influencing normal microglial responses. Previous studies have demonstrated that the re-localisation of the purinergic P2Y12 receptor from microglial processes to the soma may be a predictor of non-responsive microglial processes (Kluge et al., 2018). A comparison between microglial P2Y12 receptor localisation within wild-type and $Cx_3Cr_1^{eGFP/+}$ mice could help elucidate process motility changes following BCAS and determine if such changes are affected due to Cx_3Cr_1 receptor heterozygosity.

4.4.3 BCAS elicits significant and sustained reductions in cerebral blood flow within $Cx_3Cr_1^{eGFP/+}$ mice

In the present study BCAS surgery was found to induce mild, sustained reductions in CBF. Laser speckle imaging revealed a modest ≈26% reduction in CBF at 24-hours which progressed to ≈30% at 3-months. Such blood flow reductions, following milder BCAS surgery, are in agreement with the 30-40% reductions previously reported within wild-type mice (Maki et al., 2011; McQueen et al., 2014; Nishio et al., 2010; Shibata et al., 2004).

The results demonstrate comparable blood flow reductions between wild-type and $Cx_3Cr_1^{eGFP/+}$ mice following BCAS surgery. Thus, indicating that any downstream effects of Cx_3Cr_1 receptor heterozygosity can be assessed without the confound of flow-related differences.

4.4.4 Neurovascular coupling response are unaltered following BCAS within $Cx_3Cr_1^{eGFP/+}$ mice

Neurovascular coupling is a crucial mechanism by which components of the neuro-glial-vascular unit communicate to match local blood flow to neuronal activity, allowing perfusion to satisfy metabolic demands. In human patients reduced vascular function is associated with cognitive impairment as well as progression from mild cognitive impairment to dementia (Buratti et al., 2015; Viticchi et al., 2012). Previous work in aged mice demonstrated that neurovascular coupling impairments were associated with increased astrogliosis, loss of astrocytic end-feet as well as increased microglial numbers (Duncombe, Lennen, et al., 2017). In the present study neurovascular coupling responses, within the somatosensory cortex following whisker stimulation, were found to be unaltered following BCAS surgery within $Cx_3Cr_1^{eGFP/+}$ mice. These results are in direct contradiction with wild-type data which shows a ≈20% reduction in blood flow responses to stimulation following BCAS surgery (Duncombe, Kitamura, et al., 2017). Thus, inferring that Cx_3Cr_1 receptor heterozygosity is conferring protection against BCAS mediated neurovascular coupling impairments.

Astrocytes, and more specifically end-feet connections to blood vessels, have been identified as key components of the neurovascular coupling signalling cascade (Bazargani & Attwell, 2016). Previous BCAS studies have demonstrated that astrogliosis occurs subsequent to microglial alterations (Holland et al., 2015). It has also been shown that the release of microglial factors is a key mechanism by which astrogliosis can be stimulated (Liddelow et al., 2017). Therefore, following BCAS, astrocytes may become reactive in response to microglial expansion and activation. Thus, one explanation for preserved neurovascular coupling, within Cx_3Cr_1 receptor heterozygous mice, is that the attenuation of microglial responses prevents the activation of astrocytes. In the absence of astrocyte proliferation and activation, end-feet connections remain intact and preserve haemodynamic functions. To confirm this theory, additional immunohistochemical investigations, using markers for reactive astrocytes (GFAP) and astrocytic end-feet (AQP4), would be required to determine if astrogliosis and end-feet retraction is absent following BCAS within $Cx_3Cr_1^{eGFP/+}$ mice.

4.4.5 Spatial memory is impaired within $Cx_3Cr_1^{eGFP/+}$ mice following BCAS

In the present study, the Barnes maze test of visuo-spatial learning and memory was performed 3-months following sham/BCAS surgery. Spatial learning was found to be unaffected following BCAS within $Cx_3Cr_1^{eGFP/+}$ mice, however, in contrast spatial memory was found to be significantly impaired. The same effects were also observed within the

reversal phase, with no impairment in reversal learning but a clear deficit in adaptive spatial memory. In chapter 3 we reported clear evidence demonstrating that microglial expansion is a key factor driving white matter damage and spatial learning impairments, following BCAS. Furthermore, it was demonstrated that the blockade of microglial proliferation, through GW2580 treatment, was able to protect against spatial learning impairments following BCAS but was unable to rescue spatial memory deficiencies. In the present study, we observed a lack of microglial expansion within $Cx_3Cr_1^{eGFP/+}$ mice in response to BCAS, which was associated with impaired spatial memory but not learning. These findings provide additional evidence to suggest that microglial expansion is a key factor driving spatial learning, but not memory impairments, following BCAS.

It therefore seems apparent that Cx_3Cr_1 receptor heterozygosity protects against BCAS mediated impairments in spatial learning through the prevention of microglial expansion. In support of our findings, reduced expression of Cx_3Cr_1 through siRNA targeting within a BCAS model was shown to attenuate microglial activation, white matter lesions and cognitive deficits (Liu et al., 2015). Furthermore, in an animal model of global cerebral ischemia, treatment with an antibody against the Cx_3Cr_1 receptor was found to inhibit microglial activation leading to the alleviation of cognitive impairment, neuronal loss and myelin deficits (Du et al., 2020). In contrast to our findings, research conducted within Cx_3Cr_1 receptor heterozygous mice, without an additional insult, reported intact spatial learning but deficient spatial memory as assessed via the hidden-platform water maze task. Cognitive deficits within Cx_3Cr_1 receptor heterozygous mice were found to correlate with a significant reduction in synaptic plasticity and hippocampal neurogenesis, despite unaltered microglial populations (Rogers et al., 2011). In the present study however, we found that spatial learning and memory was intact within $Cx_3Cr_1^{eGFP/+}$ sham mice. This may be a reflection of the different behavioural paradigms used, with the water maze being known to elicit much stronger stress responses than the Barnes maze (Pompl et al., 1999). It could therefore be the case that excessive stress can elicit spatial memory deficits, within $Cx_3Cr_1^{eGFP/+}$ mice, which are not apparent in the less stressful context of the Barnes maze.

Taken together these data would indicate that rescued spatial learning following BCAS is due to a lack of microglial response within Cx_3Cr_1 receptor heterozygous mice. It is important to note however, that the present study assessed spatial learning and memory within a milder BCAS model, at a more chronic timepoint then that reported within chapter 3.

Spatial memory, however, was found to remain impaired following BCAS. These observations further strengthen the theory that spatial memory deficits following BCAS are independent of microglial expansion. It would be important, however, to further confirm this

association by assessing white matter damage within Cx_3Cr_1 heterozygous mice following BCAS. As, within chapter 3, improvements in spatial learning were found to strongly correlate to reduced microglial numbers and reduced white matter damage following GW2580 treatment.

4.4.6 Microglial density remains unaltered following BCAS within $Cx_3Cr_1^{eGFP/+}$App23 mice

Having demonstrated a lack of microglial responses within $Cx_3Cr_1^{eGFP/+}$ mice following BCAS, the next aim was to determine if this effect is still apparent under co-morbid conditions. BCAS was carried out on App23 transgenic mice to create an additional challenge leading to a more significant insult. Previous research into aged App23 mice showed a clear increase in microglial related gene expression over-time, with a progressive increase in markers associated with microglial activation such as CD68 (Janssen et al., 2017). In the present study microglial structure and function were assessed within $Cx_3Cr_1^{eGFP/+}$App23 mice following short-term BCAS with a broader examination of microglial expansion conducted, more chronically, 3-months following surgery. Under all the conditions by which microglia were assessed within $Cx_3Cr_1^{eGFP/+}$App23 mice, with and without BCAS surgery, no apparent differences were detected. These findings directly contradict previous research which demonstrated that BCAS within App23 mice led to an exaggerated microglial response, identified by increased cell numbers in both white and grey matter regions in comparison to App23 shams (Zhai Y Fau - Yamashita, Yamashita T Fau - Nakano, Nakano Y Fau - Sun, Sun Z Fau - Shang, et al., 2016). A lack of altered microglial process dynamics also contradicts work conducted within the 5xFAD model of AD, which reported hyper-motile process movement within $Cx_3Cr_1^{eGFP/+}$ mice (Gyoneva, Swanger, Zhang, Weinshenker, & Traynelis, 2016). Although, the 5xFAD mouse line is a more aggressive model of amyloid accumulation and all motility changes were observed in close proximity to cortical beta-amyloid plaques.

In the present study therefore, we have shown an absence of microglial responses within $Cx_3Cr_1^{eGFP/+}$ mice, not only in the presence of increased amyloid, but also in the co-morbid situation of increased amyloid and BCAS.

4.4.7 Impaired neurovascular coupling responses following BCAS within $Cx_3Cr_1^{eGFP/+}$App23 mice

As discussed previously, neurovascular coupling deficiencies within $Cx_3Cr_1^{eGFP/+}$ mice were found to be unimpaired following BCAS. Here, however, neurovascular coupling deficiencies were detected within $Cx_3Cr_1^{eGFP/+}$App23 mice, 3-months following BCAS

surgery. $Cx_3Cr_1^{eGFP/+}$App23 sham mice, however, displayed normal neurovascular coupling responses, thus indicating that a co-morbid situation was required to trigger impairments.

Previous investigations have demonstrated that App23 mice develop cerebral amyloid angiopathy (CAA) progressively, from 8 months, with substantial deposits from 14-21 months (Calhoun et al., 1999; D. T. Winkler et al., 2001). Multiphoton imaging studies have demonstrated that CAA can form tight banded structures around vessels, creating an exoskeleton-like structure, acting to physically restrict hemodynamic responses as well as displace astrocytic end-feet which are crucial for neurovascular coupling (Kimbrough, Robel, Roberson, & Sontheimer, 2015). However, the present study was conducted with mice aged 12-months old and therefore substantial CAA deposits are yet to form. Interestingly, work within our group has previously shown, in models of amyloidosis, that BCAS surgery causes a redistribution of amyloid aggregates from the parenchyma to the vessels (Salvadores et al., 2017). This evidence, therefore, could explain why neurovascular coupling deficits are only apparent in $Cx_3Cr_1^{eGFP/+}$App23 mice when subjected to BCAS. In the present study, BCAS could be exacerbating vascular amyloid accumulation leading to increased CAA formation, resulting in impairments in neurovascular coupling responses either directly by physically restricting vessels and dislodging astrocytic end-feet or indirectly through the onset of inflammation. To prove such a theory additional experiments would be required using amyloid markers such as methoxy-XO4 and multiphoton microscopy to track the onset of CAA within the somatosensory cortex of mice following BCAS surgery. Such dynamic imaging approaches would allow hemodynamic responses following whisker stimulation to be conducted *in vivo* in real time alongside CAA assessment of the same vessels. Thus, potentially providing *in vivo* real time assessments of blood vessels longitudinally as CAA deposits form following BCAS surgery. Alternatively, *in vivo* multiphoton experiments have demonstrated that Aβ peptides themselves can act on cerebral arteries to cause localised constriction, through the release of reactive oxygen species (Niwa et al., 2001). These localised constriction events, therefore, alongside BCAS mediated endothelial stress, could coincide to lead to impairments in neurovascular coupling responses. Additional experiments, however, would be required to confirm the presence of Aβ peptides in the vicinity of poorly responding cerebral arteries to confirm such a relationship.

4.4.8 Impaired spatial learning and memory within $Cx_3Cr_1^{eGFP/+}$App23 mice, with no clear additional BCAS mediated impairment

Neurodegenerative diseases such as AD, are characterised by spatial memory deficits (Kaskie & Storandt, 1995). Previous studies, using the App23 mouse line, have demonstrated significant impairments in spatial learning and memory, as measured by the Barnes maze, at 12-months of age (Prut et al., 2007). It has also been demonstrated that severe BCAS leads to more significant memory impairments within APPswe/PS1 mice, which is associated with increased microglial dysfunction (Maude Bordeleau, Ayman ElAli, & Serge Rivest, 2016). Therefore, the aim was to determine if Cx_3Cr_1 receptor heterozygosity could rescue the cognitive impairments previously identified within App23 mice at 12-months of age, and to determine if this benefit would extend to a co-morbid situation. Within, both training and reversal phases both $Cx_3Cr_1^{eGFP/+}$App23 sham and BCAS groups showed a degree of learning. However, when learning profiles were compared to $Cx_3Cr_1^{eGFP/+}$ sham mice, $Cx_3Cr_1^{eGFP/+}$App23 sham mice demonstrated a significantly impaired rate of learning. Training and reversal probes highlighted significantly impaired spatial memory in both $Cx_3Cr_1^{eGFP/+}$App23 sham and BCAS groups.

Within $Cx_3Cr_1^{eGFP/+}$App23 mice we have demonstrated a lack of microglial response following BCAS surgery, however spatial learning and memory deficits were still identified with no apparent additional BCAS mediated deficit. These data indicate that spatial learning deficits, within $Cx_3Cr_1^{eGFP/+}$App23 mice, are not mediated by white matter microglial expansion, as was determined to be the cause in chapter 3. Previous studies within App23 transgenic mice have demonstrated hippocampal loss of cell bodies adjacent to Aβ peptide deposits at 12-months of age (Sturchler-Pierrat et al., 1997). Studies have also reported hippocampal CA1 neuronal loss (Calhoun Me Fau - Wiederhold et al., 1998) and altered synaptic function within aged App23 mice (Roder et al., 2003). It is therefore likely that neuronal damage and altered synaptic signalling within the hippocampus underlie cognitive deficits, within $Cx_3Cr_1^{eGFP/+}$App23 mice, independent of microglial expansion and activation.

4.4.9 Study limitations and future directions

One limitation of the present study was the lack of pathological insight. For example, an assessment of white matter damage would have been advantageous to help further strengthen the link established within chapter 3, that the blockade of white matter expansion prevents white matter damage and cognitive impairment following BCAS. The current study is also

lacking any detailed information regarding the soluble and insoluble burden of Aβ. Evidence of the relocation of Aβ from the parenchyma to cerebral vessels following BCAS has previously been reported in another amyloidosis model (Salvadores et al., 2017). If such a change were apparent in the present study, this could provide mechanistic insight to explain neurovascular coupling deficiencies within App23 mice following BCAS.

The study also lacks a more detailed evaluation of microglial activation. Although, structural analysis demonstrated no change, indicative of a homeostatic state, this evaluation was only completed 1-week following BCAS surgery. Therefore, information regarding microglial activation state at the more chronic 3-month time-point was not generated. In our present cranial window set up, window clarity cannot be guaranteed at such timepoints due to excessive regrowth. Microglial activation, at chronic time-points, could however be assessed using immunohistochemical markers such as Lamp2 or CD68, or alternatively through qPCR evaluation of genes associated with activation such as the pro-inflammatory cytokines TNF-α and IL-1β.

A fundamental issue with the study design was the lack of adequate wild-type mice to enable comparisons to be directly made to outcomes within $Cx_3Cr_1^{eGFP/+}$ mice. This, however, was out of our control as the original aim of this study was to track microglial responses following BCAS, with the notion that the widely used $Cx_3Cr_1^{eGFP/+}$ mouse line had normally functioning microglia. We were, however, able to make comparisons to previously published data which was gathered within comparable aged mice with the similar durations of BCAS surgery. Therefore, the addition of such comparisons to wild-type data helped elucidate key differences in functional and cognitive outcomes following BCAS surgery within $Cx_3Cr_1^{eGFP/+}$ mice. Future studies, however, could make use of the newly developed transgenic microglial mouse lines which achieve microglial visualisation without a loss of Cx_1Cr_1 receptor expression (Miron & Priller, 2020). A comparison between BCAS mediated microglial changes within $Cx_3Cr_1^{eGFP/+}$ mice and reporter lines without Cx_1Cr_1 receptor targeting would help clearly demonstrate the role of Cx_1Cr_1 receptor signalling in such responses.

In the present study microglial process dynamics were assessed, *in vivo*, under the anaesthetic isoflurane. Recent evidence has emerged, however, suggesting that microglial behaviour, with reference to process dynamics, can be influenced differentially depending on the anaesthetic used. For example, both acute and chronic cranial window preparations found that isoflurane increased the length of surveillant microglial processes when compared to awake mice (Sun et al., 2019). The effect of arousal state therefore, appears to have a significant impact on process motility, with awake mice showing reduced process motility in comparison to anaesthetised mice (Stowell et al., 2019). It is therefore important in future

studies to employ multiphoton set-ups that can be performed within awake mice, to ensure that anaesthetic effects do not cloud true pathological differences.

4.5 Conclusion

In the present study, within $Cx_3Cr_1^{eGFP/+}$ mice, microglial were shown to be unchanged alongside intact neurovascular coupling and spatial learning following BCAS. The replacement of 1 copy of the Cx_3Cr_1 receptor was found to lead to a ≈5-fold reduction in receptor expression. Thus, suggesting that fractalkine signalling may be an important pathway by which microglial proliferation and activation can be initiated following BCAS. The addition of amyloidosis, as a comorbidity, led to neurovascular coupling and spatial learning and memory deficits despite the absence of microglial expansion. Indicating that the presence of increased amyloid alone triggers other neuro-glial-vascular unit changes leading to damage and dysfunction, independent of microglial expansion. The present study therefore highlights, the Cx_3CL_1-Cx_3Cr_1 signalling pathway as a key potential mechanism by which microglial proliferate and activate in response to BCAS.

Chapter 5

Investigating dynamic alterations within the cerebrovasculature in response to BCAS with the use of intravital imaging

5.1 Introduction

The development of intravital multiphoton imaging approaches within chapter 4 provided a unique opportunity within the laboratory to evaluate, *in vivo*, dynamic microglial processes in the context of VCI. These technologies have been scarcely used in the field of VCI, and therefore the aim of the present study was to use multiphoton microscopy to allow dynamic changes within the cerebrovasculature to be assessed following BCAS.

There is increasing evidence from epidemiological, clinical and experimental studies to suggest that cerebrovascular damage and dysfunction play a fundamental role in the pathogenesis of many types of dementia (Toth et al., 2017). Furthermore, endothelial dysfunction has been highlighted as an initiating mechanism driving downstream pathological processes, including microvascular inflammation, contributing to the onset and progression of VCI (Poggesi A Fau - Pasi et al., 2016; J. M. Wardlaw et al., 2013).

The endothelium dynamically regulates the inflammatory response within the brain through control of vascular permeability to peripheral macromolecules and leukocytes (Videm & Albrigtsen, 2008). In response to an array of different compounds, endothelial cells can become activated leading to increased surface expression of adhesion molecules (Videm & Albrigtsen, 2008). Adhesion molecules interact with leukocytes travelling within the blood stream triggering down-stream proinflammatory signalling cascades (Schnoor et al., 2015). The shedding and circulation of these adhesion molecules, following endothelial activation, may therefore reflect endothelial dysfunction and/or microvascular inflammation (Poggesi et al., 2016). In support of this, increased soluble ICAM-1 levels ,within human patients, have been observed in alongside lacunar infarcts and WMH (Han et al., 2009; Hassan et al., 2003), with longitudinal MRI studies also showing an association between increased ICAM-1 levels and WMH progression (Markus et al., 2005).

A role for endothelial dysfunction and microvascular inflammation has also been demonstrated within animal models of BCAS. Microarray analysis conducted 3-days following BCAS revealed alterations within endothelial related genes alongside increased pro-inflammatory associated genes (Reimer et al., 2011). ICAM-1 expression was also shown to be significantly increased subcortically at 3-months following BCAS, which was associated with poorer cognitive outcomes (Kitamura et al., 2017).

Alongside roles in vascular permeability and inflammation, the endothelium has also been proposed to facilitate the transport and clearance of waste products from the brain. Perivascular spaces are compartments that form around the surface of blood vessels within the brain (Jeffrey J. Iliff et al., 2013b). A key role of these spaces is to facilitate the exchange of brain interstitial fluid (ISF) and cerebral spinal fluid (CSF), which allows the clearance of interstitial solutes and waste products from the brain parenchyma, in a process known as paravascular drainage (Abbott, 2004; Cserr Hf Fau - Ostrach & Ostrach, 1974; S. Yamada et al., 1991). Vascular pulsation, generated through spontaneous arteriole smooth muscle contractions, has been proposed as the predominant driving force facilitating paravascular drainage pathways (MacGregor Sharp et al., 2020). Such mechanisms are therefore fundamental to the clearance of potentially harmful waste products from the brain (Jeffrey J. Iliff et al., 2013b). However, the function of pulsatory mechanisms in the context of BCAS has never been studied.

Therefore, the aim of the present study was to use multiphoton microscopy to access endothelial dysfunction and activation, alongside pulsatory mechanisms *in* vivo following BCAS.

5.1.1 Hypothesis

This study tests the hypothesis that BCAS causes vascular dysfunction resulting in endothelial cell activation and impaired vascular pulsation leading to the onset of neuro-glial-vascular damage through downstream signalling to the immune system.

5.1.2 Aims

Using a model of BCAS within wild-type C57BL/6J mice, alongside intravital multiphoton microscopy, the studies aimed to:

1. Assess temporal changes in CBF following 4-weeks of BCAS
2. Assess RBC velocity, within leptomeningeal veins and arteries, following 4-weeks of BCAS
3. Assess changes in vascular pulsation in response to 4-weeks of BCAS
4. Determine if leukocyte trafficking behaviours, within leptomeningeal veins and arteries, are altered in response to 4-weeks of BCAS

5.2 Materials and Methods

5.2.1 Experimental mice

Adult male C57BL/6J mice were used for all experiments and were group housed on a 12-hour light and dark cycle with ab libitum access to food and water. For the studies described in this chapter, 2 cohorts of mice were used. Initially a cohort of 6 C57BL/6J mice were used to ensure that RBC velocity could be accurately measured via multiphoton microscopy in our hands. For all remaining experiments, a second cohort of 18 mice were used. At the start of the experiment all mice were coded and randomly assigned to different experimental groups, to ensure that all investigators were blinded to surgical status for the duration of experiments and analysis. Mice were separated into sham (n=8) and BCAS groups (n=10) randomly. Details of group numbers and exclusions can be found in the relevant methods sections below, alternatively an overall summary can be found within Table 5.1.

Table 5.1 Number of mice within each experimental group with details of exclusions

RBC velocity optimisation cohort	C57BL/6J	
Cranial window surgery	*6*	
Exclusion criteria:		
Cranial window detachment	*0*	
Final group	*6*	
1-month study cohort	*Sham*	*BCAS*
Sham/BCAS surgery	*8*	*10*
Exclusion criteria:		
Cranial window detachment	*1*	*0*
<25% CBF reduction following BCAS surgery	*0*	*3*
Finals groups	*7*	*7*

5.2.2 Bilateral common carotid artery stenosis

Bilateral common carotid artery stenosis (BCAS) surgery was performed according the method previously described (Section 2.2). For the present study, a milder form of BCAS was achieved through the application of 0.18mm diameter micro-coils to both the left and right

common carotid arteries. As a control for all experiments sham mice underwent an identical procedure with the only exception being the application of micro-coils. All mice recovered well following surgery and therefore no mice were excluded due to poor health.

5.2.3 Craniotomy and cranial window surgery in preparation for multiphoton microscopy

Cranial window surgery was carried out 4-weeks prior to multiphoton microscopy according to the method outlined within Section 2.4. Strict exclusion criteria were applied to minimise any effect of cranial window implantation on the neuro-inflammatory response (detailed in Section 2.4). According to these criteria 1 sham mouse was excluded due to a cranial window detachment (Table 5.1)

5.2.4 Laser speckle imaging to measure cortical cerebral blood flow

Laser speckle imaging was used to assess CBF within sham and BCAS mice following surgery as previously described in Section 2.3. For the present study, scalp opening, and retraction was not necessary as imaging could be performed directly through the cranial window. Blood flow was analysed at baseline, 24-hours, 1-week, and 1-month following surgery. A total of 3 BCAS mice were excluded from the study due to no obvious blood flow reductions 1-week following BCAS surgery (Table 5.1).

5.2.5 Multiphoton microscopy

Multiphoton microscopy was carried out using the set-up and parameters detailed within Section 2.5. Approximately 30-minutes prior to imaging, mice receive a tail vein injection of 100µl fluorescein isothiocyanate (FITC)-dextran (15mg/ml) to allow the cerebral vasculature to be visualised (Table 2.2). Multiphoton imaging was performed 4-weeks following sham/BCAS surgery and 8-weeks following cranial window surgery.

5.2.6 In vivo cerebral RBC velocity measurement via line scan analysis

The assessment of RBC velocity was carried out using line scans and assessed according to the method outlined in Section 2.5.3. RBC velocity was assessed within 5 veins and 5 arteries per mouse. The values for each vessel type were averaged and presented as median±interquartile range. Strict exclusion criteria were applied, such that any linescan

recording whose quality was not sufficient to give accurate readings of RBC velocity were excluded (detailed within Section 2.5.3). Based on these criteria 5 veins and 6 arteries were excluded from sham mice and 3 veins and 2 arteries were excluded from BCAS mice.

5.2.7 *In vivo* vascular pulsation measurement via line scan analysis

Cerebral vascular pulsatility was evaluated with the use of multiphoton microscopy as detailed within Section 2.5.4. Briefly, the pulsatility of individual vessels was determined by positioning linescans orthogonal to the vessel's axis. To calculate dynamic vessel width changes over time, vessel width (μm) within each region was plotted against time (ms). Vessel wall pulsatility (μm per ms) was calculated from the resulting graphs as the absolute value of area under the diameter-time plot, integrated to the running average calculated across the entire 3600ms sampling time. To calculate the total number of dynamic vessel pulses (pulsation frequency) across the sampling time, the total number of peaks were also calculated from the same diameter-time plots.

5.2.8 *In vivo* assessment of leukocyte trafficking behaviours

The i*n vivo* assessment of leukocyte trafficking behaviours was carried out according to method outlined within Section 2.5.5. Leukocyte rolling and adhesion were assessed, and values summated to calculate leukocyte trafficking per 100μm per minute. Leukocyte trafficking was calculated within 5 secondary leptomeningeal veins and 5 secondary leptomeningeal arteries per mouse and values were averaged. Due to the positioning of the cranial window, 1 sham mouse only had 3 secondary veins visible and therefore assessed. In terms of secondary arteries only 3/5 were visible in 1 sham animal and 4/5 for 1 BCAS mouse.

5.2.9 Statistical analysis

Statistical analysis was performed using SPSS (v22, IBM Corp.) and Prism (v8, GraphPad Software Inc, La Jolla, USA) software packages. Repeated measures one-way ANOVA's were used to assess CBF differences as well as RBC velocity within veins and arteries over-time. Independent samples Mann-Whitney U tests were used to analyse sham and BCAS differences in RBC velocity, vein/artery widths used for RBC assessment, pulsation area, pulsation frequency, widths of vessels used for pulsation assessments, and leukocyte trafficking. Correlations were analysed using the Spearman's ranked correlation coefficient. For parametric statistical tests, data is presented as mean ± standard error of the mean (SEM) and for nonparametric testing data is presented as median ± interquartile range (IQR) (specified in

relevant figure legend). Vessel wall pulsatility (μm per ms) was calculated as the absolute value of area under a plot of vessel diameter versus time, integrated to the running average calculated across the entire 3600ms sampling time. To calculate the total number of dynamic vessel pulses (pulsation frequency) across the sampling time, the total number of peaks were also calculated from the same diameter-time plots. All statistical analysis was completed within SPSS, apart from vascular pulsation assessments, which were analysed using Prism software. Statistical significance was determined at $p<0.05$.

5.2.10 Experimental contributions

The majority of experiments and analysis detailed within this chapter were conducted by myself. The studies, however, were also supported by Dr Juraj Koudelka and Professor Karen Horsburgh. I performed multiphoton imaging and completed all the data analysis presented. Dr Juraj Koudelka performed cranial window surgery and operated the software for image capture during multiphoton imaging sessions. Professor Karen Horsburgh carried out sham and BCAS surgery on all mice.

5.3 Results

5.3.1 Cerebral blood flow is significantly and persistently reduced following BCAS

Results to date have demonstrated a robust, predominantly microglial, inflammatory response following BCAS leading to white matter damage and cognitive impairments. The mechanisms by which BCAS stimulates neuroinflammatory responses, however, remain largely unknown. In the present study we employed a mild BCAS model and selected a timepoint following surgery at which pathological damage and cognitive impairments are not yet present. The aim was to try and uncover early mechanisms by which BCAS stimulates the activation and proliferation of microglial cells leading to neuroinflammation, white matter damage and spatial learning impairments.

Initially laser speckle imaging was employed to confirm mild CBF reductions following BCAS surgery, as well as to allow the exclusion of any mice that show resistance to BCAS surgery (Figure 2.2). Laser speckle analysis was conducted directly through the cranial window at baseline, 24-hours, 1-week, and 4-weeks following surgery (Figure 5.1). BCAS surgery elicited a ≈30% reduction in CBF, which decreased further to a ≈50% reduction at 1-week, finally stabilising at a ≈30% reduction by 4-weeks following surgery. Sham mice demonstrated stable CBF values across the same period (Figure 5.1A). Statistical analysis revealed a significant overall effect of time ($F_{(1.5,10.7)} = 16.057$, $p<0.01$), group ($F_{(1,7)} = 13.851$, $p<0.01$) as well as a significant time-group interaction ($F_{(1.5,10.7)} = 11.926$, $p<0.01$) (Figure 5.1A). Bonferroni *post hoc* analysis revealed that BCAS surgery elicited a significant reduction in blood flow at 24-hours (Sham; 103.02%±4.7, BCAS; 69.50%±8.6, $p<0.05$), 1-week (Sham; 95.06%±6.0, BCAS; 50.84%±7.1, $p<0.01$) and 4-weeks (Sham; 101.96%±5.5, BCAS; 70.61%±7.7, $p<0.05$) following surgery when compared to shams (Figure 5.1A).

Overall, these data show a modest reduction in CBF following BCAS surgery which is maintained over the course of the study.

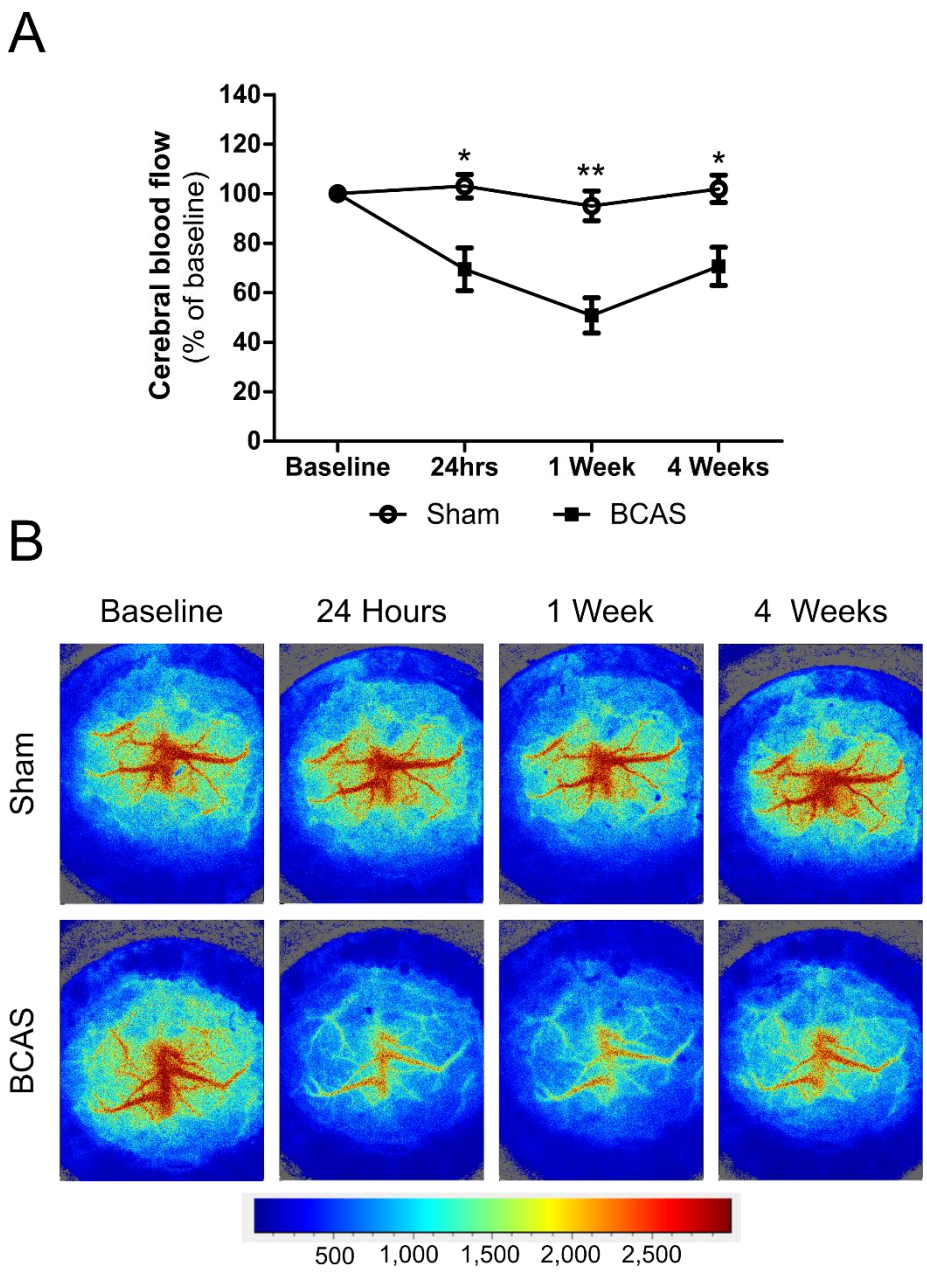

Figure 5.1 BCAS induces a sustained reduction in CBF. **(A)** BCAS surgery reduced CBF by ≈30%, with sham mice showing stable blood flow over the same period. Data presented as Mean±SEM. *p<0.05, **p<0.01. **(B)** Representative images displaying laser speckle imaging of the cerebral vasculature within sham and BCAS mice at baseline, 24-hours, 1-week, and 1-month following surgery. Blue colours represent low and red high blood flow.

5.3.2 RBC velocity can be accurately and reliable measured *in vivo* via multiphoton microscopy

Laser speckle imaging allows superficial cortical blood flow responses to be tracked following BCAS surgery, however this method only generates an overview of blood flow changes and provides no information regarding more subtle changes to the cerebral vasculature. Here, multiphoton microscopy was applied to allow individual vessels to be analysed following BCAS allowing a more detailed evaluation of BCAS mediated vascular flow changes.

The first aim was to assess red blood cell (RBC) velocity within individual leptomeningeal veins and arteries of the cortex to determine if BCAS surgery leads to altered blood flow within individual vessels. As this method was new to the group, it was important to first optimise multiphoton imaging protocols to allow RBC velocity to be calculated accurately and reliably. To image the cerebral vasculature, *in vivo*, mice were fitted with cranial windows 4-weeks prior to imaging to allow any procedural inflammation to resolve. The cerebral vasculature was then visualised through the introduction of a FITC-dextran tracer via the tail vein. Veins and arteries were distinguished based on structure as well as direction of blood flow, with veins having convergent, and arteries divergent, flow. To image RBCs flowing through individual vessels, high speed line scans were captured. The slope of each RBC within the line scan image was calculated to generate a RBC velocity value for each vessel (Figure 5.2). RBC velocity values were gathered for leptomeningeal veins (8.61±3.85) (Figure 5.2A) and arteries (12.04±5.49) (Figure 5.2B) and were found to fall within the range of values previously reported within the literature (Veins: 3.9-9.2mm/s, Arteries: 8.4-23mm/s) (Figure 5.2C). Having demonstrated the accuracy of the imaging setup, the reproducibility of the method was then tested by longitudinal RBC velocity measurements, of the same vessels, at baseline, 1-week, and 6-weeks (Figure 5.2D). No significant differences were identified between values gathered across imaging sessions within veins ($F_{(2,10)}$ = 1.150, p=0.36) or arteries ($F_{(2,8)}$ = 0.985, p=0.42) (Figure 5.2D).

Overall, these data demonstrate that RBC velocity can be accurately and reliably measured, *in vivo*, by multiphoton microscopy.

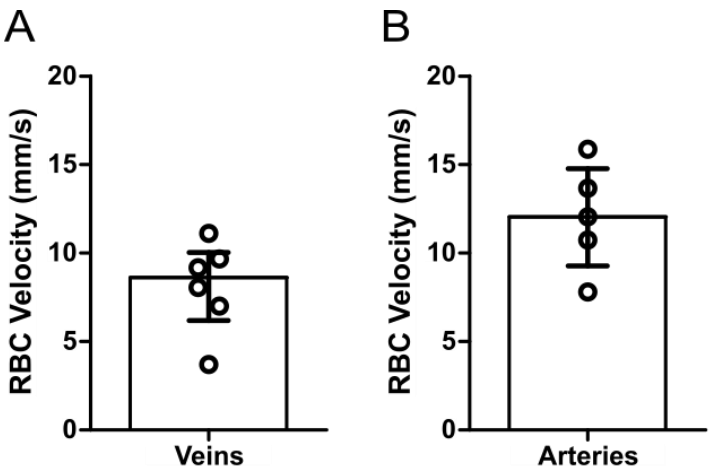

C

Publication	Vessels Analysed	Reported Speed (mm/second)
Kim et al 2012	Veins Arteries	5.9-9.2 14.1-23
Schaffer et al 2006	Veins Arteries	3.9-8.5 8.4-12.5
Ishikawa et al 2016	Arteries	10.4-14.8
Literature range	Veins Arteries	3.9-9.2 8.4-23

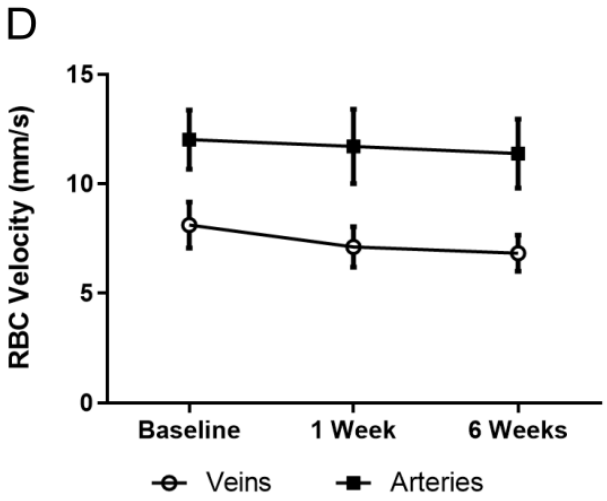

Figure 5.2 RBC velocity measurements align with previously published data. Line scanning was used to measure RBC velocity within leptomeningeal veins and arteries. Line scans were gathered from 2 veins and 2 arteries per mouse and values were averaged to give a RBC velocity value (mm per second). RBC velocity was found to be 9.2±4.5 mm/s in veins **(A)**, and 12.0±5.5 mm/s in arteries **(B)**. Values presented as median±interquartile range. **(C)**

Values published within the literature using multiphoton microscopy and line scanning methods to assess RBC velocity. **(D)** Repeated measurements of the same veins and arteries across multiple imaging sessions were found to be consistent. Values presented as mean± SEM.

5.3.3 RBC velocity is significantly reduced following BCAS

Having demonstrated the accuracy and reliability of *in vivo* RBC velocity measurements, the next aim was to investigate the impact of BCAS on these measures. Following the 4-week rest period after cranial window implantation, mice underwent sham/BCAS surgery and RBC velocity was assessed 1-month later (Figure 5.3). Line scan analysis within leptomeningeal veins revealed a significant reduction in RBC velocity within BCAS mice (4.44±7.49) when compared to shams (10.47±6.75) ($U=8.00$, $p<0.05$) (Figure 5.3A). The same effect was also observed within leptomeningeal arteries, with BCAS mice showing significantly reduced RBC velocity values (12.24±4.66) when compared to shams (19.13±6.52) ($U=4.00$, $p<0.01$) (Figure 5.3B). To ensure that these findings could not be attributed to differences in the size of vessel analysed, average vessel width was compared between sham and BCAS mice (Figure 5.3C/D). Statistical analysis revealed no significant differences between vessel widths of veins and arteries imaged from sham (veins: 58.78µm±29.95, arteries: 37.94µm±9.49) and BCAS mice (veins: 60.24µm±14.74, arteries: 39.57µm±6.04) (veins: $U=25.00$, $p=1.00$, arteries: $U=33.00$, $p=0.318$) (Figure 5.3C/D).

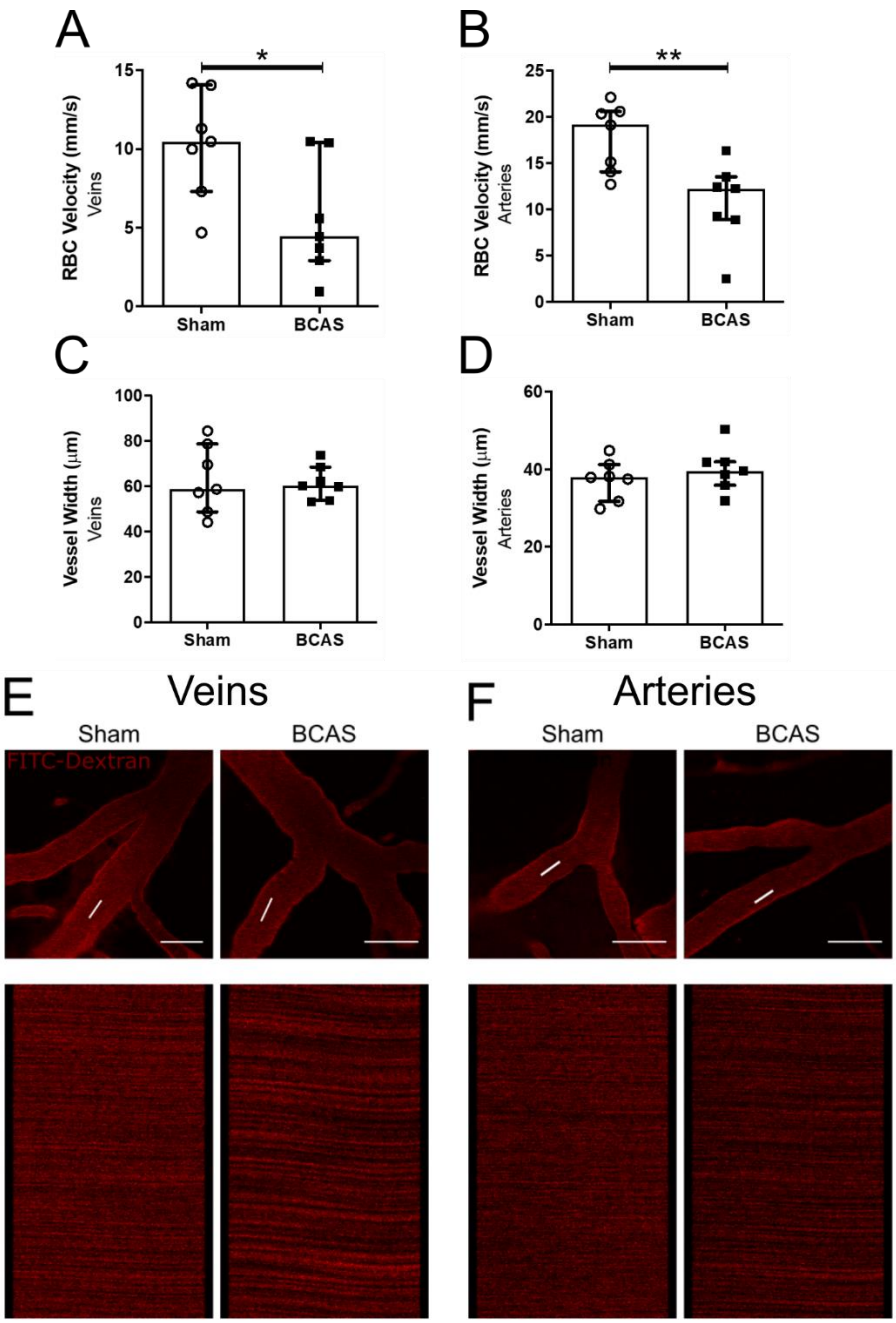

Figure 5.3 RBC velocity is significantly reduced following BCAS. RBC velocity was found to be significantly reduced within leptomeningeal veins **(A)** and arteries **(B)** following BCAS surgery. The vessel widths of both veins **(C)** and arteries **(D)** assessed for RBC velocity were found to be comparable between sham and BCAS groups. Data presented as median ± interquartile range. *p<0.05, **p<0.01. Representative images of leptomeningeal veins **(E)** and arteries **(F)** line scans taken from sham and BCAS mice 1-month following surgery. White lines indicate the position of the linescan. Scale bar 50μm.

As RBC velocity and laser speckle imaging measures had been completed within the same animals, the values were compared to assess the relationship between superficial blood flow changes and those occurring at the single vessel level (Figure 5.4). Veins RBC velocity was found to positively correlate to CBF measures at 1-month following surgery ($r_{s(7)}$ = 0.733, $p<0.05$) (Figure 5.4A). Thus, indicating that the most severe blood flow reductions following BCAS, as measured by laser speckle analysis, are associated with the slowest RBC velocities within secondary leptomeningeal veins. Artery RBC velocity was then compared to 1-month laser speckle blood flow (Figure 5.4B). Statistical analysis revealed a trend for a positive correlation between artery RBC velocity and superficial blood flow measurements ($r_{s(7)}$ = 0.650, p=0.058) (Figure 5.4B).

Overall, these data demonstrate that BCAS induced reductions in superficial cortical flow are also reflected in significantly reduced RBC velocity within secondary leptomeningeal veins and arteries found deeper within the cortex.

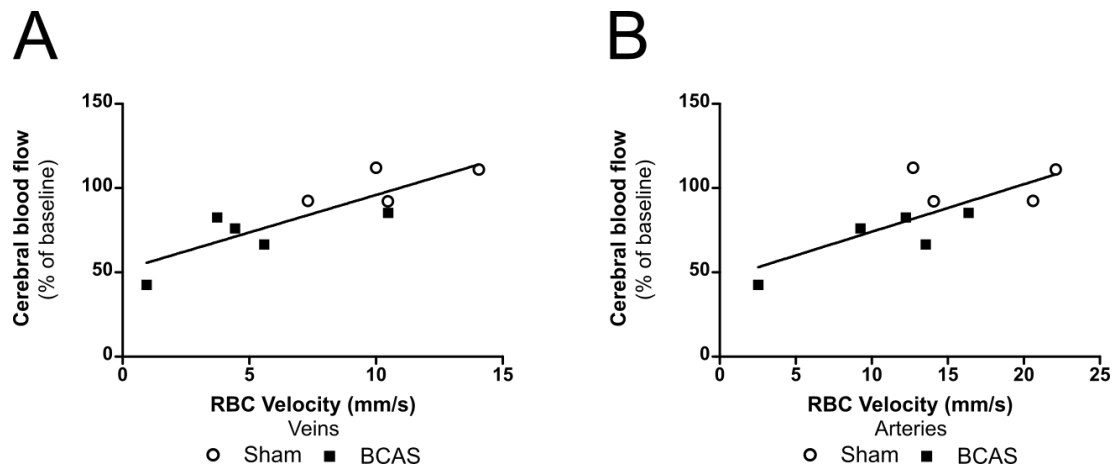

Figure 5.4 RBC velocity is positively correlated to superficial CBF measurements within leptomeningeal veins. **(A)** RBC velocity was positively correlated to superficial cortical blood flow within leptomeningeal veins. **(B)** A trend for a correlation between RBC velocity and superficial cortical blood flow was identified within leptomeningeal arteries. Data presented as Mean.

5.3.4 Arterial pulsation is significantly impaired following BCAS

Having demonstrated that BCAS leads to blood flow reductions within individual vessels of the leptomeningeal cortical vasculature, the next aim was to determine if vascular function was also impaired. Vascular pulsation is a mechanism proposed to be fundamental to paravascular CSF-ISF exchange, which is a crucial process facilitating waste clearance from

the brain (Jeffrey J. Iliff et al., 2013a). To investigate the effect of BCAS surgery on vascular pulsation, multiphoton microscopy was utilised to allow the pulsatility of individual vessels to be determined. Vascular pulsation was measured at multiple levels of the vascular tree encompassing leptomeningeal veins, ascending veins, leptomeningeal arteries, and penetrating arteries. Line scans were carried out across the width of each vessel to determine pulsation area as well as the frequency of pulsation (Figure 5.5). The area of vascular pulsation was found to be significantly reduced within the leptomeningeal arteries of BCAS mice (433.2±206.7) when compared to shams (654.2±350.8) ($U=6.00$, $p<0.05$) (Figure 5.5A). Vascular pulsation, however, was found to be unaffected within leptomeningeal veins ($p=0.45$), ascending veins ($p=0.18$) and penetrating arteries ($p=0.18$) following BCAS surgery (Figure 5.5A). The frequency of vascular pulsation was also analysed as the number of width changes (peaks) per second (Figure 5.5B). The frequency of pulsation was found to be significantly increased within the leptomeningeal arteries of BCAS mice (23.2±3.6) in comparison to shams (19.3±3.6) ($U=41.00$, $p<0.05$) (Figure 5.5B). However, no significant differences in pulsation frequency were identified within leptomeningeal veins ($p=1.00$), ascending veins ($p=0.53$) or penetrating arteries ($p=0.07$) following BCAS surgery (Figure 5.5B). To confirm that pulsation effects following BCAS were not due to differences in the width of vessels analysed, vessel widths for all vessel assessed, within sham and BCAS mice were measured and compared (Figure 5.5E). No significant differences between sham and BCAS groups were identified for vessel widths sampled from leptomeningeal arteries ($p=0.90$), penetrating arteries ($p=0.53$), leptomeningeal veins (0.53) or ascending veins (0.23) (Figure 5.5E).

Taken together these data demonstrate a vascular pulsation deficit, specifically within secondary leptomeningeal arteries, following BCAS surgery.

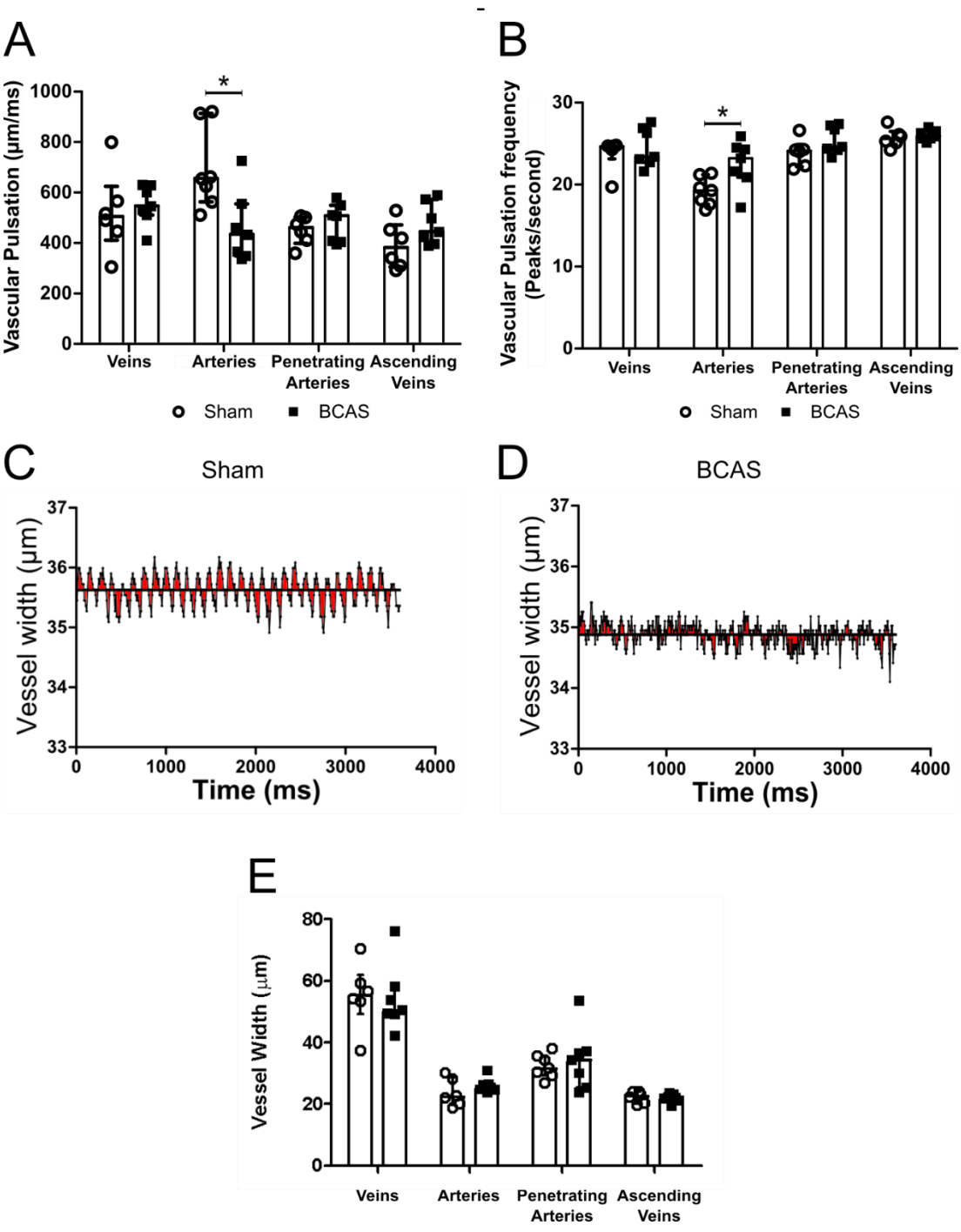

Figure 5.5 Arterial pulsation is significantly impaired following BCAS surgery. **(A)** The area of vascular pulsation was found to be significantly impaired within secondary leptomeningeal arteries following BCAS surgery. Leptomeningeal veins, ascending veins, and penetrating arteries were found to be unaltered. **(B)** The frequency of vascular pulsation was found to be significantly increased within leptomeningeal arteries of BCAS mice in comparison to shams. Frequency was found to be unaltered within the other vessels analysed.

Representative plots of vessel width changes over-time within a leptomeningeal artery taken from both sham **(C)** and BCAS mice **(D)**. Red denotes the area under the curve which is used as a measure of pulsation **(E)** The width of vessels analysed for all vessel types were found to be comparable between sham and BCAS groups. Data presented as median ± interquartile range. *p<0.05.

5.3.5 Leukocyte trafficking is significantly increased following BCAS

Having demonstrated that BCAS leads to altered blood flow and pulsation within the cerebral vasculature, the next aim was to determine if there was any evidence of endothelial cell activation following surgery. Endothelial cells can become activated in response to a wide range of signalling molecules leading to increased surface expression of adhesion molecules such as ICAM-1 and VCAM-1. Adhesion molecules act to contact peripheral immune cells within the circulation causing leukocytes to roll along the endothelial surface until enough physical bonds are formed to facilitate adherence (Videm & Albrigtsen, 2008). Such leukocyte trafficking behaviours lead to the onset of inflammatory signalling cascades and in some circumstance's extravasation of immune cells into the brain (Schnoor et al., 2015). To determine if leukocyte behaviours, associated with endothelial activation, were altered following BCAS, time-lapse recordings were carried out *in vivo* via multiphoton microscopy (Figure 5.6).

Leukocyte trafficking was found to be significantly increased within the leptomeningeal veins of BCAS mice (0.24±1.62) when compared to shams (0±0.21) ($U=40.00$, $p<0.05$) (Figure 5.6A). The percentage of leptomeningeal veins analysed that showed leukocyte trafficking was also quantified for sham and BCAS groups. The frequency of leukocyte trafficking was found to be significantly increased within BCAS mice (40±40) when compared to shams (0±20) (Figure 5.6B). Leukocyte trafficking within leptomeningeal arteries, however, was found to be extremely rare with behaviours only evident in 2 of the 70 arteries analysed across both sham and BCAS groups (Data not shown). To confirm that the cells seen travelling through the vasculature were indeed leukocytes, we injected acridine orange which is a florescent dye that specifically binds to cells containing DNA and therefore will not bind to RBCs. Acridine orange staining confirmed that these cells are indeed nucleic and therefore strongly indicates that we are observing leukocyte behaviours *in vivo* (Figure 5.6C).

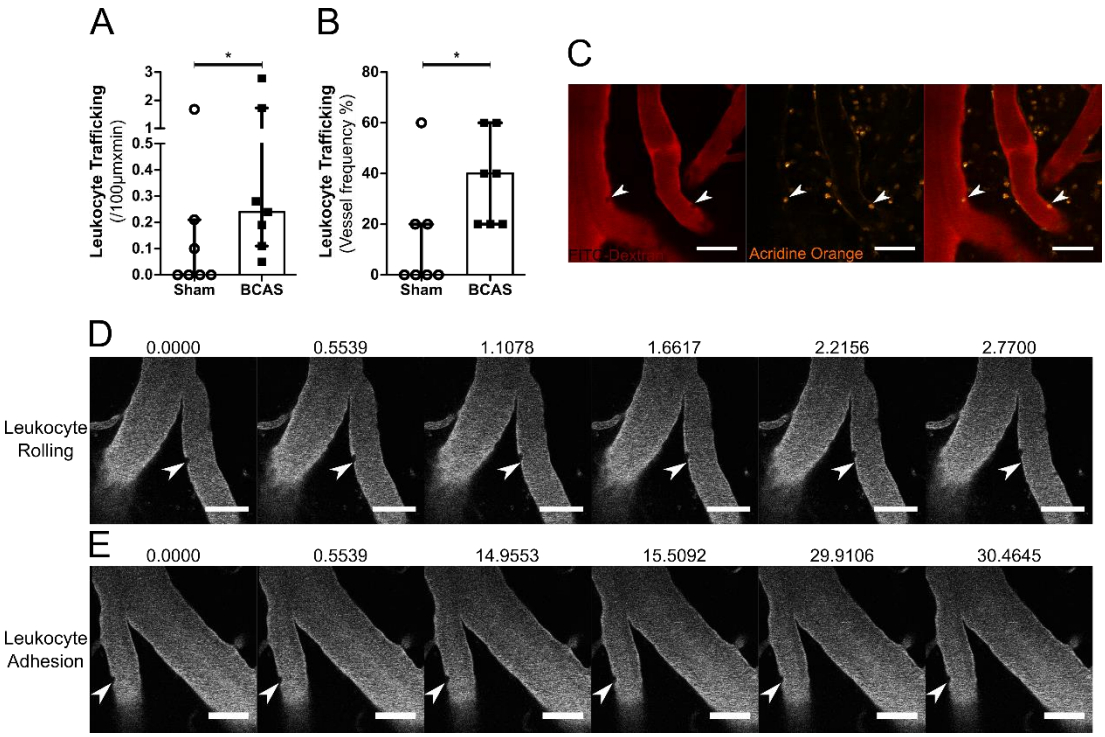

Figure 5.6 Leukocyte trafficking is significantly increased within leptomeningeal veins following BCAS. **(A)** The number of leukocytes trafficking, within secondary leptomeningeal veins, was found to be significantly increased within BCAS mice in comparison to shams. **(B)** The frequency of leukocyte trafficking events was also found to be significantly increased within leptomeningeal veins following BCAS surgery. Data presented as median± interquartile range. *p<0.05. Leukocyte trafficking within leptomeningeal arteries was observed to be extremely rare, data not shown. **(C)** Acridine orange staining confirming that the black loss of signal spheres observed contain a nucleus. White arrowhead denotes a leukocyte within the leptomeningeal vein. A sequence of images to display an example of leukocyte rolling **(D)** and adhesion **(E)**. White arrows indicate a leukocyte of interest and are positioned in the same location within every image, numbers above the image represent time in seconds.

As measures of RBC velocity had also been carried out within the same secondary leptomeningeal veins as measured here, the relationship between RBC velocity and leukocyte trafficking was assessed (Figure 5.7). Statistical analysis revealed a significant negative correlation between RBC velocity and leukocyte trafficking ($r_{s(15)}$ = -0.652, p<0.01) (Figure 5.7). Thus, indicating that as RBC velocity within leptomeningeal veins decreases the number of leukocytes trafficking along the endothelial cell wall increases.

In conclusion these data show evidence of increased leukocyte trafficking, indicative of endothelial activation, within leptomeningeal veins in response to BCAS.

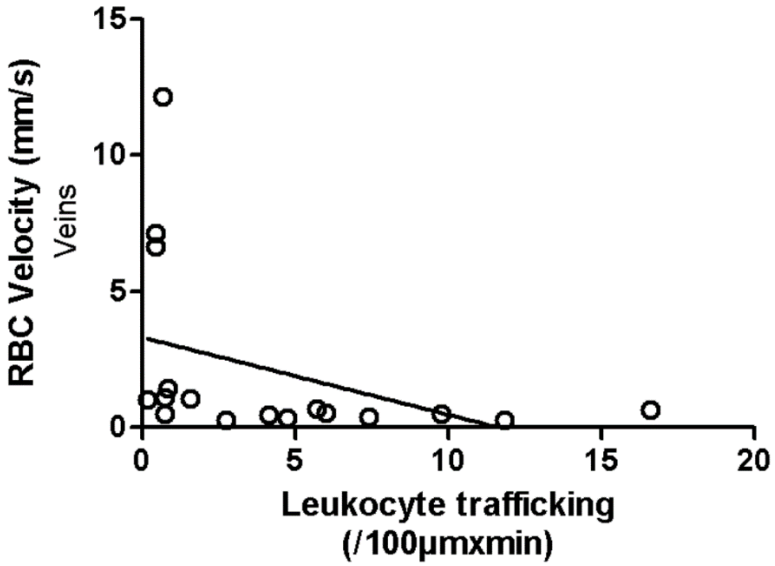

Figure 5.7 RBC velocity is negatively correlated to leukocyte trafficking. As RBC velocity within leptomeningeal veins decreases the number of leukocytes trafficking along the endothelial cell wall increases. Individual vessel data presented from both sham and BCAS mice, only leptomeningeal veins that showed some degree of leukocyte trafficking were included.

5.4 Discussion

The present study set out to utilise newly established intravital multiphoton imaging approaches to investigate dynamic alterations within the cerebral vasculature in response to BCAS. The results demonstrate that BCAS results in reduced RBC velocity alongside impaired arterial pulsation, and increased leukocyte trafficking. Taken together these findings highlight alterations in vascular mechanisms, in response to BCAS, that could lead to pathological damage and functional impairments.

5.4.1 BCAS mediated cortical blood flow reductions can be detected globally as well as at the single vessel resolution

In the present study laser speckle imaging was once again used to assess superficial CBF changes following BCAS. BCAS surgery was found to reduce blood flow by ≈30% at 24-hours, dipping to ≈50% at 1-week before stabilising at ≈30%, 1 month following surgery. Such blood flow reductions are in agreement with previous studies using the milder BCAS model including the study detailed in chapter 4 (Maki et al., 2011; McQueen et al., 2014; Nishio et al., 2010; Shibata et al., 2004). In the present study, however, laser speckle imaging was conducted directly through the cranial window, whereas previous studies had imaged through the intact skull. It is therefore, reassuring that comparable values were generated lending support to the accuracy of the laser speckle imaging set up.

The BCAS model has been shown across numerous investigations within our laboratory and others to elicit a robust and reliable reduction of CBF to the forebrain (Holland et al., 2015; Manso et al., 2017; McQueen et al., 2014; Reimer et al., 2011; Shibata et al., 2004). However, the effect of mild BCAS on the speed of RBC velocity within individual blood vessels of the cortex, had not previously been investigated. Therefore, multiphoton microscopy was employed to allow the speed of RBC velocity to be determined, *in vivo*, via line scan imaging. BCAS surgery was shown to significantly reduce the speed of RBC velocity within leptomeningeal veins and arteries. These changes are in agreement with previously published work using the mixed coil BCAS model (Yata et al., 2014). Furthermore, reduced blood flow velocity, within human patients, was shown to be associated with increasing age as well as increased white matter lesion burden (Joanna M. Wardlaw et al., 2011).

In the present study, the extent of RBC velocity reductions following BCAS were significant, with decreases of ≈47% within leptomeningeal veins and ≈39% within leptomeningeal arteries following surgery. As first order vessels have been shown to have a faster RBC velocity than those more distal to the primary vessel (T. N. Kim et al., 2012), primary vessels were tracked to branch points to ensure that only secondary vessels were

analysed. This helped to ensure that the same level of the vascular tree was being analysed across mice and surgery groups, thus helping to limit speed variations. Care was also taken to position linescans away from vessel branch points to help limit the influence of turbulent blood flow on velocity measures.

BCAS is achieved through the application of micro-coils to both the common carotid arteries delivering blood to the brain. Here we have identified that blood flow is affected within both leptomeningeal veins and arteries. Giving evidence to suggest that blood flow speeds are affected throughout the vascular tree following BCAS. Thus, lending support to the theory that blood flow is reduced throughout the brain and not preserved through compensatory mechanisms.

5.4.2 BCAS leads to impaired arterial pulsation

Vascular pulsation is a mechanism proposed to be fundamental to paravascular cerebral spinal fluid-interstitial fluid exchange, such clearance pathways function to remove harmful waste products, such as Aβ, from the brain (Carare, Hawkes Ca Fau - Jeffrey, Jeffrey M Fau - Kalaria, Kalaria Rn Fau - Weller, & Weller, 2013; Jeffrey J. Iliff et al., 2013b; Laman & Weller, 2013).

Dysfunctional waste clearance could result in harmful metabolic by-products or neuroinflammatory molecules being present within the brain for extended periods of time. The accumulation of such harmful molecules could contribute to prolonged neuroinflammatory environments leading to damage and dysfunction. In the present study we made use of high temporal resolution *in vivo* multiphoton line scanning to allow the assessment of vascular pulsation within an array of components of the vascular tree. Vascular pulsation was found to be significantly reduced within leptomeningeal arteries, with no BCAS related changes observed in the other vessels analysed. Thus, indicating a specific susceptibility within the leptomeningeal arteries. Interestingly, although vascular pulsation within leptomeningeal arteries was found to impaired, the frequency at which these vessels were pulsing was shown to be increased following BCAS. This is likely an attempt to compensate for the lack of pulsatory drive through an increase in pulsatory frequency. This compensatory mechanism, however, was shown to be insufficient to rescue pulsation deficiencies following BCAS.

Previous research into paravascular clearance pathways in response to BCAS, demonstrated significantly impaired waste clearance mechanisms (Appendix Figure 1). In agreement with these findings, impaired glymphatic influx alongside impaired arterial pulsation, were also identified following 30-minutes of unilateral ligation of the internal carotid artery (J. J. Iliff et al., 2013). However, the pulsation deficit was identified specifically

within penetrating arteries following unilateral ligation, in contrast to the leptomeningeal artery deficit identified here following BCAS surgery. This difference most likely reflects the source of insult, as BCAS is specifically restricted to the common carotid arteries whereas unilateral ligation impacts the internal carotid artery. Taken together these data demonstrate that arterial pulsation is a predominant driver of CSF-ISF exchange. Therefore, reductions in arterial pulsation, as a result of cerebrovascular disease, has the potential to impair waste clearance mechanisms allowing the build-up of toxic molecules, such as Aβ, within the aged brain (Hawkes, Jayakody N Fau - Johnston, Johnston Da Fau - Bechmann, Bechmann I Fau - Carare, & Carare, 2014). In support of this, mechanical compliance of human posterior cerebral arteries was shown be impaired within aged patients, which was associated with elastin loss and impaired responses to changes in pressure (Fonck et al., 2009). Interestingly, human population-based studies have also demonstrated a link between common carotid arterial stiffness and the occurrence of cerebral microbleeds (Ding et al., 2015). Such microbleeds are also identified following prolonged (6-month) BCAS in mice and therefore pulsatory deficiencies could potentially be the underlying cause (Holland et al., 2015).

It is important to note however, that in the present set up we are unable to rule out the contribution of cardiac derived vascular pulsations. Historically, perivascular drainage was assumed to be driven solely by the cardiac rhythm as drainage was found to cease upon cardiac arrest (Weller, Djuanda E Fau - Yow, Yow Hy Fau - Carare, & Carare, 2009). Mathematic modelling and *in vivo* multiphoton experiments, however, demonstrate that cardiac pulsation would not provide sufficient motive force and that spontaneous vasomotor contraction and relaxation of smooths muscle cells is likely the primary driver of perivascular drainage (Aldea, Weller, Wilcock, Carare, & Richardson, 2019; Diem et al., 2017; van Veluw et al., 2020).

Overall, these data demonstrate that arterial pulsation is specifically impaired following BCAS, which could lead to detrimental inflammatory responses through impaired waste clearance mechanisms, leading to the build-up of toxic molecules.

5.4.3 BCAS leads to increased leukocyte trafficking, indicative of endothelial activation

Endothelial activation can occur in response to an array of stimuli leading the increased surface expression of adhesion molecules (Videm & Albrigtsen, 2008). Adhesion molecules on the surface of activated endothelial cells act to interact with leukocytes travelling within the blood stream. Such endothelial-leukocyte interactions trigger down-stream proinflammatory signalling cascades, as well as in some cases leukocyte transmigration into the brain (Schnoor et al., 2015).

In the present study leukocyte trafficking was assessed within leptomeningeal veins and arteries of mice following 1-month of BCAS. A significant increase in the number and frequency of leukocytes trafficking was observed within leptomeningeal veins following BCAS surgery. This finding is in agreement with previous research in models of BCAS and cerebral ischemia which report a significant increase in leukocyte trafficking following CBF reductions (Kataoka, Kim Sw Fau - Plesnila, & Plesnila, 2004; Yata et al., 2014). A key difference between the current study and the past literature is the timing of observations following CBF reductions. Yata et al report a steady reduction in leukocyte trafficking from 1 day to 2-weeks following BCAS. Therefore, in our milder BCAS model it is likely that leukocyte trafficking behaviours occur later following CBF reductions, allowing trafficking to be still observable 1-month following surgery.

In the present study we identified very little evidence of leukocyte trafficking within the leptomeningeal veins of sham mice. Which is in agreement with previous research that found, under normal conditions, leukocyte trafficking within leptomeningeal veins to be extremely rare or even entirely absent (Kataoka et al., 2004; Yata et al., 2014). Leukocyte trafficking within leptomeningeal arteries was also found to be at extremely low levels within both sham and BCAS mice. These findings are in agreement with the previous literature (Kataoka et al., 2004; Yata et al., 2014) and is consistent with the widely regarded notion that post capillary venules are the primary site of vascular permeability in response to inflammation (dela Paz & D'Amore, 2009). An observation which has been attributed to the fact that the venous vasculature possess a slower flow rate, thinner walls and fewer tight junctions in comparison to their arterial counterparts and therefore is better suited to the dynamics of leukocyte trafficking (dela Paz & D'Amore, 2009).

The studies detailed within chapters 3 and 4 have clearly demonstrated that endogenous brain microglia are key drivers of neuroinflammation and white matter damage following BCAS. However, the signalling mechanisms by which microglia become activated and proliferate in response to BCAS remain unclear. Within the present study leptomeningeal veins were shown to have increased leukocyte trafficking following BCAS, indicating increased endothelial activation. In response to certain stimuli, such as severe cerebral hypoperfusion, leukocytes have been shown to cross the BBB leading to neuroinflammation, neuro-glial-vascular unit disruption and the onset of white matter pathology (Huang et al., 2010; Yata et al., 2014). Leukocyte adhesion to the endothelial wall alone, without extravasation into the brain, has also been shown to lead to downstream signalling facilitating the recruitment and activation of microglial cells (H. Wang et al., 2015). In support of this connection, microglial cultures exposed to endothelial cell media, following hypoxic

challenge, showed a switch to an amoeboid conformation associated with the release of pro-inflammatory molecules, inhibited migration and phagocytosis as well as increased neuronal toxicity (Xing, Li, Deng, Ning, & Lo, 2018). As additional evidence for a link between endothelial activation and microglial activation, aged blood was found to impair hippocampal neural precursor activity and activate microglia via increased endothelial VCAM1 expression (Yousef et al., 2019). Interestingly, recent evidence has demonstrated that microglial dynamically interact with vessels, through the extension of processes to occupy areas void of astrocytic end-feet, through Cx_3Cr_1 signalling mechanisms (Mondo et al., 2020). This new evidence further elucidates endothelial-microglial cross talk and could help explain the lack of microglial responses observed within Cx_3Cr_1 receptor heterozygous mice following BCAS, as described in chapter 4.

Previous studies have demonstrated impaired clearance mechanisms in response to BCAS (Appendix Figure 1) which is likely the result of impairments in arterial pulsation that were identified here. Impaired waste clearance from the brain could lead to the prolonged presence of harmful metabolites, reactive oxygen species as well as neuroinflammatory mediators (Jeffrey J. Iliff et al., 2013b). These molecules have the potential themselves to activate microglial cells and could trigger neuroinflammatory responses following BCAS.

The present study, therefore, demonstrates evidence of endothelial activation and impaired arterial pulsation following BCAS. This data is significant as it adds support to the growing body of human evidence challenging the view that reduced blood flow post-stenosis is the only major contributor to VCI (Alhusaini et al., 2018; Aribisala et al., 2014; Shi et al., 2020; Joanna M. Wardlaw et al., 2017). Thus, highting that reduced CBF is just one of the consequences following BCAS surgery, and that additional vascular mechanisms, such as impaired pulsation and endothelial activation, could also be significantly contributing to downstream mechanisms.

5.4.4 Study limitations and future directions

In the present study leukocyte trafficking was found to be significantly increased following BCAS, indicating an increase in endothelial activation. It would, however, be important in future experiments to confirm this finding through the assessment of adhesion molecule expression. In the current study an attempt was made to assess ICAM-1 expression through multiphoton microscopy with the use of a PE-conjugated antibody. If successful this would have allowed the speed of RBC velocity, pulsation, leukocyte trafficking and ICAM-1 expression to all be determined within the same vessel. Early imaging sessions however, demonstrated that ICAM-1 florescence was significantly influenced by the clarity of the

cranial window, with increased laser power resulting in increased ICAM-1 signal (data not shown). As a result, ICAM-1 expression was not quantified within the present study. Previous BCAS studies, however, demonstrated a significant increase in ICAM-1 expression, subcortically, over-time following surgery (Kitamura et al., 2017). Though, this analysis was not restricted to blood vessels and was also not conducted within the cortex, which is the region in which leukocyte trafficking was assessed in the present study. In future studies, endothelial activation could be assessed within the cerebral cortex through immunohistochemical staining with ICAM-1/VCAM-1 alongside a vascular marker such as collagen IV. Increased co-localisation of markers following 1-month of BCAS would strengthen evidence for increased endothelial activation following BCAS.

In previous studies it has been shown that leukocyte plugging can occur, following BCAS, which leads to the cessation of blood flow through individual capillaries (Yata et al., 2014). This is a phenomenon that was not assessed within the present study, however given the significant increase in leukocyte trafficking within leptomeningeal veins, following BCAS surgery, it is likely that such events are occurring here post-BCAS. It would therefore be interesting in future studies to analyse these behaviours as leukocyte plugging leads to a complete cessation in blood flow and therefore could be a mechanism by which BCAS could mediated ischemic conditions within these areas. Such changes could serve as an important explanation as to why sub-regional vulnerability is evident within the BCAS model, which has shown specific white matter and thalamic susceptibility.

A limitation of the present study is the lack of direct evidence demonstrating endothelial-microglial crosstalk following BCAS. In future studies multiphoton microscopy could be used to monitor microglial-endothelial interactions following BCAS. For example, structural z-stacks could be carried out, longitudinally across multiple imaging sessions, within areas of reduced RBC velocity following surgery. Such images would allow for 3D reconstructions to be generated allowing endothelial-microglial contact to be assessed chronically, as well as the structural evaluation of microglial cells to help provide a temporal profile of phenotypical changes during the progression of cerebral hypoperfusion. Alongside this, microglial and endothelial cells could be isolated via FACS at multiple timepoints following BCAS surgery and analysed through RNA sequencing methods (Swartzlander et al., 2018). Such an in-depth analysis at multiple stages following BCAS would help elucidate the order of responses and help identify signalling mechanisms by which endothelial cells could stimulate microglial activation and proliferation.

5.5 Conclusion

The present study demonstrates that reduced CBF is just one of the consequences following BCAS surgery, and that additional vascular mechanisms, such pulsatory dysfunction and endothelial activation, are likely to be key contributors to downstream neuroinflammation, white matter damage and cognitive dysfunction. Reduced CBF, impaired vascular pulsation, and endothelial dysfunction have all been implicated in the pathogenesis of human VCI. The present evidence, therefore, highlights BCAS surgery in mice as an accurate model for the study of human VCI.

Chapter 6

General Discussion

6.1 CSF1R as a target for therapeutic intervention

The approaches currently used for dementia treatment can only temporarily relieve symptoms, with no therapeutic options available that have the ability to halt or reverse disease progression (Dong, Li, Cheng, & Hou, 2019). Evidence from human *post mortem* studies demonstrates that the vast majority, up to 75%, of old aged dementia cases show mixed pathology, thus highlighting the need for multi-faceted therapeutic approaches (*Pathological correlates of late-onset dementia in a multicentre, community-based population in England and Wales. Neuropathology Group of the Medical Research Council Cognitive Function and Ageing Study (MRC CFAS)*, 2001). Despite such evidence, the primary focus for the development of disease altering dementia treatment has been concerned with the removal of Aβ aggregates, with such treatments found to be largely unsuccessful at clinical trial. The ineffectiveness of amyloid targeted treatments likely reflects the need for therapeutic approaches that target all aspects of mixed dementia syndromes. A theory which is further strengthened by the fact that neuroinflammation, synapse loss, and neurofibrillary tau tangles more accurately correlate to cognitive decline (Gray, Kinghorn, & Woodling, 2020; Ismail et al., 2020; Nelson et al., 2012).

Pharmacological approaches targeting inflammation have been considered for the treatment of dementia. The first indication that anti-inflammatory drugs may have a potentially beneficial impact, came from observations within a rheumatoid arthritis cohort that reported an unexpectedly low dementia prevalence (McGeer Pl Fau - McGeer, McGeer E Fau - Rogers, Rogers J Fau - Sibley, & Sibley, 1990). Further support for such a link came from the Rotterdam study which demonstrated, within middle age and elderly people, a considerable reduction in AD risk when anti-inflammatory drugs were taken for at least 2-years (in t' Veld et al., 2001). Non-steroidal anti-inflammatory drugs, however, have not always been shown to have a beneficial impact (Imbimbo, Solfrizzi, & Panza, 2010). Such negative findings likely reflect the heterogenous nature of dementia, the significance of intervention timing within disease progression, as well as the fact that these approaches are broad spectrum and therefore do not specifically target the key inflammatory mediators and mechanisms. Despite

compelling evidence for the role of microglial proliferation and activation in dementia onset and progression, microglial specific treatments are yet to be tested in human patients.

The experiments presented within the first chapter of this thesis utilised a pharmacological approach to investigate the role of microglial proliferation, in the development of white matter damage and cognitive impairment, following BCAS surgery. The results demonstrate that microglial proliferation is fundamental to white matter damage and cognitive impairment following BCAS, as blocking microglial proliferation was found to reverse these effects. Such findings are promising, given that GW2580 treatment only blocks microglial proliferation, and does not deplete the existing microglia population even at high doses (Adrian Olmos-Alonso et al., 2016b). Therefore, providing a distinct advantage over microglial ablation approaches, as residual microglial will still be able to fulfil crucial homeostatic functions following treatment.

An important consideration, however, is the fact that human CSF1R mutations lead to a autosomal dominant condition known as hereditary diffuse leukoencephalopathy with spheroids, which is characterised by white matter damage as well as behavioural and cognitive abnormalities (Rademakers et al., 2011). CSF1R human mutations are found within the tyrosine kinase domain of the receptor (Rademakers et al., 2011), which is the same target by which GW2580 elicits its mode of action. These findings highlight the need for more comprehensive study of GW2580 treatment, as duration as well as developmental timing of treatment could be crucial to avoid potentially detrimental effects.

An additional consideration regarding GW2580 treatment, is the current lack of understanding concerning the phenotypic state of residual microglial cells following treatment. As these cells may still be activated following BCAS and thus could potentially alter the capacity of microglia to carry out normal homeostatic functions. As mentioned, previously, following the completion of this study, bulk RNA sequencing has been carried out within the white matter to access the inflammatory environment following BCAS and GW2580 treatment. RNA sequencing analysis demonstrated reduced expression of genes associated with inflammatory signalling such as Tlr2, Tlr4, Tlr13, Itgam, Ccl6, and Ccl9 within BCAS mice following GW2580 treatment. Additionally, microglial and endothelial-enriched genes set were found to be significantly increased following BCAS and subsequently reduced following GW2580 treatment. Implicating microglial proliferation in the signalling of endothelial related pathways following BCAS. Minor changes were also reported within oligodendrocyte progenitor cell and astrocytic-enriched gene sets following BCAS, however these were found to be unaffected following GW2580 treatment. Previous studies have also suggested that GW2580 treatment leads to an overall shift of inflammatory profile from pro-

to anti-inflammatory (Gomez-Nicola et al., 2013; A. Olmos-Alonso et al., 2016). Such findings therefore demonstrate that alongside a block of microglial proliferation, GW2580 is able to reduce pro-inflammatory signalling which likely implicates all of the components of the neuro-glial-vascular-unit. Such mechanisms, however, still lack the cell specific information needed to help determine exactly how residual microglial cells are behaving following GW2580 treatment. Furthermore, when microglial heterogeneity is considered, the true effects of microglial action within the context of BCAS remains to be fully elucidated.

6.2 Microglial heterogeneity

An important overall consideration for the role of microglial proliferation and activation in the context of VCI is the emerging evidence for intra- and inter-regional microglial heterogeneity within the brain. The emergence of single cell RNA sequencing techniques has provided unprecedented access to the genetic encoding that is occurring within individual cells. Studies analysing microglia isolated from cortical tissue biopsies taken from epileptic and MS patients, as well as cancer-free marginal tissue, demonstrated 14 distinct microglial subpopulations. These subpopulations were found to represent disease associated, pro-inflammatory, and homeostatic microglial clusters (Olah et al., 2018). Such approaches have also been applied to mice which helped to further demonstrate the sophisticated nature of microglial heterogeneity, through the identification of specific time, region, and context dependent microglial subpopulations (Hammond et al., 2019; Masuda et al., 2019). It will therefore be necessary in future studies for such approaches to be applied to the study of VCI to help further elucidate the spectrum of microglial changes, as well as the specific effects of drug modifying treatments. Such cell specific heterogeneity may also help to explain regional vulnerabilities evident in disease, such as the white matter vulnerability observed within VCI.

6.3 $Cx_3Cr_1^{eGFP}$ reporter mice: A reliable model to assess microglial function in health and disease?

The aim of chapter 2 was to use the $Cx_3Cr_1^{eGFP}$ microglial reporter line, alongside intravital imaging, to help further elucidate the role of microglia in disease progression following BCAS. The experimental findings, however, found Cx_3Cr_1 receptor signalling to be an important mediator of microglial proliferation and activation in response to BCAS. As demonstrated by a lack of proliferative, structural, or functional changes within microglial cells following BCAS surgery, which was associated with intact neurovascular coupling responses and spatial learning. These results therefore indicate that perturbation of Cx_3Cr_1 receptor signalling,

through the replacement of one gene copy with eGFP, is sufficient to significantly alter microglial responses following BCAS surgery.

Such findings are significant on two grounds. Firstly, $Cx_3Cr_1^{eGFP}$ microglial reporter mice display abnormal responses under certain disease conditions and therefore should be used with caution in future experiments. Secondary, this is the first evidence to implicate Cx_3Cr_1 receptor signalling in the pathogenesis of VCI.

Cx_3CL_1 (fractalkine) is a chemokine that has been shown to regulate microglial activation through binding to its only receptor, Cx_3Cr_1R. Cx_3CL_1 is constitutively expressed by normal neurons and binds to the Cx_3Cr_1R which is exclusively expressed on microglial cells. The fractalkine signalling system therefore represents a direct line of communication between neuron and microglial cells (J. K. Harrison et al., 1998). The traditional view of fractalkine signalling was that it functions to inhibit microglial activity (J. K. Harrison et al., 1998). A view point that came from evidence demonstrating that neuronal damage leads to a reduced fractalkine level in the immediate hours following injury, thus reducing Cx_3Cr_1R signalling that resulted in the recruitment and activation of microglia (Desforges, Hebron, Algarzae, Lonskaya, & Moussa, 2012). More recently, however, alterations within Cx_3Cr_1R signalling has been reported to sequester microglial responses leading to beneficial effects in various disease conditions (Ho et al., 2020; A. McDonough et al., 2019). Such findings mirror our own, with a supressed microglial proliferative response within $Cx_3Cr_1^{eGFP/+}$ mice following BCAS. Thus, highlighting that fractalkine signalling has an important role to play in the activation of microglia, which may be pro or anti-inflammatory in nature depending on the stimulus.

Having demonstrated that the removal of 1 Cx_3Cr_1R gene copy is sufficient to alter normal Cx_3Cr_1R signalling, $Cx_3Cr_1^{eGFP}$ microglial reporter mice should be used with caution in future experiments. The fact that $Cx_3Cr_1^{eGFP}$ reporter mice are the most routinely used microglial reporter line (Wieghofer et al., 2015) is therefore concerning, as results should be readdressed in the context of potential abnormal microglial responses.

6.4 Co-morbid models: Essential for the discovery of clinically relevant mechanisms?

Within chapter 4 the addition of amyloidosis, as a co-morbidity alongside BCAS surgery, was found to lead to no alterations in structural, functional, or proliferative microglial responses within $Cx_3Cr_1^{eGFP}$ mice. Spatial learning and memory, however, was found to be impaired within $Cx_3Cr_1^{eGFP}$App23 mice. Furthermore, neurovascular coupling was found to be

impaired within $Cx_3Cr_1^{eGFP}$App23 mice following BCAS, indicating the presence of additional harmful mechanisms outside the role of microglia.

Given the increasing evidence to suggest a significant overlap between dementia syndrome pathologies (Toledo et al., 2013), the need for accurate models of mixed dementia grows. Although, disease models such as BCAS can provide a fundamental understanding of key pathogenic mechanisms that lead to damage and impairment, the true nature of these events may in fact be very different in the face of multiple co-morbidities. For example, within chapter 4, neurovascular coupling was found to be impaired within $Cx_3Cr_1^{eGFP/+}$App23 mice following BCAS, despite a lacking microglial response. In studies within wild-type C57BL/6J mice, neurovascular coupling impairments are found to be significantly correlated to microglial expansion following BCAS, implicating a causative role of microglia in such dysfunction (Duncombe, Kitamura, et al., 2017). These results therefore indicate an alternative mechanism of neurovascular coupling impairment following BCAS when amyloidosis is present as a co-morbidity. In future research therefore, more consideration should be made to mixed models of dementia to allow the study of pathogenic mechanisms in more clinically relevant models.

6.5 BCAS: A more accurate model of human VCI than originally anticipated

The BCAS model has been extensively studied and shown to recapitulate pathological features relevant to the study of human VCI (Duncombe, Kitamura, et al., 2017). Due to the physical nature of the BCAS surgery, to date these downstream effects have almost exclusively been attributed to chronic reductions in CBF. Cerebral hypoperfusion is undoubtable a key contributing factor to downstream pathology within the BCAS model. However, within chapter 5, arterial pulsation was found to be significantly impaired following BCAS surgery. This provided the first clear evidence to suggest that BCAS is more than simply a model of cerebral hypoperfusion, and therefore, downstream damage and dysfunction is not wholly the result of reduced CBF. Vascular pulsation has been proposed to be a key mediator of waste clearance from the brain (Jeffrey J. Iliff et al., 2013b). Such findings are significant as they highlight additional mechanism by which BCAS can significantly contribute to damage and disease progression. Such as through the aberrant clearance of potentially harmful waste products from the brain. Given that there is also clinical evidence to suggest pulsatory impairments associated with advanced age (Fonck et al., 2009), impaired pulsation leading to dysfunctional clearance pathways could represent a key pathogenic mechanism within VCI and dementia that requires additional research.

6.6 Final Conclusions

In conclusion the data presented within this thesis highlights microglia as fundamental mediators of downstream white matter damage and cognitive impairment following BCAS. The effectiveness of GW2580 treatment demonstrates the value of such tools to the discovery of key pathogenic mechanisms, as well as highlighting microglial proliferation as a therapeutic target for the treatment of VCI. Additionally, the lack of microglial responses within $Cx_3Cr_1^{eGFP/+}$ mice highlights Cx_3CL_1-Cx_3Cr_1 signalling as a potentially crucial pathway for the regulation of microglial responses, following BCAS surgery. Furthermore, studies have demonstrated that BCAS surgery is an accurate model of human VCI, with evidence of reduced CBF, deficient pulsation, and endothelial dysfunction. Future studies should, therefore, consider all BCAS mediated vascular changes when investigating pathogenic mechanisms and not simply attribute all changes to cerebral hypoperfusion.

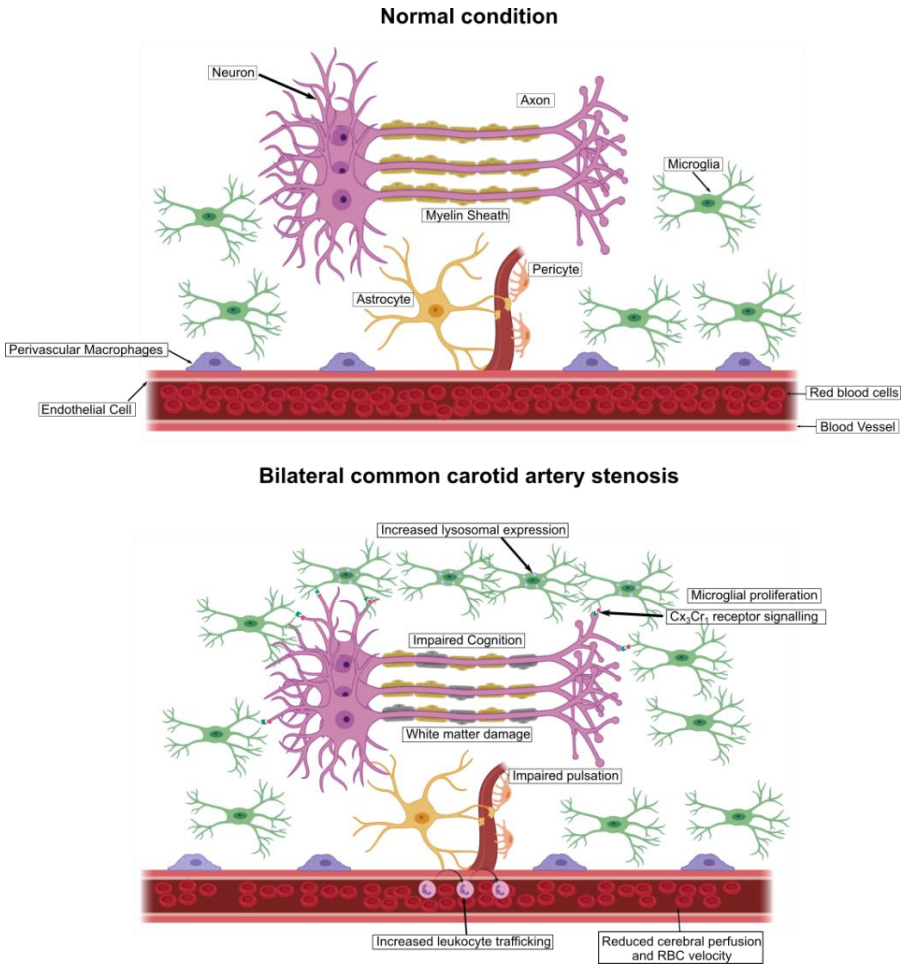

Figure 6.1 Graphical illustration of the main thesis findings. Image created with software from BioRender.com.

References

Abbott, N. J. (2004). Evidence for bulk flow of brain interstitial fluid: significance for physiology and pathology. (0197-0186 (Print)).

Aboul-Enein, F., Rauschka H Fau - Kornek, B., Kornek B Fau - Stadelmann, C., Stadelmann C Fau - Stefferl, A., Stefferl A Fau - Bruck, W., Bruck W Fau - Lucchinetti, C., . . . Lassmann, H. (2003). Preferential loss of myelin-associated glycoprotein reflects hypoxia-like white matter damage in stroke and inflammatory brain diseases. (0022-3069 (Print)).

Adams, D. H., & Shaw, S. (1994). Leucocyte-endothelial interactions and regulation of leucocyte migration. (0140-6736 (Print)).

Akiguchi, I., Tomimoto H Fau - Suenaga, T., Suenaga T Fau - Wakita, H., Wakita H Fau - Budka, H., & Budka, H. (1997). Alterations in glia and axons in the brains of Binswanger's disease patients. (0039-2499 (Print)).

Aldea, R., Weller, R. O., Wilcock, D. M., Carare, R. O., & Richardson, G. (2019). Cerebrovascular Smooth Muscle Cells as the Drivers of Intramural Periarterial Drainage of the Brain. *Frontiers in Aging Neuroscience, 11*, 1-1. doi:10.3389/fnagi.2019.00001

Alhusaini, S., Karama, S., Nguyen, T.-V., Thiel, A., Bernhardt, B. C., Cox, S. R., . . . Ducharme, S. (2018). Association between carotid atheroma and cerebral cortex structure at age 73 years. *Annals of neurology, 84*(4), 576-587. doi:10.1002/ana.25324

Alsop, D. C., Dai, W., Grossman, M., & Detre, J. A. (2010). Arterial Spin Labeling Blood Flow MRI: Its Role in the Early Characterization of Alzheimer's Disease. *Journal of Alzheimer's disease : JAD, 20*(3), 871-880. doi:10.3233/JAD-2010-091699

Altaf, N., Daniels L Fau - Morgan, P. S., Morgan Ps Fau - Lowe, J., Lowe J Fau - Gladman, J., Gladman J Fau - MacSweeney, S. T., MacSweeney St Fau - Moody, A., . . . Auer, D. P. (2006). Cerebral white matter hyperintense lesions are associated with unstable carotid plaques. (1078-5884 (Print)).

Alzheimer's Disease International. (2018). World Alzheimer's Report 2018. Retrieved from https:// www.alz.co.uk/research/world-report-2018

Andresen, J., Shafi Ni Fau - Bryan, R. M., Jr., & Bryan, R. M., Jr. (2006). Endothelial influences on cerebrovascular tone. (8750-7587 (Print)).

Aribisala, B. S., Morris, Z., Eadie, E., Thomas, A., Gow, A., Valdés Hernández, M. C., . . . Wardlaw, J. M. (2014). Blood pressure, internal carotid artery flow parameters, and age-related white matter hyperintensities. *Hypertension (Dallas, Tex. : 1979), 63*(5), 1011-1018. doi:10.1161/HYPERTENSIONAHA.113.02735

Armstrong, N. J., Mather, K. A., Sargurupremraj, M., Knol, M. J., Malik, R., Satizabal, C. L., . . . Nyquist, P. A. (2020). Common Genetic Variation Indicates Separate Causes for Periventricular and Deep White Matter Hyperintensities. (1524-4628 (Electronic)).

Arvanitakis, Z., Capuano, A. W., Leurgans, S. E., Buchman, A. S., Bennett, D. A., & Schneider, J. A. (2017). The Relationship of Cerebral Vessel Pathology to Brain Microinfarcts. *Brain pathology (Zurich, Switzerland), 27*(1), 77-85. doi:10.1111/bpa.12365

Askew, K., Li, K., Olmos-Alonso, A., Garcia-Moreno, F., Liang, Y., Richardson, P., . . . Gomez-Nicola, D. (2017). Coupled Proliferation and Apoptosis Maintain the Rapid Turnover of Microglia in the Adult Brain. *Cell reports, 18*(2), 391-405. doi:10.1016/j.celrep.2016.12.041

Attems, J., Jellinger K Fau - Thal, D. R., Thal Dr Fau - Van Nostrand, W., & Van Nostrand, W. (2011). Review: sporadic cerebral amyloid angiopathy. (1365-2990 (Electronic)).

Austin, B. P., Nair, V. A., Meier, T. B., Xu, G., Rowley, H. A., Carlsson, C. M., . . . Prabhakaran, V. (2011). Effects of Hypoperfusion in Alzheimer's Disease. *Journal of Alzheimer's Disease, 26*(Suppl 3), 123-133. doi:10.3233/JAD-2011-0010

Bachiller, S., Jiménez-Ferrer, I., Paulus, A., Yang, Y., Swanberg, M., Deierborg, T., & Boza-Serrano, A. (2018). Microglia in Neurological Diseases: A Road Map to Brain-Disease Dependent-Inflammatory Response. *Frontiers in Cellular Neuroscience, 12*, 488-488. doi:10.3389/fncel.2018.00488

Bagher, P., & Segal, S. S. (2011). Regulation of blood flow in the microcirculation: role of conducted vasodilation. *Acta physiologica (Oxford, England), 202*(3), 271-284. doi:10.1111/j.1748-1716.2010.02244.x

Balestrini, S., Perozzi C Fau - Altamura, C., Altamura C Fau - Vernieri, F., Vernieri F Fau - Luzzi, S., Luzzi S Fau - Bartolini, M., Bartolini M Fau - Provinciali, L., . . . Silvestrini, M. (2013). Severe carotid stenosis and impaired cerebral hemodynamics can influence cognitive deterioration. (1526-632X (Electronic)).

Balucani, C., Viticchi G Fau - Falsetti, L., Falsetti L Fau - Silvestrini, M., & Silvestrini, M. (2012). Cerebral hemodynamics and cognitive performance in bilateral asymptomatic carotid stenosis. (1526-632X (Electronic)).

Baradaran, H., Mtui, E. E., Richardson, J. E., Delgado, D., Dunning, A., Marshall, R. S., . . . Gupta, A. (2016). White Matter Diffusion Abnormalities in Carotid Artery Disease: A Systematic Review and Meta-Analysis. (1552-6569 (Electronic)).

Barker, R., Ashby, E. L., Wellington, D., Barrow, V. M., Palmer, J. C., Kehoe, P. G., . . . Love, S. (2014). Pathophysiology of white matter perfusion in Alzheimer's disease and vascular dementia. *Brain, 137*(5), 1524-1532. doi:10.1093/brain/awu040

Barker, R., Wellington, D., Esiri, M. M., & Love, S. (2013). Assessing white matter ischemic damage in dementia patients by measurement of myelin proteins. *Journal of cerebral blood flow and metabolism : official journal of the International Society of Cerebral Blood Flow and Metabolism, 33*(7), 1050-1057. doi:10.1038/jcbfm.2013.46

Barnes, C. A. (1979). Memory deficits associated with senescence: a neurophysiological and behavioral study in the rat. (0021-9940 (Print)).

Barnes, D. E., & Yaffe, K. (2011). The projected effect of risk factor reduction on Alzheimer's disease prevalence. *The Lancet. Neurology, 10*(9), 819-828. doi:10.1016/S1474-4422(11)70072-2

Baykara, E., Gesierich, B., Adam, R., Tuladhar, A. M., Biesbroek, J. M., Koek, H. L., . . . Duering, M. (2016). A Novel Imaging Marker for Small Vessel Disease Based on Skeletonization of White Matter Tracts and Diffusion Histograms. (1531-8249 (Electronic)).

Bazargani, N., & Attwell, D. A.-O. h. o. o. (2016). Astrocyte calcium signaling: the third wave. (1546-1726 (Electronic)).

Ben-Ari, H., Lifschytz, T., Wolf, G., Rigbi, A., Blumenfeld-Katzir, T., Merzel, T. K., . . . Lerer, B. (2019). White matter lesions, cerebral inflammation and cognitive function in a mouse model of cerebral hypoperfusion. (1872-6240 (Electronic)).

Bernbaum, M., Menon, B. K., Fick, G., Smith, E. E., Goyal, M., Frayne, R., & Coutts, S. B. (2015). Reduced blood flow in normal white matter predicts development of leukoaraiosis. *Journal of cerebral blood flow and metabolism*

: official journal of the International Society of Cerebral Blood Flow and Metabolism, 35(10), 1610-1615. doi:10.1038/jcbfm.2015.92
Beutner, C., Linnartz-Gerlach B Fau - Schmidt, S. V., Schmidt Sv Fau - Beyer, M., Beyer M Fau - Mallmann, M. R., Mallmann Mr Fau - Staratschek-Jox, A., Staratschek-Jox A Fau - Schultze, J. L., . . . Neumann, H. (2013). Unique transcriptome signature of mouse microglia. (1098-1136 (Electronic)).
Biber, K., Neumann H Fau - Inoue, K., Inoue K Fau - Boddeke, H. W. G. M., & Boddeke, H. W. (2007). Neuronal 'On' and 'Off' signals control microglia. (0166-2236 (Print)).
Black, S., Gao F Fau - Bilbao, J., & Bilbao, J. (2009). Understanding white matter disease: imaging-pathological correlations in vascular cognitive impairment. (1524-4628 (Electronic)).
Blinder, P., Tsai, P. S., Kaufhold, J. P., Knutsen, P. M., Suhl, H., & Kleinfeld, D. (2013). The cortical angiome: an interconnected vascular network with noncolumnar patterns of blood flow. *Nature neuroscience, 16*(7), 889-897. doi:10.1038/nn.3426
Boehm-Sturm, P., Füchtemeier, M., Foddis, M., Mueller, S., Trueman, R. C., Zille, M., . . . Farr, T. D. (2017). Neuroimaging Biomarkers Predict Brain Structural Connectivity Change in a Mouse Model of Vascular Cognitive Impairment. *Stroke, 48*(2), 468-475. doi:10.1161/STROKEAHA.116.014394
Bonelli, R. M., & Cummings, J. L. (2007). Frontal-subcortical circuitry and behavior. *Dialogues in clinical neuroscience, 9*(2), 141-151. Retrieved from https://pubmed.ncbi.nlm.nih.gov/17726913

https://www.ncbi.nlm.nih.gov/pmc/articles/PMC3181854/
Bordeleau, M., ElAli, A., & Rivest, S. (2016). Severe chronic cerebral hypoperfusion induces microglial dysfunction leading to memory loss in APPswe/PS1 mice. (1949-2553 (Electronic)). doi:D - NLM: PMC4914254 OTO - NOTNLM
Bordeleau, M., ElAli, A., & Rivest, S. (2016). Severe chronic cerebral hypoperfusion induces microglial dysfunction leading to memory loss in APPswe/PS1 mice. *Oncotarget, 7*(11), 11864-11880. doi:10.18632/oncotarget.7689
Brickman, A. M., Zahra, A., Muraskin, J., Steffener, J., Holland, C. M., Habeck, C., . . . Stern, Y. (2009). Reduction in cerebral blood flow in areas appearing as white matter hyperintensities on magnetic resonance imaging. *Psychiatry research, 172*(2), 117-120. doi:10.1016/j.pscychresns.2008.11.006
Brown, W. R., & Thore, C. R. (2011). Review: cerebral microvascular pathology in ageing and neurodegeneration. *Neuropathology and applied neurobiology, 37*(1), 56-74. doi:10.1111/j.1365-2990.2010.01139.x
Buratti, L., Balestrini, S., Altamura, C., Viticchi, G., Falsetti, L., Luzzi, S., . . . Silvestrini, M. (2015). Markers for the risk of progression from mild cognitive impairment to Alzheimer's disease. (1875-8908 (Electronic)).
Burton, E. J., Kenny Ra Fau - O'Brien, J., O'Brien J Fau - Stephens, S., Stephens S Fau - Bradbury, M., Bradbury M Fau - Rowan, E., Rowan E Fau - Kalaria, R., . . . Ballard, C. (2004). White matter hyperintensities are associated with impairment of memory, attention, and global cognitive performance in older stroke patients. (1524-4628 (Electronic)).
Button, E. B., Mitchell As Fau - Domingos, M. M., Domingos Mm Fau - Chung, J. H. J., Chung Jh Fau - Bradley, R. M., Bradley Rm Fau - Hashemi, A., Hashemi A Fau - Marvyn, P. M., . . . Duncan, R. E. (2014). Microglial cell activation increases saturated and decreases monounsaturated fatty acid content, but both lipid species are proinflammatory. (1558-9307 (Electronic)).
Buvelot, H., Jaquet, V., & Krause, K. H. (2019). Mammalian NADPH Oxidases. (1940-6029 (Electronic)).

Cahoy, J. D., Emery, B., Kaushal, A., Foo, L. C., Zamanian, J. L., Christopherson, K. S., . . . Barres, B. A. (2008). A transcriptome database for astrocytes, neurons, and oligodendrocytes: a new resource for understanding brain development and function. *The Journal of neuroscience : the official journal of the Society for Neuroscience, 28*(1), 264-278. doi:10.1523/JNEUROSCI.4178-07.2008

Calhoun, M. E., Burgermeister, P., Phinney, A. L., Stalder, M., Tolnay, M., Wiederhold, K. H., . . . Jucker, M. (1999). Neuronal overexpression of mutant amyloid precursor protein results in prominent deposition of cerebrovascular amyloid. *Proceedings of the National Academy of Sciences of the United States of America, 96*(24), 14088-14093. doi:10.1073/pnas.96.24.14088

Calhoun Me Fau - Wiederhold, K. H., Wiederhold Kh Fau - Abramowski, D., Abramowski D Fau - Phinney, A. L., Phinney Al Fau - Probst, A., Probst A Fau - Sturchler-Pierrat, C., Sturchler-Pierrat C Fau - Staufenbiel, M., . . . Jucker, M. (1998). Neuron loss in APP transgenic mice. (0028-0836 (Print)).

Carare, R. O., Hawkes Ca Fau - Jeffrey, M., Jeffrey M Fau - Kalaria, R. N., Kalaria Rn Fau - Weller, R. O., & Weller, R. O. (2013). Review: cerebral amyloid angiopathy, prion angiopathy, CADASIL and the spectrum of protein elimination failure angiopathies (PEFA) in neurodegenerative disease with a focus on therapy. (1365-2990 (Electronic)).

Cardona, A. E., Pioro Ep Fau - Sasse, M. E., Sasse Me Fau - Kostenko, V., Kostenko V Fau - Cardona, S. M., Cardona Sm Fau - Dijkstra, I. M., Dijkstra Im Fau - Huang, D., . . . Ransohoff, R. M. (2006). Control of microglial neurotoxicity by the fractalkine receptor. (1097-6256 (Print)).

Chandra, A., Li, W. A., Stone, C. R., Geng, X., & Ding, Y. (2017). The cerebral circulation and cerebrovascular disease I: Anatomy. *Brain circulation, 3*(2), 45-56. doi:10.4103/bc.bc_10_17

Chao, L. L., Buckley, S. T., Kornak, J., Schuff, N., Madison, C., Yaffe, K., . . . Weiner, M. W. (2010). ASL Perfusion MRI Predicts Cognitive Decline and Conversion From MCI to Dementia. *Alzheimer disease and associated disorders, 24*(1), 19-27. doi:10.1097/WAD.0b013e3181b4f736

Charidimou, A., Gang Q Fau - Werring, D. J., & Werring, D. J. (2012). Sporadic cerebral amyloid angiopathy revisited: recent insights into pathophysiology and clinical spectrum. (1468-330X (Electronic)).

Cheng, H. L., Lin Cj Fau - Soong, B.-W., Soong Bw Fau - Wang, P.-N., Wang Pn Fau - Chang, F.-C., Chang Fc Fau - Wu, Y.-T., Wu Yt Fau - Chou, K.-H., . . . Lee, I. H. (2012). Impairments in cognitive function and brain connectivity in severe asymptomatic carotid stenosis. (1524-4628 (Electronic)).

Cohen, D. L., Hedera P Fau - Premkumar, D. R., Premkumar Dr Fau - Friedland, R. P., Friedland Rp Fau - Kalaria, R. N., & Kalaria, R. N. (1997). Amyloid-beta protein angiopathies masquerading as Alzheimer's disease? (0077-8923 (Print)).

Coltman, R., Spain A Fau - Tsenkina, Y., Tsenkina Y Fau - Fowler, J. H., Fowler Jh Fau - Smith, J., Smith J Fau - Scullion, G., Scullion G Fau - Allerhand, M., . . . Horsburgh, K. (2011). Selective white matter pathology induces a specific impairment in spatial working memory. (1558-1497 (Electronic)).

Conway, J. G., McDonald, B., Parham, J., Keith, B., Rusnak, D. W., Shaw, E., . . . Hutchins, J. T. (2005). Inhibition of colony-stimulating-factor-1 signaling in vivo with the orally bioavailable cFMS kinase inhibitor GW2580. *Proceedings of the National Academy of Sciences of the United States of America, 102*(44), 16078-16083. doi:10.1073/pnas.0502000102

Corder, E. H., Saunders Am Fau - Strittmatter, W. J., Strittmatter Wj Fau - Schmechel, D. E., Schmechel De Fau - Gaskell, P. C., Gaskell Pc Fau -

Small, G. W., Small Gw Fau - Roses, A. D., . . . Pericak-Vance, M. A. (1993). Gene dose of apolipoprotein E type 4 allele and the risk of Alzheimer's disease in late onset families. (0036-8075 (Print)).

Cox, S. B., Woolsey Ta Fau - Rovainen, C. M., & Rovainen, C. M. (1993). Localized dynamic changes in cortical blood flow with whisker stimulation corresponds to matched vascular and neuronal architecture of rat barrels. (0271-678X (Print)).

Crespo, O., Kang, S. C., Daneman, R., Lindstrom, T. M., Ho, P. P., Sobel, R. A., . . . Robinson, W. H. (2011). Tyrosine kinase inhibitors ameliorate autoimmune encephalomyelitis in a mouse model of multiple sclerosis. *Journal of clinical immunology, 31*(6), 1010-1020. doi:10.1007/s10875-011-9579-6

Cserr Hf Fau - Ostrach, L. H., & Ostrach, L. H. (1974). Bulk flow of interstitial fluid after intracranial injection of blue dextran 2000. (0014-4886 (Print)).

Cuadros, M. A., & Navascués, J. (1998). The origin and differentiation of microglial cells during development. (0301-0082 (Print)).

Dai, X. M., Ryan Gr Fau - Hapel, A. J., Hapel Aj Fau - Dominguez, M. G., Dominguez Mg Fau - Russell, R. G., Russell Rg Fau - Kapp, S., Kapp S Fau - Sylvestre, V., . . . Stanley, E. R. (2002). Targeted disruption of the mouse colony-stimulating factor 1 receptor gene results in osteopetrosis, mononuclear phagocyte deficiency, increased primitive progenitor cell frequencies, and reproductive defects. (0006-4971 (Print)).

Davalos, D., Grutzendler J Fau - Yang, G., Yang G Fau - Kim, J. V., Kim Jv Fau - Zuo, Y., Zuo Y Fau - Jung, S., Jung S Fau - Littman, D. R., . . . Gan, W. B. (2005). ATP mediates rapid microglial response to local brain injury in vivo. (1097-6256 (Print)).

Davis, B. M., Salinas-Navarro, M., Cordeiro, M. F., Moons, L. A.-O., & De Groef, L. A.-O. (2017). Characterizing microglia activation: a spatial statistics approach to maximize information extraction. (2045-2322 (Electronic)).

Davis, J., Xu F Fau - Deane, R., Deane R Fau - Romanov, G., Romanov G Fau - Previti, M. L., Previti Ml Fau - Zeigler, K., Zeigler K Fau - Zlokovic, B. V., . . . Van Nostrand, W. E. (2004). Early-onset and robust cerebral microvascular accumulation of amyloid beta-protein in transgenic mice expressing low levels of a vasculotropic Dutch/Iowa mutant form of amyloid beta-protein precursor. (0021-9258 (Print)).

De Biase, L. M., Schuebel, K. E., Fusfeld, Z. H., Jair, K., Hawes, I. A., Cimbro, R., . . . Bonci, A. (2017). Local Cues Establish and Maintain Region-Specific Phenotypes of Basal Ganglia Microglia. *Neuron, 95*(2), 341-356.e346. doi:10.1016/j.neuron.2017.06.020

de Eulate, R. G., Goni, I., Galiano, A., Vidorreta, M., Recio, M., Riverol, M., . . . Fernandez-Seara, M. A. (2017). Reduced Cerebral Blood Flow in Mild Cognitive Impairment Assessed Using Phase-Contrast MRI. (1875-8908 (Electronic)).

de Groot, J. C., de Leeuw Fe Fau - Oudkerk, M., Oudkerk M Fau - van Gijn, J., van Gijn J Fau - Hofman, A., Hofman A Fau - Jolles, J., Jolles J Fau - Breteler, M. M., & Breteler, M. M. (2000). Cerebral white matter lesions and cognitive function: the Rotterdam Scan Study. (0364-5134 (Print)).

de la Torre, J. C. (2000). Critically attained threshold of cerebral hypoperfusion: can it cause Alzheimer's disease? (0077-8923 (Print)).

de la Torre, J. C. (2002). Alzheimer disease as a vascular disorder: nosological evidence. (1524-4628 (Electronic)).

De Reuck, J. (1971). The human periventricular arterial blood supply and the anatomy of cerebral infarctions. (0014-3022 (Print)).

Debette, S., Schilling, S., Duperron, M.-G., Larsson, S. C., & Markus, H. S. (2019). Clinical Significance of Magnetic Resonance Imaging Markers of Vascular Brain Injury: A Systematic Review and Meta-analysis. *JAMA neurology, 76*(1), 81-94. doi:10.1001/jamaneurol.2018.3122

dela Paz, N. G., & D'Amore, P. A. (2009). Arterial versus venous endothelial cells. *Cell and tissue research, 335*(1), 5-16. doi:10.1007/s00441-008-0706-5

den Abeelen As Fau - Lagro, J., Lagro J Fau - van Beek, A. H. E. A., van Beek Ah Fau - Claassen, J. A. H. R., & Claassen, J. A. (2014). Impaired cerebral autoregulation and vasomotor reactivity in sporadic Alzheimer's disease. (1875-5828 (Electronic)).

Desforges, N. M., Hebron, M. L., Algarzae, N. K., Lonskaya, I., & Moussa, C. E. H. (2012). Fractalkine Mediates Communication between Pathogenic Proteins and Microglia: Implications of Anti-Inflammatory Treatments in Different Stages of Neurodegenerative Diseases. *International journal of Alzheimer's disease, 2012*, 345472-345472. doi:10.1155/2012/345472

Di Marco, L. Y., Venneri, A., Farkas, E., Evans, P. C., Marzo, A., & Frangi, A. F. (2015). Vascular dysfunction in the pathogenesis of Alzheimer's disease--A review of endothelium-mediated mechanisms and ensuing vicious circles. (1095-953X (Electronic)).

Dichgans, M., & Leys, D. (2017). Vascular Cognitive Impairment. (1524-4571 (Electronic)).

Diem, A. K., MacGregor Sharp, M., Gatherer, M., Bressloff, N. W., Carare, R. O., & Richardson, G. (2017). Arterial Pulsations cannot Drive Intramural Periarterial Drainage: Significance for Aβ Drainage. *Frontiers in neuroscience, 11*, 475-475. doi:10.3389/fnins.2017.00475

Ding, J., Mitchell, G. F., Bots, M. L., Sigurdsson, S., Harris, T. B., Garcia, M., . . . Launer, L. J. (2015). Carotid arterial stiffness and risk of incident cerebral microbleeds in older people: the Age, Gene/Environment Susceptibility (AGES)-Reykjavik study. *Arteriosclerosis, thrombosis, and vascular biology, 35*(8), 1889-1895. doi:10.1161/ATVBAHA.115.305451

Dong, Y., Li, X., Cheng, J., & Hou, L. (2019). Drug Development for Alzheimer's Disease: Microglia Induced Neuroinflammation as a Target? *International journal of molecular sciences, 20*(3), 558. doi:10.3390/ijms20030558

Drew, P. J., Shih, A. Y., Driscoll, J. D., Knutsen, P. M., Blinder, P., Davalos, D., . . . Kleinfeld, D. (2010). Chronic optical access through a polished and reinforced thinned skull. *Nature methods, 7*(12), 981-984. doi:10.1038/nmeth.1530

Du, B., Liang, M., Zheng, H., Fan, C., Zhang, H., Lu, X., . . . Bi, X. (2020). Anti-mouse CX3CR1 antibody alleviates cognitive impairment, neuronal loss and myelin deficits in an animal model of brain ischemia. LID - S0306-4522(20)30305-5 [pii] LID - 10.1016/j.neuroscience.2020.05.011 [doi]. (1873-7544 (Electronic)).

Duncombe, J., Kitamura, A., Hase, Y., Ihara, M., Kalaria, R. N., & Horsburgh, K. (2017). Chronic cerebral hypoperfusion: a key mechanism leading to vascular cognitive impairment and dementia. Closing the translational gap between rodent models and human vascular cognitive impairment and dementia. (1470-8736 (Electronic)).

Duncombe, J., Lennen, R. J., Jansen, M. A., Marshall, I., Wardlaw, J. M., & Horsburgh, K. (2017). Ageing causes prominent neurovascular dysfunction associated with loss of astrocytic contacts and gliosis. (1365-2990 (Electronic)).

Dyrna, F., Hanske S Fau - Krueger, M., Krueger M Fau - Bechmann, I., & Bechmann, I. (2013). The blood-brain barrier. (1557-1904 (Electronic)).

Easley-Neal, C., Foreman, O., Sharma, N., Zarrin, A. A., & Weimer, R. M. (2019). CSF1R Ligands IL-34 and CSF1 Are Differentially Required for Microglia Development and Maintenance in White and Gray Matter Brain Regions. *Frontiers in Immunology, 10*, 2199-2199. doi:10.3389/fimmu.2019.02199

Ellis, R. J., Olichney Jm Fau - Thal, L. J., Thal Lj Fau - Mirra, S. S., Mirra Ss Fau - Morris, J. C., Morris Jc Fau - Beekly, D., Beekly D Fau - Heyman, A., & Heyman, A. (1996). Cerebral amyloid angiopathy in the brains of patients with Alzheimer's disease: the CERAD experience, Part XV. (0028-3878 (Print)).

Fan, W., Liu, Q., Zhu, X., Wu, Z., Li, D., Huang, F., & He, H. (2016). Regulatory effects of anesthetics on nitric oxide. (1879-0631 (Electronic)).

Farkas, E., De Jong Gi Fau - de Vos, R. A., de Vos Ra Fau - Jansen Steur, E. N., Jansen Steur En Fau - Luiten, P. G., & Luiten, P. G. (2000). Pathological features of cerebral cortical capillaries are doubled in Alzheimer's disease and Parkinson's disease. (0001-6322 (Print)).

Farkas, E., Luiten Pg Fau - Bari, F., & Bari, F. (2007). Permanent, bilateral common carotid artery occlusion in the rat: a model for chronic cerebral hypoperfusion-related neurodegenerative diseases. (0165-0173 (Print)).

Farooq, M. U., & Gorelick, P. B. (2013). Vascular cognitive impairment. (1534-6242 (Electronic)).

Fitzpatrick, A. L., Kuller Lh Fau - Lopez, O. L., Lopez Ol Fau - Kawas, C. H., Kawas Ch Fau - Jagust, W., & Jagust, W. (2005). Survival following dementia onset: Alzheimer's disease and vascular dementia. (0022-510X (Print)).

Fonck, E., Feigl Gg Fau - Fasel, J., Fasel J Fau - Sage, D., Sage D Fau - Unser, M., Unser M Fau - Rüfenacht, D. A., Rüfenacht Da Fau - Stergiopulos, N., & Stergiopulos, N. (2009). Effect of aging on elastin functionality in human cerebral arteries. (1524-4628 (Electronic)).

Fowler, J. H., McQueen, J., Holland, P. R., Manso, Y., Marangoni, M., Scott, F., . . . Horsburgh, K. (2017). Dimethyl fumarate improves white matter function following severe hypoperfusion: Involvement of microglia/macrophages and inflammatory mediators. (1559-7016 (Electronic)).

Fricker, M., Neher, J. J., Zhao, J.-W., Théry, C., Tolkovsky, A. M., & Brown, G. C. (2012). MFG-E8 mediates primary phagocytosis of viable neurons during neuroinflammation. *The Journal of neuroscience : the official journal of the Society for Neuroscience, 32*(8), 2657-2666. doi:10.1523/JNEUROSCI.4837-11.2012

Frohman, E. M., Frohman Tc Fau - Gupta, S., Gupta S Fau - de Fougerolles, A., de Fougerolles A Fau - van den Noort, S., & van den Noort, S. (1991). Expression of intercellular adhesion molecule 1 (ICAM-1) in Alzheimer's disease. (0022-510X (Print)).

Fuger, P., Hefendehl, J. K., Veeraraghavalu, K., Wendeln, A. C., Schlosser, C., Obermuller, U., . . . Jucker, M. (2017). Microglia turnover with aging and in an Alzheimer's model via long-term in vivo single-cell imaging. (1546-1726 (Electronic)).

Fumagalli, S., Perego C Fau - Ortolano, F., Ortolano F Fau - De Simoni, M.-G., & De Simoni, M. G. (2013). CX3CR1 deficiency induces an early protective inflammatory environment in ischemic mice. (1098-1136 (Electronic)).

Garcia-Agudo, L. F., Janova, H., Sendler, L. E., Arinrad, S., Steixner, A. A., Hassouna, I., . . . Ehrenreich, H. (2019). Genetically induced brain inflammation by Cnp deletion transiently benefits from microglia depletion. (1530-6860 (Electronic)).

Gefen, T., Kim, G., Bolbolan, K., Geoly, A., Ohm, D., Oboudiyat, C., . . . Geula, C. (2019). Activated Microglia in Cortical White Matter Across Cognitive Aging

Trajectories. *Frontiers in Aging Neuroscience, 11*, 94-94. doi:10.3389/fnagi.2019.00094
Gerber, Y. N., Saint-Martin, G. P., Bringuier, C. M., Bartolami, S., Goze-Bac, C., Noristani, H. N., & Perrin, F. E. (2018). CSF1R Inhibition Reduces Microglia Proliferation, Promotes Tissue Preservation and Improves Motor Recovery After Spinal Cord Injury. *Frontiers in Cellular Neuroscience, 12*, 368-368. doi:10.3389/fncel.2018.00368
Ginhoux, F., Greter, M., Leboeuf, M., Nandi, S., See, P., Gokhan, S., . . . Merad, M. (2010). Fate mapping analysis reveals that adult microglia derive from primitive macrophages. *Science (New York, N.Y.), 330*(6005), 841-845. doi:10.1126/science.1194637
Girouard, H., & Iadecola, C. (2006). Neurovascular coupling in the normal brain and in hypertension, stroke, and Alzheimer disease. (8750-7587 (Print)).
Giwa, M. O., Williams J Fau - Elderfield, K., Elderfield K Fau - Jiwa, N. S., Jiwa Ns Fau - Bridges, L. R., Bridges Lr Fau - Kalaria, R. N., Kalaria Rn Fau - Markus, H. S., . . . Hainsworth, A. H. (2012). Neuropathologic evidence of endothelial changes in cerebral small vessel disease. (1526-632X (Electronic)).
Gomez-Nicola, D., Fransen Nl Fau - Suzzi, S., Suzzi S Fau - Perry, V. H., & Perry, V. H. (2013). Regulation of microglial proliferation during chronic neurodegeneration. (1529-2401 (Electronic)).
Gomez-Nicola, D., & Perry, V. H. (2015). Microglial dynamics and role in the healthy and diseased brain: a paradigm of functional plasticity. (1089-4098 (Electronic)). doi:D - NLM: PMC4412879 OTO - NOTNLM
Gomez-Nicola, D., & Perry, V. H. (2015). Microglial dynamics and role in the healthy and diseased brain: a paradigm of functional plasticity. *The Neuroscientist : a review journal bringing neurobiology, neurology and psychiatry, 21*(2), 169-184. doi:10.1177/1073858414530512
Gorelick, P. B., & Nyenhuis, D. (2013). Understanding and treating vascular cognitive impairment. (1538-6899 (Electronic)).
Gorelick, P. B., Scuteri, A., Black, S. E., Decarli, C., Greenberg, S. M., Iadecola, C., . . . Anesthesia. (2011). Vascular contributions to cognitive impairment and dementia: a statement for healthcare professionals from the american heart association/american stroke association. *Stroke, 42*(9), 2672-2713. doi:10.1161/STR.0b013e3182299496
Grammas, P. (2011). Neurovascular dysfunction, inflammation and endothelial activation: implications for the pathogenesis of Alzheimer's disease. (1742-2094 (Electronic)). doi:D - NLM: PMC3072921 EDAT- 2011/03/29 06:00 MHDA- 2011/07/23 06:00 CRDT- 2011/03/29 06:00 PHST- 2011/01/06 [received] PHST- 2011/03/25 [accepted] AID - 1742-2094-8-26 [pii] AID - 10.1186/1742-2094-8-26 [doi] PST - epublish
Gray, S. C., Kinghorn, K. J., & Woodling, N. S. (2020). Shifting equilibriums in Alzheimer's disease: the complex roles of microglia in neuroinflammation, neuronal survival and neurogenesis. *Neural Regeneration Research, 15*(7), 1208-1219. doi:10.4103/1673-5374.272571
Greter, M., Lelios, I., Pelczar, P., Hoeffel, G., Price, J., Leboeuf, M., . . . Becher, B. (2012). Stroma-derived interleukin-34 controls the development and maintenance of langerhans cells and the maintenance of microglia. *Immunity, 37*(6), 1050-1060. doi:10.1016/j.immuni.2012.11.001
Guan, Z., Kuhn, J. A., Wang, X., Colquitt, B., Solorzano, C., Vaman, S., . . . Basbaum, A. I. (2016). Injured sensory neuron-derived CSF1 induces microglial proliferation and DAP12-dependent pain. *Nature neuroscience, 19*(1), 94-101. doi:10.1038/nn.4189

Guerreiro, R., Wojtas, A., Bras, J., Carrasquillo, M., Rogaeva, E., Majounie, E., . . . Alzheimer Genetic Analysis, G. (2013). TREM2 variants in Alzheimer's disease. *The New England journal of medicine, 368*(2), 117-127. doi:10.1056/NEJMoa1211851

Gyoneva, S., Swanger, S. A., Zhang, J., Weinshenker, D., & Traynelis, S. F. (2016). Altered motility of plaque-associated microglia in a model of Alzheimer's disease. (1873-7544 (Electronic)). doi:D - NLM: NIHMS793929 [Available on 08/25/17]

D - NLM: PMC4927418 [Available on 08/25/17] OTO - NOTNLM

Hamilton, S. J., & Watts, G. F. (2013). Endothelial dysfunction in diabetes: pathogenesis, significance, and treatment. (1614-0575 (Electronic)). doi:D - NLM: PMC4063100 EDAT- 2014/01/01 06:00 MHDA- 2014/09/18 06:00 CRDT- 2014/01/01 06:00 AID - 10.1900/RDS.2013.10.133 [doi] PST - ppublish

Hammond, T. R., Dufort, C., Dissing-Olesen, L., Giera, S., Young, A., Wysoker, A., . . . Stevens, B. (2019). Single-Cell RNA Sequencing of Microglia throughout the Mouse Lifespan and in the Injured Brain Reveals Complex Cell-State Changes. *Immunity, 50*(1), 253-271.e256. doi:10.1016/j.immuni.2018.11.004

Han, J. H., Wong Ks Fau - Wang, Y. Y., Wang Yy Fau - Fu, J. H., Fu Jh Fau - Ding, D., Ding D Fau - Hong, Z., & Hong, Z. (2009). Plasma level of sICAM-1 is associated with the extent of white matter lesion among asymptomatic elderly subjects. (1872-6968 (Electronic)).

Hanisch, U.-K., & Kettenmann, H. (2007). Microglia: active sensor and versatile effector cells in the normal and pathologic brain. *Nature neuroscience, 10*(11), 1387-1394. doi:10.1038/nn1997

Hanisch, U. K., & Kettenmann, H. (2007). Microglia: active sensor and versatile effector cells in the normal and pathologic brain. (1097-6256 (Print)).

Harris, J. J., & Attwell, D. (2012). The energetics of CNS white matter. *The Journal of neuroscience : the official journal of the Society for Neuroscience, 32*(1), 356-371. doi:10.1523/JNEUROSCI.3430-11.2012

Harrison, J. K., Jiang, Y., Chen, S., Xia, Y., Maciejewski, D., McNamara, R. K., . . . Feng, L. (1998). Role for neuronally derived fractalkine in mediating interactions between neurons and CX3CR1-expressing microglia. *Proceedings of the National Academy of Sciences of the United States of America, 95*(18), 10896-10901. doi:10.1073/pnas.95.18.10896

Harrison, J. K., Jiang, Y., Chen, S., Xia, Y., Maciejewski, D., McNamara, R. K., . . . Feng, L. (1998). Role for neuronally derived fractalkine in mediating interactions between neurons and CX3CR1-expressing microglia. *Proceedings of the National Academy of Sciences, 95*(18), 10896. Retrieved from http://www.pnas.org/content/95/18/10896.abstract

Hart, A. D., Wyttenbach, A., Perry, V. H., & Teeling, J. L. (2012). Age related changes in microglial phenotype vary between CNS regions: grey versus white matter differences. *Brain, behavior, and immunity, 26*(5), 754-765. doi:10.1016/j.bbi.2011.11.006

Hase, Y., Craggs, L., Hase, M., Stevenson, W., Slade, J., Chen, A., . . . Kalaria, R. N. (2018). The effects of environmental enrichment on white matter pathology in a mouse model of chronic cerebral hypoperfusion. *Journal of cerebral blood flow and metabolism : official journal of the International Society of Cerebral Blood Flow and Metabolism, 38*(1), 151-165. doi:10.1177/0271678X17694904

Hassan, A., Hunt Bj Fau - O'Sullivan, M., O'Sullivan M Fau - Parmar, K., Parmar K Fau - Bamford, J. M., Bamford Jm Fau - Briley, D., Briley D Fau - Brown, M.

M., . . . Markus, H. S. (2003). Markers of endothelial dysfunction in lacunar infarction and ischaemic leukoaraiosis. (0006-8950 (Print)).
Hatori, K., Nagai A Fau - Heisel, R., Heisel R Fau - Ryu, J. K., Ryu Jk Fau - Kim, S. U., & Kim, S. U. (2002). Fractalkine and fractalkine receptors in human neurons and glial cells. (0360-4012 (Print)).
Hattori, Y., Enmi, J.-I., Iguchi, S., Saito, S., Yamamoto, Y., Nagatsuka, K., . . . Ihara, M. (2016). Substantial Reduction of Parenchymal Cerebral Blood Flow in Mice with Bilateral Common Carotid Artery Stenosis. *Scientific reports, 6*, 32179-32179. doi:10.1038/srep32179
Hawkes, C. A., Jayakody N Fau - Johnston, D. A., Johnston Da Fau - Bechmann, I., Bechmann I Fau - Carare, R. O., & Carare, R. O. (2014). Failure of perivascular drainage of β-amyloid in cerebral amyloid angiopathy. (1750-3639 (Electronic)).
Haynes, S. E., Hollopeter G Fau - Yang, G., Yang G Fau - Kurpius, D., Kurpius D Fau - Dailey, M. E., Dailey Me Fau - Gan, W.-B., Gan Wb Fau - Julius, D., & Julius, D. (2006). The P2Y12 receptor regulates microglial activation by extracellular nucleotides. (1097-6256 (Print)).
He, H.-Y., Ren, L., Guo, T., & Deng, Y.-H. (2019). Neuronal autophagy aggravates microglial inflammatory injury by downregulating CX3CL1/fractalkine after ischemic stroke. *Neural Regeneration Research, 14*(2), 280-288. doi:10.4103/1673-5374.244793
Heneka, M. T., Carson, M. J., El Khoury, J., Landreth, G. E., Brosseron, F., Feinstein, D. L., . . . Kummer, M. P. (2015). Neuroinflammation in Alzheimer's disease. *The Lancet. Neurology, 14*(4), 388-405. doi:10.1016/S1474-4422(15)70016-5
Heppner, F. L., Ransohoff, R. M., & Becher, B. (2015). Immune attack: the role of inflammation in Alzheimer disease. (1471-0048 (Electronic)).
Hickman, S. E., Kingery, N. D., Ohsumi, T. K., Borowsky, M. L., Wang, L.-c., Means, T. K., & El Khoury, J. (2013). The microglial sensome revealed by direct RNA sequencing. *Nature neuroscience, 16*(12), 1896-1905. doi:10.1038/nn.3554
Hierro-Bujalance, C., Bacskai, B. J., & Garcia-Alloza, M. (2018). In Vivo Imaging of Microglia With Multiphoton Microscopy. *Frontiers in Aging Neuroscience, 10*, 218-218. doi:10.3389/fnagi.2018.00218
Hill, J., Fillit H Fau - Shah, S. N., Shah Sn Fau - del Valle, M. C., del Valle Mc Fau - Futterman, R., & Futterman, R. (2005). Patterns of healthcare utilization and costs for vascular dementia in a community-dwelling population. (1387-2877 (Print)).
Ho, C. Y., Lin, Y. T., Chen, H. H., Ho, W. Y., Sun, G. C., Hsiao, M., . . . Tseng, C. A.-O. (2020). CX3CR1-microglia mediates neuroinflammation and blood pressure regulation in the nucleus tractus solitarii of fructose-induced hypertensive rats. (1742-2094 (Electronic)).
Holland, P. R., Bastin Me Fau - Jansen, M. A., Jansen Ma Fau - Merrifield, G. D., Merrifield Gd Fau - Coltman, R. B., Coltman Rb Fau - Scott, F., Scott F Fau - Nowers, H., . . . Horsburgh, K. (2011). MRI is a sensitive marker of subtle white matter pathology in hypoperfused mice. (1558-1497 (Electronic)).
Holland, P. R., Searcy, J. L., Salvadores, N., Scullion, G., Chen, G., Lawson, G., . . . Horsburgh, K. (2015). Gliovascular disruption and cognitive deficits in a mouse model with features of small vessel disease. (1559-7016 (Electronic)). doi:D - NLM: PMC4640247 EDAT- 2015/02/12 06:00 MHDA- 2015/08/11 06:00 CRDT- 2015/02/12 06:00 PHST- 2014/10/29 [received] PHST- 2015/01/12 [revised] PHST- 2015/01/13 [accepted] AID - jcbfm201512 [pii] AID - 10.1038/jcbfm.2015.12 [doi] PST - ppublish

Hosmane, S., Tegenge, M. A., Rajbhandari, L., Uapinyoying, P., Ganesh Kumar, N., Thakor, N., & Venkatesan, A. (2012). Toll/interleukin-1 receptor domain-containing adapter inducing interferon-β mediates microglial phagocytosis of degenerating axons. *The Journal of neuroscience : the official journal of the Society for Neuroscience, 32*(22), 7745-7757. doi:10.1523/JNEUROSCI.0203-12.2012

Hossmann, K. A. (1994). Viability thresholds and the penumbra of focal ischemia. (0364-5134 (Print)).

Hossmann, K. A. (2006). Pathophysiology and therapy of experimental stroke. (0272-4340 (Print)).

Howell, O. W., Rundle, J. L., Garg, A., Komada, M., Brophy, P. J., & Reynolds, R. (2010). Activated microglia mediate axoglial disruption that contributes to axonal injury in multiple sclerosis. *Journal of neuropathology and experimental neurology, 69*(10), 1017-1033. doi:10.1097/NEN.0b013e3181f3a5b1

Huang, Y., Zhang W Fau - Lin, L., Lin L Fau - Feng, J., Feng J Fau - Chen, F., Chen F Fau - Wei, W., Wei W Fau - Zhao, X., . . . Li, L. (2010). Is endothelial dysfunction of cerebral small vessel responsible for white matter lesions after chronic cerebral hypoperfusion in rats? (1878-5883 (Electronic)).

Hume, D. A., & MacDonald, K. P. (2012). Therapeutic applications of macrophage colony-stimulating factor-1 (CSF-1) and antagonists of CSF-1 receptor (CSF-1R) signaling. (1528-0020 (Electronic)).

Hunt, B. J., & Jurd, K. M. (1998). Endothelial cell activation. A central pathophysiological process. *BMJ (Clinical research ed.), 316*(7141), 1328-1329. doi:10.1136/bmj.316.7141.1328

Huynh, K. K., Eskelinen, E.-L., Scott, C. C., Malevanets, A., Saftig, P., & Grinstein, S. (2007). LAMP proteins are required for fusion of lysosomes with phagosomes. *The EMBO journal, 26*(2), 313-324. doi:10.1038/sj.emboj.7601511

Iadecola, C. (2004). Neurovascular regulation in the normal brain and in Alzheimer's disease. (1471-003X (Print)).

Iadecola, C. (2010). The overlap between neurodegenerative and vascular factors in the pathogenesis of dementia. *Acta neuropathologica, 120*(3), 287-296. doi:10.1007/s00401-010-0718-6

Iadecola, C. (2013). The pathobiology of vascular dementia. *Neuron, 80*(4), 844-866. doi:10.1016/j.neuron.2013.10.008

Iadecola, C., & Davisson, R. L. (2008). Hypertension and cerebrovascular dysfunction. (1932-7420 (Electronic)). doi:D - NLM: NIHMS54023

D - NLM: PMC2475602 EDAT- 2008/06/05 09:00 MHDA- 2008/08/08 09:00 CRDT- 2008/06/05 09:00 PHST- 2007/12/26 [received] PHST- 2008/03/13 [revised] PHST- 2008/03/19 [accepted] AID - S1550-4131(08)00081-8 [pii] AID - 10.1016/j.cmet.2008.03.010 [doi] PST - ppublish

Iadecola, C., Duering, M., Hachinski, V., Joutel, A., Pendlebury, S. T., Schneider, J. A., & Dichgans, M. (2019). Vascular Cognitive Impairment and Dementia: JACC Scientific Expert Panel. *Journal of the American College of Cardiology, 73*(25), 3326-3344. doi:10.1016/j.jacc.2019.04.034

Iadecola, C., & Nedergaard, M. (2007). Glial regulation of the cerebral microvasculature. (1097-6256 (Print)).

Iadecola, C., Park, L., & Capone, C. (2009). Threats to the mind: aging, amyloid, and hypertension. *Stroke, 40*(3 Suppl), S40-S44. doi:10.1161/STROKEAHA.108.533638

Ichimura, T., Fraser Pa Fau - Cserr, H. F., & Cserr, H. F. (1991). Distribution of extracellular tracers in perivascular spaces of the rat brain. (0006-8993 (Print)).
Ihara, M., & Tomimoto, H. (2011). Lessons from a mouse model characterizing features of vascular cognitive impairment with white matter changes. *Journal of aging research, 2011*, 978761-978761. doi:10.4061/2011/978761
Ihara, M., & Yamamoto, Y. (2016). Emerging Evidence for Pathogenesis of Sporadic Cerebral Small Vessel Disease. (1524-4628 (Electronic)).
Ii, S., Kitade, H., Ishida, S., Imai, Y., Watanabe, Y., & Wada, S. (2020). Multiscale modeling of human cerebrovasculature: A hybrid approach using image-based geometry and a mathematical algorithm. *PLoS computational biology, 16*(6), e1007943-e1007943. doi:10.1371/journal.pcbi.1007943
Iliff, J. J., Wang M Fau - Zeppenfeld, D. M., Zeppenfeld Dm Fau - Venkataraman, A., Venkataraman A Fau - Plog, B. A., Plog Ba Fau - Liao, Y., Liao Y Fau - Deane, R., . . . Nedergaard, M. (2013). Cerebral arterial pulsation drives paravascular CSF-interstitial fluid exchange in the murine brain. (1529-2401 (Electronic)).
Iliff, J. J., Wang, M., Liao, Y., Plogg, B. A., Peng, W., Gundersen, G. A., . . . Nedergaard, M. (2012). A paravascular pathway facilitates CSF flow through the brain parenchyma and the clearance of interstitial solutes, including amyloid β. *Science translational medicine, 4*(147), 147ra111-147ra111. doi:10.1126/scitranslmed.3003748
Iliff, J. J., Wang, M., Zeppenfeld, D. M., Venkataraman, A., Plog, B. A., Liao, Y., . . . Nedergaard, M. (2013a). Cerebral arterial pulsation drives paravascular CSF-interstitial fluid exchange in the murine brain. *The Journal of neuroscience : the official journal of the Society for Neuroscience, 33*(46), 18190-18199. doi:10.1523/JNEUROSCI.1592-13.2013
Iliff, J. J., Wang, M., Zeppenfeld, D. M., Venkataraman, A., Plog, B. A., Liao, Y., . . . Nedergaard, M. (2013b). Cerebral Arterial Pulsation Drives Paravascular CSF–Interstitial Fluid Exchange in the Murine Brain. *The Journal of Neuroscience, 33*(46), 18190-18199. doi:10.1523/JNEUROSCI.1592-13.2013
Imbimbo, B. P., Solfrizzi, V., & Panza, F. (2010). Are NSAIDs useful to treat Alzheimer's disease or mild cognitive impairment? *Frontiers in Aging Neuroscience, 2*, 19. doi:10.3389/fnagi.2010.00019
in t' Veld, B. A., Ruitenberg A Fau - Hofman, A., Hofman A Fau - Launer, L. J., Launer Lj Fau - van Duijn, C. M., van Duijn Cm Fau - Stijnen, T., Stijnen T Fau - Breteler, M. M., . . . Stricker, B. H. (2001). Nonsteroidal antiinflammatory drugs and the risk of Alzheimer's disease. (0028-4793 (Print)).
Inaba, T., Miyamoto, N., Hira, K., Ueno, Y., Yamashiro, K., Watanabe, M., . . . Urabe, T. (2019). Protective Role of Levetiracetam Against Cognitive Impairment And Brain White Matter Damage in Mouse prolonged Cerebral Hypoperfusion. (1873-7544 (Electronic)).
Inzitari, D., Pracucci, G., Poggesi, A., Carlucci, G., Barkhof, F., Chabriat, H., . . . Group, L. S. (2009). Changes in white matter as determinant of global functional decline in older independent outpatients: three year follow-up of LADIS (leukoaraiosis and disability) study cohort. *BMJ (Clinical research ed.), 339*, b2477-b2477. doi:10.1136/bmj.b2477
Ismail, R., Parbo, P., Madsen, L. S., Hansen, A. K., Hansen, K. V., Schaldemose, J. L., . . . Brooks, D. J. (2020). The relationships between neuroinflammation, beta-amyloid and tau deposition in Alzheimer's disease: a longitudinal PET

study. *Journal of Neuroinflammation, 17*(1), 151-151. doi:10.1186/s12974-020-01820-6
Jackson, L., Dumanli, S., Johnson, M. H., Fagan, S. C., & Ergul, A. (2020). Microglia knockdown reduces inflammation and preserves cognition in diabetic animals after experimental stroke. *Journal of Neuroinflammation, 17*(1), 137-137. doi:10.1186/s12974-020-01815-3
Janova, H., Arinrad, S., Balmuth, E., Mitjans, M., Hertel, J., Habes, M., . . . Nave, K.-A. (2018). Microglia ablation alleviates myelin-associated catatonic signs in mice. *The Journal of Clinical Investigation, 128*(2), 734-745. doi:10.1172/JCI97032
Janssen, L., Dubbelaar, M. L., Holtman, I. R., de Boer-Bergsma, J., Eggen, B. J., Boddeke, H. W., . . . Van Dam, D. (2017). Aging, microglia and cytoskeletal regulation are key factors in the pathological evolution of the APP23 mouse model for Alzheimer's disease. (0925-4439 (Print)).
Jellinger, K. A. (2013). Pathology and pathogenesis of vascular cognitive impairment-a critical update. *Frontiers in Aging Neuroscience, 5*, 17-17. doi:10.3389/fnagi.2013.00017
Jiang-Shieh, Y. F., Wu Ch Fau - Chang, M. L., Chang Ml Fau - Shieh, J. Y., Shieh Jy Fau - Wen, C. Y., & Wen, C. Y. (2003). Regional heterogeneity in immunoreactive macrophages/microglia in the rat pineal gland. (0742-3098 (Print)).
Johnston, S. C., O'Meara Es Fau - Manolio, T. A., Manolio Ta Fau - Lefkowitz, D., Lefkowitz D Fau - O'Leary, D. H., O'Leary Dh Fau - Goldstein, S., Goldstein S Fau - Carlson, M. C., . . . Longstreth, W. T., Jr. (2004). Cognitive impairment and decline are associated with carotid artery disease in patients without clinically evident cerebrovascular disease. (1539-3704 (Electronic)).
Jokinen, H., Ryberg, C., Kalska, H., Ylikoski, R., Rostrup, E., Stegmann, M. B., . . . group, L. (2007). Corpus callosum atrophy is associated with mental slowing and executive deficits in subjects with age-related white matter hyperintensities: the LADIS Study. *Journal of neurology, neurosurgery, and psychiatry, 78*(5), 491-496. doi:10.1136/jnnp.2006.096792
Jones, E. G. (1970). On the mode of entry of blood vessels into the cerebral cortex. *Journal of anatomy, 106*(Pt 3), 507-520. Retrieved from https://pubmed.ncbi.nlm.nih.gov/5423942

https://www.ncbi.nlm.nih.gov/pmc/articles/PMC1233426/
Jung S, A. J., Graemmel P, Sunshine MJ, Kreutzberg GW, Sher A, Littman DR. (2000). Analysis of fractalkine receptor CX(3)CR1 function by targeted deletion and green fluorescent protein reporter gene insertion. *Mol Cell Biol*.
Jung, S., Aliberti J Fau - Graemmel, P., Graemmel P Fau - Sunshine, M. J., Sunshine Mj Fau - Kreutzberg, G. W., Kreutzberg Gw Fau - Sher, A., Sher A Fau - Littman, D. R., & Littman, D. R. (2000). Analysis of fractalkine receptor CX(3)CR1 function by targeted deletion and green fluorescent protein reporter gene insertion. (0270-7306 (Print)). doi:D - NLM: PMC85780 EDAT- 2000/05/11 09:00 MHDA- 2000/07/08 11:00 CRDT- 2000/05/11 09:00 PST - ppublish
Jung, S., Aliberti, J., Graemmel, P., Sunshine, M. J., Kreutzberg, G. W., Sher, A., & Littman, D. R. (2000). Analysis of fractalkine receptor CX(3)CR1 function by targeted deletion and green fluorescent protein reporter gene insertion. *Molecular and cellular biology, 20*(11), 4106-4114. doi:10.1128/mcb.20.11.4106-4114.2000
Kakae, M., Tobori, S., Morishima, M., Nagayasu, K., Shirakawa, H., & Kaneko, S. (2019a). Depletion of microglia ameliorates white matter injury and cognitive

impairment in a mouse chronic cerebral hypoperfusion model. (1090-2104 (Electronic)).
Kakae, M., Tobori, S., Morishima, M., Nagayasu, K., Shirakawa, H., & Kaneko, S. (2019b). Depletion of microglia ameliorates white matter injury and cognitive impairment in a mouse chronic cerebral hypoperfusion model. LID - S0006-291X(19)30923-4 [pii] LID - 10.1016/j.bbrc.2019.05.055 [doi]. (1090-2104 (Electronic)).
Kalaria, R. N. (2012). Cerebrovascular disease and mechanisms of cognitive impairment: evidence from clinicopathological studies in humans. (1524-4628 (Electronic)).
Kalaria, R. N. (2016). Neuropathological diagnosis of vascular cognitive impairment and vascular dementia with implications for Alzheimer's disease. *Acta neuropathologica, 131*(5), 659-685. doi:10.1007/s00401-016-1571-z
Kalaria, R. N. (2016). Neuropathological diagnosis of vascular cognitive impairment and vascular dementia with implications for Alzheimer's disease. (1432-0533 (Electronic)). doi:D - NLM: PMC4835512 OTO - NOTNLM
Kalaria, R. N., Kenny Ra Fau - Ballard, C. G., Ballard Cg Fau - Perry, R., Perry R Fau - Ince, P., Ince P Fau - Polvikoski, T., & Polvikoski, T. (2004). Towards defining the neuropathological substrates of vascular dementia. (0022-510X (Print)).
Kandiah, N., Goh, O., Mak, E., Marmin, M., & Ng, A. (2012). Carotid stenosis: a risk factor for cerebral white-matter disease. (1532-8511 (Electronic)).
Kapasi, A., DeCarli, C., & Schneider, J. A. (2017). Impact of multiple pathologies on the threshold for clinically overt dementia. (1432-0533 (Electronic)).
Karperien, A., Ahammer, H., & Jelinek, H. F. (2013). Quantitating the subtleties of microglial morphology with fractal analysis. *Frontiers in Cellular Neuroscience, 7*, 3-3. doi:10.3389/fncel.2013.00003
Kaskie, B., & Storandt, M. (1995). Visuospatial deficit in dementia of the Alzheimer type. (0003-9942 (Print)).
Kataoka, H., Kim Sw Fau - Plesnila, N., & Plesnila, N. (2004). Leukocyte-endothelium interactions during permanent focal cerebral ischemia in mice. (0271-678X (Print)).
Kettenmann, H., Hanisch Uk Fau - Noda, M., Noda M Fau - Verkhratsky, A., & Verkhratsky, A. (2011). Physiology of microglia. (1522-1210 (Electronic)).
Kilkenny, C., Browne, W. J., Cuthill, I. C., Emerson, M., & Altman, D. G. (2010). Improving bioscience research reporting: the ARRIVE guidelines for reporting animal research. *PLoS biology, 8*(6), e1000412-e1000412. doi:10.1371/journal.pbio.1000412
Kim, H. A., Miller Aa Fau - Drummond, G. R., Drummond Gr Fau - Thrift, A. G., Thrift Ag Fau - Arumugam, T. V., Arumugam Tv Fau - Phan, T. G., Phan Tg Fau - Srikanth, V. K., . . . Sobey, C. G. (2012). Vascular cognitive impairment and Alzheimer's disease: role of cerebral hypoperfusion and oxidative stress. (1432-1912 (Electronic)).
Kim, T. N., Goodwill, P. W., Chen, Y., Conolly, S. M., Schaffer, C. B., Liepmann, D., & Wang, R. A. (2012). Line-Scanning Particle Image Velocimetry: An Optical Approach for Quantifying a Wide Range of Blood Flow Speeds in Live Animals. *PLoS ONE, 7*(6), e38590. doi:10.1371/journal.pone.0038590
Kimbrough, I. F., Robel, S., Roberson, E. D., & Sontheimer, H. (2015). Vascular amyloidosis impairs the gliovascular unit in a mouse model of Alzheimer's disease. *Brain : a journal of neurology, 138*(Pt 12), 3716-3733. doi:10.1093/brain/awv327
Kitagawa, K., Matsumoto M Fau - Yang, G., Yang G Fau - Mabuchi, T., Mabuchi T Fau - Yagita, Y., Yagita Y Fau - Hori, M., Hori M Fau - Yanagihara, T., &

Yanagihara, T. (1998). Cerebral ischemia after bilateral carotid artery occlusion and intraluminal suture occlusion in mice: evaluation of the patency of the posterior communicating artery. (0271-678X (Print)).
Kitamura, A., Manso, Y., Duncombe, J., Searcy, J., Koudelka, J., Binnie, M., . . . Horsburgh, K. (2017). Long-term cilostazol treatment reduces gliovascular damage and memory impairment in a mouse model of chronic cerebral hypoperfusion. (2045-2322 (Electronic)).
Klein, D., Patzkó, Á., Schreiber, D., van Hauwermeiren, A., Baier, M., Groh, J., . . . Martini, R. (2015). Targeting the colony stimulating factor 1 receptor alleviates two forms of Charcot–Marie–Tooth disease in mice. *Brain, 138*(11), 3193-3205. doi:10.1093/brain/awv240
Kleinfeld, D., Mitra, P. P., Helmchen, F., & Denk, W. (1998). Fluctuations and stimulus-induced changes in blood flow observed in individual capillaries in layers 2 through 4 of rat neocortex. *Proceedings of the National Academy of Sciences of the United States of America, 95*(26), 15741-15746. doi:10.1073/pnas.95.26.15741
Kluge, M. A.-O., Kracht, L., Abdolhoseini, M., Ong, L. K., Johnson, S. J., Nilsson, M., & Walker, F. R. (2017). Impaired microglia process dynamics post-stroke are specific to sites of secondary neurodegeneration. (1098-1136 (Electronic)).
Kluge, M. G. A.-O. h. o. o., Abdolhoseini, M., Zalewska, K., Ong, L. K. A.-O. h. o. o., Johnson, S. J., Nilsson, M., & Walker, F. R. (2018). Spatiotemporal analysis of impaired microglia process movement at sites of secondary neurodegeneration post-stroke. (1559-7016 (Electronic)).
Kluge, M. G. A.-O. h. o. o., Kracht, L., Abdolhoseini, M., Ong, L. K., Johnson, S. J., Nilsson, M., & Walker, F. R. (2017). Impaired microglia process dynamics post-stroke are specific to sites of secondary neurodegeneration. (1098-1136 (Electronic)).
Knopman, D. S., Rocca Wa Fau - Cha, R. H., Cha Rh Fau - Edland, S. D., Edland Sd Fau - Kokmen, E., & Kokmen, E. (2003). Survival study of vascular dementia in Rochester, Minnesota. (0003-9942 (Print)).
Kocur, M., Schneider, R., Pulm, A.-K., Bauer, J., Kropp, S., Gliem, M., . . . Scheu, S. (2015). IFNβ secreted by microglia mediates clearance of myelin debris in CNS autoimmunity. *Acta neuropathologica communications, 3*, 20-20. doi:10.1186/s40478-015-0192-4
Kondo, Y., & Duncan, I. D. (2009). Selective reduction in microglia density and function in the white matter of colony-stimulating factor-1-deficient mice. *Journal of neuroscience research, 87*(12), 2686-2695. doi:10.1002/jnr.22096
Konno, T., Kasanuki, K., Ikeuchi, T., Dickson, D. W., & Wszolek, Z. K. (2018). CSF1R-related leukoencephalopathy: A major player in primary microgliopathies. *Neurology, 91*(24), 1092-1104. doi:10.1212/WNL.0000000000006642
Kozai, T. D. Y., Vazquez, A. L., Weaver, C. L., Kim, S.-G., & Cui, X. T. (2012). In vivo two-photon microscopy reveals immediate microglial reaction to implantation of microelectrode through extension of processes. *Journal of neural engineering, 9*(6), 066001-066001. doi:10.1088/1741-2560/9/6/066001
Kozlowski, C., & Weimer, R. M. (2012). An Automated Method to Quantify Microglia Morphology and Application to Monitor Activation State Longitudinally In Vivo. *PLoS ONE, 7*(2), e31814. doi:10.1371/journal.pone.0031814
Kress, B. T., Iliff Jj Fau - Xia, M., Xia M Fau - Wang, M., Wang M Fau - Wei, H. S., Wei Hs Fau - Zeppenfeld, D., Zeppenfeld D Fau - Xie, L., . . . Nedergaard, M. (2014). Impairment of paravascular clearance pathways in the aging brain. (1531-8249 (Electronic)). doi:D - NLM: NIHMS628368

D - NLM: PMC4245362 EDAT- 2014/09/11 06:00 MHDA- 2015/01/27 06:00 CRDT- 2014/09/11 06:00 PHST- 2014/06/27 00:00 [received] PHST- 2014/09/04 00:00 [revised] PHST- 2014/09/06 00:00 [accepted] PHST- 2014/09/11 06:00 [entrez] PHST- 2014/09/11 06:00 [pubmed] PHST- 2015/01/27 06:00 [medline] AID - 10.1002/ana.24271 [doi] PST - ppublish

Kreutzberg, G. W. (1996). Microglia: a sensor for pathological events in the CNS. (0166-2236 (Print)).

Kunz, A., & Iadecola, C. (2009). Cerebral vascular dysregulation in the ischemic brain. *Handbook of clinical neurology, 92*, 283-305. doi:10.1016/S0072-9752(08)01914-3

Laman, J. D., & Weller, R. O. (2013). Drainage of cells and soluble antigen from the CNS to regional lymph nodes. *Journal of neuroimmune pharmacology : the official journal of the Society on NeuroImmune Pharmacology, 8*(4), 840-856. doi:10.1007/s11481-013-9470-8

Lammie, G. A., Brannan F Fau - Slattery, J., Slattery J Fau - Warlow, C., & Warlow, C. (1997). Nonhypertensive cerebral small-vessel disease. An autopsy study. (0039-2499 (Print)).

Lanza, G., Bramanti, P., Cantone, M., Pennisi, M., Pennisi, G., & Bella, R. (2017). Vascular Cognitive Impairment through the Looking Glass of Transcranial Magnetic Stimulation. *Behavioural neurology, 2017*, 1421326-1421326. doi:10.1155/2017/1421326

Lartey, F. M., Ahn, G. O., Shen, B., Cord, K.-T., Smith, T., Chua, J. Y., . . . Loo, B. W., Jr. (2014). PET imaging of stroke-induced neuroinflammation in mice using [18F]PBR06. *Molecular imaging and biology, 16*(1), 109-117. doi:10.1007/s11307-013-0664-5

Lawson, L. J., Perry Vh Fau - Dri, P., Dri P Fau - Gordon, S., & Gordon, S. (1990). Heterogeneity in the distribution and morphology of microglia in the normal adult mouse brain. (0306-4522 (Print)).

Lawson, L. J., Perry Vh Fau - Gordon, S., & Gordon, S. (1992). Turnover of resident microglia in the normal adult mouse brain. (0306-4522 (Print)).

Levene, M. J., Dombeck Da Fau - Kasischke, K. A., Kasischke Ka Fau - Molloy, R. P., Molloy Rp Fau - Webb, W. W., & Webb, W. W. (2003). In vivo multiphoton microscopy of deep brain tissue. (0022-3077 (Print)).

Levit, A., Hachinski, V., & Whitehead, S. N. (2020). Neurovascular unit dysregulation, white matter disease, and executive dysfunction: the shared triad of vascular cognitive impairment and Alzheimer disease. *GeroScience, 42*(2), 445-465. doi:10.1007/s11357-020-00164-6

Li, Q., Yang, Y., Reis, C., Tao, T., Li, W., Li, X., & Zhang, J. H. (2018). Cerebral Small Vessel Disease. *Cell transplantation, 27*(12), 1711-1722. doi:10.1177/0963689718795148

Liang, K. J., Lee, J. E., Wang, Y. D., Ma, W., Fontainhas, A. M., Fariss, R. N., & Wong, W. T. (2009). Regulation of dynamic behavior of retinal microglia by CX3CR1 signaling. *Investigative ophthalmology & visual science, 50*(9), 4444-4451. doi:10.1167/iovs.08-3357

Liddelow, S. A., Guttenplan, K. A., Clarke, L. E., Bennett, F. C., Bohlen, C. J., Schirmer, L., . . . Barres, B. A. (2017). Neurotoxic reactive astrocytes are induced by activated microglia. *Nature, 541*(7638), 481-487. doi:10.1038/nature21029

Liu, Y., Wu, X.-M., Luo, Q.-Q., Huang, S., Yang, Q.-W. Q., Wang, F.-X., . . . Qian, Z.-M. (2015). CX3CL1/CX3CR1-mediated microglia activation plays a detrimental role in ischemic mice brain via p38MAPK/PKC pathway. *Journal of Cerebral Blood Flow & Metabolism, 35*(10), 1623-1631. doi:10.1038/jcbfm.2015.97

Lok, J., Gupta P Fau - Guo, S., Guo S Fau - Kim, W. J., Kim Wj Fau - Whalen, M. J., Whalen Mj Fau - van Leyen, K., van Leyen K Fau - Lo, E. H., & Lo, E. H. (2007). Cell-cell signaling in the neurovascular unit. (0364-3190 (Print)).
Longstreth, W. T., Jr., Manolio Ta Fau - Arnold, A., Arnold A Fau - Burke, G. L., Burke Gl Fau - Bryan, N., Bryan N Fau - Jungreis, C. A., Jungreis Ca Fau - Enright, P. L., . . . Fried, L. (1996). Clinical correlates of white matter findings on cranial magnetic resonance imaging of 3301 elderly people. The Cardiovascular Health Study. (0039-2499 (Print)).
Looi, J. C., & Sachdev, P. S. (1999). Differentiation of vascular dementia from AD on neuropsychological tests. (0028-3878 (Print)).
Lull, M. E., & Block, M. L. (2010). Microglial activation and chronic neurodegeneration. (1878-7479 (Electronic)).
MacGregor Sharp, M., Saito, S., Keable, A., Gatherer, M., Aldea, R., Agarwal, N., . . . Carare, R. O. (2020). Demonstrating a reduced capacity for removal of fluid from cerebral white matter and hypoxia in areas of white matter hyperintensity associated with age and dementia. *Acta neuropathologica communications, 8*(1), 131-131. doi:10.1186/s40478-020-01009-1
Magnus, T., Chan A Fau - Grauer, O., Grauer O Fau - Toyka, K. V., Toyka Kv Fau - Gold, R., & Gold, R. (2001). Microglial phagocytosis of apoptotic inflammatory T cells leads to down-regulation of microglial immune activation. (0022-1767 (Print)).
Majumdar, A., Cruz, D., Asamoah, N., Buxbaum, A., Sohar, I., Lobel, P., & Maxfield, F. R. (2007). Activation of microglia acidifies lysosomes and leads to degradation of Alzheimer amyloid fibrils. *Molecular biology of the cell, 18*(4), 1490-1496. doi:10.1091/mbc.e06-10-0975
Maki, T., Ihara M Fau - Fujita, Y., Fujita Y Fau - Nambu, T., Nambu T Fau - Miyashita, K., Miyashita K Fau - Yamada, M., Yamada M Fau - Washida, K., . . . Tomimoto, H. (2011). Angiogenic and vasoprotective effects of adrenomedullin on prevention of cognitive decline after chronic cerebral hypoperfusion in mice. (1524-4628 (Electronic)).
Malpetti, M., Kievit, R. A., Passamonti, L., Jones, P. S., Tsvetanov, K. A., Rittman, T., . . . Rowe, J. B. (2020). Microglial activation and tau burden predict cognitive decline in Alzheimer's disease. *Brain, 143*(5), 1588-1602. doi:10.1093/brain/awaa088
Mancia, G., Parati G Fau - Albini, F., Albini F Fau - Villani, A., & Villani, A. (1988). Circadian blood pressure variations and their impact on disease. (0160-2446 (Print)).
Manso, Y., Holland, P. R., Kitamura, A., Szymkowiak, S., Duncombe, J., Hennessy, E., . . . Horsburgh, K. A.-O. h. o. o. (2017). Minocycline reduces microgliosis and improves subcortical white matter function in a model of cerebral vascular disease. LID - 10.1002/glia.23190 [doi]. (1098-1136 (Electronic)).
Markus, H. S., Hunt B Fau - Palmer, K., Palmer K Fau - Enzinger, C., Enzinger C Fau - Schmidt, H., Schmidt H Fau - Schmidt, R., & Schmidt, R. (2005). Markers of endothelial and hemostatic activation and progression of cerebral white matter hyperintensities: longitudinal results of the Austrian Stroke Prevention Study. (1524-4628 (Electronic)).
Marshall, R. S., Festa, J. R., Cheung, Y. K., Chen, R., Pavol, M. A., Derdeyn, C. P., . . . Lazar, R. M. (2012). Cerebral hemodynamics and cognitive impairment: baseline data from the RECON trial. *Neurology, 78*(4), 250-255. doi:10.1212/WNL.0b013e31824365d3
Martin-Estebane, M., & Gomez-Nicola, D. (2020). Targeting Microglial Population Dynamics in Alzheimer's Disease: Are We Ready for a Potential Impact on

Immune Function? *Frontiers in Cellular Neuroscience, 14*, 149-149. doi:10.3389/fncel.2020.00149
Martínez-Muriana, A., Mancuso, R., Francos-Quijorna, I., Olmos-Alonso, A., Osta, R., Perry, V. H., . . . López-Vales, R. (2016). CSF1R blockade slows the progression of amyotrophic lateral sclerosis by reducing microgliosis and invasion of macrophages into peripheral nerves. *Scientific reports, 6*, 25663-25663. doi:10.1038/srep25663
Masuda, T., Sankowski, R., Staszewski, O., Böttcher, C., Amann, L., Sagar, . . . Prinz, M. (2019). Spatial and temporal heterogeneity of mouse and human microglia at single-cell resolution. (1476-4687 (Electronic)).
Mattison, H. A., Nie, H., Gao, H., Zhou, H., Hong, J.-S., & Zhang, J. (2013). Suppressed pro-inflammatory response of microglia in CX3CR1 knockout mice. *Journal of neuroimmunology, 257*(1-2), 110-115. doi:10.1016/j.jneuroim.2013.02.008
McDonough, A., Noor, S., Lee, R. V., Dodge Iii, R., Strosnider, J. S., Shen, J., . . . Weinstein, J. R. (2019). Ischemic preconditioning induces cortical microglial proliferation and a transcriptomic program of robust cell cycle activation. *Glia, 68*(1), 76-94. doi:10.1002/glia.23701
McDonough, A. A.-O., Noor, S., Lee, R. V., Dodge, R., 3rd, Strosnider, J. S., Shen, J., . . . Weinstein, J. A.-O. (2019). Ischemic preconditioning induces cortical microglial proliferation and a transcriptomic program of robust cell cycle activation. (1098-1136 (Electronic)).
McGeer Pl Fau - McGeer, E., McGeer E Fau - Rogers, J., Rogers J Fau - Sibley, J., & Sibley, J. (1990). Anti-inflammatory drugs and Alzheimer disease. (0140-6736 (Print)).
McGeer, P. L., Itagaki S Fau - Tago, H., Tago H Fau - McGeer, E. G., & McGeer, E. G. (1988). Occurrence of HLA-DR reactive microglia in Alzheimer's disease. (0077-8923 (Print)).
McQueen, J., Reimer, M. M., Holland, P. R., Manso, Y., McLaughlin, M., Fowler, J. H., & Horsburgh, K. (2014). Restoration of oligodendrocyte pools in a mouse model of chronic cerebral hypoperfusion. (1932-6203 (Electronic)). doi:D - NLM: PMC3911923 EDAT- 2014/02/06 06:00 MHDA- 2014/12/15 06:00 CRDT- 2014/02/06 06:00 PHST- 2013/07/16 [received] PHST- 2013/12/25 [accepted] AID - 10.1371/journal.pone.0087227 [doi] AID - PONE-D-13-30433 [pii] PST - epublish
Miki, K., Ishibashi S Fau - Sun, L., Sun L Fau - Xu, H., Xu H Fau - Ohashi, W., Ohashi W Fau - Kuroiwa, T., Kuroiwa T Fau - Mizusawa, H., & Mizusawa, H. (2009). Intensity of chronic cerebral hypoperfusion determines white/gray matter injury and cognitive/motor dysfunction in mice. (1097-4547 (Electronic)).
Miron, V. E., & Priller, J. (2020). Investigating Microglia in Health and Disease: Challenges and Opportunities. (1471-4981 (Electronic)).
Mittelbronn, M., Dietz K Fau - Schluesener, H. J., Schluesener Hj Fau - Meyermann, R., & Meyermann, R. (2001). Local distribution of microglia in the normal adult human central nervous system differs by up to one order of magnitude. (0001-6322 (Print)).
Miyanohara, J., Kakae, M., Nagayasu, K., Nakagawa, T., Mori, Y., Arai, K., . . . Kaneko, S. (2018). TRPM2 Channel Aggravates CNS Inflammation and Cognitive Impairment via Activation of Microglia in Chronic Cerebral Hypoperfusion. *The Journal of neuroscience : the official journal of the Society for Neuroscience, 38*(14), 3520-3533. doi:10.1523/JNEUROSCI.2451-17.2018

Mondo, E., Becker, S. C., Kautzman, A. G., Schifferer, M., Baer, C. E., Chen, J., . . . Schafer, D. P. (2020). A developmental analysis of juxtavascular microglia dynamics and interactions with the vasculature. *bioRxiv*, 2020.2005.2025.110908. doi:10.1101/2020.05.25.110908

Mosher, K. I., & Wyss-Coray, T. (2014). Microglial dysfunction in brain aging and Alzheimer's disease. *Biochemical pharmacology, 88*(4), 594-604. doi:10.1016/j.bcp.2014.01.008

Muñoz Maniega, S., Chappell, F. M., Valdés Hernández, M. C., Armitage, P. A., Makin, S. D., Heye, A. K., . . . Wardlaw, J. M. (2017). Integrity of normal-appearing white matter: Influence of age, visible lesion burden and hypertension in patients with small-vessel disease. *Journal of cerebral blood flow and metabolism : official journal of the International Society of Cerebral Blood Flow and Metabolism, 37*(2), 644-656. doi:10.1177/0271678X16635657

Neal, M. L., Fleming, S. M., Budge, K. M., Boyle, A. M., Kim, C., Alam, G., . . . Richardson, J. R. (2020). Pharmacological inhibition of CSF1R by GW2580 reduces microglial proliferation and is protective against neuroinflammation and dopaminergic neurodegeneration. (1530-6860 (Electronic)).

Neher, J. J., Emmrich, J. V., Fricker, M., Mander, P. K., Théry, C., & Brown, G. C. (2013). Phagocytosis executes delayed neuronal death after focal brain ischemia. *Proceedings of the National Academy of Sciences of the United States of America, 110*(43), E4098-E4107. doi:10.1073/pnas.1308679110

Neher, J. J., Neniskyte U Fau - Zhao, J.-W., Zhao Jw Fau - Bal-Price, A., Bal-Price A Fau - Tolkovsky, A. M., Tolkovsky Am Fau - Brown, G. C., & Brown, G. C. (2011). Inhibition of microglial phagocytosis is sufficient to prevent inflammatory neuronal death. (1550-6606 (Electronic)).

Nelson, P. T., Alafuzoff, I., Bigio, E. H., Bouras, C., Braak, H., Cairns, N. J., . . . Beach, T. G. (2012). Correlation of Alzheimer disease neuropathologic changes with cognitive status: a review of the literature. *Journal of neuropathology and experimental neurology, 71*(5), 362-381. doi:10.1097/NEN.0b013e31825018f7

Ngai, A. C., Ko Kr Fau - Morii, S., Morii S Fau - Winn, H. R., & Winn, H. R. (1988). Effect of sciatic nerve stimulation on pial arterioles in rats. (0002-9513 (Print)).

Nguyen, J., Nishimura, N., Fetcho, R. N., Iadecola, C., & Schaffer, C. B. (2011). Occlusion of cortical ascending venules causes blood flow decreases, reversals in flow direction, and vessel dilation in upstream capillaries. *Journal of cerebral blood flow and metabolism : official journal of the International Society of Cerebral Blood Flow and Metabolism, 31*(11), 2243-2254. doi:10.1038/jcbfm.2011.95

Nielsen, H. H., Ladeby R Fau - Fenger, C., Fenger C Fau - Toft-Hansen, H., Toft-Hansen H Fau - Babcock, A. A., Babcock Aa Fau - Owens, T., Owens T Fau - Finsen, B., & Finsen, B. (2009). Enhanced microglial clearance of myelin debris in T cell-infiltrated central nervous system. (0022-3069 (Print)).

Nimmerjahn, A., Kirchhoff F Fau - Helmchen, F., & Helmchen, F. (2005). Resting microglial cells are highly dynamic surveillants of brain parenchyma in vivo. (1095-9203 (Electronic)).

Nishimura, N., Rosidi, N. L., Iadecola, C., & Schaffer, C. B. (2010). Limitations of collateral flow after occlusion of a single cortical penetrating arteriole. *Journal of cerebral blood flow and metabolism : official journal of the International Society of Cerebral Blood Flow and Metabolism, 30*(12), 1914-1927. doi:10.1038/jcbfm.2010.157

Nishio, K., Ihara M Fau - Yamasaki, N., Yamasaki N Fau - Kalaria, R. N., Kalaria Rn Fau - Maki, T., Maki T Fau - Fujita, Y., Fujita Y Fau - Ito, H., . . . Tomimoto, H. (2010). A mouse model characterizing features of vascular dementia with hippocampal atrophy. (1524-4628 (Electronic)).
Nishiyori, A., Minami M Fau - Ohtani, Y., Ohtani Y Fau - Takami, S., Takami S Fau - Yamamoto, J., Yamamoto J Fau - Kawaguchi, N., Kawaguchi N Fau - Kume, T., . . . Satoh, M. (1998). Localization of fractalkine and CX3CR1 mRNAs in rat brain: does fractalkine play a role in signaling from neuron to microglia? (0014-5793 (Print)).
Nissen, J. C., Thompson, K. K., West, B. L., & Tsirka, S. E. (2018). Csf1R inhibition attenuates experimental autoimmune encephalomyelitis and promotes recovery. *Experimental neurology, 307*, 24-36. doi:10.1016/j.expneurol.2018.05.021
Niwa, K., Porter Va Fau - Kazama, K., Kazama K Fau - Cornfield, D., Cornfield D Fau - Carlson, G. A., Carlson Ga Fau - Iadecola, C., & Iadecola, C. (2001). A beta-peptides enhance vasoconstriction in cerebral circulation. (0363-6135 (Print)).
O'Leary, T. P., & Brown, R. E. (2009). Visuo-spatial learning and memory deficits on the Barnes maze in the 16-month-old APPswe/PS1dE9 mouse model of Alzheimer's disease. (1872-7549 (Electronic)).
Okamoto, Y., Yamamoto, T., Kalaria, R. N., Senzaki, H., Maki, T., Hase, Y., . . . Ihara, M. (2012). Cerebral hypoperfusion accelerates cerebral amyloid angiopathy and promotes cortical microinfarcts. *Acta neuropathologica, 123*(3), 381-394. doi:10.1007/s00401-011-0925-9
Okello, A., Edison, P., Archer, H. A., Turkheimer, F. E., Kennedy, J., Bullock, R., . . . Brooks, D. J. (2009). Microglial activation and amyloid deposition in mild cognitive impairment: a PET study. *Neurology, 72*(1), 56-62. doi:10.1212/01.wnl.0000338622.27876.0d
Olah, M., Menon, V., Habib, N., Taga, M., Yung, C., Cimpean, M., . . . De Jager, P. L. (2018). A single cell-based atlas of human microglial states reveals associations with neurological disorders and histopathological features of the aging brain. *bioRxiv*, 343780. doi:10.1101/343780
Olichney, J. M., Hansen La Fau - Hofstetter, C. R., Hofstetter Cr Fau - Grundman, M., Grundman M Fau - Katzman, R., Katzman R Fau - Thal, L. J., & Thal, L. J. (1995). Cerebral infarction in Alzheimer's disease is associated with severe amyloid angiopathy and hypertension. (0003-9942 (Print)).
Olmos-Alonso, A., Schetters, S. T., Sri, S., Askew, K., Mancuso, R., Vargas-Caballero, M., . . . Gomez-Nicola, D. (2016). Pharmacological targeting of CSF1R inhibits microglial proliferation and prevents the progression of Alzheimer's-like pathology. (1460-2156 (Electronic)).
Olmos-Alonso, A., Schetters, S. T. T., Sri, S., Askew, K., Mancuso, R., Vargas-Caballero, M., . . . Gomez-Nicola, D. (2016a). Pharmacological targeting of CSF1R inhibits microglial proliferation and prevents the progression of Alzheimer's-like pathology. *Brain : a journal of neurology, 139*(Pt 3), 891-907. doi:10.1093/brain/awv379
Olmos-Alonso, A., Schetters, S. T. T., Sri, S., Askew, K., Mancuso, R., Vargas-Caballero, M., . . . Gomez-Nicola, D. (2016b). Pharmacological targeting of CSF1R inhibits microglial proliferation and prevents the progression of Alzheimer’s-like pathology. *Brain, 139*(3), 891-907. doi:10.1093/brain/awv379
Pathological correlates of late-onset dementia in a multicentre, community-based population in England and Wales. Neuropathology Group of the Medical

Research Council Cognitive Function and Ageing Study (MRC CFAS). (2001). Retrieved from
Paulson, O. B., Strandgaard S Fau - Edvinsson, L., & Edvinsson, L. (1990). Cerebral autoregulation. (1040-8827 (Print)).
Paxinos, G. F., K. B. J. (2001). The Mouse Brain in Stereotaxic Coordinates. *Academic Press*.
Persyn, E., Hanscombe, K. B., Howson, J. M. M., Lewis, C. M., Traylor, M., & Markus, H. S. (2020). Genome-wide association study of MRI markers of cerebral small vessel disease in 42,310 participants. *Nature communications, 11*(1), 2175-2175. doi:10.1038/s41467-020-15932-3
Poggesi A Fau - Pantoni, L., Pantoni L Fau - Inzitari, D., Inzitari D Fau - Fazekas, F., Fazekas F Fau - Ferro, J., Ferro J Fau - O'Brien, J., O'Brien J Fau - Hennerici, M., . . . Wahlund, A. (2011). 2001-2011: A Decade of the LADIS (Leukoaraiosis And DISability) Study: What Have We Learned about White Matter Changes and Small-Vessel Disease? (1421-9786 (Electronic)).
Poggesi A Fau - Pasi, M., Pasi M Fau - Pescini, F., Pescini F Fau - Pantoni, L., Pantoni L Fau - Inzitari, D., & Inzitari, D. (2016). Circulating biologic markers of endothelial dysfunction in cerebral small vessel disease: A review. (1559-7016 (Electronic)). doi:D - NLM: PMC4758546 [Available on 01/01/17] EDAT- 2015/06/11 06:00 MHDA- 2016/05/18 06:00 CRDT- 2015/06/11 06:00 PHST- 2014/12/31 [received] PHST- 2015/04/17 [revised] PHST- 2015/05/05 [accepted] AID - jcbfm2015116 [pii] AID - 10.1038/jcbfm.2015.116 [doi] PST - ppublish
Poggesi, A., Pasi, M., Pescini, F., Pantoni, L., & Inzitari, D. (2016). Circulating biologic markers of endothelial dysfunction in cerebral small vessel disease: A review. *Journal of cerebral blood flow and metabolism : official journal of the International Society of Cerebral Blood Flow and Metabolism, 36*(1), 72-94. doi:10.1038/jcbfm.2015.116
Pompl, P. N., Mullan Mj Fau - Bjugstad, K., Bjugstad K Fau - Arendash, G. W., & Arendash, G. W. (1999). Adaptation of the circular platform spatial memory task for mice: use in detecting cognitive impairment in the APP(SW) transgenic mouse model for Alzheimer's disease. (0165-0270 (Print)).
Poniatowski, Ł. A., Wojdasiewicz, P., Krawczyk, M., Szukiewicz, D., Gasik, R., Kubaszewski, Ł., & Kurkowska-Jastrzębska, I. (2017). Analysis of the Role of CX3CL1 (Fractalkine) and Its Receptor CX3CR1 in Traumatic Brain and Spinal Cord Injury: Insight into Recent Advances in Actions of Neurochemokine Agents. *Molecular neurobiology, 54*(3), 2167-2188. doi:10.1007/s12035-016-9787-4
Postnov, D. D., Cheng, X., Erdener, S. E., & Boas, D. A. (2019). Choosing a laser for laser speckle contrast imaging. *Scientific reports, 9*(1), 2542-2542. doi:10.1038/s41598-019-39137-x
Prins, N. D., & Scheltens, P. (2015). White matter hyperintensities, cognitive impairment and dementia: an update. (1759-4766 (Electronic)).
Prinz, M., & Mildner, A. (2011). Microglia in the CNS: immigrants from another world. (1098-1136 (Electronic)).
Promjunyakul, N., Lahna, D., Kaye, J. A., Dodge, H. H., Erten-Lyons, D., Rooney, W. D., & Silbert, L. C. (2015). Characterizing the white matter hyperintensity penumbra with cerebral blood flow measures. *NeuroImage. Clinical, 8*, 224-229. doi:10.1016/j.nicl.2015.04.012
Prut, L., Abramowski D Fau - Krucker, T., Krucker T Fau - Levy, C. L., Levy Cl Fau - Roberts, A. J., Roberts Aj Fau - Staufenbiel, M., Staufenbiel M Fau - Wiessner, C., & Wiessner, C. (2007). Aged APP23 mice show a delay in switching to the use of a strategy in the Barnes maze. (0166-4328 (Print)).

Qian, B., Rudy, R. F., Cai, T., & Du, R. (2018). Cerebral Artery Diameter in Inbred Mice Varies as a Function of Strain. *Frontiers in neuroanatomy, 12*, 10-10. doi:10.3389/fnana.2018.00010

Qin, C., Fan, W.-H., Liu, Q., Shang, K., Murugan, M., Wu, L.-J., . . . Tian, D.-S. (2017). Fingolimod Protects Against Ischemic White Matter Damage by Modulating Microglia Toward M2 Polarization via STAT3 Pathway. *Stroke, 48*(12), 3336-3346. doi:10.1161/STROKEAHA.117.018505

Qin, Y. Y., Li, M., Feng, X., Wang, J., Cao, L., Shen, X. K., . . . Qin, Z. H. (2017). Combined NADPH and the NOX inhibitor apocynin provides greater anti-inflammatory and neuroprotective effects in a mouse model of stroke. (1873-4596 (Electronic)).

Rademakers, R., Baker, M., Nicholson, A. M., Rutherford, N. J., Finch, N., Soto-Ortolaza, A., . . . Wszolek, Z. K. (2011). Mutations in the colony stimulating factor 1 receptor (CSF1R) gene cause hereditary diffuse leukoencephalopathy with spheroids. *Nature genetics, 44*(2), 200-205. doi:10.1038/ng.1027

Raivich, G., Bohatschek M Fau - Kloss, C. U., Kloss Cu Fau - Werner, A., Werner A Fau - Jones, L. L., Jones Ll Fau - Kreutzberg, G. W., & Kreutzberg, G. W. (1999). Neuroglial activation repertoire in the injured brain: graded response, molecular mechanisms and cues to physiological function.

Raivich, G., Haas S Fau - Werner, A., Werner A Fau - Klein, M. A., Klein Ma Fau - Kloss, C., Kloss C Fau - Kreutzberg, G. W., & Kreutzberg, G. W. (1998). Regulation of MCSF receptors on microglia in the normal and injured mouse central nervous system: a quantitative immunofluorescence study using confocal laser microscopy. (0021-9967 (Print)).

Raivich, G., & Kreutzberg, G. W. (1994). Pathophysiology of glial growth factor receptors. (0894-1491 (Print)).

Rajani, R. M., & Williams, A. (2017). Endothelial cell-oligodendrocyte interactions in small vessel disease and aging. *Clinical science (London, England : 1979), 131*(5), 369-379. doi:10.1042/CS20160618

Ransohoff, R. M., & El Khoury, J. (2015). Microglia in Health and Disease. (1943-0264 (Electronic)).

Ransohoff, R. M., & El Khoury, J. (2015). Microglia in Health and Disease. *Cold Spring Harbor perspectives in biology, 8*(1), a020560-a020560. doi:10.1101/cshperspect.a020560

Raz, L., Knoefel, J., & Bhaskar, K. (2016). The neuropathology and cerebrovascular mechanisms of dementia. *Journal of cerebral blood flow and metabolism : official journal of the International Society of Cerebral Blood Flow and Metabolism, 36*(1), 172-186. doi:10.1038/jcbfm.2015.164

Reimer, M. M., McQueen J Fau - Searcy, L., Searcy L Fau - Scullion, G., Scullion G Fau - Zonta, B., Zonta B Fau - Desmazieres, A., Desmazieres A Fau - Holland, P. R., . . . Horsburgh, K. (2011). Rapid disruption of axon-glial integrity in response to mild cerebral hypoperfusion. (1529-2401 (Electronic)). doi:D - NLM: EMS61895

D - NLM: PMC4337974 EDAT- 2011/12/14 06:00 MHDA- 2012/02/03 06:00 CRDT-2011/12/14 06:00 AID - 31/49/18185 [pii] AID - 10.1523/JNEUROSCI.4936-11.2011 [doi] PST - ppublish

Rentzos, M., Michalopoulou M Fau - Nikolaou, C., Nikolaou C Fau - Cambouri, C., Cambouri C Fau - Rombos, A., Rombos A Fau - Dimitrakopoulos, A., Dimitrakopoulos A Fau - Vassilopoulos, D., & Vassilopoulos, D. (2005). The role of soluble intercellular adhesion molecules in neurodegenerative disorders. (0022-510X (Print)).

Roberts, A. C., & Porter, K. E. (2013). Cellular and molecular mechanisms of endothelial dysfunction in diabetes. (1752-8984 (Electronic)).
Roberts, J. M., Maniskas, M. E., & Bix, G. J. (2018). Bilateral carotid artery stenosis causes unexpected early changes in brain extracellular matrix and blood-brain barrier integrity in mice. *PLoS ONE, 13*(4), e0195765-e0195765. doi:10.1371/journal.pone.0195765
Roder, S., Danober L Fau - Pozza, M. F., Pozza Mf Fau - Lingenhoehl, K., Lingenhoehl K Fau - Wiederhold, K. H., Wiederhold Kh Fau - Olpe, H. R., & Olpe, H. R. (2003). Electrophysiological studies on the hippocampus and prefrontal cortex assessing the effects of amyloidosis in amyloid precursor protein 23 transgenic mice. (0306-4522 (Print)).
Rogers, J. T., Morganti, J. M., Bachstetter, A. D., Hudson, C. E., Peters, M. M., Grimmig, B. A., . . . Gemma, C. (2011). CX3CR1 deficiency leads to impairment of hippocampal cognitive function and synaptic plasticity. *The Journal of neuroscience : the official journal of the Society for Neuroscience, 31*(45), 16241-16250. doi:10.1523/JNEUROSCI.3667-11.2011
Rojo, R., Raper, A., Ozdemir, D. D., Lefevre, L., Grabert, K., Wollscheid-Lengeling, E., . . . Pridans, C. (2019). Deletion of a Csf1r enhancer selectively impacts CSF1R expression and development of tissue macrophage populations. *Nature communications, 10*(1), 3215-3215. doi:10.1038/s41467-019-11053-8
Rombouts, S. A., Barkhof F Fau - Veltman, D. J., Veltman Dj Fau - Machielsen, W. C., Machielsen Wc Fau - Witter, M. P., Witter Mp Fau - Bierlaagh, M. A., Bierlaagh Ma Fau - Lazeron, R. H., . . . Scheltens, P. (2000). Functional MR imaging in Alzheimer's disease during memory encoding. (0195-6108 (Print)).
Ruitenberg, A., den Heijer T Fau - Bakker, S. L. M., Bakker Sl Fau - van Swieten, J. C., van Swieten Jc Fau - Koudstaal, P. J., Koudstaal Pj Fau - Hofman, A., Hofman A Fau - Breteler, M. M. B., & Breteler, M. M. (2005). Cerebral hypoperfusion and clinical onset of dementia: the Rotterdam Study. (0364-5134 (Print)).
Ryberg, C., Rostrup E Fau - Paulson, O. B., Paulson Ob Fau - Barkhof, F., Barkhof F Fau - Scheltens, P., Scheltens P Fau - van Straaten, E. C. W., van Straaten Ec Fau - van der Flier, W. M., . . . Waldemar, G. (2011). Corpus callosum atrophy as a predictor of age-related cognitive and motor impairment: a 3-year follow-up of the LADIS study cohort. (1878-5883 (Electronic)).
Safaiyan, S., Kannaiyan, N., Snaidero, N., Brioschi, S., Biber, K., Yona, S., . . . Simons, M. (2016). Age-related myelin degradation burdens the clearance function of microglia during aging. (1546-1726 (Electronic)).
Salter, M. W., & Stevens, B. (2017). Microglia emerge as central players in brain disease. (1546-170X (Electronic)).
Salvadores, N., Searcy, J. L., Holland, P. R., & Horsburgh, K. (2017). Chronic cerebral hypoperfusion alters amyloid-β peptide pools leading to cerebral amyloid angiopathy, microinfarcts and haemorrhages in Tg-SwDI mice. (1470-8736 (Electronic)).
Sam, K., Crawley, A. P., Conklin, J., Poublanc, J., Sobczyk, O., Mandell, D. M., . . . Mikulis, D. J. (2016). Development of White Matter Hyperintensity Is Preceded by Reduced Cerebrovascular Reactivity. (1531-8249 (Electronic)).
Schafer, D. P., Lehrman, E. K., Kautzman, A. G., Koyama, R., Mardinly, A. R., Yamasaki, R., . . . Stevens, B. (2012). Microglia sculpt postnatal neural circuits in an activity and complement-dependent manner. *Neuron, 74*(4), 691-705. doi:10.1016/j.neuron.2012.03.026

Schley, D., Carare-Nnadi R Fau - Please, C. P., Please Cp Fau - Perry, V. H., Perry Vh Fau - Weller, R. O., & Weller, R. O. (2006). Mechanisms to explain the reverse perivascular transport of solutes out of the brain. (0022-5193 (Print)).
Schneider, J. A., Arvanitakis Z Fau - Bang, W., Bang W Fau - Bennett, D. A., & Bennett, D. A. (2007). Mixed brain pathologies account for most dementia cases in community-dwelling older persons. (1526-632X (Electronic)).
Schnoor, M., Alcaide, P., Voisin, M.-B., & van Buul, J. D. (2015). Crossing the Vascular Wall: Common and Unique Mechanisms Exploited by Different Leukocyte Subsets during Extravasation. *Mediators of Inflammation, 2015*, 946509. doi:10.1155/2015/946509
Schreiber, S., Bueche, C. Z., Garz, C., & Braun, H. (2013). Blood brain barrier breakdown as the starting point of cerebral small vessel disease? - New insights from a rat model. *Experimental & translational stroke medicine, 5*(1), 4-4. doi:10.1186/2040-7378-5-4
Schuff, N., Matsumoto, S., Kmiecik, J., Studholme, C., Du, A., Ezekiel, F., . . . Weiner, M. W. (2009). Cerebral blood flow in ischemic vascular dementia and Alzheimer's disease, measured by arterial spin-labeling magnetic resonance imaging. *Alzheimer's & dementia : the journal of the Alzheimer's Association, 5*(6), 454-462. doi:10.1016/j.jalz.2009.04.1233
Seo, J. H., Miyamoto, N., Hayakawa, K., Pham, L.-D. D., Maki, T., Ayata, C., . . . Arai, K. (2013). Oligodendrocyte precursors induce early blood-brain barrier opening after white matter injury. *The Journal of Clinical Investigation, 123*(2), 782-786. doi:10.1172/JCI65863
Shang J Fau - Yamashita, T., Yamashita T Fau - Zhai, Y., Zhai Y Fau - Nakano, Y., Nakano Y Fau - Morihara, R., Morihara R Fau - Fukui, Y., Fukui Y Fau - Hishikawa, N., . . . Abe, K. (2016). Strong Impact of Chronic Cerebral Hypoperfusion on Neurovascular Unit, Cerebrovascular Remodeling, and Neurovascular Trophic Coupling in Alzheimer's Disease Model Mouse. (1875-8908 (Electronic)).
Sharma, S., Rakoczy, S., & Brown-Borg, H. (2010). Assessment of spatial memory in mice. *Life sciences, 87*(17-18), 521-536. doi:10.1016/j.lfs.2010.09.004
Shi, Y., Thrippleton, M. J., Blair, G. W., Dickie, D. A., Marshall, I., Hamilton, I., . . . Wardlaw, J. A.-O. (2020). Small vessel disease is associated with altered cerebrovascular pulsatility but not resting cerebral blood flow. (1559-7016 (Electronic)).
Shibata, M., Ohtani R Fau - Ihara, M., Ihara M Fau - Tomimoto, H., & Tomimoto, H. (2004). White matter lesions and glial activation in a novel mouse model of chronic cerebral hypoperfusion. (1524-4628 (Electronic)).
Shibata, M., Yamasaki N Fau - Miyakawa, T., Miyakawa T Fau - Kalaria, R. N., Kalaria Rn Fau - Fujita, Y., Fujita Y Fau - Ohtani, R., Ohtani R Fau - Ihara, M., . . . Tomimoto, H. (2007). Selective impairment of working memory in a mouse model of chronic cerebral hypoperfusion. (1524-4628 (Electronic)).
Shih, A. Y., Blinder, P., Tsai, P. S., Friedman, B., Stanley, G., Lyden, P. D., & Kleinfeld, D. (2013). The smallest stroke: Occlusion of one penetrating vessel leads to infarction and a cognitive deficit. *Nature neuroscience, 16*(1), 55-63. doi:10.1038/nn.3278
Sierra, A., Abiega, O., Shahraz, A., & Neumann, H. (2013). Janus-faced microglia: beneficial and detrimental consequences of microglial phagocytosis. *Frontiers in Cellular Neuroscience, 7*, 6-6. doi:10.3389/fncel.2013.00006
Sierra, A., Encinas, J. M., Deudero, J. J. P., Chancey, J. H., Enikolopov, G., Overstreet-Wadiche, L. S., . . . Maletic-Savatic, M. (2010). Microglia shape adult hippocampal neurogenesis through apoptosis-coupled phagocytosis. *Cell stem cell, 7*(4), 483-495. doi:10.1016/j.stem.2010.08.014

Silva, A. C., Lee Sp Fau - Iadecola, C., Iadecola C Fau - Kim, S. G., & Kim, S. G. (2000). Early temporal characteristics of cerebral blood flow and deoxyhemoglobin changes during somatosensory stimulation. (0271-678X (Print)).

Simpson, J. E., Fernando Ms Fau - Clark, L., Clark L Fau - Ince, P. G., Ince Pg Fau - Matthews, F., Matthews F Fau - Forster, G., Forster G Fau - O'Brien, J. T., . . . Wharton, S. B. (2007). White matter lesions in an unselected cohort of the elderly: astrocytic, microglial and oligodendrocyte precursor cell responses. (0305-1846 (Print)).

Simpson, J. E., Hosny O Fau - Wharton, S. B., Wharton Sb Fau - Heath, P. R., Heath Pr Fau - Holden, H., Holden H Fau - Fernando, M. S., Fernando Ms Fau - Matthews, F., . . . Ince, P. G. (2009). Microarray RNA expression analysis of cerebral white matter lesions reveals changes in multiple functional pathways. (1524-4628 (Electronic)).

Simpson, J. E., Ince Pg Fau - Higham, C. E., Higham Ce Fau - Gelsthorpe, C. H., Gelsthorpe Ch Fau - Fernando, M. S., Fernando Ms Fau - Matthews, F., Matthews F Fau - Forster, G., . . . Wharton, S. B. (2007). Microglial activation in white matter lesions and nonlesional white matter of ageing brains. (0305-1846 (Print)).

Skrobot, O. A., Black, S. E., Chen, C., DeCarli, C., Erkinjuntti, T., Ford, G. A., . . . Kehoe, P. G. (2018). Progress toward standardized diagnosis of vascular cognitive impairment: Guidelines from the Vascular Impairment of Cognition Classification Consensus Study. (1552-5279 (Electronic)).

Smallwood, A., Oulhaj A Fau - Joachim, C., Joachim C Fau - Christie, S., Christie S Fau - Sloan, C., Sloan C Fau - Smith, A. D., Smith Ad Fau - Esiri, M., & Esiri, M. (2012). Cerebral subcortical small vessel disease and its relation to cognition in elderly subjects: a pathological study in the Oxford Project to Investigate Memory and Ageing (OPTIMA) cohort. (1365-2990 (Electronic)).

Smith, E. E. (2017). Clinical presentations and epidemiology of vascular dementia. (1470-8736 (Electronic)).

Smith, J. A., Das A Fau - Ray, S. K., Ray Sk Fau - Banik, N. L., & Banik, N. L. (2012). Role of pro-inflammatory cytokines released from microglia in neurodegenerative diseases. (1873-2747 (Electronic)).

Sperandio, M., Pickard J Fau - Unnikrishnan, S., Unnikrishnan S Fau - Acton, S. T., Acton St Fau - Ley, K., & Ley, K. (2006). Analysis of leukocyte rolling in vivo and in vitro. (0076-6879 (Print)).

Stefani, A., Sancesario G Fau - Pierantozzi, M., Pierantozzi M Fau - Leone, G., Leone G Fau - Galati, S., Galati S Fau - Hainsworth, A. H., Hainsworth Ah Fau - Diomedi, M., & Diomedi, M. (2009). CSF biomarkers, impairment of cerebral hemodynamics and degree of cognitive decline in Alzheimer's and mixed dementia. (1878-5883 (Electronic)).

Stence, N., Waite M Fau - Dailey, M. E., & Dailey, M. E. (2001). Dynamics of microglial activation: a confocal time-lapse analysis in hippocampal slices. (0894-1491 (Print)).

Stowell, R. A.-O., Sipe, G. O., Dawes, R. P., Batchelor, H. N., Lordy, K. A., Whitelaw, B. S., . . . Majewska, A. A.-O. (2019). Noradrenergic signaling in the wakeful state inhibits microglial surveillance and synaptic plasticity in the mouse visual cortex. (1546-1726 (Electronic)).

Stratoulias, V., Venero, J. L., Tremblay, M.-È., & Joseph, B. (2019). Microglial subtypes: diversity within the microglial community. *The EMBO journal, 38*(17), e101997-e101997. doi:10.15252/embj.2019101997

Sturchler-Pierrat, C., Abramowski, D., Duke, M., Wiederhold, K. H., Mistl, C., Rothacher, S., . . . Sommer, B. (1997). Two amyloid precursor protein

transgenic mouse models with Alzheimer disease-like pathology. *Proceedings of the National Academy of Sciences of the United States of America, 94*(24), 13287-13292. doi:10.1073/pnas.94.24.13287
Sturtzel, C. (2017). Endothelial Cells. (0065-2598 (Print)).
Sun, W., Suzuki, K., Toptunov, D., Stoyanov, S., Yuzaki, M., Khiroug, L., & Dityatev, A. (2019). In vivo Two-Photon Imaging of Anesthesia-Specific Alterations in Microglial Surveillance and Photodamage-Directed Motility in Mouse Cortex. *Frontiers in neuroscience, 13*, 421-421. doi:10.3389/fnins.2019.00421
Swartzlander, D. B., Propson, N. E., Roy, E. R., Saito, T., Saido, T., Wang, B., & Zheng, H. (2018). Concurrent cell type-specific isolation and profiling of mouse brains in inflammation and Alzheimer's disease. *JCI insight, 3*(13), e121109. doi:10.1172/jci.insight.121109
Sweeney, M. D., Kisler, K., Montagne, A., Toga, A. W., & Zlokovic, B. V. (2018). The role of brain vasculature in neurodegenerative disorders. *Nature neuroscience, 21*(10), 1318-1331. doi:10.1038/s41593-018-0234-x
Takano, T., Tian Gf Fau - Peng, W., Peng W Fau - Lou, N., Lou N Fau - Libionka, W., Libionka W Fau - Han, X., Han X Fau - Nedergaard, M., & Nedergaard, M. (2006). Astrocyte-mediated control of cerebral blood flow. (1097-6256 (Print)).
Tan, Y.-L., Yuan, Y., & Tian, L. (2020). Microglial regional heterogeneity and its role in the brain. *Molecular psychiatry, 25*(2), 351-367. doi:10.1038/s41380-019-0609-8
Tang Z Fau - Gan, Y., Gan Y Fau - Liu, Q., Liu Q Fau - Yin, J.-X., Yin Jx Fau - Liu, Q., Liu Q Fau - Shi, J., Shi J Fau - Shi, F.-D., & Shi, F. D. (2014). CX3CR1 deficiency suppresses activation and neurotoxicity of microglia/macrophage in experimental ischemic stroke. (1742-2094 (Electronic)).
Thal, D. R., Capetillo-Zarate E Fau - Larionov, S., Larionov S Fau - Staufenbiel, M., Staufenbiel M Fau - Zurbruegg, S., Zurbruegg S Fau - Beckmann, N., & Beckmann, N. (2009). Capillary cerebral amyloid angiopathy is associated with vessel occlusion and cerebral blood flow disturbances. (1558-1497 (Electronic)).
Thambisetty, M., Beason-Held L Fau - An, Y., An Y Fau - Kraut, M. A., Kraut Ma Fau - Resnick, S. M., & Resnick, S. M. (2010). APOE epsilon4 genotype and longitudinal changes in cerebral blood flow in normal aging. (1538-3687 (Electronic)). doi:D - NLM: NIHMS182673

D - NLM: PMC2856443 EDAT- 2010/01/13 06:00 MHDA- 2010/02/13 06:00 CRDT- 2010/01/13 06:00 AID - 67/1/93 [pii] AID - 10.1001/archneurol.2009.913 [doi] PST - ppublish
Toledo, J. B., Arnold, S. E., Raible, K., Brettschneider, J., Xie, S. X., Grossman, M., . . . Trojanowski, J. Q. (2013). Contribution of cerebrovascular disease in autopsy confirmed neurodegenerative disease cases in the National Alzheimer's Coordinating Centre. *Brain : a journal of neurology, 136*(Pt 9), 2697-2706. doi:10.1093/brain/awt188
Tomimoto, H., Lin Jx Fau - Matsuo, A., Matsuo A Fau - Ihara, M., Ihara M Fau - Ohtani, R., Ohtani R Fau - Shibata, M., Shibata M Fau - Miki, Y., . . . Shibasaki, H. (2004). Different mechanisms of corpus callosum atrophy in Alzheimer's disease and vascular dementia. (0340-5354 (Print)).
Toth, P., Tarantini, S., Csiszar, A., & Ungvari, Z. (2017). Functional vascular contributions to cognitive impairment and dementia: mechanisms and consequences of cerebral autoregulatory dysfunction, endothelial impairment, and neurovascular uncoupling in aging. *American journal of*

physiology. Heart and circulatory physiology, 312(1), H1-H20. doi:10.1152/ajpheart.00581.2016
Tremblay, M.-È., Lowery, R. L., & Majewska, A. K. (2010). Microglial interactions with synapses are modulated by visual experience. *PLoS biology, 8*(11), e1000527-e1000527. doi:10.1371/journal.pbio.1000527
van der Flier, W. M., Skoog, I., Schneider, J. A., Pantoni, L., Mok, V., Chen, C. L. H., & Scheltens, P. (2018). Vascular cognitive impairment. (2056-676X (Electronic)).
van Rossum, D., & Hanisch, U. K. (2004). Microglia. (0885-7490 (Print)).
van Veluw, S. J., Hou, S. S., Calvo-Rodriguez, M., Arbel-Ornath, M., Snyder, A. C., Frosch, M. P., . . . Bacskai, B. J. (2020). Vasomotion as a Driving Force for Paravascular Clearance in the Awake Mouse Brain. (1097-4199 (Electronic)).
van Veluw, S. J., Shih, A. Y., Smith, E. E., Chen, C., Schneider, J. A., Wardlaw, J. M., . . . Biessels, G. J. (2017). Detection, risk factors, and functional consequences of cerebral microinfarcts. (1474-4465 (Electronic)).
Vendemiale, G., Romano Ad Fau - Dagostino, M., Dagostino M Fau - de Matthaeis, A., de Matthaeis A Fau - Serviddio, G., & Serviddio, G. (2013). Endothelial dysfunction associated with mild cognitive impairment in elderly population. (1720-8319 (Electronic)).
Videm, V., & Albrigtsen, M. (2008). Soluble ICAM-1 and VCAM-1 as markers of endothelial activation. (1365-3083 (Electronic)).
Vinters, H. A.-O., Zarow, C., Borys, E., Whitman, J. D., Tung, S., Ellis, W. G., . . . Chui, H. C. (2018). Review: Vascular dementia: clinicopathologic and genetic considerations. (1365-2990 (Electronic)).
Virdis, A., Bacca A Fau - Colucci, R., Colucci R Fau - Duranti, E., Duranti E Fau - Fornai, M., Fornai M Fau - Materazzi, G., Materazzi G Fau - Ippolito, C., . . . Taddei, S. (2013). Endothelial dysfunction in small arteries of essential hypertensive patients: role of cyclooxygenase-2 in oxidative stress generation. (1524-4563 (Electronic)).
Viticchi, G., Falsetti L Fau - Vernieri, F., Vernieri F Fau - Altamura, C., Altamura C Fau - Bartolini, M., Bartolini M Fau - Luzzi, S., Luzzi S Fau - Provinciali, L., . . . Silvestrini, M. (2012). Vascular predictors of cognitive decline in patients with mild cognitive impairment. (1558-1497 (Electronic)).
Wagshul, M. E., Eide, P. K., & Madsen, J. R. (2011). The pulsating brain: A review of experimental and clinical studies of intracranial pulsatility. *Fluids and barriers of the CNS, 8*(1), 5-5. doi:10.1186/2045-8118-8-5
Wake, H., Moorhouse Aj Fau - Jinno, S., Jinno S Fau - Kohsaka, S., Kohsaka S Fau - Nabekura, J., & Nabekura, J. (2009). Resting microglia directly monitor the functional state of synapses in vivo and determine the fate of ischemic terminals. (1529-2401 (Electronic)).
Wakita, H., Tomimoto H Fau - Akiguchi, I., Akiguchi I Fau - Kimura, J., & Kimura, J. (1994). Glial activation and white matter changes in the rat brain induced by chronic cerebral hypoperfusion: an immunohistochemical study. (0001-6322 (Print)).
Walker, D. G., Tang, T. M., & Lue, L.-F. (2017). Studies on Colony Stimulating Factor Receptor-1 and Ligands Colony Stimulating Factor-1 and Interleukin-34 in Alzheimer's Disease Brains and Human Microglia. *Frontiers in Aging Neuroscience, 9*, 244-244. doi:10.3389/fnagi.2017.00244
Waller, R., Baxter, L., Fillingham, D. J., Coelho, S., Pozo, J. M., Mozumder, M., . . . Highley, J. R. (2019). Iba-1-/CD68+ microglia are a prominent feature of age-associated deep subcortical white matter lesions. *PLoS ONE, 14*(1), e0210888-e0210888. doi:10.1371/journal.pone.0210888

Wang, F., Cao, Y., Ma, L., Pei, H., Rausch, W. D., & Li, H. (2018). Dysfunction of Cerebrovascular Endothelial Cells: Prelude to Vascular Dementia. *Frontiers in Aging Neuroscience, 10*, 376-376. doi:10.3389/fnagi.2018.00376

Wang, H., Hong, L.-J., Huang, J.-Y., Jiang, Q., Tao, R.-R., Tan, C., . . . Han, F. (2015). P2RX7 sensitizes Mac-1/ICAM-1-dependent leukocyte-endothelial adhesion and promotes neurovascular injury during septic encephalopathy. *Cell research, 25*(6), 674-690. doi:10.1038/cr.2015.61

Wang, Y., Szretter, K. J., Vermi, W., Gilfillan, S., Rossini, C., Cella, M., . . . Colonna, M. (2012). IL-34 is a tissue-restricted ligand of CSF1R required for the development of Langerhans cells and microglia. *Nature immunology, 13*(8), 753-760. doi:10.1038/ni.2360

Ward, N. L., & Lamanna, J. C. (2004). The neurovascular unit and its growth factors: coordinated response in the vascular and nervous systems. (0161-6412 (Print)).

Wardlaw, J. M., Allerhand, M., Eadie, E., Thomas, A., Corley, J., Pattie, A., . . . Deary, I. J. (2017). Carotid disease at age 73 and cognitive change from age 70 to 76 years: A longitudinal cohort study. *Journal of cerebral blood flow and metabolism : official journal of the International Society of Cerebral Blood Flow and Metabolism, 37*(8), 3042-3052. doi:10.1177/0271678X16683693

Wardlaw, J. M., Doubal, F. N., Eadie, E., Chappell, F., Shuler, K., & Cvoro, V. (2011). Little association between intracranial arterial stenosis and lacunar stroke. *Cerebrovascular diseases (Basel, Switzerland), 31*(1), 12-18. doi:10.1159/000319773

Wardlaw, J. M., Smith, C., & Dichgans, M. (2013). Mechanisms of sporadic cerebral small vessel disease: insights from neuroimaging. *The Lancet. Neurology, 12*(5), 483-497. doi:10.1016/S1474-4422(13)70060-7

Wardlaw, J. M., Smith, C., & Dichgans, M. (2013). Mechanisms underlying sporadic cerebral small vessel disease: insights from neuroimaging. *Lancet neurology, 12*(5), 10.1016/S1474-4422(1013)70060-70067. doi:10.1016/S1474-4422(13)70060-7

Wardlaw, J. M., Smith, C., & Dichgans, M. (2019). Small vessel disease: mechanisms and clinical implications. (1474-4465 (Electronic)).

Wardlaw, J. M., Smith, E. E., Biessels, G. J., Cordonnier, C., Fazekas, F., Frayne, R., . . . nEuroimaging, S. T. f. R. V. c. o. (2013). Neuroimaging standards for research into small vessel disease and its contribution to ageing and neurodegeneration. *The Lancet. Neurology, 12*(8), 822-838. doi:10.1016/S1474-4422(13)70124-8

Wardlaw, J. M., Valdés Hernández, M. C., & Muñoz-Maniega, S. (2015). What are white matter hyperintensities made of? Relevance to vascular cognitive impairment. *Journal of the American Heart Association, 4*(6), 001140-001140. doi:10.1161/JAHA.114.001140

Washida, K., Ihara M Fau - Nishio, K., Nishio K Fau - Fujita, Y., Fujita Y Fau - Maki, T., Maki T Fau - Yamada, M., Yamada M Fau - Takahashi, J., . . . Takahashi, R. (2010). Nonhypotensive dose of telmisartan attenuates cognitive impairment partially due to peroxisome proliferator-activated receptor-gamma activation in mice with chronic cerebral hypoperfusion. (1524-4628 (Electronic)).

Weller, R. O., Djuanda E Fau - Yow, H.-Y., Yow Hy Fau - Carare, R. O., & Carare, R. O. (2009). Lymphatic drainage of the brain and the pathophysiology of neurological disease. (1432-0533 (Electronic)).

Wieghofer, P., Knobeloch Kp Fau - Prinz, M., & Prinz, M. (2015). Genetic targeting of microglia. (1098-1136 (Electronic)).

Williams, L. R., & Leggett, R. W. (1989). Reference values for resting blood flow to organs of man. (0143-0815 (Print)).
Winkler, D. T., Bondolfi, L., Herzig, M. C., Jann, L., Calhoun, M. E., Wiederhold, K. H., . . . Jucker, M. (2001). Spontaneous hemorrhagic stroke in a mouse model of cerebral amyloid angiopathy. *The Journal of neuroscience : the official journal of the Society for Neuroscience, 21*(5), 1619-1627. doi:10.1523/JNEUROSCI.21-05-01619.2001
Winkler, E. A., Lu, A. Y., Raygor, K. P., Linzey, J. R., Jonzzon, S., Lien, B. V., . . . Abla, A. A. (2019). Defective vascular signaling & prospective therapeutic targets in brain arteriovenous malformations. (1872-9754 (Electronic)).
Wong, W. T. (2013). Microglial aging in the healthy CNS: phenotypes, drivers, and rejuvenation. *Frontiers in Cellular Neuroscience, 7*, 22-22. doi:10.3389/fncel.2013.00022
Wu, C. H., Chien Hf Fau - Chang, C. Y., Chang Cy Fau - Ling, E. A., & Ling, E. A. (1997). Heterogeneity of antigen expression and lectin labeling on microglial cells in the olfactory bulb of adult rats. (0168-0102 (Print)).
Xie, L., Kang, H., Xu, Q., Chen, M. J., Liao, Y., Thiyagarajan, M., . . . Nedergaard, M. (2013). Sleep drives metabolite clearance from the adult brain. *Science (New York, N.Y.), 342*(6156), 373-377. doi:10.1126/science.1241224
Xing, C., Li, W., Deng, W., Ning, M., & Lo, E. H. (2018). A potential gliovascular mechanism for microglial activation: differential phenotypic switching of microglia by endothelium versus astrocytes. *Journal of Neuroinflammation, 15*(1), 143-143. doi:10.1186/s12974-018-1189-2
Yamada, M., Ihara, M., Okamoto, Y., Maki, T., Washida, K., Kitamura, A., . . . Takahashi, R. (2011). The influence of chronic cerebral hypoperfusion on cognitive function and amyloid β metabolism in APP overexpressing mice. *PLoS ONE, 6*(1), e16567-e16567. doi:10.1371/journal.pone.0016567
Yamada, S., DePasquale M Fau - Patlak, C. S., Patlak Cs Fau - Cserr, H. F., & Cserr, H. F. (1991). Albumin outflow into deep cervical lymph from different regions of rabbit brain. (0002-9513 (Print)).
Yamashita M Fau - Oka, K., Oka K Fau - Tanaka, K., & Tanaka, K. (1983). Histopathology of the brain vascular network in moyamoya disease. (0039-2499 (Print)).
Yang, G., Kitagawa K Fau - Matsushita, K., Matsushita K Fau - Mabuchi, T., Mabuchi T Fau - Yagita, Y., Yagita Y Fau - Yanagihara, T., Yanagihara T Fau - Matsumoto, M., & Matsumoto, M. (1997). C57BL/6 strain is most susceptible to cerebral ischemia following bilateral common carotid occlusion among seven mouse strains: selective neuronal death in the murine transient forebrain ischemia. (0006-8993 (Print)).
Yang, Y., & Rosenberg, G. A. (2011). Blood-brain barrier breakdown in acute and chronic cerebrovascular disease. *Stroke, 42*(11), 3323-3328. doi:10.1161/STROKEAHA.110.608257
Yata, K., Nishimura, Y., Unekawa, M., Tomita, Y., Suzuki, N., Tanaka, T., . . . Tomimoto, H. (2014). In vivo imaging of the mouse neurovascular unit under chronic cerebral hypoperfusion. (1524-4628 (Electronic)).
Yezhuvath, U. S., Uh, J., Cheng, Y., Martin-Cook, K., Weiner, M., Diaz-Arrastia, R., . . . Lu, H. (2012). Forebrain-dominant deficit in cerebrovascular reactivity in Alzheimer's disease. *Neurobiol Aging, 33*(1), 75-82. doi:10.1016/j.neurobiolaging.2010.02.005
Yousef, H., Czupalla, C. J., Lee, D., Chen, M. B., Burke, A. N., Zera, K. A., . . . Wyss-Coray, T. (2019). Aged blood impairs hippocampal neural precursor activity and activates microglia via brain endothelial cell VCAM1. *Nature medicine, 25*(6), 988-1000. doi:10.1038/s41591-019-0440-4

Zhai Y Fau - Yamashita, T., Yamashita T Fau - Nakano, Y., Nakano Y Fau - Sun, Z., Sun Z Fau - Morihara, R., Morihara R Fau - Fukui, Y., Fukui Y Fau - Ohta, Y., . . . Abe, K. (2016). Disruption of White Matter Integrity by Chronic Cerebral Hypoperfusion in Alzheimer's Disease Mouse Model. (1875-8908 (Electronic)).

Zhai Y Fau - Yamashita, T., Yamashita T Fau - Nakano, Y., Nakano Y Fau - Sun, Z., Sun Z Fau - Shang, J., Shang J Fau - Feng, T., Feng T Fau - Morihara, R., . . . Abe, K. (2016). Chronic Cerebral Hypoperfusion Accelerates Alzheimer's Disease Pathology with Cerebrovascular Remodeling in a Novel Mouse Model. (1875-8908 (Electronic)).

Zhang, L.-Y., Pan, J., Mamtilahun, M., Zhu, Y., Wang, L., Venkatesh, A., . . . Yang, G.-Y. (2020). Microglia exacerbate white matter injury via complement C3/C3aR pathway after hypoperfusion. *Theranostics, 10*(1), 74-90. doi:10.7150/thno.35841

Zhu, J., Wang Y Fau - Li, J., Li J Fau - Deng, J., Deng J Fau - Zhou, H., & Zhou, H. (2014). Intracranial artery stenosis and progression from mild cognitive impairment to Alzheimer disease. (1526-632X (Electronic)).

Appendix

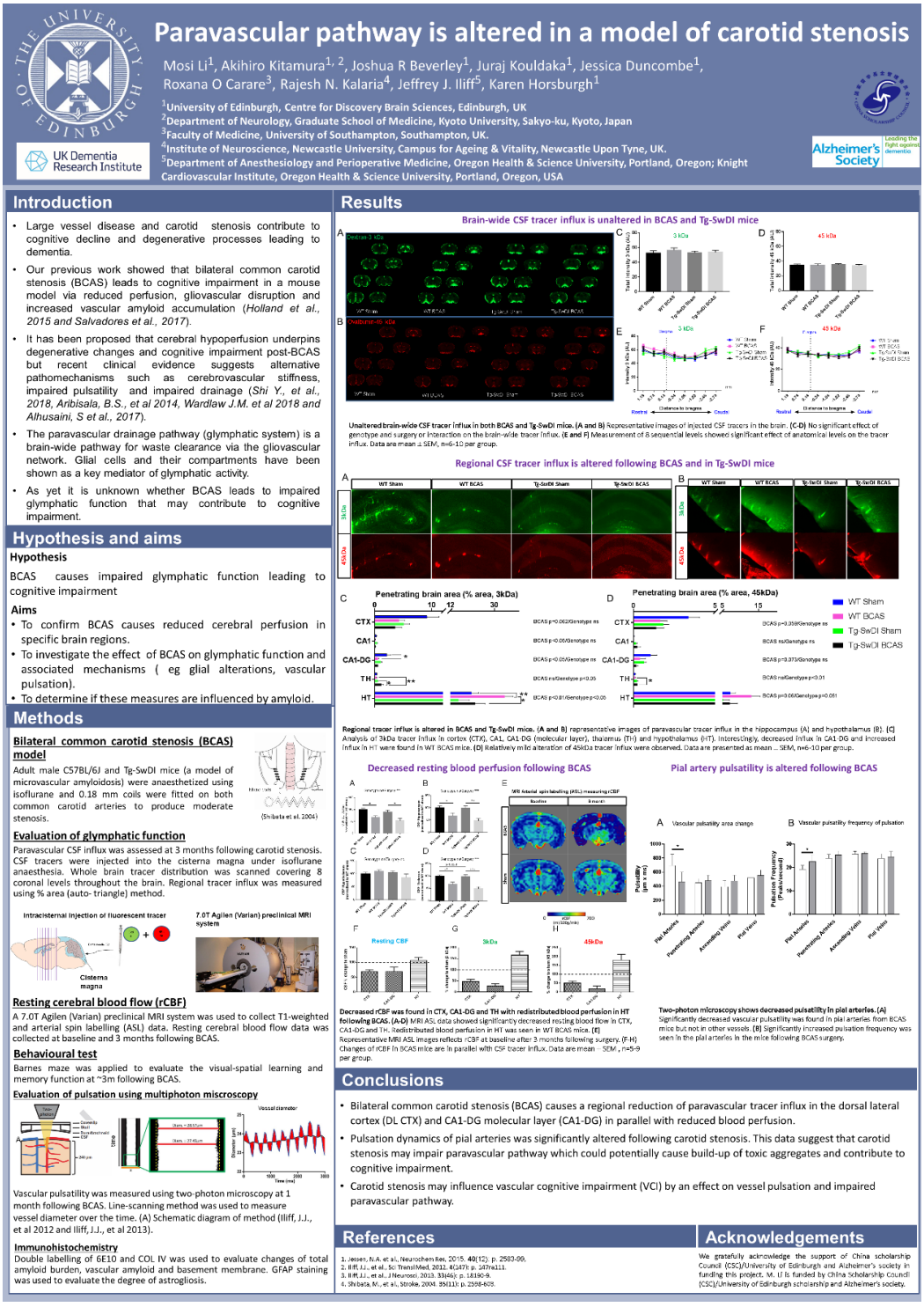

Appendix Figure 1 Impaired paravascular drainage following BCAS. Poster generated and presented by Dr Mosi Li, demonstrates impairments in paravascular drainage pathways following BCAS which is associated with impaired arterial pulsation.